



Università degli Studi di Genova
Facoltà di Scienze M.F.N.

The Forward Tagger detector for CLAS12 at Jefferson Laboratory and the MesonEx experiment

Andrea Celentano

Advisors:
Prof. Mauro Taiuti
Dott. Marco Battaglieri

External advisor:
Prof. Adam Szczepaniak

Introduction

The phenomenology of hadrons and, in particular, the study of their spectrum, led more than forty years ago to the development of the Quark Model, where baryons and mesons are described as bound systems of three quarks or of a quark-antiquark pair, respectively. While this picture still holds and has been proven to reproduce many features of the hadron spectrum, we now know that the hadron mass cannot be explained only in terms of the quark masses, but it is mainly due to the dynamics of the gluons that bind them. Measuring the spectrum of hadrons, studying their properties and inner structure is therefore crucial to achieve a deep knowledge of the strong force.

Mesons, being made by a quark and an anti-quark, are the simplest quark bound system and therefore the ideal benchmark to study the interaction between quarks, understand what the role of gluons is, and investigate the origin of confinement. Meson spectroscopy is, therefore, a powerful tool to investigate how QCD works at the proton mass scale. Theoretical calculations suggest that these studies, traditionally dealt with hadronic probes, can be performed through the scattering of high-energy photons. This kind of reaction, in fact, is expected to be more effective in the production of “exotic mesons”, i.e. states with quantum numbers that are not compatible with the Constituent Quark Model, that would be clear evidence for the presence of gluons in hadron dynamic.

This work is part of the “MesonEx” experiment, that will run during 2016 in experimental Hall B of the Thomas Jefferson National Accelerator Facility (Jefferson Lab or JLab) in Virginia, USA. The main goal is to perform a comprehensive study of the meson spectrum in the light quark sector, within the mass range 1.0-3.0 GeV/ c^2 , with precise determination of resonance properties, looking for rare states and exotic mesons. Quantum numbers will be accessed via Partial Wave Analysis (PWA) of the decay products. A high flux of quasi-real, linearly polarized, photons will be produced by low Q^2 electron scattering. The 11 GeV/ c electrons from the CEBAF accelerator will impinge on a liquid hydrogen target. Electrons scattered at low angle will be detected by the Forward Tagger (FT), a new dedicated facility. Hadrons in the final state will be measured using the CLAS12 detector.

In this work I performed a feasibility study of the reaction $\gamma^*p \rightarrow p\pi^0\eta$. This is one of the “golden-channels” that the experiment will measure, searching for exotic states. In the past, different experiments showed evidence for an exotic meson in the $\pi^0\eta$ system, the $\pi_1(1400)$. However, the situation is still unclear and a definite answer about the existence of an exotic state is not yet known. A better study of this state is therefore very attractive.

I obtained a preliminary estimate of the experimental sensitivity to the exotic state through a MonteCarlo simulation. First, I generated MonteCarlo events according to a theoretical model that I constructed together with V. Mathieu and A. Szczepaniak. These were then projected to the CLAS12+FT detector. Finally, I performed the partial wave analysis of the reconstructed events, to verify if the reaction amplitude could be correctly reconstructed.

I developed the production amplitude in the Regge theory framework of high-energy scattering. To validate the model, and fix the free parameters, I compared the results to the data collected,

at lower energy, by the CLAS-g12 experiment for the reaction $\gamma p \rightarrow p\pi^0\eta$, that I analyzed as part of this work. I obtained a first estimate of the differential reaction cross-section, as a function of the $\pi^0\eta$ invariant mass, in different bins of the photon beam energy. This experimental observable can be directly compared with the theoretical prediction from the model, whose free parameters can be extracted by performing a fit to the data. All analysis tools and procedures, tested on data collected in similar kinematics, have been applied to MesonEx pseudo-data, ready to be used in the real analysis, as soon as data will be available.

In parallel to the analysis activity, I participated in the design and construction of the Forward Tagger facility for CLAS12. The Forward Tagger consists of an electromagnetic calorimeter (FT-Cal), to identify and measure the energy of the scattered electron, a hodoscope of scintillators (FT-Hodo), to discriminate charged versus neutral particles, and a tracker (FT-Trck), for the precise determination of the scattering plane.

The FT-Cal is the “core” component of the Forward Tagger. It is meant to detect electrons in the energy range 0.5-4.5 GeV, with energy resolution of the order of 1 – 2%, and almost 100% efficiency. It will also provide a fast trigger signal, to perform coincidences with the CLAS12 detector. The calorimeter is made of 332 lead tungstate (PbWO_4) scintillating crystals, each coupled to an Avalanche PhotoDiode (APD), arranged symmetrically around the beamline, to cover the scattering angles between 2.5° and 4.5° .

To reach these goals, as well as to fulfill the strong requirements dictated by the CLAS12 experimental setup, each component of the FT-Cal needed to be designed and characterized, before the final detector setup is validated. In addition to the design of the analog circuits for the signal acquisition, I performed a measurement of all the critical FT-Cal components, i.e. crystals, APDs, amplifiers, and DAQ chain. This required the development of specific measurement techniques and tools. Finally, I contributed to the construction of two small-scale FT-Cal prototypes, measuring the response to cosmic rays and to electromagnetic showers.

This document is organized as follows. The first Chapter illustrates the physical motivations of the MesonEx program, and presents the experiment. The second Chapter describes the CLAS spectrometer, its upgrade to CLAS12, and the new Forward Tagger Facility. Chapter 3 shows the detailed characterization of the FT-Cal components, and the results obtained from the two small-scale prototypes. Chapters 4 and 5 contain, respectively, the description of the amplitude used to generate pseudo-events for the reaction $\gamma^*p \rightarrow p\pi^0\eta$, and the analysis of the CLAS data used to validate the model and fix the free parameters. Finally, the sixth Chapter describes the full partial wave analysis performed on the MesonEx pseudo-data, used to estimate the sensitivity of the experiment to the discovery of a possible exotic meson.

Contents

1	Introduction to Meson Spectroscopy	5
1.1	Quantum Chromodynamics and Confinement	5
1.2	Models	6
1.3	Lattice QCD	10
1.4	Experimental techniques	13
1.4.1	Peripheral Production	13
1.4.2	$p\bar{p}$ and $n\bar{n}$ reactions	14
1.4.3	Central production	15
1.4.4	e^+e^- experiments	15
1.5	Amplitude analysis	15
1.5.1	Extended maximum likelihood fits	17
1.6	The MesonEx experiment at Jefferson Laboratory	18
1.6.1	Electroproduction at small Q^2	18
2	Experimental equipment in Hall B at JLab	21
2.1	Jefferson Laboratory	21
2.1.1	CEBAF Accelerator	21
2.2	The Hall B Photon Tagger	23
2.3	The CLAS detector	24
2.4	The CLAS12 detector	27
2.4.1	CLAS12 Forward detector	27
2.4.2	CLAS12 Central detector	31
2.5	The Forward Tagger	33
2.5.1	The Electromagnetic Calorimeter (FT-Cal)	35
2.5.2	The Hodoscope (FT-Hodo)	36
2.5.3	The Tracker (FT-Trck)	38
2.5.4	Kinematic, rates and backgrounds	38
3	The Forward Tagger Calorimeter	41
3.1	PbWO ₄ crystals	41
3.1.1	ACCOS measurements	42
3.1.2	Crystals characterization at low temperature	45
3.1.3	Radiation Hardness	46
3.2	Photo Detectors	47
3.2.1	APD layout and operation	47
3.2.2	APD internal gain and dark current measurement	48
3.2.3	APD working point selection	51

3.2.4	Facility for APD Gain Measurement	54
3.2.5	FT-CAL APDs characterization	57
3.3	Amplifiers	57
3.3.1	Requirements	58
3.3.2	Circuit design	58
3.3.3	Performances	60
3.4	Readout electronics and raw data elaboration	61
3.4.1	Signal integration	62
3.5	Online Monitoring System	64
3.6	FT-Cal prototypes	65
3.6.1	FT Proto-9	65
3.6.2	FT Proto-16	71
4	The $\pi^0 \eta$ channel in the MesonEx experiment	75
4.1	Phenomenology of the $\pi^0 \eta$ channel	75
4.2	Production amplitudes in the Regge theory framework	78
4.2.1	Two-body reactions	79
4.2.2	Extension to multi-particles final states	82
4.3	Parametrization of the amplitude for the reaction $\gamma + p \rightarrow p + \pi^0 + \eta$	84
4.3.1	Resonance production	85
4.3.2	Double Regge exchange	86
4.4	Photo-production amplitudes in the low Q^2 framework	88
4.5	Partial wave analysis formalism for $\gamma^* + p \rightarrow p + \pi^0 + \eta$	89
5	Analysis of the reaction $\gamma p \rightarrow p \pi^0 \eta$ measured with CLAS	93
5.1	Events selection	94
5.1.1	Initial state photon selection	94
5.1.2	Vertex selection	95
5.1.3	Exclusive events selection of $\gamma p \rightarrow p \gamma \gamma \gamma$	95
5.1.4	π^0 and η identification	96
5.1.5	Further selections and signal events properties	98
5.2	Detector acceptance	101
5.2.1	MonteCarlo events generation	102
5.2.2	Results	102
5.3	Reaction cross-section	104
5.4	Comparison with theoretical results	105
6	Study of the reaction $\gamma^* p \rightarrow p \pi^0 \eta$ in the MesonEx experiment	109
6.1	AmpTools	109
6.2	Pseudo-events generation	110
6.2.1	Phase-space generator	111
6.2.2	Properties of generated events	112
6.3	Detector simulation and acceptance evaluation	113
6.4	PWA procedure	116
6.5	PWA results	117
6.5.1	Fit 0-a: no exotic contribution, no background	117
6.5.2	Fit 0-b: no exotic contribution	119
6.5.3	Fit 1: 50% a_2 exotic contribution	121

6.5.4	Fit 2: 5% a_2 exotic contribution	124
6.6	Summary and future perspectives	127
	Conclusions	129
	A Leptonic vertex term in the low Q^2 reactions amplitudes	131
	B Resonances decay couplings	133
	Bibliography	135
	Ringraziamenti	143

Chapter 1

Introduction to Meson Spectroscopy

It has been more than thirty years since QCD was postulated as the theory of strong interactions. While much progress has been made in understanding high energy phenomena through this theory, the strong-interaction at low energy has remained obscure. A clear understanding of the non-perturbative regime is necessary since it is here we have the dominant manifestation of the strong force, binding quarks in hadrons that constitute the bulk of the visible mass of the universe.

Mesons, being made by a quark and an anti-quark, are the simplest quark bound system and therefore the ideal benchmark to study the interaction between quarks, understand the role of gluons and investigate the origin of confinement. Meson spectroscopy is a powerful tool to investigate how the QCD partons manifest themselves under the strong interaction at the energy scale of the nucleon mass (GeV).

1.1 Quantum Chromodynamics and Confinement

Quantum Chromodynamics (QCD) is the field theory that describes the *strong interaction* acting between quarks and gluons. Such renormalizable gauge theory is based on the following assumptions:

- The interaction between quarks and gluons corresponds to a conserved charge, the *color*, in analogy to the electric charge for electromagnetic interaction. There are three color charges, conventionally referred to as “green”, “red”, and “blue”, and three corresponding *anti-colors*.
- *Quarks* are massive, spin 1/2 fermions, with fractional electric charge. Other than the latter, quarks bring also a color charge, and anti-quarks an anti-color charge. There are six quarks, referred to as “flavors”, with different masses.
- *Gluons* are massless, spin 1 gauge bosons, with no electric charge, color charge, and anti-color charge. There are 8 allowed color/anti-color charge combinations for gluons.
- The strong interaction between quarks manifests via the exchange of gluons, in analogy to the QED exchange of photons between charged leptons. However, since gluons bring color charge, they can also self interact.

The color group $SU_c(3)$ corresponds to the local symmetry whose gauging gives rise to QCD. Quarks and anti-quarks reside in the fundamental $\mathbf{3}$ representation of the group and in its conjugate $\bar{\mathbf{3}}$ respectively, while gluons reside in the adjoint $\mathbf{8}$ representation.

QCD is governed by the following Lagrangian density:

$$\mathcal{L}_{QCD} = \bar{\psi}_i (i\gamma^\mu (D_\mu)_{i,j} - m \delta_{i,j}) \psi_j - \frac{1}{4} G_a^{\mu,\nu} G_{\mu,\nu}^a \quad (1.1)$$

where:

- $\bar{\psi}_i$ and ψ_j are Dirac spinors representing quark fields, with anti-color and color indexes i and j respectively, while m is the quark mass,
- $(D_\mu)_{i,j}$ is the covariant derivative, that embeds the quark-gluon interaction term,
- $G_a^{\mu,\nu}$ is the gluonic field tensor, defined as:

$$G_a^{\mu,\nu} = \partial^\mu A_a^\nu - \partial^\nu A_a^\mu + g_s f_{abc} A_b^\mu A_c^\nu \quad (1.2)$$

where A_a is the vector field for a gluon with color charge/anti-charge combination a , f_{abc} are the $SU_c(3)$ structure constants, and g_s is the strong interaction coupling constant (the analogous of the electric charge e in QED lagrangian).

The QCD Lagrangian also includes a sum over the six quark flavors, the only flavor-dependent term being the quark mass m .

Formally, the QCD Lagrangian written as in Eq. 1.1 is almost identical to the QED one. Both theories describe the interaction between massive leptons through the exchange of massless vector bosons, with an underlying local symmetry group corresponding to a conserved charge. The main difference is the fact that, unlike photons, gluons have non-zero color charge, thus they can self-interact. This is explicitly described by the third term in the gluonic field tensor (Eq. 1.2), absent in the QED counterpart.

Gluonic self-interaction is a necessary component to describe one of the most peculiar QCD features, the *color confinement*. According to this property, only colour singlets, i.e. states with zero total colour charge, can exist as physical states. This behavior can be naively explained considering that, as two quarks move apart, the intensity of their interaction does not decrease with distance, as happens in QED, but remains constant. In a specific model, the gluonic field narrows like a tube, because of gluons self-interaction, and acts like a stretched string binding the quarks together. When the energy stored in the gluonic field is high enough, a new quark/anti-quark pair is produced, and all the quarks re-organize in color singlets.

The non-abelian nature of the $SU_c(3)$ group, corresponding to gluonic self-interaction terms in the QCD lagrangian, makes the theory deeply non-linear and very hard to solve analytically. Apart from few regimes, involving very high momentum transfer processes, a perturbative approach is not possible. In other words, a multi-gluon-exchange diagrams have the same intensity than the single-gluon exchange, thus can not be neglected in calculations.

1.2 Models

Because of the difficulties in solving QCD exactly to obtain the properties of the physical states, approximation methods have to be used. The most promising redefines the theory on a discrete spacetime lattice, formulating the problem in terms of the path integral in Euclidian space-time, and evaluating the expectation value of the appropriate operator using a MonteCarlo integration

over the field configurations. Such technique is referred to as “Lattice QCD”. However, important results can also be derived, in a more direct way, using QCD-motivated models for hadrons.

The first model that has been developed to describe hadrons is the so-called “Constituent Quark Model” (CQM), derived independently by Gell-Mann [1] and Zweig [2]. In spite of its simplicity, the CQM efficiently introduces a general structure to organize hadrons and explains some of their properties. In the CQM, hadrons are built of massive, spin 1/2 *constituent quarks*, which carry fractional electric charge. Barions and mesons are made respectively of three constituent quarks (qqq) and of a quark/anti-quark pair ($q\bar{q}$).

Mesons quantum numbers are derived from their $q\bar{q}$ structure. Considering that the two quarks can combine their spins to have total spin \mathbf{S} equal to 0 or 1, and can have a relative orbital angular momentum \mathbf{L} , the following expressions hold for the total angular momentum \mathbf{J} , the parity \mathbf{P} , and the charge conjugation parity \mathbf{C} :

$$\mathbf{J} = \mathbf{L} \oplus \mathbf{S} \quad (1.3)$$

$$\mathbf{P} = (-1)^{\mathbf{L}+1} \quad (1.4)$$

$$\mathbf{C} = (-1)^{\mathbf{L}+\mathbf{S}} \quad (1.5)$$

Using these relationships to build up possible $\mathbf{J}^{\mathbf{PC}}$ combinations for mesons, the following allowed quantum numbers are found:

$$0^{-+}, 0^{++}, 1^{--}, 1^{+-}, 1^{-+}, 2^{--}, 2^{-+}, 2^{++}, \dots$$

There is a sequence of $\mathbf{J}^{\mathbf{PC}}$ combinations that are *not* allowed for a simple $q\bar{q}$ system:

$$0^{--}, 0^{+-}, 1^{-+}, 2^{+-}, \dots$$

These latter quantum numbers are known as *explicitly exotic* quantum numbers. If a meson with these quantum numbers is found, it would be a clear evidence of a state other than a simple $q\bar{q}$ configuration.

The original CQM version developed by Gell-Mann foresees three quark flavors, namely “up” (u), “down” (d), and “strange” (s), with electric charges $+2/3$, $-1/3$, $-1/3$ respectively. The model is governed by an underlying $SU_f(3)$ flavor symmetry, such that quarks belong to the fundamental $\mathbf{3}$ representation and anti-quarks to its conjugate $\bar{\mathbf{3}}$. Hadrons are built summing quarks and anti-quarks according to the $SU_f(3)$ algebra. For the specific case of mesons, with a $q\bar{q}$ structure, the following relation holds:

$$\mathbf{3} \otimes \bar{\mathbf{3}} = \mathbf{1} \oplus \mathbf{8} \quad (1.6)$$

Thus a quark and an anti-quark couple together to a flavor singlet or a flavor octet, resulting in a nonet of states. This defines the possible mesons flavor states.

According to the $SU_f(3)$ symmetry, mesons are expected to be organized in “nonets” of particles with the same $\mathbf{J}^{\mathbf{PC}}$ quantum numbers and similar masses. As an example, Figure 1.1 shows two nonets of mesons as predicted by the model, and the observed particles conventionally assigned to these states. The mass of particles belonging to same multiplet is actually not exactly the same due to the partial breaking of the $SU_f(3)$ symmetry, that manifests in a difference between the constituent quark masses.

The Constituent Quark Model formulates a general mass formula that holds for particles belonging to the same multiplet, simply derived from the $SU_f(3)$ algebra rules, neglecting the mass differences between isospin multiplets [swart]:

$$(m_f + m_{f'}) \cdot (4m_k - m_a) - 3m_f m_{f'} = 8m_k^2 - 8m_k m_a + 3m_a^2 \quad (1.7)$$

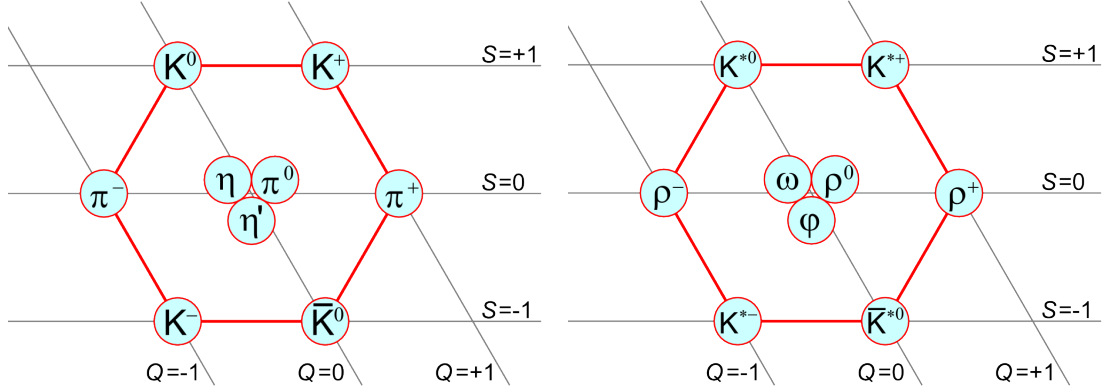


Figure 1.1: 0^{-+} and 1^{-+} nonets from the CQM model, and the experimentally observed particles assigned to these states.

In the equation above, f and f' are the two isospin-0 states, belonging respectively to the $SU_f(3)$ octet and singlet respectively, a are the isospin-1 states, and k are the isospin-1/2 state. For example, for the ground state 0^{-+} nonet, $f = \eta$, $f' = \eta'$, and $a = \pi$. Such formula is useful in predicting the masses of nonet members, and also in verifying that a set of states actually forms a nonet. When applied to the well established nonets, the mass equation holds at 10% level. Another consequence of the $SU_f(3)$ violation is that flavor states do not correspond necessarily to the physical states. The two isospin zero states can mix to form the observed states. This mixing is conventionally parametrized in terms of a mixing angle θ_n such that:

$$\begin{pmatrix} |f\rangle \\ |f'\rangle \end{pmatrix} = \begin{pmatrix} \cos \theta_n & \sin \theta_n \\ -\sin \theta_n & \cos \theta_n \end{pmatrix} \begin{pmatrix} |1\rangle \\ |8\rangle \end{pmatrix} \quad (1.8)$$

The case $\theta_n \simeq 35.26^\circ$ is referred to as “ideal mixing”, because the $s\bar{s}$ quark component is completely separated from the $u\bar{u}$ and $d\bar{d}$ terms:

$$\begin{pmatrix} |f\rangle \\ |f'\rangle \end{pmatrix} = \begin{pmatrix} \frac{1}{\sqrt{2}}(u\bar{u} + d\bar{d}) \\ -s\bar{s} \end{pmatrix} \quad (1.9)$$

Using the $SU_f(3)$ algebra rules, it is possible to predict the nonet mixing angle θ_n purely from the particle masses [3, 4]:

$$\tan^2 \theta_n = \frac{3m_{f'}^2 - 4m_k^2 + m_a^2}{4m_k^2 - m_a^2 - 3m_f^2} \quad (1.10)$$

When θ_n is calculated for well established nonets, it appears that they are all reasonably close to ideal mixing. In fact, there are only two important exceptions, namely the ground state pseudoscalar mesons and the scalar mesons.

Experimentally, the partial $SU_f(3)$ symmetry breaking prevents a certain assignment of the observed resonances to the states predicted by the CQM. The measurement of mesons decays helps in solving this problem since providing information on internal quark composition. For example, the structure of neutral mesons can be investigated from $e^- e^+$ leptonic decay, as sketched in Figure 1.2. The amplitude of this electromagnetic process, calculable from within QED, is proportional to the electric charge of the constituent quarks. The ratio of decay widths for mesons belonging to the same multiplet can be derived assuming the flavor wave functions as predicted by CQM, and results can be then compared to experimental data.

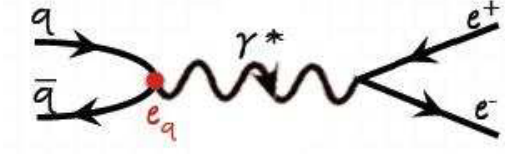


Figure 1.2: Leptonic decay of a neutral meson.

For the vector mesons (ρ , ω , and ϕ), Eq. 1.10 predicts a mixing angle $\theta_n \simeq 40^\circ$, very close to the “ideal mixing” case. Therefore, the flavor wave functions are:

$$\rho = \frac{1}{\sqrt{2}}(u\bar{u} - d\bar{d}) \quad \omega = \frac{1}{\sqrt{2}}(u\bar{u} + d\bar{d}) \quad \phi = s\bar{s}$$

The ratio of leptonic decay widths is therefore:

$$\begin{array}{ccc} \Gamma(\rho \rightarrow e^- e^+) & : & \Gamma(\omega \rightarrow e^- e^+) & : & \Gamma(\phi \rightarrow e^- e^+) = \\ \left\{ \frac{1}{\sqrt{2}} \left(\frac{2}{3} - \left(-\frac{1}{3} \right) \right) \right\}^2 & : & \left\{ \frac{1}{\sqrt{2}} \left(\frac{2}{3} + \left(-\frac{1}{3} \right) \right) \right\}^2 & : & (-1/3)^2 = \\ 9 & : & 1 & : & 2 \end{array} \quad (1.11)$$

The agreement with the experimental data is pretty good:

$$\begin{array}{l} \Gamma(\rho \rightarrow e^- e^+) = (7.04 \pm 0.06) \text{ keV} \\ \Gamma(\omega \rightarrow e^- e^+) = (0.60 \pm 0.02) \text{ keV} \\ \Gamma(\phi \rightarrow e^- e^+) = (1.27 \pm 0.04) \text{ keV} \end{array} \quad (1.12)$$

These results confirm the validity of the “ideal-mixing”, derived from the CQM, and using the experimental values for the particle masses. In conclusion, the Constituent Quark Model is successful in introducing a general scheme to organize mesons in the light-quark sector according to the $SU_f(3)$ flavor symmetry. Also, it reproduces the main features of the meson spectrum, such as the presence of multiplets with same quantum numbers and similar widths, and explains part of the known phenomenology. However, the CQM has some limitations. The involved “quarks” are only massive constituents that carry effective degrees of freedom, and differ from the QCD quarks, the ultimate degree of freedom of the strong interaction. Gluons are not included in the model, and confinement is not explained. Finally, the model is unable to make absolute predictions on masses or decay widths, needing input from experimental data.

The “Bag Model” [5, 6], developed in 1974 by A. Chodos, explicitly introduces gluonic degrees of freedom in hadron dynamics. Hadrons are described as a system of quark, anti-quarks and gluons confined in a finite volume. In such a model, with a suitable tuning of the model parameters, the spectrum of conventional observed mesons can be reproduced [7]. Furthermore, the model predicts four gluonic *hybrid nonets*, i.e. $q\bar{q}g$ states with manifest gluonic degree of freedoms in addition to those of the quark/anti-quark pair, with numbers are 0^{-+} , 1^{--} , 1^{-+} , and 2^{-+} , in the mass range between 1 and 2 GeV. In particular, the mass of the particles belonging to the 1^{-+} exotic nonet is predicted to be approximately 1.4 - 1.6 GeV [8, 9].

Another model that explicitly includes gluonic degrees of freedom in meson dynamics is the “Flux Tube Model” [10], developed in 1984 by N. Isgur and J. Paton. This model concerns the QCD strong-coupling regime, where the gluonic degrees of freedom have condensed into a collective string-like flux tube that binds a quark/anti-quark pair. When the flux tube is in the ground state, the excitation of the $q\bar{q}$ system yields the conventional meson spectrum. “Hybrid” states correspond to the excited modes of the flux tube.

The Flux Tube Model has been used to predict decay width ratios for hybrid mesons. First calculations were carried out by Isgur [10]. Later, Close and Page confirmed the results, and expanded the calculations to include additional hybrids [11]. In the model, the decay of a hybrid meson occurs when the flux tube breaks at any point along its length, producing a new $q\bar{q}$ pair in a relative $\mathbf{J}^{\mathbf{PC}} = \mathbf{0}^{++}$ state, same quantum numbers of the vacuum. The preferred decay mode of hybrids is to an $L = 0$ and $L = 1$ meson. The decay to a pair of $L = 0$ mesons is suppressed, depending on how close the two inverse radii are, assuming the simple harmonic oscillator (SHO) wave function approximation. For the specific case of a 1^{-+} hybrid with mass approximately $2 \text{ GeV}/c^2$ this led to the following decay ratios prediction [11]:

$$\pi f_1 : \pi b_1 : \pi \rho : \pi \eta : \pi \eta' = 60 : 170 : 5 - 20 : 0 - 10 : 0 - 10 \quad (1.13)$$

The decay width of exotic hybrids has been calculated by Page, Swanson and Szccepaniak, within their flux-tube like model [12]. For the exotic π_1 state ($J^{PC} = 1^{-+}$) they obtained $\Gamma = 81 - 168 \text{ MeV}$, the variation coming from different mass values employed in the calculation, between 1.6 and $2.0 \text{ GeV}/c^2$. They also confirmed that the preferred decay modes involve narrow mesons, with daughters that in turn decay, such as $b_1\pi$ or $\rho\pi$. This makes the overall reconstruction and analysis of these states much more complicated than then simple two pseudoscalar decays.

1.3 Lattice QCD

In principle, the knowledget of the QCD lagrangian, Eq. 1.1, should provide insights to compute any quantity of interest, removing the necessity for QCD-inspired models. Applying the path integral formalism, the QCD eigenstates properties are evaluated calculating the expectation values of a suitable operator \mathcal{O} corresponding to the observable of interest:

$$\langle \mathcal{O} \rangle = \frac{1}{\mathcal{Z}} \int dA d\psi d\bar{\psi} \mathcal{O} e^{-S_q} e^{-S_g} \quad (1.14)$$

$$\mathcal{Z} = \int dA d\psi d\bar{\psi} e^{-S_q} e^{-S_g}, \quad (1.15)$$

where S_q and S_g are the quantum-mechanical actions for the fermions and for the gluons respectively, and the operator \mathcal{O} is defined in terms of the quarks and gluon fields. The path integral is defined in Euclidean space for the convergence of the measure. However, fields in Eq. 1.14 fluctuate on all distance scales, and short distance fluctuations needs to be regulated.

Lattice QCD provides a practical way to perform numerical calculation of the path integrals, by evaluating the quantum-mechanical action over a discrete set of spacetime points rather than over the continuum. This also introduces a natural momentum cutoff, approximately equal to the reciprocal of the lattice spacing, so that the theory can be regularized. In the standard lattice QCD formulation, the quark fields are placed on lattice vertexes, while gauge fields connect adjacent lattice points. The gauge invariant operators are either products of gauge links between quark and anti-quark fields, or products of gauge links that form closed paths. Choosing a suitable form for the quark action, the fermion integral in Eq. 1.14 is exactly calculable, while the gauge field integral is evaluated via importance sampled MonteCarlo methods.

Hadron masses are calculated in lattice QCD evaluating the “time-sliced” correlator:

$$C(t_i) = \langle \sum_{\vec{x}_j} \mathcal{O}(\vec{x}_j, t_i) \mathcal{O}^\dagger(\vec{0}, 0) \rangle, \quad (1.16)$$

where the sum is extended all over the lattice site, and the mean value calculated via Eq. 1.14. \mathcal{O} is a suitable gauge-invariant combination of quarks fields and gauge links with the same quan-

tum numbers of the state under study. For example, when calculating the mass of a pion-like pseudo-scalar state with 0^{-+} quantum numbers, a suitable operator would be $\mathcal{O}(\vec{x}_j, t_i) = \bar{\psi}(\vec{x}_j, t_i) \gamma_5 \psi(\vec{x}_j, t_i)$.

The time-sliced correlator embeds information about the energy spectrum, in terms of a weighted sum of exponentials whose coefficients are the eigenstate energies, i.e. the masses, of the states with \mathcal{O} quantum numbers. By inserting a complete set of QCD eigenstates $|\mathcal{N}\rangle$ in Eq. 1.16 one obtains:

$$C(t_i) = \sum_{\mathcal{N}} e^{-E_{\mathcal{N}} t_i} \sum_{\vec{x}_j} \langle 0 | \mathcal{O} | \mathcal{N} \rangle \langle \mathcal{N} | (\vec{x}_j, t_i) \mathcal{O}^\dagger(\vec{0}, 0) | 0 \rangle \equiv \sum_{\mathcal{N}} A_{\mathcal{N}} e^{-E_{\mathcal{N}} t_i} \quad (1.17)$$

The above equation can be used to derive the mass of the ground state. At large times, only the corresponding exponential survives, $C(t_i \rightarrow +\infty) \rightarrow A_0 e^{-E_0 t_i}$. The ground state energy is thus calculated from large-time plateau of the so-called “effective mass”:

$$m_{eff} = \frac{1}{a} \log \left(\frac{C(t_i)}{C(t_{i+1})} \right), \quad (1.18)$$

where a is the lattice spacing. The mass extraction of the excited state from Eq. 1.17 through a multi-exponential fit is non trivial [13]. The region in time for the fit has to be selected, as well as the number of exponentials, and the stability of obtained results to be checked with respect to these parameters. The masses of excited states are indeed calculated computing a matrix of correlator functions, i.e. inserting in Eq. 1.16 two different operators \mathcal{O}_i and \mathcal{O}_j with same quantum numbers of the particles under study, and then solving a “generalized eigenvalue problem” [14].

There are three physical sources of systematic errors in lattice calculations [15, 16]. These are the finite box volume V , the finite lattice spacing a , and the quark mass which is always heavier than the physical value. In principle, the final results from several calculations performed with different parameters could be extrapolated to the continuum limit and to the physical quark masses to predict absolute values of observable quantities. However, since the behavior of QCD on the lattice close to the physical quark masses is still unknown, lattice results are usually interpreted as a “guide” for the existence of certain states, providing a mass hierarchy in the meson spectrum.

A very comprehensive study of the meson spectrum from lattice QCD has been recently carried out by the Hadron Spectrum Collaboration, obtaining predictions for both the isovector and states [17, 18]. In the isovector spectrum calculation authors used three quark flavors, corresponding to u , d , and s , with four different mass settings. Two spatial volumes have been used, with grid sizes $16^3 \times 128$ and $20^3 \times 128$ respectively, both with spatial lattice spacing $a = 0.12$ fm. The isoscalar spectrum has been calculated on the same lattice, using the $16^3 \times 128$ grid size. Results are reported in Figure 1.3. To remove the explicit scale dependence from the lattice spacing, masses have been normalized by fixing the Ω baryon mass (1.67 GeV) to its nominal value. The quark masses scale corresponds to a pion mass of $\simeq 400$ MeV, as reported in the inset. The good agreement between lattice results and experimental data for conventional states, both in terms of number of states and mass hierarchy, proves the advanced stage of the calculation. In the exotic sector (non $q\bar{q}$ states), particles with J^{PC} quantum numbers 1^{-+} , 0^{+-} , and 2^{+-} are predicted. The lightest state has 1^{-+} quantum numbers, while the 0^{+-} and 2^{+-} ground states are almost degenerate and slightly heavier. Excited exotic states with J^{PC} equal to 1^{-+} and 2^{+-} are also predicted. In Figure 1.4, a compilation of several lattice results on the mass of the lightest $J^{PC} = 1^{-+}$ exotic meson as a function of the pion mass is reported. It is evident that there is a good agreement between various lattice calculations and convergence towards the physical pion mass limit is expected in the near future.

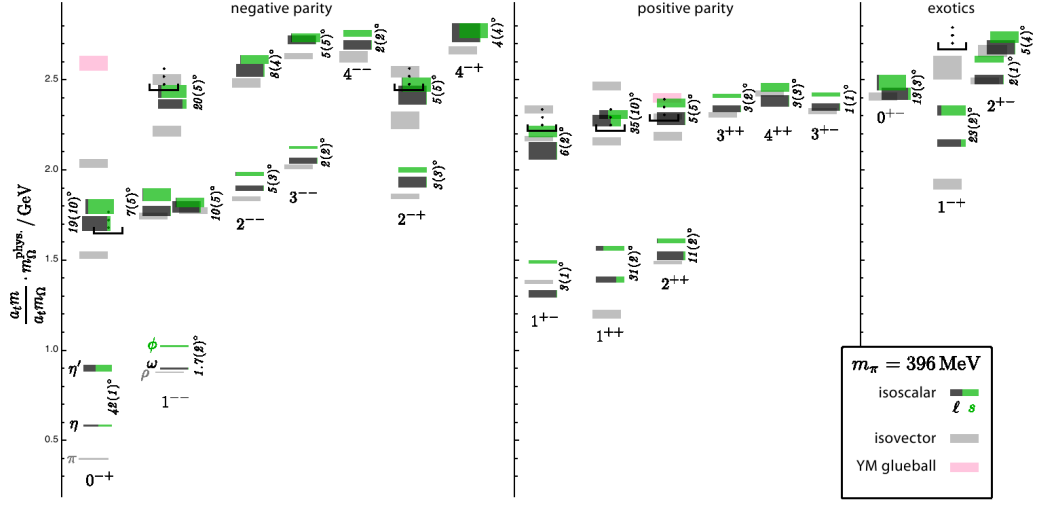


Figure 1.3: Isoscalar and isovector meson spectrum labeled by J^{PC} , from [17, 18]. Results are normalized fixing the Ω baryon mass to its physical value. The box height indicates the one sigma statistical uncertainty above and below the mean value. For isoscalar $SU_f(3)$ doublets, the light-strange content of each state is shown by the fraction of black-green, and the mixing angle is reported. Isovector states are reported in gray. Pink boxes indicate the position of glueballs in the quark-less Yang-Mills theory [19].

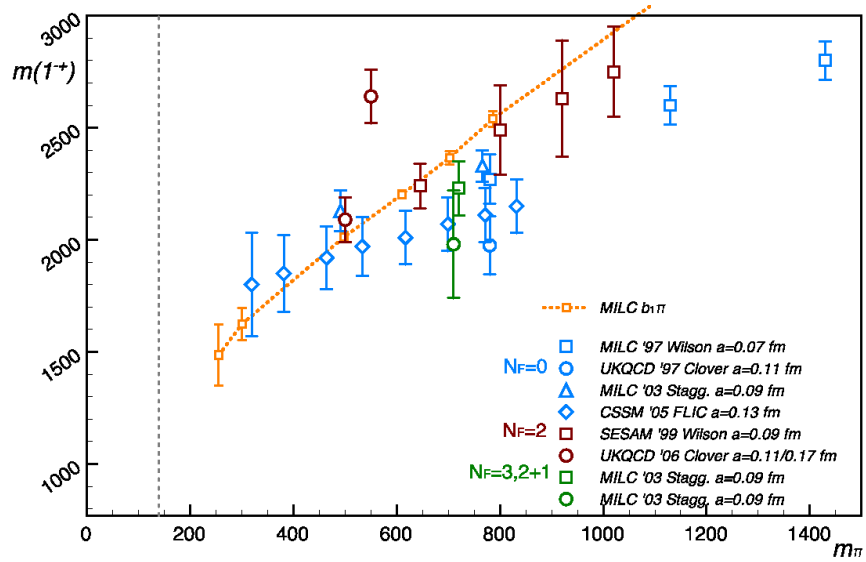


Figure 1.4: Summary of lattice results for the mass of the lightest $J^{PC} = 1^{-+}$ exotic meson. Data are from Refs. [20, 21, 22, 23, 24, 25]

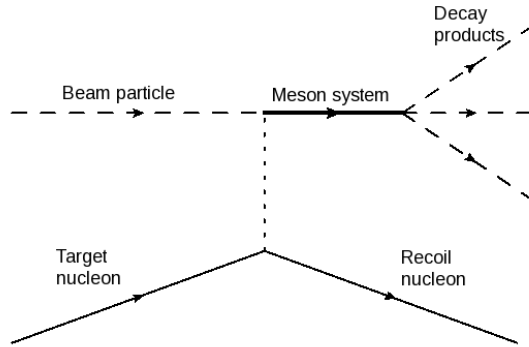


Figure 1.5: Schematic diagram of a peripheral production process. Momentum is exchanged between beam and target through an off-mass-shell particle.

1.4 Experimental techniques

The meson spectrum in the light quarks sector consists of an increasingly large number of broad, overlapping states, crowded into the mass region between 0 and $\simeq 3$ GeV. Experiments can disentangle the spectrum following two complementary approaches. First, different states have different sensitivity to the various production mechanisms. Second, mesons usually decay in more than one mode, thus the measurement of various final states provides specific sensitivity to the signal because of the different background sources.

In *production* experiments, the total energy is shared between a recoil particle and a multi-meson final state. Angular momentum can be transferred in the process, thus the multi-meson system can have contributions from several resonances with different quantum numbers. Spin, parity, and charge conjugation (or C -parity) are restricted only by conservation laws, allowing production of resonances with exotic quantum numbers. In *formation* experiments there is no recoil particle, and therefore mass and quantum numbers of the final state are uniquely determined by the initial state. The direct formation of exotic mesons in e^+e^- or $p\bar{p}$ annihilation is thus forbidden.

1.4.1 Peripheral Production

In the last decades, most of the meson spectroscopy data came from hadronic peripheral production experiments. In these experiments, an intense and energetic beam of pion or kaons hits a nucleon or nuclear target, thus exciting the beam particle through the exchange of momentum and quantum numbers with the recoil nucleon. The target particle is left almost unchanged in the process. The reaction mechanism is sketched in Figure 1.5. The meson state produced has quantum numbers determined by the particle exchanged in the interaction. The cross section of these processes is typically peaked forward, with respect to the incoming beam direction. This behavior is often parametrized with an exponential behaviour in the t variable¹, i.e. $\frac{d\sigma}{dt} \sim e^{-b|t|}$, with slopes $b \sim 2.0 - 5.0$ GeV². Different t ranges correspond to different exchange mechanisms: for example, in charge-exchange reactions at small values of $|t|$, one pion exchange (OPE) dominates. Analysis are usually performed for specific t values, to extract information about the dynamics of exchanged particles.

Examples of hadronic peripheral production experiments include the LASS experiment at SLAC [26], with a 11 GeV/c negative kaon beam impinging on a hydrogen target, the E852 experiment at

¹ The Lorentz-invariant variable t is defined as the square of the four-momentum exchanged between the beam and the target.

BNL [27, 28], with a 18 GeV/c negative pion beam, and the VES experiment at IHEP (Protvino) [29]. The COMPASS experiment at CERN [30], currently under data taking, employs a 190 GeV/c negative pion beam, with both nucleon and nuclear targets.

Because of the generality of the production mechanism, the wide range of kinematics available, and the accessibility and high cross sections of hadron beams, the hadronic peripheral production was the “golden” experimental technique in meson spectroscopy. The main disadvantage is the limited selectivity for specific meson states, the only possible selection being based on the transferred momentum, or explicitly introducing strange quarks using kaon beams. Experiments with hadron beams are limited to the excitation of the $q\bar{q}$ pseudoscalar ground state, because pions and kaons are the only particles stable enough against strong decay to produce intense beams for experiments.

Peripheral *photo*-production provides a valid alternative. Photon properties in hadronic interactions are well known, and are summarized in the so-called “vector-meson dominance” mechanism [31]. Essentially, at sufficiently high energy, a photon interacts with hadrons as if it has an effective hadronic structure, derived from its coupling to a $q\bar{q}$ pair. Such couple must have the same quantum numbers as the photon, i.e. $J^{PC} = 1^{--}$. The “vector-meson dominance” hypothesis assumes that the sole hadronic constituents of the photon are the ρ^0 , ω , and ϕ mesons. In peripheral *photo*-production experiments the scheme of Figure 1.5 still applies, but the incoming beam is a spin *triplet* ground state $q\bar{q}$. Consequently, the series of preferred excitations is likely to be different. Phenomenological models, like the flux-tube model, indicate that photons may be more effective in producing exotic mesons in peripheral production on a hydrogen target. There are also indications that exotic mesons can be produced with photon probes with cross sections comparable with ordinary mesons [32, 33].

The use of this technique was limited in the past, due to the lack of high intense, high quality photon beams. Significant contributions to meson spectroscopy using peripheral photoproduction came from the LAMP2 experiment at Daresbury [34, 35], and the CLAS experiment at Jefferson Laboratory [36, 37]. Both employed a tagged photon beam obtained by having a primary electron beam impinging on a thin target, producing Bremsstrahlung photons. Analyzing the momentum of recoiling electrons, the photon energy is derived as the difference between the incident and recoiling electron energies.

The GlueX experiment [38] at Jefferson Laboratory, currently under construction, will perform a comprehensive study of the light quark meson spectrum using this technique, searching for exotic and hybrid mesons, with a 11 GeV linearly polarized photon beam, obtained via coherent Bremsstrahlung.

The MesonEx experiment [39] at Jefferson Laboratory will also study the light quark meson spectrum via photo-production. The photon beam, however, will be obtained having a primary electron beam hitting a hydrogen target and detecting those electrons scattered at very low angle, corresponding to low Q^2 events. This solution will provide a high flux of quasi-real, linearly polarized photons, thus representing a competitive and complementary way to study the meson spectrum and production mechanisms with respect to real photoproduction experiments.

1.4.2 $p\bar{p}$ and $n\bar{n}$ reactions

Reactions involving the $p\bar{p}$ and the $n\bar{n}$ initial state provide a direct way to annihilate antiquarks on quarks. In such reactions, all neutral mesons that decay directly to $p\bar{p}$ can be produced exclusively, if the center of mass energy \sqrt{s} is matched to their mass. Also, mesons states recoiling against a light, stable meson can be formed.

The first case is referred to as “exclusive production”. The quantum number of the produced state are those of the $p\bar{p}$ system that annihilates. These are the same of a $q\bar{q}$ system, because both

are a fermion-antifermion pair with relative angular momentum, and therefore can not be exotic. The advantage of this technique is that the resolution on particle masses and widths is solely determined by the proton-antiproton center-of-mass energy, typically of the order of hundreds of keV. In fact, these observables are extracted by measuring the resonance formation rate as a function of the center of mass energy \sqrt{s} , performing a scan by varying the beam momentum. The detector is used to tag resonances production and to determine quantum numbers, by measuring angular distribution of decay products.

Since the mass of the produced resonance is always greater than 1.87 GeV, this technique has been applied for spectroscopy of charmonia and bottomonia. The JETSET experiment at CERN [40] explored meson spectroscopy in the strange-quark sector, looking for resonances decaying in the $\phi\phi$ channel. The PANDA experiment at GSI [41], currently under construction, will be focused on charmonia spectroscopy, with a center-of-mass energy resolution of tenths of keV.

$p\bar{p}$ reactions can also proceed through the production of a meson state X that recoils against a stable meson. In this process the $q\bar{q}$ degrees of freedom of the X state can be excited, since there are not a priori rules for their exclusion. In fact, these processes have been suggested as a fine way to excite gluonic degrees of freedom. Since center-of-mass energy is shared between the X meson and the recoil, even for $p\bar{p}$ annihilation at rest different final states, with different quantum numbers, can be produced.

The Crystal Barrel experiment at LEAR [42] employed such technique to study the light quark meson spectrum, with particular focus on scalar mesons. As an example, the reaction $p\bar{p} \rightarrow 3\pi^0$ has been studied in detail [43], resulting in the first observation of the $f_0(1500)$ state.

1.4.3 Central production

In central production experiments, a hadronic beam (protons, pions, or kaons) scatters on a nucleon target, producing a neutral meson X_0 and leaving both the beam and the target almost unchanged. The X_0 state is thus seen as produced by the scattering of two off-shell exchanged particles. At sufficiently high energy, and low transverse momentum, the process is believed to be dominated by double Pomeron collision [44, 45]. As the Pomeron may have a large gluonic content, one might expect that the X_0 state is dominated by gluonic degrees of freedom. This technique has been employed at CERN in the WA76 [46], WA91 [47], and WA102 [48] experiments.

1.4.4 e^+e^- experiments

e^+e^- experiments provided contributions to light quark meson spectroscopy in different ways. e^+e^- annihilation reactions are mediated by a single virtual photon, with quantum numbers $J^{PC} = 1^{--}$, thus providing a powerful filter on the final states that can be formed, limited only to vector mesons. The resonance shape of the produced particles is traced out by scanning the center of mass energy \sqrt{s} , while other properties, such as the isospin, are measured by looking at the final state particle combination. This experimental technique has been widely employed by the DM2 collaboration [49] at Orsay. Another very fruitful source of data on meson spectroscopy in high energy e^+e^- collisions is the reaction $e^+e^- \rightarrow e^+e^-X$ where the state X is produced by the collision of two photons radiated from the beam electron and positron. A detailed review of “two-photon” physics has been written by Morgan [50].

1.5 Amplitude analysis

The goal of a meson spectroscopy program is to identify resonances through the measurement of their decay products, and to determine their masses, widths, and couplings. A resonance is formally

described as a complex pole in the production amplitude with defined angular momentum and isospin. The resonance properties are uniquely determined by the corresponding pole position in the complex energy plane. In practice, resonances are numerous, often broad and overlapping each other. Only for a narrow and well-isolated state the resonant structure can be identified as a peak by looking at the invariant mass spectrum of the corresponding decay products. The identification of a precise state requires the extraction of the corresponding waves from the measured data.

This task is performed through the “Partial Wave Analysis” technique (PWA). The cross-section of the reaction under study is parametrized as a coherent sum of different interfering amplitudes, with definite quantum numbers. The intensity is then fitted to the experimental data, by employing an extended maximum likelihood technique, where the free parameters are the wave intensities and phases. Fits can be performed as a function of the invariant mass of the measured decay products and other relevant kinematic variables. The PWA is a crucial component for a meson spectroscopy program since the final results are strictly dependent on the reliability of the PWA tools and rely on the theoretical assumptions used in building the waves. From the technical side, the improvement in computer science has removed the most part of the limitations that were common in the past, allowing the analysis of large data sets with adequate number of waves in a reasonable time. From the theoretical side, partial wave analysis can be improved introducing known constraints on the amplitudes, and including basic and fundamental properties, such as analyticity and unitarity, required by a very general ground.

There are no a priori limitations on the structure of the amplitudes used to parametrize the intensity of the process. These can thus vary from simple expressions that reproduce data in an effective way, without a complete theoretical supporting structure, to more complex functions derived in a rigorous way from the general properties that characterize a scattering process.

The “Isobar model” has been extensively used in the past to perform amplitude analysis of peripheral production experiments. This model assumes a complete factorization of each wave in the scattering process in a *production* part, and a subsequent *decay* part (see Figure 1.6). The first term refers to the production of a meson system X_α via beam excitation and exchange of an off-shell particle with the target, and it is parametrized via a complex number V_α to be extracted from the data. The second term, instead, corresponds to the decay of X_α , and is parametrized via a chain of two-body decays. This fixes the kinematic of each wave, leaving only the V_α as free parameters. Each wave is labeled by the quantum numbers of the meson system X_α and of the particles involved in the decay chain, referred to as “isobars”. The presence of resonances, with defined quantum numbers, in each wave is then investigated looking both at the intensity and phase of the V_α obtained from the fit. A common way to proceed is to parametrize resonances in terms of Breit-Wigner functions, and then to fit them to the V_α to obtain masses and widths of the states. Such a procedure is based on the phenomenological observation that, for intense and well-isolated states, far from the decay threshold, a Breit-Wigner function well reproduces the invariant mass shape of a resonance, as well as the behavior of its phase. However, for broad states, overlapping each other, this parametrization can not be adopted. Resonances are not simply “peaks” in the invariant mass spectrum of a given J^{PC} production amplitude, but are formally described as poles of the corresponding production amplitude in the complex s -plane. They thus have to be found studying the analytic properties of the production amplitudes. A rigorous way to perform this task is to use Dispersion Relations (DR) [51, 52, 53]. They are derived by only assuming causality, and allows to extend analytically the production amplitudes from the real s -axis, experimentally accessible, to the complex s -plane, where resonance poles lie. Dispersion relations translate to very precise constraints that the amplitudes must satisfy on the real axis, and guarantee that the particular form of the amplitude used is irrelevant, insuring that results are actually model independent.

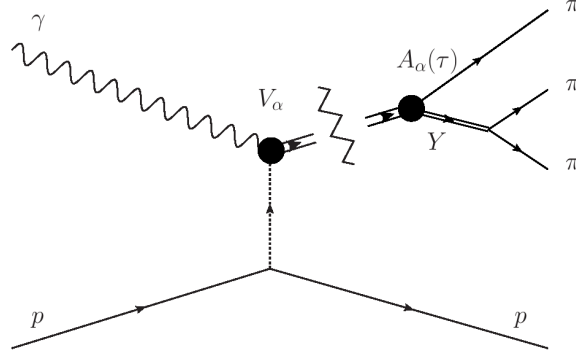


Figure 1.6: The isobar model applied to the reaction $\gamma p \rightarrow p + 3\pi$. The reaction amplitude is factorized as the product of a complex parameter V_α for the production part and a known A_α kinematic term describing the decay of X_α in three mesons, through a chain of two-body decays. τ is a complete set of kinematic variables describing the final state.

1.5.1 Extended maximum likelihood fits

The extended maximum likelihood technique is employed in partial wave analysis to fit the parametrized intensity to the data, and extract free parameters. The main quantity of interest is the *likelihood* \mathcal{L} , defined as the product of the occurrence probabilities of the measured events, according to the model used to derive the process intensity:

$$\mathcal{L} = \prod_i^n P_i(\tau_i, \vec{x}), \quad (1.19)$$

where the product is extended over all the n measured events, each described by a set of kinematic variables τ_i , and \vec{x} are the parameters to be extracted from the data. For each event, the probability is proportional to the intensity multiplied by the detector acceptance ε , which in turns is a function of the final state kinematic variables:

$$P_i(\tau_i, \vec{x}) \propto I(\tau_i, \vec{x}) \cdot \varepsilon(\tau_i) \quad (1.20)$$

The overall normalization is fixed requiring that the integral of the intensity multiplied by the detector acceptance, over the full final state phase space, is equal to the average number of expected events μ :

$$\mu(\vec{x}) = \int I(\tau, \vec{x}) \cdot \varepsilon(\tau) d\tau \quad (1.21)$$

$$P_i(\tau_i, \vec{x}) = \frac{I(\tau_i, \vec{x}) \cdot \varepsilon(\tau_i)}{\int I(\tau, \vec{x}) \cdot \varepsilon(\tau) d\tau} \quad (1.22)$$

The total number of measured events n itself is a statistical variable, distributed according to the Poisson statistics. A proper factor accounting for the probability to measure *exactly* n events has thus to be introduced into the likelihood expression, getting its final expression:

$$\mathcal{L} = \frac{\mu^n e^{-\mu}}{n!} \cdot \prod_i^n \frac{I(\tau_i, \vec{x}) \cdot \varepsilon(\tau_i)}{\int I(\tau, \vec{x}) \cdot \varepsilon(\tau) d\tau} \quad (1.23)$$

The expression for \mathcal{L} in Eq. 1.23 can be simplified noting that, for the n events that have been actually measured in the experiment, the acceptance was one. Also, Eq. 1.21 can be used to cancel the factor μ^n , thus leaving the following expression:

$$\mathcal{L} = \frac{e^{-\mu}}{n!} \cdot \prod_i^n I(\tau_i, \vec{x}) \quad (1.24)$$

The goal of an extended maximum likelihood fit is to maximize the likelihood to obtain the value of the free parameters \vec{x} . For computational reasons, it is preferable instead to *minimize* the inverse of its natural logarithm, that, a part from inessential constant factors, is given by the following expression:

$$-\ln \mathcal{L} \propto \left(- \sum_i^n \ln I(\tau_i, \vec{x}) \right) + \mu(\vec{x}) \quad (1.25)$$

The first term in Eq. 1.25 involves a sum over all the measured events, and it is calculable exactly given the expression for the intensity, for each combination of the parameters \vec{x} . The second term, instead, requires the knowledge of the detector acceptance as a function of the final state phase space (Eq. 1.21), and has to be calculated by MonteCarlo, generating a large set of N_{gen} MonteCarlo events, projecting to the experimental detector, and finally reconstructing using the *same* algorithm employed for the data. This leaves N_{acc} reconstructed events, for which $\varepsilon(\tau_i) = 1$.

The mean value of total expected events is then given by:

$$\mu(\vec{x}) = \frac{\tau}{N_{gen}} \sum_i^{N_{acc}} I(\tau_i, \vec{x}) \quad , \quad (1.26)$$

where the factor τ , represents the total volume of the final state phase space. This factor contributes with a constant, additive term to the likelihood expression (Eq. 1.25), and can thus be neglected in the fit. Finally, it is worth to mention that, since the reaction dynamics is explicitly included in the definition of μ via the intensity I , MonteCarlo events have to be generated according to a flat phase space distribution, therefore no “a-priori” knowledge of the reaction cross-section is required.

1.6 The MesonEx experiment at Jefferson Laboratory

MesonEx (JLab Exp-11-005 [39]) is an experimental program to study meson spectroscopy using quasi-real photo-production. The experimental goal is to perform a comprehensive study of the meson spectrum in the mass range $1.0 - 2.5 \text{ GeV}/c^2$, with precise determination of resonance masses and properties, looking for rare $q\bar{q}$ states, and for unconventional mesons with exotic quantum numbers. MesonEx will run in the Hall B of the Jefferson Laboratory, using the low Q^2 electron scattering technique to obtain a high flux of linearly polarized, quasi-real photons. In the experiment, 12 GeV electrons from the CEBAF accelerator [36] will impinge on a liquid hydrogen target. Final state hadrons will be detected in the CLAS12 detector [54], while the low-angle scattered electrons will be measured with the new “Forward Tagger” dedicated facility.

1.6.1 Electroproduction at small Q^2

Peripheral photo-production is an interesting experimental technique to study the meson spectrum in the light quark sector. Phenomenological models suggest that the photon may be more effective in producing exotics hybrids than probes widely used for this scope (as the pion). Moreover, the

photon linear polarization is a powerful tool in the amplitude analysis, since it acts as a filter on background, and can also be used to disentangle different production mechanisms. The use of this technique was quite limited in the past, mainly due to the lack of intense, high quality, and energetic photon beams. Low Q^2 electron scattering provides a competitive, and complementary, alternative to real photo-production. In this process, a high energy electron beam impinges on a nucleon target, and only the electrons scattered at very low angle are detected. The electron-target interaction proceeds through the exchange of a virtual photon, whose four momentum $q \equiv (\nu, \vec{q})$ is the difference between the beam and the scattered electron momenta. The virtual photon effective mass, or “virtuality”, Q^2 , defined as $-q^2$, is:

$$Q^2 = 4EE' \sin^2(\theta_{e'}/2) \quad , \quad (1.27)$$

where E and E' are, respectively, the beam and the scattered electron energy in the laboratory frame, $\theta_{e'}$ is the electron scattering angle, and the electron mass has been neglected. At low scattering angle, Q^2 is \simeq zero, and therefore the virtual photon behaves as a quasi-real photon.

Moreover, the virtual photon polarization corresponds to real photon polarization in the low Q^2 limit. The polarization density matrix, proportional to the 3×3 space-like minor of the leptonic tensor $L_{\mu\nu}$, in the case of an unpolarized electron beam, reads:

$$\rho_{ij} = \frac{1-\epsilon}{Q^2} \cdot L_{ij} = \begin{pmatrix} \frac{1}{2}(1+\epsilon) & 0 & -[\frac{1}{2}\epsilon_L(1+\epsilon)]^{1/2} \\ 0 & \frac{1}{2}(1-\epsilon) & 0 \\ -[\frac{1}{2}\epsilon_L(1+\epsilon)]^{1/2} & 0 & \epsilon_L \end{pmatrix} \quad , \quad (1.28)$$

where ϵ and ϵ_L are, respectively, the virtual photon transverse and linear degree of polarization, given by

$$\epsilon = \left[1 + 2 \frac{(Q^2 + \nu^2)}{Q^2} \tan^2(\theta_{e'}/2) \right]^{-1} \quad (1.29)$$

$$\epsilon_L = \frac{Q^2}{\nu^2} \epsilon \quad (1.30)$$

At very low Q^2 the virtual photon beam becomes, for all practical purposes, almost a real photon beam, since

$$\epsilon_L = \frac{Q^2}{\nu^2} \epsilon \rightarrow 0$$

and the polarization matrix ρ_{ij} corresponds to the spin density matrix of real, transverse polarized photons [55, 56].

The photon polarization can be defined, via these relations, on an event-by-event basis, by measuring the scattered electron three-momentum. At low Q^2 the quasi-real photon polarization ϵ depends only on the scattered electron energy:

$$\epsilon = \left[1 + 2 \frac{(Q^2 + \nu^2)}{Q^2} \tan^2(\theta_{e'}/2) \right]^{-1} \xrightarrow{Q^2 \rightarrow 0} \left[1 + \frac{\nu^2}{2EE'} \right]^{-1} \quad , \quad (1.31)$$

and the polarization plane is perpendicular to the electron scattering plane. The associated systematic uncertainty is only affected by the electron detection resolution. These are significant advantages with respect to coherent Bremsstrahlung, where only the average polarization can be determined and the value is based on model calculation, or derived by measuring reactions with known asymmetries.

The quasi-real photon technique was used in the past to produce high energy (~ 100 GeV) photon beams at CERN (Ω [57] and COMPASS [58] experiments) and at DESY (ZEUS [59] and H1 [60] experiments).

Chapter 2

Experimental equipment in Hall B at JLab

2.1 Jefferson Laboratory

The primary mission of the Thomas Jefferson National Accelerator Facility (Newport News, VA, USA) is to conduct research on the atomic nucleus at quark level with electromagnetic probes, to study how QCD works at the GeV scale. Founded in 1984, this facility houses the Continuous Electron Beam Accelerator Facility (CEBAF), an electron accelerator providing high-quality, continuous-wave polarized beam with energy up to 6 GeV and current up to 200 μA simultaneously to three experimental halls (Hall A, Hall B, and Hall C).

The experimental activity of the laboratory started in 1994, with the first beam delivered to Hall C. In 2004 a major upgrade of the facility was approved to allow JLab to pursue with even greater strength its mission. The primary electron beam maximum energy will be increased from 6 to 12 GeV, the research programs in all three current experimental halls will continue with new equipment, and a fourth hall (Hall D) specifically devoted to photoproduction experiments on nuclear targets will be built. As a consequence of the upgrade, the JLab experimental activity paused summer in 2012, to allow major changes to be finalized and to prepare the facility for the beginning of the 12 GeV era. The new experimental program is expected to start in 2014-2015.

2.1.1 CEBAF Accelerator

The Continuous Electron Beam Accelerator Facility (CEBAF) [36] is the electron accelerator of Jefferson Laboratory. It was designed and built during the 1980s as a reply to the demand from the nuclear physicist community for a new kind of electron accelerator to study the interface between nuclei and particles, in the transition region between the energy regime where strongly interacting matter is understood as nucleon bound states and the regime where the underlying quark-gluon structure appears.

To reach such a goal the machine design had to respect strict requirements: variable beam energy in the GeV scale for kinematic flexibility, high intensity to study processes with low electromagnetic cross sections, high duty factor to allow coincidence measurements, and sufficient beam quality to allow usage of high resolution detectors.

The CEBAF design was based on a innovative solution, never applied before to such large scale accelerators: the use of superconducting radiofrequency cavities (SRF) to provide the necessary

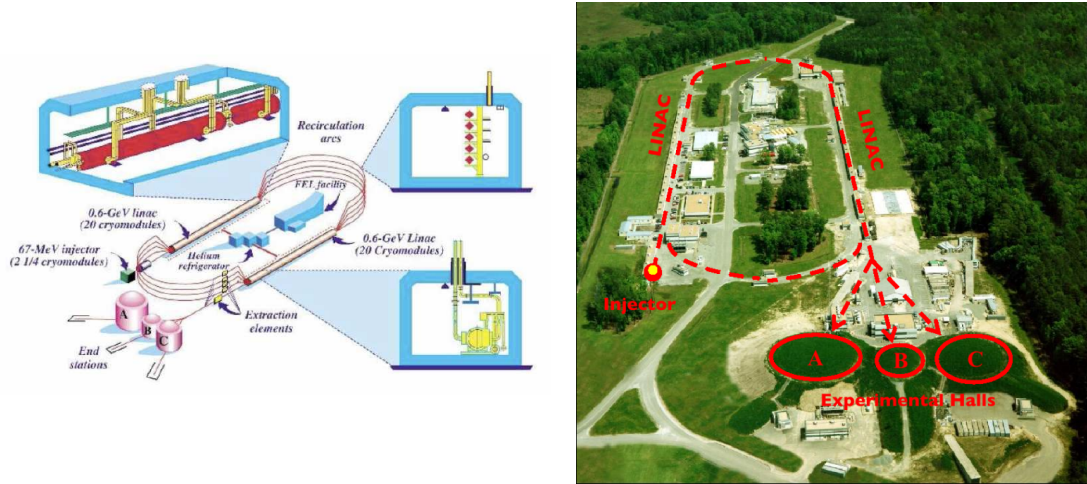


Figure 2.1: Left: schematic layout of the CEBAF accelerator. Right: aerial view of the CEBAF accelerator complex. Both figures refer to the 6 GeV period, before the 12 GeV upgrade.

accelerating gradient. The schematic layout of the complex, together with an aerial view of the accelerator site, is shown in Figure 2.1.

Primary electrons are produced at the injector by an electron gun made of a photocathode, an anode, and a laser system. The laser beam hits the photocathode, thus emitting electrons through photo-electric effect. Electrons are then accelerated up to an energy of 100 keV. Having three different lasers, the current of the beam delivered to each experimental hall can be tuned independently, by varying the corresponding laser intensity.

Before leaving the injector electrons are accelerated to 67 MeV, and then enter in the CEBAF complex where they are grouped into $90 \mu\text{m}$ bunches, separated in time by 667 ps. Electrons travel through each of the two CEBAF Linacs, acquiring 1200 MeV at each loop: the connection between the two linacs is done by Recirculating Arcs. Since electrons can circulate through the CEBAF more than once, each Recirculating Arc is made of different dipole magnets, with bending strength matched to the different electron energies. Bunches are splitted before the arc by a suitable magnet, sent to the matching set of dipoles, and then recombined. After the beam is accelerated to the final kinetic energy, magnets at the Extraction Elements are used to bend it into the correct hall. In this way, each experimental Hall can be provided with an independent electron beam, with specific intensity and energy, having bunches separated in time by 2.004 ns.

The accelerator portion of the JLab upgrade will be constructed on the framework of the existing CEBAF facility. Five new superconducting radio-frequency accelerating elements will be added to each Linac, the existing RF cavities will be increased in gradient to achieve a 1.1 GeV/Linac accelerating power, and a new recirculating arch will be added to provide an extra pass through the North Linac. Such new configuration will bring the beam up to 11 GeV for Halls A, B and C and up to 12 GeV for Hall D.

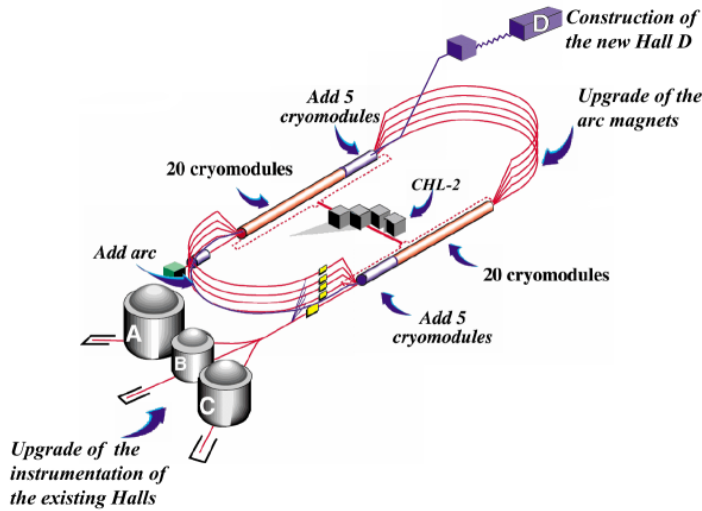


Figure 2.2: The JLab accelerator site after the 12 GeV upgrade

2.2 The Hall B Photon Tagger

In addition to the primary CEBAF electron beam, experiments in Hall B have also been performed with a real photon beam produced by a dedicated facility, the “Photon Tagger” [37]. This system operates on the Bremsstrahlung principle and is capable to tag photon energies over a range from 20% to 95% of the incident electron energy.

Electrons from the CEBAF accelerator imping on a thin nuclear target (“radiator”) placed behind a magnetic spectrometer (“tagger”). A small fraction of them emits a Bremsstrahlung photon through the interaction with nuclei of the radiator. The energy transferred to the nucleus in this process is negligible, so the energy conservation law is written as:

$$E_\gamma = E_e - E_{e'} \quad , \quad (2.1)$$

where E_e is the energy of the primary electron, $E_{e'}$ is the energy of the scattered electron and E_γ is the energy of the emitted photon. E_e is determined by CEBAF, so the measurement of $E_{e'}$ with the magnetic spectrometer determines uniquely the energy of the photon.

After the radiator, both photons and electrons still travel along the original beam direction. Photons continue straight ahead the tagger magnet, passing through a collimating system, and hit the target, placed further downstream in the experimental hall. Electrons are bended by the dipole field of the tagger magnet. The field intensity is matched to the primary beam energy, so that electrons that did not undergo Bremsstrahlung are directed into a shielded beam dump below the floor of the experimental hall. Electrons losing energy in the radiator are deflected, emerging from the field along a focal plane, where a scintillator hodoscope is placed.

The hodoscope is composed by two layers of plastic scintillator detectors. The first layer is made of 384 partially overlapping small plastic scintillator counters (“E-counters”), that determine the energy of the scattered electron by tracking it in the magnetic field. The indetermination of the electron energy is determined by the finite width of these counters. Considering their overlap, this corresponds to $\Delta E_\gamma/E_\gamma \simeq 0.1\%$. The second layer is made of 61 bigger scintillator counters (“T-counter”), that precisely determine the time of the electron hit. This information is used to make

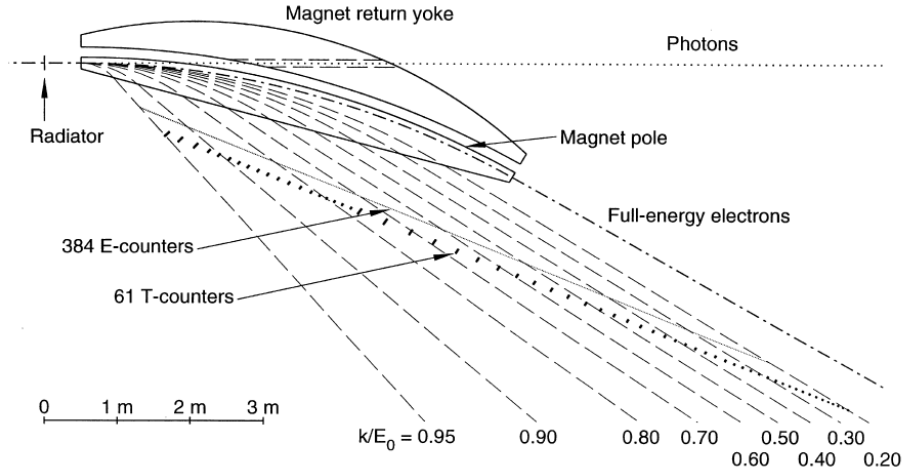


Figure 2.3: Overall geometry of the Hall B tagging system, with typical electron trajectories labeled according to the fraction of energy k/E_0 transferred to the emitted photon [37].

a coincidence with the corresponding event measured by the CLAS detector, and to determine which photon triggered the interaction.

The tagger magnet is unable to deflect the primary electrons with energy greater than 6 GeV. However, the Photon Tagger will be kept in Hall B after the 12 GeV upgrade, to still have the opportunity to run photo-production experiments at lower energies.

2.3 The CLAS detector

CLAS (CEBAF Large Acceptance Spectrometer) is the multi-particle spectrometer that was installed and operated in Hall B during the 6 GeV run period. It provided efficient detection of neutral and charged particles over a good fraction of the full solid angle and momentum range, to study photo- and electro-induced nuclear and hadronic reactions.

The detector design is based on a toroidal magnet made by six superconducting coils arranged around the beam line to produce a field pointing primarily in the azimuthal direction [61]. The detector itself was composed by six independent magnetic spectrometers, with a common target, trigger and data acquisition system. A view of the particle detection system in the beam direction and normal to it is given in Figure 2.4. A summary of the CLAS detector main is reported in Tab. 2.1. Each spectrometer was equipped with drift chambers to determine the trajectories of charged particles, gas Cherenkov counters for particle identification, scintillator counters to measure time-of-flight, and electromagnetic calorimeters to detect showering particles (electrons and photons) and neutrons. During photo-production experiments, CLAS was also equipped with a scintillator counter (the Start Counter) close to the target for precise event timing.

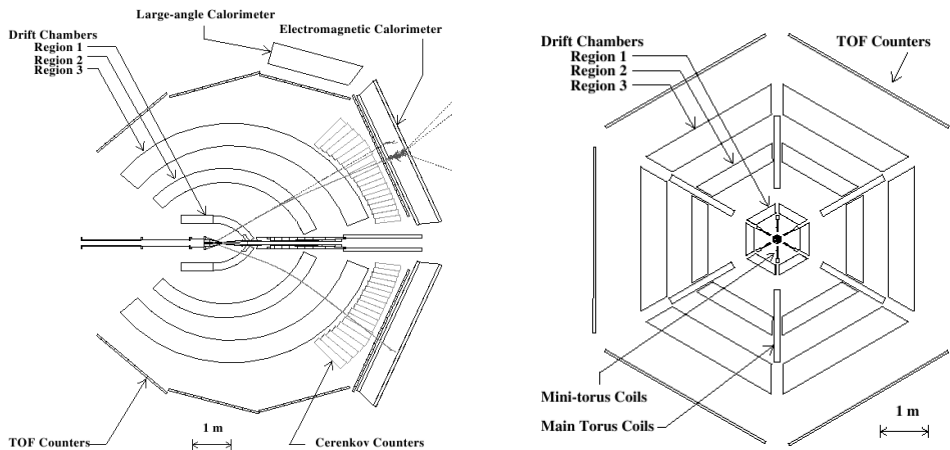


Figure 2.4: Schematic view of the CLAS detector parallel (left) and perpendicular (right) to the beam direction.

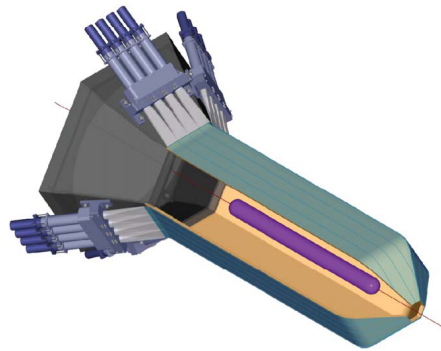


Figure 2.5: The CLAS Start Counter. In purple, the target [62].

Start Counter

The Start Counter was the first detector encountered by the spray of particles emerging from the target, and provided the fast and precise time information needed to match tracks in CLAS with photons from the Hall B photon tagger. This detector, shown in Figure 2.5, was built of six identical sectors surrounding the target cell. Each sector consists of four scintillator paddles coupled to a photomultiplier tube through a light guide. Further details can be found in [62].

Drift Chambers

The Drift Chamber System (DC) was the core of the CLAS detector. It worked in conjunction with the toroidal field generated by the superconducting magnet and provided information about charged particles momentum by measuring the curvature inside the field. The magnet and the DC together defined the spherical, axially segmented geometry of CLAS.

Each of the six DC sectors consisted of three regions. Region 1 (R1) was the innermost one,

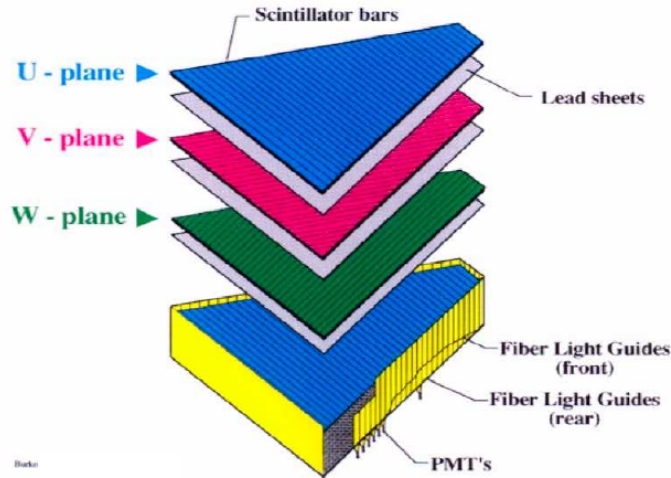


Figure 2.6: Exploded view of one of the six CLAS electromagnetic calorimeter modules [65].

situated close to the target and out of the magnetic field, and was used to determine the initial direction of tracks. Region 2 (R2) was located between the torus coils, in a region with high magnetic field to maximize track curvature for momentum measurement. Region 3 (R3) was the outermost and largest one, and lay outside the field region. It measured the final direction of charged particles headed towards the outer detectors (Cherenkov Counters, Time of Flight, Electromagnetic Calorimeters). Further details about the CLAS Drift Chamber system can be found in [63].

Time-Of-Flight

The CLAS Time-Of-Flight system (TOF) provided precise timing information for charged particles, mainly used for particle identification. Due to the fast response, it was commonly used to provide the trigger of an hadronic interaction.

The system, covering an area of 206 m^2 , was composed by scintillation counters 5.08 cm thick, 15 and 22 cm wide, with lengths which varying from 32 cm at the most forward angle to 450 cm at larger angles. It covered the polar angles ranging between 8° and 142° and the entire active range in azimuthal angle. All the components of the system have been designed to optimize the time resolution, that varies from about 80 ps for the short counters to 160 ps for the longer counters. Further details about the CLAS time of flight system can be found in [64].

Electromagnetic Calorimeters

The CLAS forward Electromagnetic Calorimeters (EC) has been used for electron detection and triggering on electrons at energies above 0.5 GeV , detection of photons at energies above 0.2 GeV (for reconstruction π^0 and η through their 2γ decays), and detection of neutrons.

The detector, covering polar angles up to 45° , was a sampling calorimeter made of alternating layers of scintillator strips and lead sheets with a total thickness of 16 radiation lengths. The lead-to-scintillator ratio is 0.24. Each of the six EC modules, one for each CLAS sector, was made by triangular panels arranged radially according to CLAS hexagonal symmetry. There were 39 layers

Parameter	Value
Charged tracks:	
Polar angular range (θ)	8° to 140°
Polar angular resolution ($\delta\theta$)	$\simeq 1$ mr
Azimuthal angular resolution ($\delta\phi$)	$\simeq 4$ mr
Momentum resolution ($\delta p/p$)	$\simeq 1\%$
Neutral particles:	
Polar angular range (θ)	8° to 45°
Energy/momentum resolution	$\simeq 0.1/\sqrt{E}$
Particle identification:	
π/p	< 3.5 GeV/c
K/ π	< 2.0 GeV/c

Table 2.1: CLAS detector performances.

in the sandwich, each consisting of 10-mm thick scintillator followed by a 2.2-mm thick lead sheet. Scintillator layers consisted of 36 strips parallel to one side of the triangle, with the orientation of the strips rotated by 120° in successive layers. There were three orientations (labeled U, V, and W) which provided stereo information on the location of energy deposition. The energy resolution was roughly $\frac{\sigma}{E} = 0.003 + 0.093/\sqrt{E}$. Further details about the CLAS Electromagnetic Calorimeters can be found in [65].

2.4 The CLAS12 detector

As a consequence of the Jefferson Laboratory 12 GeV upgrade, the existing CLAS detector in Hall B will be upgraded to CLAS12 [54]. This detector is designed to perform experiments with high energy electron beam impinging on polarized and unpolarized targets at luminosity up to $10^{35} \text{ cm}^{-2} \text{ s}^{-1}$. As well as to match the increased beam energy and intensity, the detector is designed to meet the requirements of the foreseen experimental program, such as the operation of a longitudinal polarized target, the capability to detect forward-going, high momentum particles, and the separation of electrons, pions, and kaons in a large momentum range.

The exclusive and semi-inclusive reactions that will be measured with CLAS12 are characterized by the production of a low-momentum baryon at large angles and one or more forward mesons with high momentum. To cover both these kinematic regions the detector is made by a Forward Detector (FD) covering the angular range between 5° and 35° and a Central Detector (CD) covering larger angles up to 125°. The performances of the CLAS12 detector are summarized in Tab. 2.2.

2.4.1 CLAS12 Forward detector

The Forward Detector will measure and identify charged and neutral particles scattered between 5° and 35°, in the full momentum range. Particles will be detected by six identical magnetic spectrometers working in conjunction with a toroidal field, generated by a six coil superconducting magnet. Each spectrometer, corresponding to a sector of the Forward Detector, will be equipped with a Micromegas tracker, high threshold Cherenkov counter (HTCC), a set of drift chambers (FDC), low threshold Cherenkov counter (LTCC), scintillation counters (FTOF), and electromagnetic calorimeters (FEC). The Forward Detector makes use of some of the existing components of CLAS and of the Hall B infrastructure.

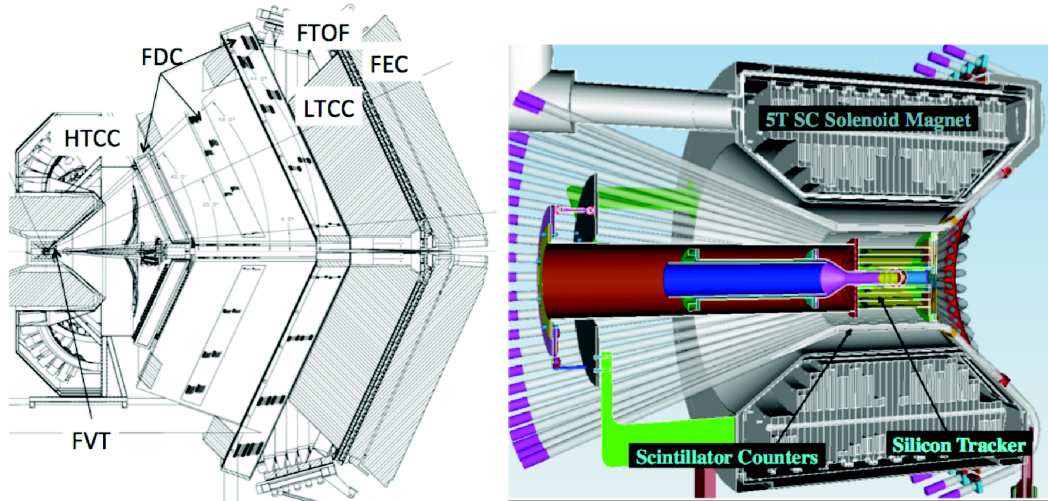


Figure 2.7: Left: the CLAS12 Forward Detector. Right: the CLAS12 Central Detector.

Forward Tracking system

The Forward Micromegas Tracker and the Forward Drift Chambers, together with the superconducting magnet, form the Forward Tracking system. The detector momentum resolution is a function of the polar angle, ranging from 0.3% at 5° to 1.0% at 30° , and is nearly constant as a function of the momentum. The foreseen resolution for the polar and azimuthal angle are respectively 1 mrad and $1 \text{ mrad}/\sin\theta$.

Micromegas detectors (“Micro Mesh Gaseous Structure”) are gaseous particle detectors and thus measure the passage of charged particles through the ionization induced in the gas volume [66]. In a Micromegas this volume is divided in two parts by a metallic micro-mesh: the “conversion” volume, typically 3 mm thick, and the “amplification” volume, typically $25\text{--}100 \mu\text{m}$ thick. The detector is oriented with the “conversion” volume facing the target. When a charged particle hits the detector, an electron-ion pair is produced by ionization. The electric field in the conversion volume forces the electron to drift toward the micro-mesh and the ion toward the cathode. When the electron enters into the amplification volume it senses the higher electric field and acquires sufficient energy to produce secondary electron-ion pairs, starting an avalanche. This induces a very high electric signal at the anode, that is then acquired with a suitable amplifier. The anode is segmented in strips or pixels to obtain the position of the impinging particle in the detector. The Forward Micromegas Tracker consists of 3 double layers of flat detector disks, designed with a new PCB technology (“bulk Micromegas”) [67]. Each layer is segmented with $500 \mu\text{m}$ strips in the transverse direction respect to the beamline, with the second layer rotated by 90° , to measure the hit position through the coincidence of the two. The foreseen spatial resolution is $500\mu\text{m}/\sqrt{12} \simeq 144 \mu\text{m}$ for both x and y directions.

The Forward Drift Chambers will measure the trajectory of charged particles moving in the toroidal field, and hence their momentum. The design of the system is very similar to that of CLAS, with some minor modifications dictated by the operation at higher luminosity and the required higher resolution. It consists of three regions: the first will be located in front of the torus coils, outside of the torus field region, the second will be positioned between the magnet coils, inside the high field region to maximize track curvature for momentum measurement, and the third will be placed outside the torus coils. Each region is made by two *superlayers*, with wires

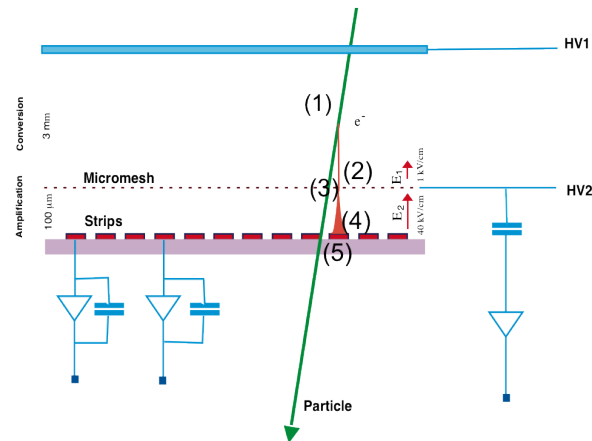


Figure 2.8: Simplified scheme of Micromegas operating principle. A charged particle ionize the gas in the “conversion volume”, and creates an electron-ion pair (1). The electron drifts in the electric field toward the micromesh (2), until it reaches the amplification volume (3). The higher electric field here presents start an avalanche (4), inducing a high electric signal at the anode (5), that is then read-out through a proper amplification circuit.

placed at a stereo angle of $\pm 6^\circ$ respect to the toroidal field, to measure polar and azimuthal angle of the trajectory.

Forward Time-Of-Flight system

The Forward Time-Of-Flight system (FTOF) is a major component of the CLAS12 forward detector, used to measure the speed β of charged particles. The design parameters were chosen to allow for separation of pions and kaons up to 3 GeV/c. Considering the average path length from the target to the CTOF of 650 cm and the fact that more energetic particles are emitted at small angles, the above request translates to a timing resolution varying from 60 ps in the very forward region to 150 ps at larger angles. Other requirements to the system are imposed by the foreseen luminosity, resulting in a high-rate environment, as well as from the integration in the first level trigger.

Each FTOT sector is made by three set of rectangular scintillator counters, referred to as “panels”. Panels “1a” and “1b” are located at forward angles, covering the range from 5° to 36° , while panels “2” are located at larger angles, covering the range from 36° to 45° . Each “1-a” panel is made of 23 plastic scintillator, 5.08 cm thick and 15 cm wide, read out through short acrylic light guides. The length of the counters ranges from 32 cm at the smallest scattering angles to 275 cm at larger angles. Panels “1-b” consist of an array of 58 scintillator, each 6 cm wide and 6 cm thick, with lengths matching the panel “1-a” counters. Finally, panels “2” counters consist of the current CLAS panel-2 TOF counters, with 22 cm wide, 5.08 cm thick scintillators.

Forward Electromagnetic Calorimeters

CLAS12 Forward Electromagnetic Calorimeters will serve three main functions: measurement and identification of electrons with energy greater than 0.5 GeV, the measurement of photons with

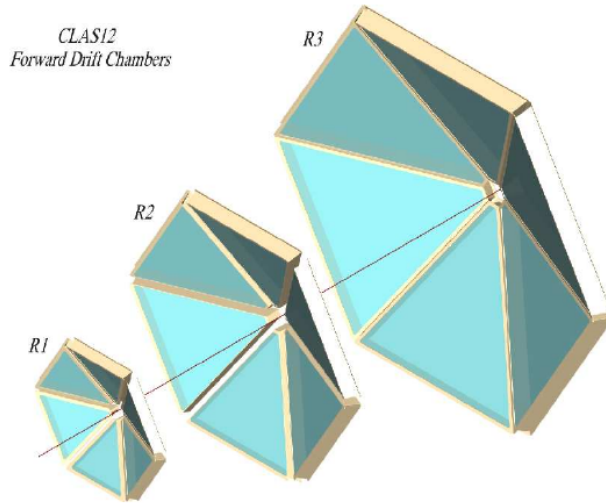


Figure 2.9: Schematic layout of the three regions of the CLAS12 Forward Drift Chambers system.

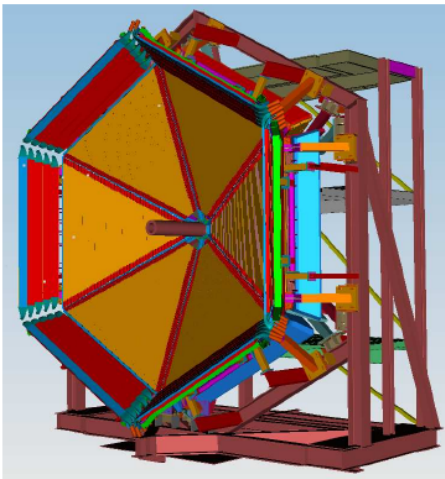


Figure 2.10: View of the FTOF counters for CLAS12 highlighting the location of the panel-1 (orange) and panel-2 (red).

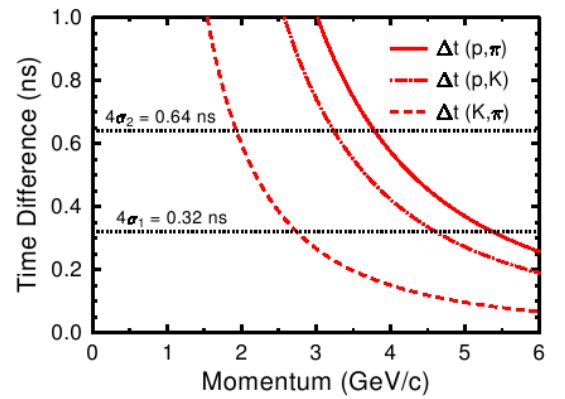


Figure 2.11: Time differences Δt between protons and pions, protons and kaons, and kaons and pions over the 650-cm flight path from the target to the FTOF system.

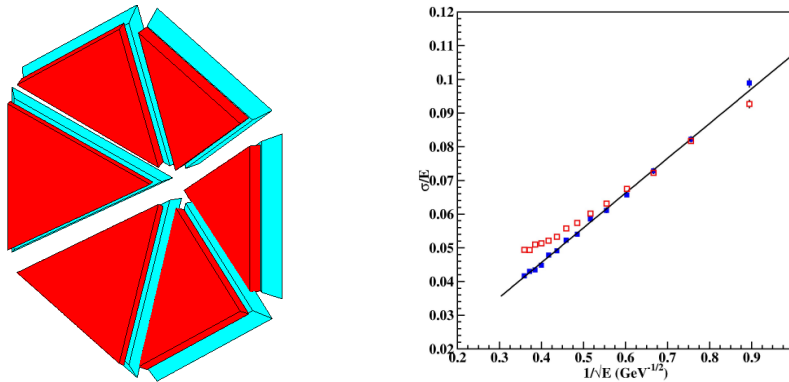


Figure 2.12: Left: schematic layout of the CLAS12 ECAL+PCAL assembly. Each PCAL sector (red) is placed in front of a corresponding ECAL one (light blue). Right: foreseen CLAS12 Electromagnetic Calorimeters energy resolution. Blue points correspond to ECAL+PCAL assembly, while red points are for the ECAL only. Note the x -scale reporting the quantity $\frac{1}{\sqrt{E}}$.

energy greater than 0.2 GeV (mainly for π^0 and η reconstruction through their neutral decays), and the neutrons/photons separation.

The existing CLAS EC will be re-employed in CLAS12, installed at a distance of $\simeq 6$ m from the target. However, this detector is not able to absorb the full energy of the electromagnetic showers produced by electrons and photons with momenta above 5 GeV, resulting in a decrease of the energy resolution. Moreover, due to the π^0 decay kinematic, for momentum higher than 5.5 GeV/c, the opening angle of the decay photons becomes too small to be resolved with this detector.

To resolve such issues, a pre-shower calorimeter (PCAL) is placed in front of the EC. The design consists of 15 overlapping layers of plastic scintillator and lead, with consecutive layers rotated of 120° . The whole assembly corresponds to 5.5 radiation lengths, and the foreseen energy resolution is $\frac{\sigma_E}{E} \simeq 0.1/\sqrt{E}$.

2.4.2 CLAS12 Central detector

The Central Detector is based on a 5T superconducting solenoid magnet and consists of a barrel tracker, Central Time-Of-Flight scintillators (CTOF), and a Central Neutron Detector (CND). It is meant to measure charged hadrons and neutrons in the angular range from 35° to 125° and with momenta < 1.5 GeV/c, in the full azimuthal angular range. The solenoidal field is used to bend charged particles for momentum measurement and to shield the Forward Detector from Moller electrons. CLAS12 target system will be located at the center of the Central Detector.

Central Tracking system

The Central Tracking system is based on a hybrid solution involving both silicon strip detectors and bulk Micromegas, with the detector mounted approximately 25 cm downstream of the nominal target center. The system is made of 3 double layers of bulk Micromegas around 2 double layers of silicon detectors. Because only about 20% of the total charged particle momentum is carried by tracks in the central region, the fractional momentum resolution at 1 GeV/c is 5% to match the

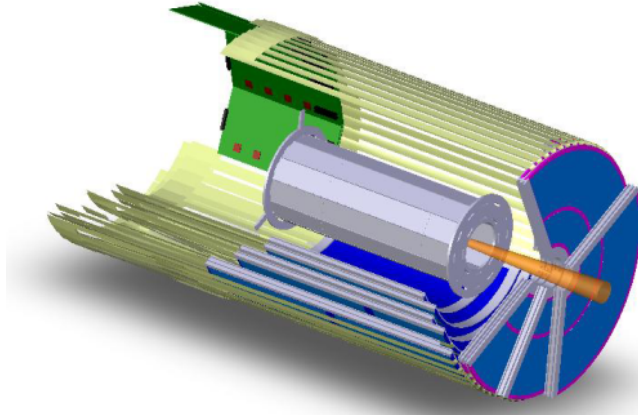


Figure 2.13: CLAS12 Central Tracking System and Forward Micromegas. From the inner to the outer, the tungstene cone (orange), the Central Silicon Detector (gray), the Central Micromegas (yellow-blue). Also shown is the Forward Micromegas Tracker (light-blue).

momentum resolution of the forward tracking system. This hybrid solution has been proved from simulations to be give a better resolution than those obtained using only one type of detector.

Central Time-Of-Flight system and Central Neutron Detector

The Central Time-Of-Flight system is part of the CLAS12 particle identification system. The design timing resolution is 50 ps, to allow 4σ separation of pions from kaons up to 0.64 GeV/c and pions from protons up to 1.25 GeV/c.

The design of the detector includes 50 plastic scintillator counters, each 66-cm long and $\simeq 3.5 \times 3 \text{ cm}^2$ in cross section, as shown in Figure 2.14. These counters will be placed inside the superconducting solenoid at a radius from the beam axis of $\simeq 25 \text{ cm}$. Scintillator counters are coupled to PMTs trough acrylic light guides for signal readout.

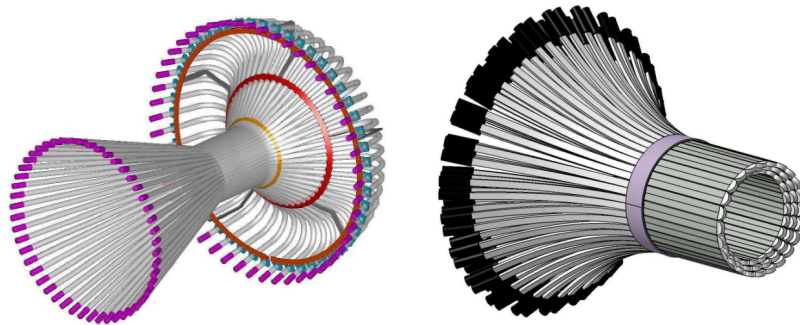


Figure 2.14: CAD drawings of the CLAS12 Central Time-of-flight system CTOF (left) and the CLAS12 Central Neutron Detector CND (right).

Parameter	Forward Detector	Central Detector
Charged tracks:		
Polar angular range (θ)	5° to 35°	35° to 125°
Polar angular resolution ($\delta\theta$)	< 1 mr	< 10 mr to 20 mr
Azimuthal angular resolution ($\delta\phi$)	< 4 mr	< 5 mr
Momentum resolution ($\delta p/p$)	< 1% at 5 GeV/c	< 5% at 1.5 GeV/c
Neutral particles:		
Polar angular range (θ)	5° to 40°	40° to 125° (neutrons only)
Polar angular resolution ($\delta\theta$)	< 4 mr	< 10 mr
Energy/momentum resolution	< 0.1/ \sqrt{E}	< 5%
Particle identification:		
e/ π	In full momentum range	NA
π/p	In full momentum range	< 1.25 GeV/c
K/ π	< 3 GeV/c	< 0.65 GeV/c
K/p	< 4 GeV/c	< 1 GeV/c

Table 2.2: CLAS12 detector performances.

The structure of the Central Neutron Detector is similar to the CTOF: it is made by 4 cylindrical layers, each composed by 30 trapezoidal scintillator counters coupled to PMTs for light readout via light guides. The design momentum resolution is $\simeq 5\%$, with 10% detection efficiency.

2.5 The Forward Tagger

The MesonEx experimental program in Hall B at JLab [39] will perform a comprehensive study of the meson spectrum in the mass range 1.0 – 2.5 GeV/ c^2 employing low Q^2 electron scattering, that represents a complementary and competitive technique to traditional photo-production experiments. While final state hadrons will be measured with the CLAS12 detector, the low-angle scattered electron will be detected with a new, dedicated facility: the Forward Tagger (FT). The purpose of the Forward Tagger is to measure scattered electrons in the polar angular range between 2.5° and 4.5°, outside the nominal CLAS12 acceptance.

The Forward Tagger is made by three components: an *electromagnetic calorimeter* (FT-Cal), to identify the electron, measure the electromagnetic shower energy and provide a fast trigger signal, a *tracker* (TF-Trck), to measure the scattering angles $\theta_{e'}$ and $\phi_{e'}$, and a *hodoscope* (FT-Hodo) to provide e/γ separation.

The Forward Tagger is placed between the High Threshold Cerenkov Counter and the torus support, at about 190 cm downstream of the target nominal position. The close proximity to the beam line¹ and the limited available space requires a compact calorimeter with small radiation length, very high radiation hardness, and compatible with the high magnetic field there present. The hodoscope, placed in front of the calorimeter, will be made of plastic scintillator tiles read-out by silicon photo-multipliers (SiPM) through wavelength-shifting fibers. The tracking detector will be located in front of the scintillator counter, thus extending CLAS12 forward tracker acceptance down to 2.5°. All these components have been designed to fit within a 5° cone around the beam axis to have no impact on the operation and acceptance of CLAS12 equipment. Figure 2.15 shows a CAD drawing of the FT integration in CLAS12. Full technical details of detector design and specifications can be found in [68].

¹ 2.5° at 190 cm corresponds roughly to 8 cm distance between the beam and the detector.

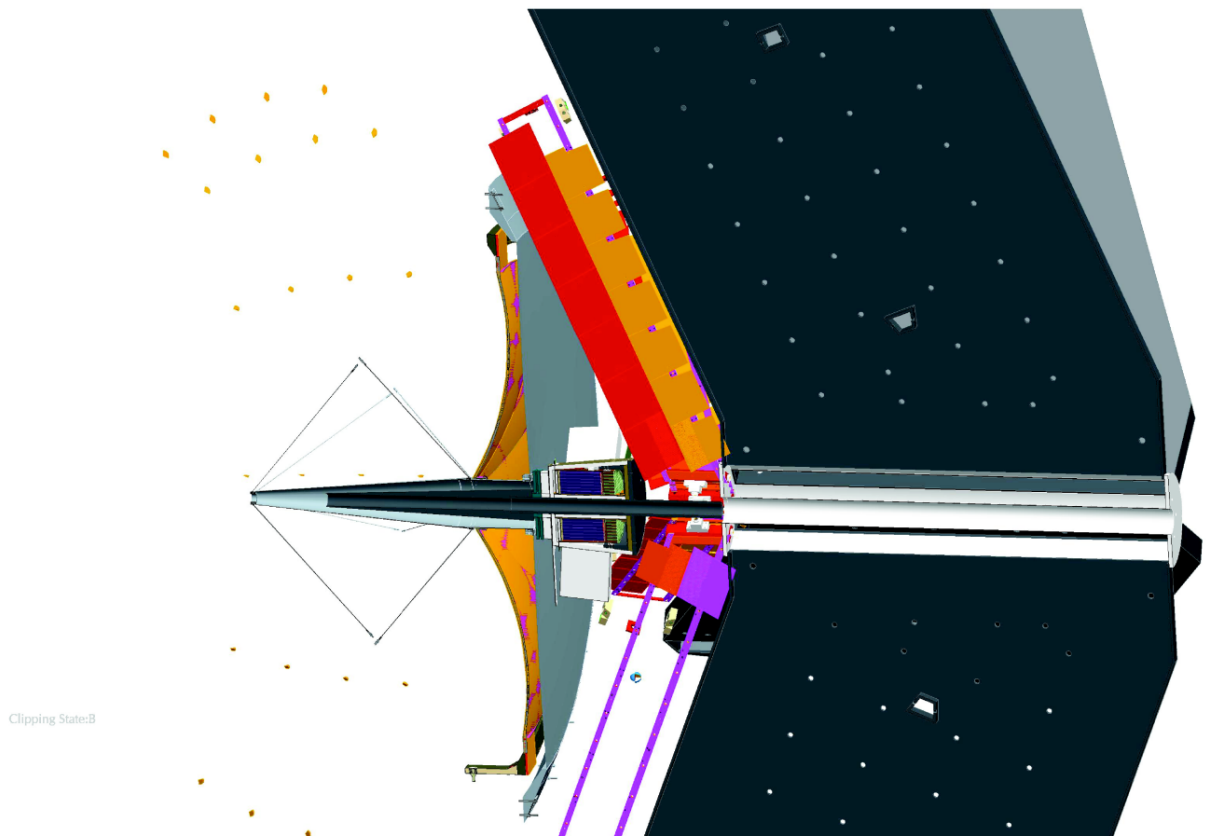


Figure 2.15: CAD drawing showing the integration of the FT in CLAS12. The FT is located in the free space between the HTCC and the first DC. The FT calorimeter (blue) is located at about 190 cm from the interaction point (green cross). The scintillator counter (green) and the tracker (red) are in front of the calorimeter. A tungsten cone (black) shields the FT from Møller electrons and electromagnetic background.

2.5.1 The Electromagnetic Calorimeter (FT-Cal)

The Forward Tagger Electromagnetic Calorimeter (FT-Cal) has to fulfill demanding requirements, dictated by the physics and the mechanical constraints in terms of:

- high radiation hardness,
- high light yield,
- small radiation length and Møliere radius,
- fast recovery time,
- good energy and timing resolution.

The electron energy resolution is a crucial factor to determine precisely the photon energy and ensure the exclusivity of the measured reaction through missing mass technique. However, since the foreseen kinematic range corresponds to low energy electrons associated with high energy quasi-real photons, the energy resolution on the latter will be significantly better than the resolution on the electron. For example, an electron energy resolution of 2% (at 1 GeV) would result in an energy resolution of $\simeq 0.2\%$ for the corresponding 10 GeV photon and would allow the use of the missing mass technique for the most part of the studied reactions.

The FT-Cal should also have a fast recovery time ($\tau \simeq 10$ ns) to sustain high rates with small pile-up effects and provide the scattered electron interaction time with good accuracy (<1 ns) to reject background and identify the signals via coincidence with CLAS12.

Due to the expected high rate from electromagnetic background, the calorimeter is highly segmented in the transverse direction to maintain each channel at a sustainable readout-rate. The size of each pixel is comparable with the characteristic transverse size of the electromagnetic shower (Møliere radius), to contain the signal induced by incident particles to few of them, thus minimizing rates and pile-up. Finally, the calorimeter is located in a region with sizable magnetic field, thus the photodetectors must be compliant with this environment. Also, they should be small enough to fit within the available space.

The choice that has been done is to construct a homogeneous calorimeter based on lead-tungstate (PbWO_4) scintillating crystals. In the latest years, such crystals have been extensively studied and shown to be very resistant to radiation damage, and have been already used in large scale detectors, such as CMS-Ecal [69], ALICE-PHOS [70], PANDA-EMC [71] and CLAS-IC [72]. PbWO_4 main characteristics are the very fast scintillation decay time (6.5 ns), the small radiation length (0.9 cm) and Møliere radius (2.1 cm), and the high density (8.28 g/cm³), while the main disadvantage is the poor light yield, only 0.3% of NaI(Tl). There are two types of commercial-available lead-tungstate crystals: PbWO_4 -type I, already employed in the CMS experiment, with a light yield of $\simeq 120 \gamma/\text{MeV}$ at room temperature, and the PbWO_4 -type II, recently developed by BTCP, with a higher light yield, $\simeq 240 \gamma/\text{MeV}$ at room temperature.

The light emitted by each crystal when hit by a particle is read by an avalanche photo-diode (APD, model Hamamatsu s8664-1010) attached to one of its ends. This sensor, other than being sufficiently small to fit in the FT-Cal design and being operable in an intense magnetic field, has a spectral response well matched to the light emission spectrum of PbWO_4 : the crystals emission peak wavelength is $\lambda = 420 \text{ nm}$, corresponding to APD quantum efficiency of $\simeq 70 - 75\%$. APD active area is $10 \times 10 \text{ mm}^2$, covering almost the whole crystal surface to achieve the maximum light collection efficiency.

APD signals are read-out through specifically designed transimpedance amplifiers, with an intrinsic gain of the order of 1800, that also provide the necessary bias voltage to the photodetectors.

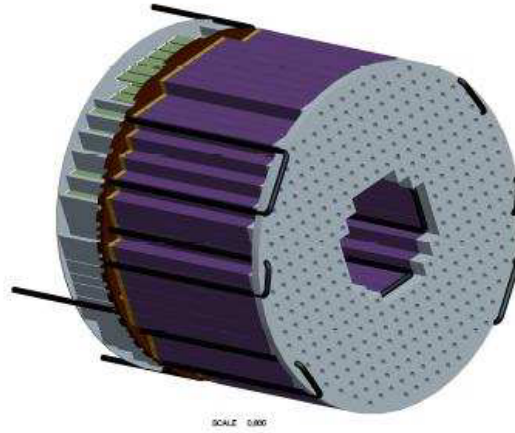


Figure 2.16: The Forward Tagger Calorimeter.

Signals, high voltages, and low voltages are collected through a dedicated motherboard placed in the downstream side of the calorimeter and delivered to the DAQ and slow-controls systems.

The FT-Cal is made by 332 PbWO_4 crystals produced by the SICCAS company, $15 \text{ mm} \times 15 \text{ mm} \times 200 \text{ mm}$ in size, arranged around the beam line with cylindrical symmetry. APDs are coupled to the downstream face of each crystal, and are directly connected to the preamplifiers.

The FT-Cal has been designed to operate at $0 \text{ }^\circ\text{C}$, to exploit the higher crystals light yield at low temperature. Mechanically, the detector has monolithic self-supporting elements each made of a crystal, an APD, reflective coating of the crystal and some support structures in PEEK plastic. The mechanical support for each crystal is provided directly by the reflective material, to avoid dead volume in the detector. Load path and positioning for crystal assemblies is provided by two copper plates, placed upstream and downstream the calorimeter, and two shaped copper vessels, one inner and one outer. An external cooling circuit is welded on the rear copper plate and on the inner and outer copper vessels. Thermal isolation is provided by 20 mm insulating foam, both out of the inner and the outer copper vessel.

2.5.2 The Hodoscope (FT-Hodo)

The primary aim of the FT-Hodo is to discriminate between photons and electrons hitting the FT-Cal, both producing indistinguishable electromagnetic showers inside the detector. Electrons are identified by observing the presence of a hit in the hodoscope which is correlated in position and time with a signal in the calorimeter.

The main requirement of the FT-Hodo is the high efficiency for charged particles detection, with spatial and timing resolution comparable with the FT-Cal. Furthermore, to minimize possible misidentification of photons, the detector is designed to suppress the contribution of false events arising from photon conversion in the FT-Hodo and from the “splashback” of the electromagnetic shower created in the FT-Cal.

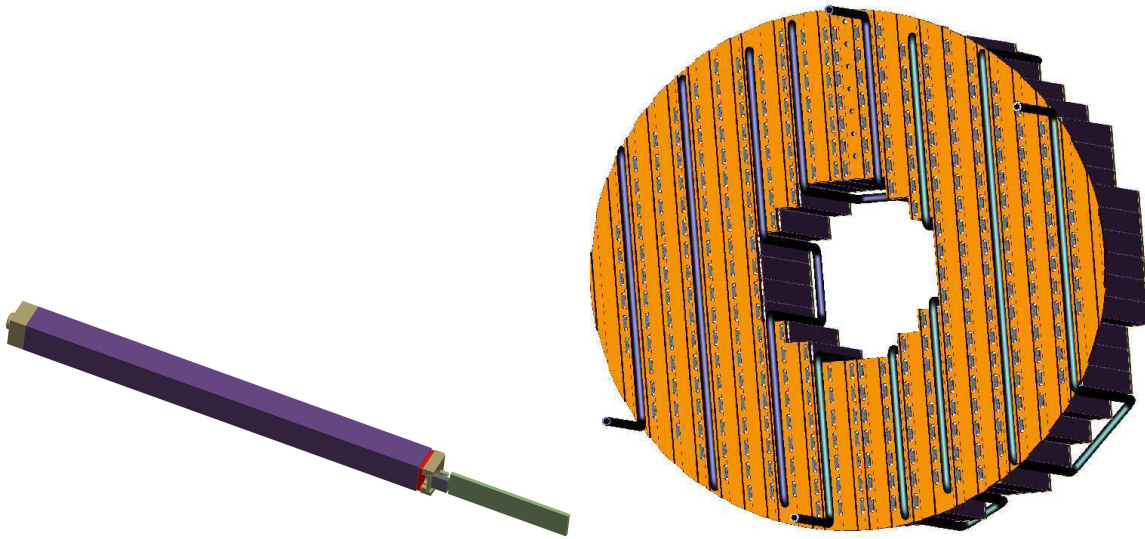


Figure 2.17: Left: FT-Cal single crystal assembly: from the front to the back, the supporting nose (gray), the wrapped crystal (purple), the APD in PEEK housing (red+gray), the preamplifier (green). Right: The FT-Cal copper thermal rear plate with welded cooling pipes.

The solution adopted to fulfill these requirements is to design the scintillation hodoscope with two layers of plastic scintillator tiles covering the FT-Cal, each layer being made of 44 small tiles (“P15”, 15 mm \times 15 mm) and by 72 larger tiles (“P30”, 30 mm \times 30 mm). Larger tiles are placed at larger distances from the beam axis, both to keep a uniform rate on each detector channel and to reduce the level of instrumentation and readout required. Small tiles cover each a single crystal in the FT-Cal, while large tiles cover an array of four. The first layer is thin (7 mm), to reduce the probability of gamma conversion in the hodoscope, while the second is thicker (20 mm), to provide a larger amount of light and to improve the time resolution of the detector.

The high segmentation and the limited space available precludes the use of standard light guides for the readout. Instead, the FT-hodo design foresees wavelength shifting scintillating fibers (WLS) embedded in each scintillator tile, twisted on it to increase the optical coupling with the surface. Part of the light emitted by the scintillator tile is absorbed by the fiber, isotropically re-emitted at lower frequency, and transported to the other extremity of the fiber, out of the hodoscope active volume, where an optical sensor reads it. Silicon photo-multipliers (SiPM) have been chosen both because of their compact dimensions and their compatibility with the high magnetic field present in the detector region. The hodoscope uses 3x3 mm² SiPM from Hamamatsu, model S12572-100P, with 100 μ m pitch and quantum efficiency of \simeq 50%. Their response is well matched to the emission spectrum of the wavelength shifting fibers.

For effective operation, the timing resolution of the FT-Hodo has to be enough to make a coincidence between calorimeter and hodoscope hits with a sufficient low rate of accidentals. The FT-Hodo foreseen timing resolution is \simeq 1 ns, comparable with the corresponding FT-Cal value.

The majority of particles impinging on the FT-Cal will be highly relativistic, resulting in a fixed minimum ionizing energy deposit in scintillator tiles regardless of particle type. Thus, measuring the energy deposition in hodoscope tiles is not critical. The main requirement of the light collection is that enough photoelectrons hit SiPMs to achieve the required time resolution. However, FT-Hodo final design includes the possibility to measure the deposited energy, since this information

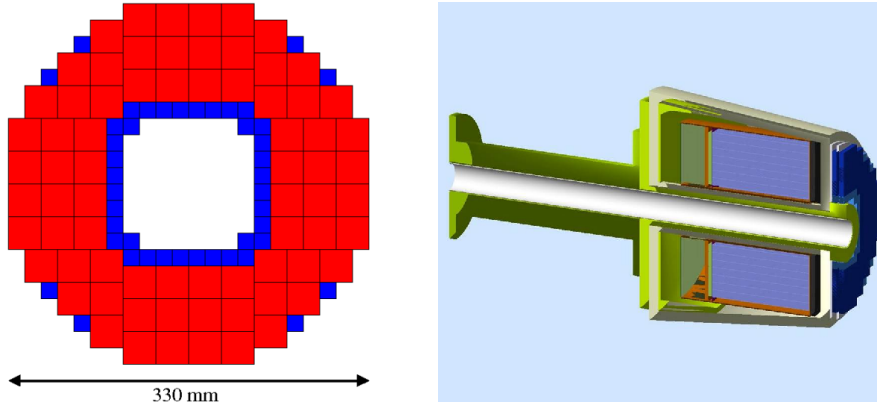


Figure 2.18: Left: simplified layout of plastic scintillator tiles of one FT-Hodo layer. Blue squares are “P15” tiles, red “P30” tiles. Right: GEANT4 visualization of the position of the 2 hodoscope layers (dark blue). FT-Cal crystals (light blue) and shielding are also shown.

can be still used to perform some timing corrections to improve resolution, as well as to monitor the behavior of the detector.

2.5.3 The Tracker (FT-Trck)

The FT-Trck provides reconstruction of polar and azimuthal angles for charged particles, essentially electrons, hitting the FT-Cal. These particles, having non-zero transverse momentum, are rotated in the x-y plane by the 5T solenoidal field while propagating from the target to the Forward Tagger, while their polar angle θ is almost conserved, as well as their momentum. The 3-momentum direction can be reconstructed measuring the rotation in ϕ between the production vertex and a tracking plane placed in front of the calorimeter.

The FT-Trck is made of two double-layers of Micromegas detectors, located in the space between the hodoscope and the High Threshold Cherenkov Counter: the use of two layers results from a compromise between efficient background rejection and track reconstruction with a low material budget. Each layer is composed of two single Micromegas detectors with strips oriented perpendicular one respect to the other, such that the (X,Y) coordinates of a track can be determined. The two layers will be located respectively at 177 cm and at 179 cm downstream of the target, and centered on the beam axis. They will cover polar angles from 2.5° to 4.5° , thus the detectors will be anular-shaped with 65 mm inner radius and 142 mm outer radius.

The angular resolution of the detector is determined by the size of the readout strips: for 500 μ m strips a spatial resolution of $\simeq 144 \mu\text{m}$ is expected, roughly corresponding to 1.7% and 2.8% resolution on θ and ϕ , respectively.

2.5.4 Kinematic, rates and backgrounds

The Forward Tagger Detector has been designed to have a kinematic coverage for electron detection such to tag large energy quasi-real photons with the smallest Q^2 compatible with the electromagnetic background.

The total electron scattering cross section contains contributions from one-photon exchange (Born process), to which quasi-real photoproduction belongs, from QED vacuum polarization loops, and from the emission of additional real photons by the electron (radiative corrections).

	<i>Range</i>
$E_{e'}$	0.5 - 4.5 GeV
$\theta_{e'}$	2.5° - 4.5°
$\phi_{e'}$	0° - 360°
E_γ	6.5 - 10.5 GeV
P_γ	70 - 10 %
Q^2	0.01 - 0.3 GeV ² ($< Q^2 > 0.1$ GeV ²)

Table 2.3: Forward Tagger covered kinematic range.

The intensity of the radiative correction respect to the Born process depends on the kinematics, increasing with E_γ and decreasing with Q^2 . To calculate the contributions of internal radiative corrections to the total inclusive cross section the program RADGEN 1.0 [73] has been used. The total inclusive electron rate within the geometrical and momentum acceptance of the Forward Tagger has been evaluated to be $\simeq 130$ kHz, for a primary electron beam luminosity of $\simeq 10^{35}$ cm⁻²s⁻¹. Inelastic processes represent about 45% of the total cross section in the kinematic range of interest, while the remaining 55% is due to elastic events with the recoil proton detected with CLAS12. Considering only events with high-energy quasi real photon (E_γ between 6.5 and 10.5 GeV), the overall rate for inelastic events is $\simeq 6.5$ kHz, while the radiative rate is $\simeq 40$ kHz.

The main sources of electromagnetic background in the FT are Bremsstrahlung and Møller processes. The characteristic angular distribution of Bremsstrahlung photons is strongly forward peaked (about $\delta\theta \approx m_e/E_{Beam} \simeq 0.05$ mrad @ 10 GeV), therefore their contribution within the FT angular acceptance ($\theta > 2^\circ$) is negligible.

Møller electrons and their secondaries are the dominant background contribution to the expected FT rate. The Møller cross section is almost constant in the kinematic range covered by the detector, $d\sigma/d\theta \approx 10 - 20$ mb/rad, however the kinematics of this 2-body process is constrained and, for angles above 2° , Møller electrons always have energy smaller than 0.5 GeV, outside the kinematic of interest. These low energy electrons are bent in the 5T solenoidal field and thus focused towards the beam line, where they enter into the tungsten cone that shields the detector from this background and from other secondaries produced along the beam-line, such as low energy photons, X-rays, and the beam halo. Those particles that exceed this shield and hits the Forward Tagger can be rejected, both at trigger level or in the offline analysis, because there is no corresponding signal in CLAS12.

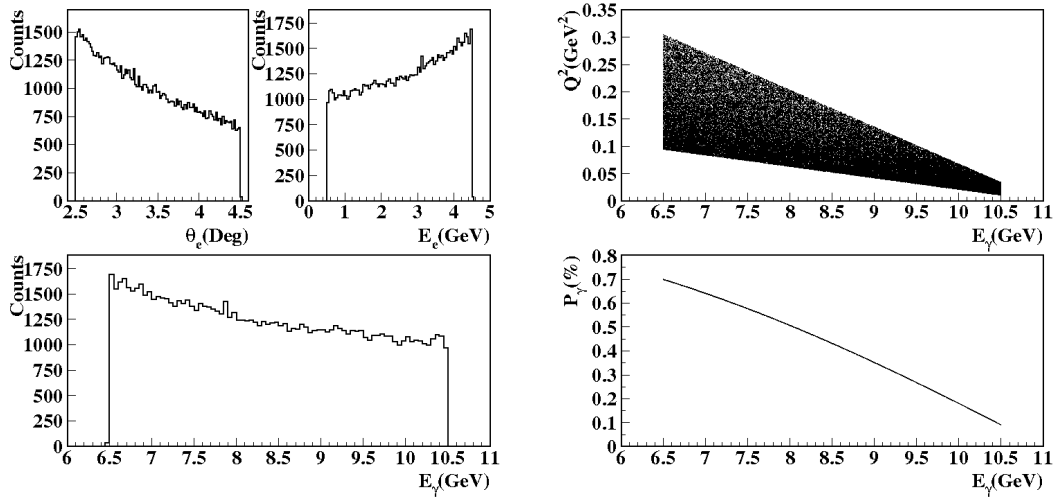


Figure 2.19: Left: angular and energy distribution of scattered electrons (top) and virtual photon energy distribution (bottom) within the geometrical and momentum acceptance of the FT. Right: Q^2 and linear polarization of inelastic events within the geometrical and momentum acceptance of the FT. For details, see Chapters 4 and 6.

Chapter 3

The Forward Tagger Calorimeter

The Forward Tagger Calorimeter (FT-Cal) is the core component of the Forward Tagger detector. It is ment to identify electrons scattered at low angle, to measure the energy of showering particles, and to provide a fast trigger signal, to make coincidences with the CLAS12 detector. The FT-Cal has to fulfill strong requirements in terms of radiation hardness, light yield, radiation length, recovery time, energy and time resolution, dictated both by the physics and by the mechanical constraints. Due to the limited space available and its position inside the CLAS12 detector, it also has to be compact and compatible with a high magnetic field environment. A dedicated characterization of each detector component was needed to verify requirements, specifications, and tolerances. Also, technical choices had to be validated by realizing and testing small-scale FT-Cal prototypes.

In this Chapter, I present the studies that I performed to characterize the components of the FT-Cal: the scintillating crystals, the APDs, and the amplifiers. I also describe the FT-Cal ancillary systems that I developed, and that were employed during these measurements. Finally, I show the results obtained from two small-scale FT-Cal prototypes, respectively with 9 and 16 channels, whose response to cosmic rays and to electromagnetic showers was measured.

3.1 PbWO₄ crystals

PbWO₄ crystals are the sensitive element of the Forward Tagger Calorimeter, converting a fraction of the *energy* deposited by the incident showering particles into *visible light* that can be detected with suitable photo-sensors. These crystals have been chosen because of the properties already mentioned in previous Chapter, in particular the small radiation length and Møliere radius, the high density, and the fast scintillation decay time. Before assembling the calorimeter, all crystals must be fully characterized to ensure that their properties match the detector requirements. The properties that have to be measured for each FT-Cal crystal and their design specifications are here summarized:

- **Dimensions:** crystals have a parallelepiped shape, $15\text{ mm} \times 15\text{ mm} \times 200\text{ mm}$, with 0.15 mm tolerance for all dimensions.
- **Longitudinal optical transmission:** the absolute longitudinal light transmission should be not lower than $25\% @ 360\text{ nm}$, $60\% @ 420\text{ nm}$, $70\% @ 620\text{ nm}$.
- **Transverse optical transmission:** the spread of the wavelength distribution corresponding to 50% transverse transmission, for 10 measurements performed every 1.5 cm along the crystal

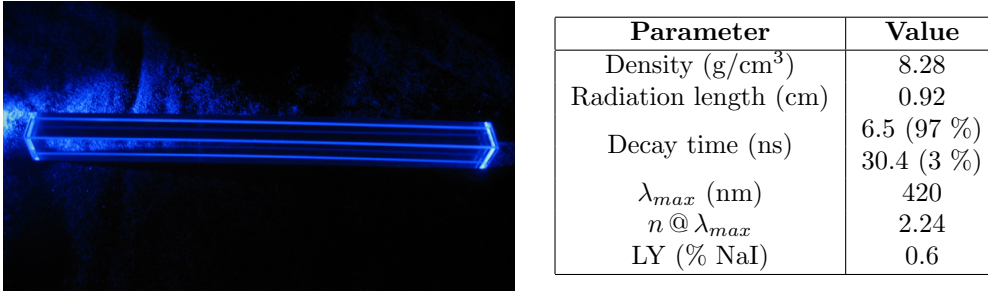


Figure 3.1: Left: a FT-Cal PbWO₄ crystal. Right: PbWO₄ main properties.

axis, should be less than $\delta\lambda = 3 \text{ nm}$.

- **Light yield:** the absolute light yield measured at room temperature with a standard PMT should be higher than 13 phe/MeV.
- **Scintillation kinematic:** the scintillation light emitted within the first 100 ns following the energy deposition event in the crystal should be more than 90 % of the total emitted light.

3.1.1 ACCOS measurements

Characterization of crystals has been extensively performed by using the ACCOS (Automatic Crystal quality COntrol System) facility at Cern [74]. ACCOS was designed to measure the properties of the $\simeq 70k$ CM/EMC PbWO₄ crystals and it is now extensively used to characterize part of the PANDA/EC PbWO₄-II crystals. Such a facility can measure all the crystal properties listed above in a semi-automatic way, for up to 30 samples at time, at +18 °C. A reference sample is installed in the machine, both to acknowledge and correct possible systematic effects between different runs, and to re-normalize light-yield.

In preparation of the measurement campaign of all the FT-Cal crystals, and to define a full characterization procedure, two samples of the FT-Cal PbWO₄ crystals from SICCAS have been measured with such a facility. Since FT-Cal crystals differ from PANDA ones only for geometrical size, a known PANDA reference sample was used during the characterization process.

Geometrical dimensions

Crystal dimensions were measured using a 3D machine. Fifteen points were measured on each side, and nine points on the two ends, allowing a precise reconstruction of the six crystal faces, with 5 μm accuracy. The analysis program reconstructs the shape by performing a best-fit to the points belonging to the same face: the six planes together define the “best-solid”, whose sizes are thus derived. The deviation of the actual crystal geometry from the nominal one is evaluated reconstructing the “minimum-solid” and the “maximum-solid”, defined as those formed by six planes, parallel to the “best-solid” faces, and passing through the innermost/outermost point of each face.

Both measured PbWO₄ crystals were found to be compliant with the requirements, within the 0.15 mm tolerance.

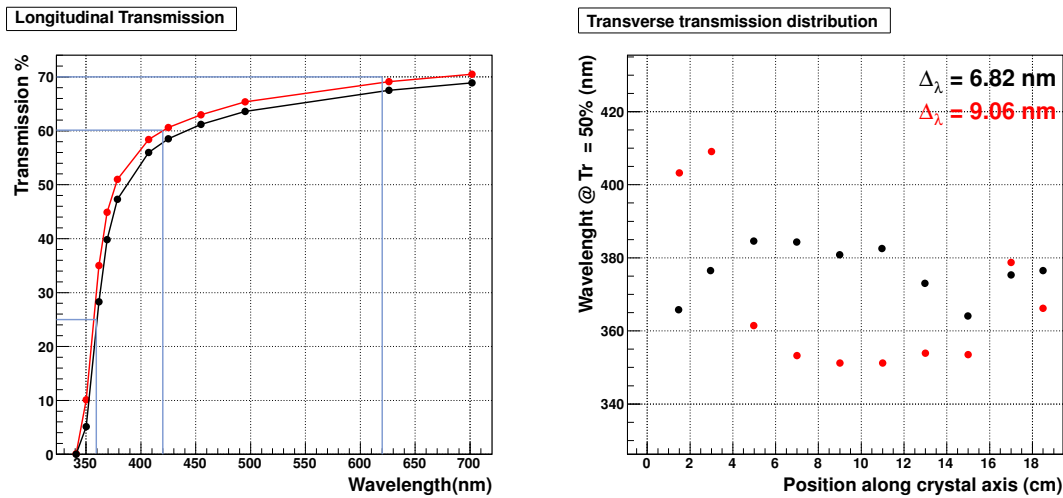


Figure 3.2: Left: longitudinal optical transmission for the two $PbWO_4$ crystals measured with the ACCOS facility as a function of the incident light wavelength. The blue lines indicate the required minimum transmission value at selected wavelengths. Lines between points have been drawn for better readability. Right: wavelength values corresponding to 50% transverse transmission, as a function of the position along the crystal axis. The two RMS spreads are also reported.

Optical properties

Two compact double-beam spectrometers, made by a 20 W halogen lamp, a set of collimators, lenses and filters, and a UV calibrated PIN photodiode, measured the optical transmission. The crystal transmission was evaluated comparing the response of the photodiode to direct light and to the beam passing through the crystal. Measurements were performed at 11 different wavelengths, placing interference filters after the lamp. Transverse transmission was measured for 10 different points along the crystal axis.

The results obtained with the two samples are reported in Figure 3.2, for both the longitudinal and transverse optical transmission. These two crystals were found to not be fully compatible with the requirements, neither for the absolute value of the longitudinal transmission at selected wavelengths nor for the transverse transmission uniformity. Such results have been communicated to the SICCAS company asking for an improvement of the production process, in order to have the final set of crystals compatible with our requirements.

Light yield and scintillation kinematics

The decay time and the light yield of $PbWO_4$ crystals were measured using the so-called “start-stop” technique, detecting the two collinear, 511 keV gamma-rays from a ^{22}Na radioactive source. One of the two photons was detected in a small BaF_2 crystal coupled to a PMT, and provides the Start signal for the measurement, while the second was detected in the $PbWO_4$. The crystal was coupled to a PMT through a proper collimator, to have the mean number of photoelectrons detected per event not larger than a few tenths. The time difference distribution of the two PMT hits, measured through a multi-hit TDC, reproduced the scintillation light emission probability per unit of time. The decay time was calculated by performing a best-fit through an exponential function, while the relative light yield was obtained by integrating it within a $\simeq 100$ ns time

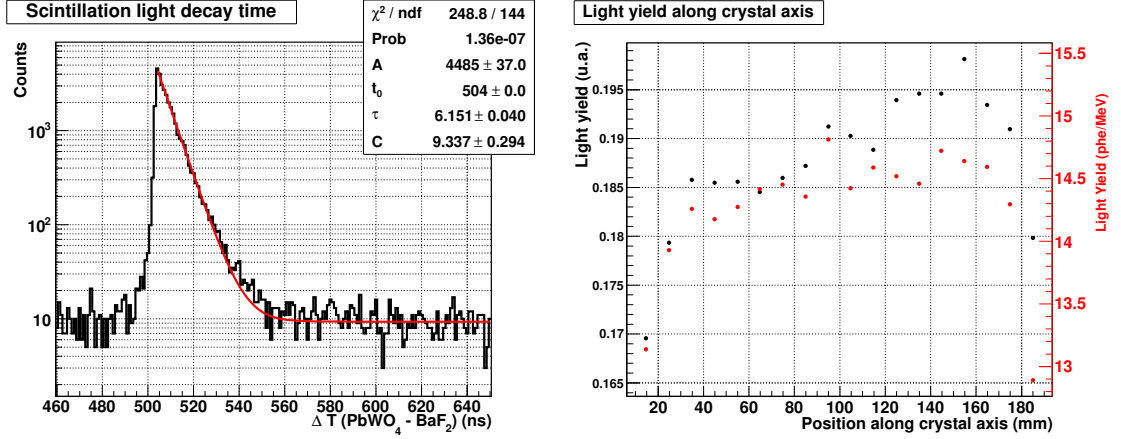


Figure 3.3: Left: time difference distribution for a light yield measurement of a PbWO₄ crystal, with superimposed the best-fit performed to extract the scintillation decay time τ . Right: light yield as a function of position along the crystal axis for the two measured crystals.

window. To estimate the light yield uniformity, this measure was repeated for 18 points along the crystal axis.

Results obtained with the samples are reported in Figure 3.3. The left plot shows the time difference distribution of the two PMT hits for a measurement performed at the crystal center. The coincidence peak is well separated from the flat, random-coincidences, background. The position t_0 of the peak, not centered at zero because of a fixed time offset in the DAQ system, is defined as the center of the bin with the highest number of counts. The scintillation decay time τ is obtained through a best-fit with an exponential function, properly translated to account for the offset, plus a constant background term, i.e.:

$$f(t) = A \cdot \exp\left(-\frac{t - t_0}{\tau}\right) + C \quad , \quad (3.1)$$

while the relative value of the light yield is obtained integrating the distribution within the first 100 ns after the coincidence peak. The corresponding results obtained for the two samples, as a function of the position along the crystal axis, are reported in the right plot, both in terms of relative and absolute light yield. The latter is obtained from the PANDA reference crystal, that gives a conversion factor of $1 \text{ u.a.} \simeq 78 \text{ phe/MeV}$.

Both crystals were found to be compliant with the requirements on light yield and scintillation kinematics. The light yield measured along the crystal axis is always greater than the required value of 13 phe/MeV, and the scintillation light is always emitted within the 100 ns time window.

FT-CAL crystals full measurement campaign

At the moment of writing of this document, all the 370 FT-CAL crystals (including spares) have been measured and characterized with the ACCOS facility. Results have been analyzed to verify the compliance with the design requirements, and to properly place them within the FT-Cal.

The measured light-yield, in absolute units, is reported in Figure 3.4 (left panel). I obtained it by multiplying the *relative* ACCOS results, defined as the average over the different measurements along the crystal axis, with the conversion factor $1 \text{ u.a.} \simeq 78 \text{ phe/MeV}$ previously obtained with the PANDA reference. This factor was also confirmed by comparing these data to the absolute

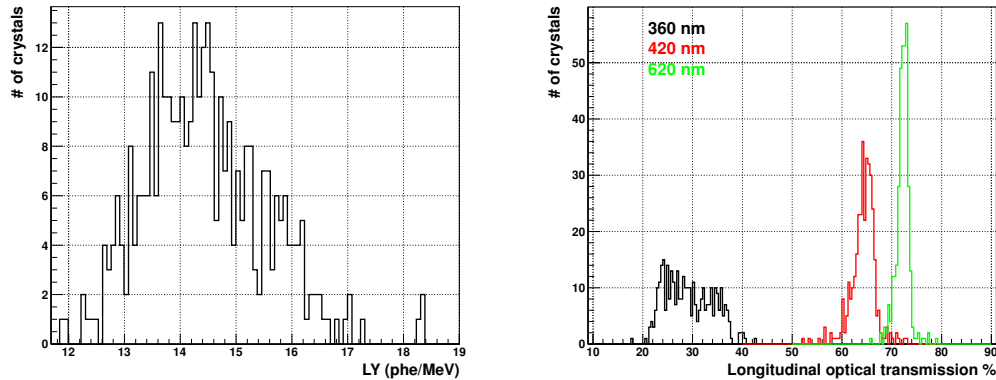


Figure 3.4: Results of the FT-Cal crystals measurement campaign with the ACCOS facility. Left: Crystals average light-yield. Right: Longitudinal optical transmission, at different wavelengths.

LY reported, for each crystal, by the manufacturer. Almost all the crystals are compliant with the minimum required LY of 13 phe/MeV. The right panel, instead, shows the crystals longitudinal optical transmission, measured at the three reference wavelengths. Results obtained with $\lambda = 360$ nm are distributed in a quite large range, between $T_{360} = 20\%$ and $T_{360} = 40\%$, and only 75% of the crystals are compliant with the requirement $T_{360} > 25\%$. Instead, at higher wavelengths, the two distributions are narrower, with more than 95% of the samples compatible with the design specifications. Since the PbWO_4 light emission spectrum is peaked at $\lambda_{max} \simeq 420$ nm, the low-wavelength spread is not expected to have a strong influence on the detector performances, that are, instead, more sensitive to the behavior at high wavelength, in correspondence to the longitudinal transmission plateau.

In summary, 112 crystals were found to be outside specifications, and were sent back to the factory for replacement. New samples are currently being delivered at CERN, where they will be characterized with ACCOS.

3.1.2 Crystals characterization at low temperature

The FT-Cal has been designed to operate between 0°C and 20°C . However, the ACCOS facility can characterize PbWO_4 crystals only at room temperature. Therefore, the measure of the main crystals properties, in particular the light yield, needs to be performed *also* at low temperature, at least for selected samples, in order to extrapolate the ACCOS measurements to the full operational range.

A dedicated cosmic-muons setup was therefore developed. The crystal, inserted in a copper enclosure for thermal stability, was read using a Photonis XP2262B fast PMT. During the measurement the temperature was kept constant within $\pm 0.5^\circ\text{C}$. The PMT was coupled to the crystal by using a silicon optical pad, and consistent results were found using, instead, optical grease. In all measurements, the crystal was wrapped by a VM2000 reflecting foil on the free 5 faces. The response of the PbWO_4 -II crystal to cosmic rays was measured as a function of the temperature, at five different working points between $+18^\circ\text{C}$ and -25°C .

The experimental setup foresaw two plastic scintillators counters, located above and below the crystal, whose coincidence signal provided the trigger for the data acquisition system. The PMT signal was digitized with a charge-to-digital converter (QDC). For each temperature setting, the

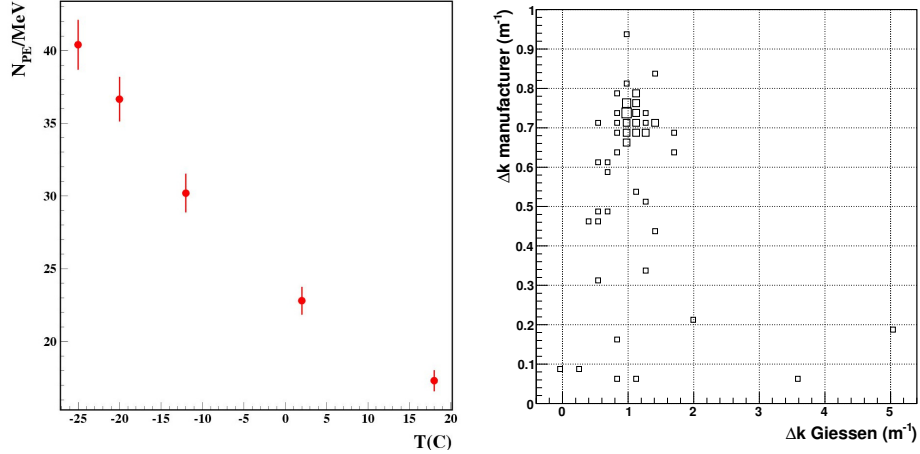


Figure 3.5: Left: $PbWO_4$ light-yield as a function of the operating temperature, measured with the cosmic ray setup. Right: “Induced absorption” Δk of a selected sample of 100 $PbWO_4$ crystals, as reported by the SICCAS manufacturer (y axis) and as measured with the Giessen facility (x axis).

pedestal subtracted spectrum was normalized to the single photoelectron charge, measured with the same DAQ system and QDC. This measurement was repeated for each working point, to ensure the gain of the PM was not affected by temperature variation.

The obtained *charge* distributions were then fitted with a Landau function to extract the position of the peak, corresponding to the most probable energy deposition. This was finally divided by the most probable energy deposition value estimated using GEANT4 [75], and corresponding roughly to 16 MeV. Measurement results are shown in Figure 3.5: the LY gain from +18 °C to -25 °C appears to be of the order of 2.5.

3.1.3 Radiation Hardness

Due to the close proximity to the beam line, during the detector operation the FT-Cal crystals will be exposed to a considerable radiation field, mainly due to low energy electrons and photons, produced by the interaction of the primary beam with the target and surrounding material, and scattered at low angle. Radiation dose can be a critical issue for the operation of scintillating crystal in high background environment, since it induces a deterioration of light transmission, creating same color centers in the lattice. These defects are not permanent, and can be removed with a thermal annealing, that, however, may be unpractical during data taking. Detailed MonteCarlo simulations [68] showed that, at the nominal $10^{35} \text{ cm}^{-2} \text{ s}^{-1}$, the expected mean radiation dose is $\simeq 1 \text{ rad/h}$, with a maximum value of $\simeq 5 \text{ rad/h}$ for the innermost crystals.

For this reason, the manufacturer company was required to characterize the radiation hardness of each crystal, after the exposure to a $\simeq 3 \text{ krad}$ ^{60}Co source. In this way, crystals can be properly arranged in the FT-Cal setup, with those more radiation-hard mounted nearer the beam line. However, radiation hardness needs to be measured independently, at least for a selected sample, to confirm data provided by the manufacturer.

Crystals radiation hardness is expressed through the “induced absorption” parameter Δk , defined as:

$$\Delta k = \frac{1}{L} \ln \frac{T_{pre}}{T_{post}} \quad , \quad (3.2)$$

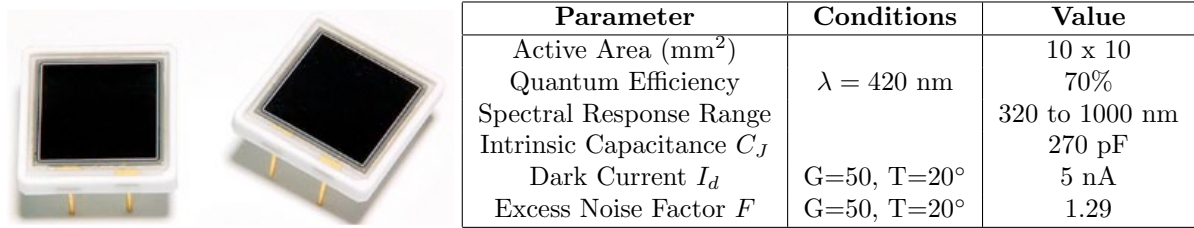


Figure 3.6: Left: Hamamatsu S8664-1010 APD. Right: the photo-detector properties.

where L is the crystal length (20 cm), and T_{pre}, T_{post} the crystal longitudinal optical transmission evaluated at a selected wavelength, typically 420 nm, respectively before and after the exposure to the radiation field. Each FT-Cal crystal is required to have $\Delta k < 1 \text{ m}^{-1}$.

During the FT-CAL crystals measurement campaign, the radiation hardness of 100 selected samples was studied, using the facility installed at the University of Giessen. The optical transmission was measured with a spectrophotometer before and after the exposure to a 30 krad ⁶⁰Co source, and the obtained Δk parameter was compared to what declared by the manufacturer. Results are reported in Figure 3.5 (right-panel). A significant disagreement is seen, both for the Δk absolute value, and in terms of correlation in between the two datasets. This result calls for the measurement of the whole batch, to better evaluate how manufacturer results are accurate and, if necessary, to reject those crystals out of specifications. The full characterization is actually planned in February 2014, at the Giessen facility.

3.2 Photo Detectors

Avalanche Photodiodes (APDs) are employed in the FT-Cal to readout the light emitted from scintillating crystals and convert it to an electrical signal. The main reasons to employ these optical sensors are: the small size (15x15 mm² for an active area of 10x10mm²), the high quantum efficiency ($\simeq 70\%$ in the spectral region of PbWO₄ emission), and the low sensitivity to magnetic fields. The main disadvantage, compared to standard photomultiplier tubes, is that, due to the low intrinsic gain ($\simeq 20 \div 250$), the output signal needs to be amplified by a suitable circuit before the acquisition. APDs must also be operated at controlled temperature to avoid gain variations that would directly affect the overall resolution of the detector.

3.2.1 APD layout and operation

APDs are reverse-biased photodiodes with an high intrinsic gain, obtained from an avalanche multiplication mechanism occurring in their internal depletion region. The detector working principle is described in Figure 3.7. When optical photons hit the detector, they move across the SiO₂ layer, the N layer, and the P layer, finally entering in the depletion region where they produce free electron-hole pairs. If a reverse bias voltage is applied, the high electric field created in the depletion region multiplies the charge-carriers by impact ionization, resulting in an avalanche process. Electrons are then collected in the N layer, while holes are collected in the P layer. The output current signal is proportional to the intensity of the incident light, i.e. to the number of photons that actually hit the photo-detector.

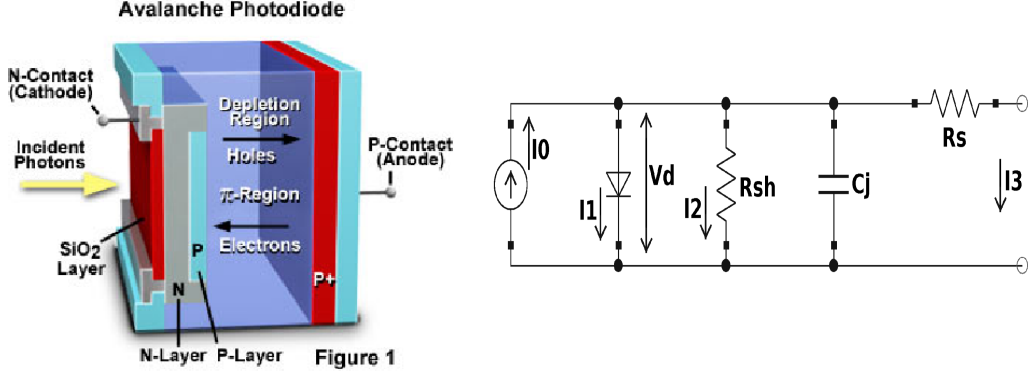


Figure 3.7: Left: APD internal layout and working principle. Right: APD equivalent electric circuit.

The APD equivalent electric circuit is similar to that of standard photodiodes. C_J is the intrinsic capacitance of the APD, R_{SH} is the shunt resistor, and R_S is the series resistor. Typically, $R_S \simeq \Omega$, while $R_{SH} \simeq 10^7 \div 10^{11} \Omega$. The current I_3 flowing through an external load R_3 in DC regime is obtained from the following relations:

$$\begin{aligned} I_3 &= I_0 - I_1 - I_2 \\ I_3 &= I_0 - I_s \cdot \left(\exp\left(\frac{q_e V_d}{KT}\right) - 1 \right) - \frac{V_d}{R_{SH}} \end{aligned} \quad (3.3)$$

where I_0 is the photo-current generated by incident photons, I_1 is the reverse bias leakage current, and I_2 is the current across the shunt resistor. Neglecting the latter due to the very high R_{SH} value and considering the reverse bias-voltage regime, $V_d \ll 0$, the following I_3 expression is derived:

$$I_3 = I_0(G) + I_s(G) \quad (3.4)$$

The DC current is thus the sum of the photo-current and the leakage dark current of the APD junction, both being a function of the device intrinsic gain G . For time-dependent signals, the detector intrinsic capacitance C_j has to be considered to determine the cut-off frequency of the system when connecting the APD to an external circuit with input resistance R . It adds a pole to the transfer function of the whole system, at a frequency $f_{cut} = \frac{1}{2\pi RC_J}$.

3.2.2 APD internal gain and dark current measurement

Both the APD intrinsic gain G and dark current I_d strongly depend on the bias voltage V and on the operating temperature T . To reach maximum performances in terms of resolution and linearity it is important that all the channels in the FT-Cal are operated at the same working point, i.e. all the APDs have the same gain. It is therefore crucial to measure the gain of each APD as a function of V and T in the proximity of the foreseen working conditions. Mapping the gain of each sensor will also permit to sort APDs with similar response and supply with the same bias voltage, thus reducing the number of independent power channels.

The procedure I employed to measure the internal gain G at fixed temperature T as a function of the bias voltage V is as follows. The dark current I_{off} and the photo-current due to a continuous illumination I_{on} were measured at different values of the reverse bias voltage V_b . The light source was a blue LED, with an emission peak similar to the maximum emission wavelength of PbWO_4

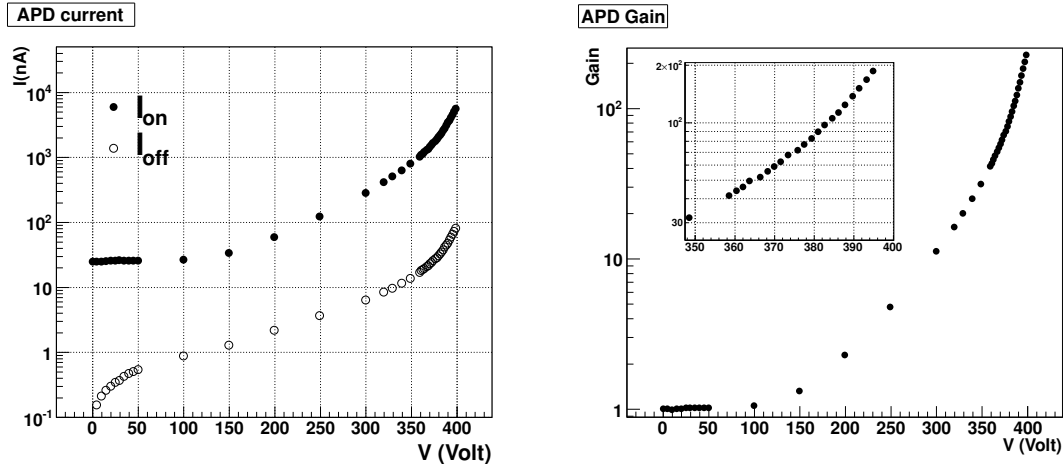


Figure 3.8: Left: dark current I_{off} and light current I_{on} for an Hamamatsu s8664-1010 APD as a function of bias voltage. Right: APD gain calculated from these measured currents with equation 3.5. The inset shows data near $G = 150$. This measurement was performed at $18.4 \pm 0.1^\circ$.

(420 nm)¹. The gain was derived using the following equation:

$$G(V_B) = \frac{I_{on}(V_B) - I_{off}(V_B)}{I_{on}(G = 1) - I_{off}(G = 1)} \quad , \quad (3.5)$$

where $I_{on}(G = 1)$ and $I_{off}(G = 1)$ are, respectively, the values of the photo-current and the dark current when the internal gain of the APD is equal to one, i.e. when the bias voltage is sufficiently low so that the avalanche mechanism is not active. These values must be measured independently to calculate the gain.

Figure 3.8 shows the typical behavior of I_{on} and I_{off} as a function of the bias voltage, at room temperature. After an initial plateau, which corresponds to the unitary gain, I_{on} grows rapidly for increasing bias voltage. I_{off} remains smaller than I_{on} by a factor $\simeq 100 - 1000$. Thus the denominator in Eq. 3.5 corresponds to the I_{on} initial plateau. The corresponding APD gain curve exhibits a constant behavior for bias values lower than $\simeq 100$ V, while it increases rapidly for higher values.

The measured dark current I_{off} is reported in Figure 3.9 (left) as a function of the intrinsic gain G . It shows a linear dependence, as expected from the most common interpretation of APD dark current as a sum of two terms: the first (“surface-current”) being independent from G , and the second (“bulk current”) being directly proportional to it.

Finally, the relative gain variation with respect to the bias voltage, between $G = 40$ and $G = 200$, is shown in Figure 3.9 (right). In particular, I got:

$$\begin{aligned} \frac{1}{G} \frac{\partial G}{\partial V} &= 3.2\%/V \quad \text{for } G = 50 \\ \frac{1}{G} \frac{\partial G}{\partial V} &= 6.5\%/V \quad \text{for } G = 150 \end{aligned}$$

These results are in very good agreement with similar measurements reported in [76].

¹The stability of the LED was checked using a stable PMT and measuring its output current while exposed at the LED light. I did not see any appreciable variation during a period of several hours.

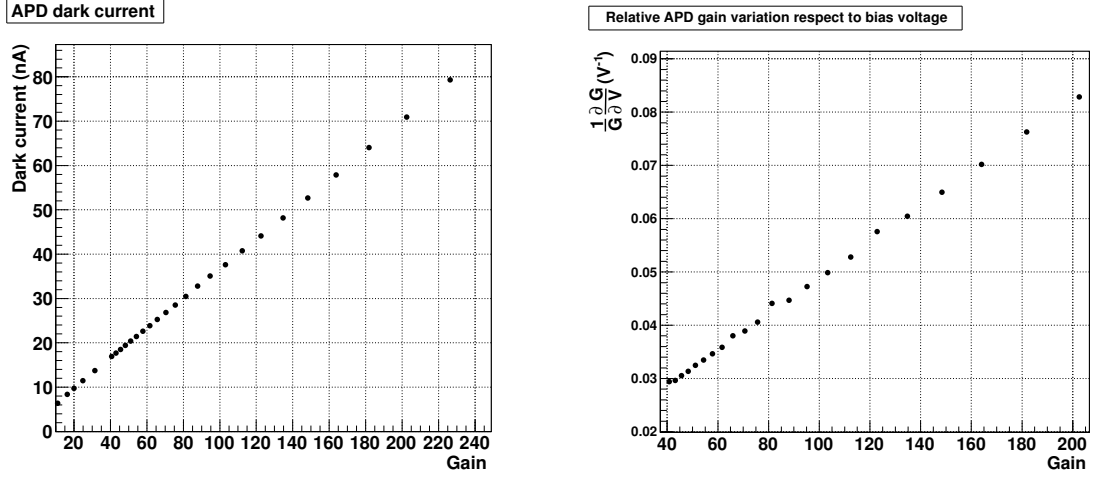


Figure 3.9: Left: APD dark current I_{off} as a function of the intrinsic gain G . Right: APD relative gain variation with respect to the bias voltage.

Temperature dependence

I investigated the APD gain temperature dependence repeating the measurement described above at different temperatures between $-1\text{ }^{\circ}\text{C}$ and $+21\text{ }^{\circ}\text{C}$. The obtained results, reported in Figure 3.10, show that, at fixed bias voltage, the intrinsic gain decreases with temperature. Also, the curves corresponding to constant gain values in the Voltage-Temperature plane are approximately straight lines, therefore the APD intrinsic gain depends on a linear combination of these two variables:

$$G(V, T) = G(\alpha V - \beta T) \equiv G(x) \quad (3.6)$$

where α and β are two proper coefficients, related to the slope of the iso-gain curves in the $V - T$ plane, and $x = \alpha V - \beta T$. From the above equation, the following expressions for the relative gain variation respect to the bias voltage and to the temperature can be derived:

$$\frac{1}{G} \frac{\partial G}{\partial V} = \alpha \frac{G'}{G} \quad (3.7)$$

$$\frac{1}{G} \frac{\partial G}{\partial T} = -\beta \frac{G'}{G} \quad (3.8)$$

I also used the the APD gain linear behaviour to derive a procedure to calculate it for any (V, T) setting. This procedure requires to characterize the device response, as a function of bias voltage, only at few different temperatures. In particular:

- Knowing the foreseen working point, i.e. the desired bias voltage V_0 and operating temperature T_0 , the combination $x_0 = \alpha V_0 - \beta T_0$ is calculated. x_0 determines uniquely the APD gain value G_0 , as follows from Eq. 3.6.
- The “equivalent-bias” V_1 , that results in the same gain value G_0 when the device is operated at a different temperature T_1 , is that corresponding to the same x_0 value, and is therefore given by:

$$x_0 = \alpha V_1 - \beta T_1 \rightarrow V_1 = V_0 - \left(\frac{\alpha}{\beta}\right)^{-1} \cdot (T_0 - T_1) \quad (3.9)$$

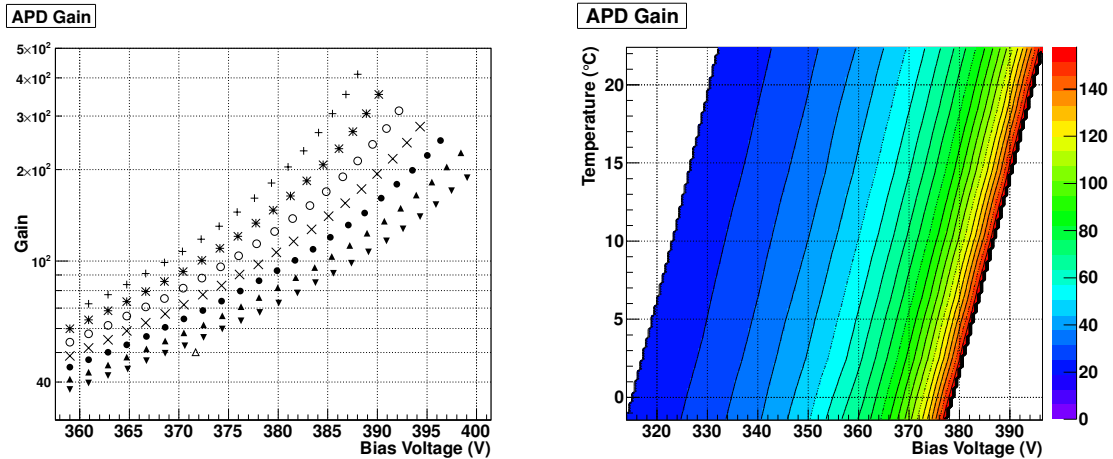


Figure 3.10: Left: APD intrinsic gain G for different temperatures. + : -1.44°C , * : 2.51°C , o : 6.47°C , × : 10.44°C , • : 14.43°C , ▲ : 18.42°C , ▼ : 22.39°C . The open triangle corresponds to the bias declared by the manufacturer for $G=50$ @ $T=+25^{\circ}\text{C}$. Right: the same data reported in a bydimensional plot, with constant gain curves highlighted in black.

- G_0 is calculated from the gain curved obtained at temperature T_1 , by evaluating it at the “equivalent-bias” V_1 defined above.

The above method, that requires to characterize the APD response only at a single temperature T_1 , is actually based on the knowledge of the ratio $k \equiv \alpha/\beta$, i.e. the slope of the constant gain lines in the $V - T$ plane.

This parameter can be obtained by comparing measurements performed at few different temperatures, and calculating for each of them the bias voltage corresponding to a certain fixed gain. Figure 3.11 shows, for example, the values corresponding to $G = 50, 100, 150, 200$ for six temperatures in the range between 0 and 25 °C. The slope of the lines points are aligned to corresponds, by definition, to k . This parameter is therefore extracted by performing a best fit with a first-order polynomial to the different data points. In particular, for the measured APD, I obtained $k = (1.26 \pm 0.01)^{\circ}\text{C}/\text{V}$.

3.2.3 APD working point selection

The APD output noise is the sum of two independent contributions, the first related to statistical fluctuations in the APD signal formation process, and the second to the electronic noise of the amplifier (see sec. (3.3)). The first term changes varying the APD internal gain, while the second is independent on it. The working point of the FT-Cal APDs has thus been chosen with to maximize the intrinsic resolution of the photodetector, i.e. the signal-over-noise ratio, finding a balance between the two noise sources.

I investigated the APD optimal working point measuring the intrinsic signal fluctuations, for different values of the intrinsic gain G , using a stable LED pulser as light source. The employed APD was previously characterized measuring its intrinsic gain and dark current as a function of the bias voltage. The gain of the amplifier was also measured and found to be $\simeq 1765$.

In practice, I measured the output charge Q and its fluctuations σ_Q as a function of the bias voltage V_B , integrating the amplifier output signal in a 150 ns gate. To measure the signal fluctua-

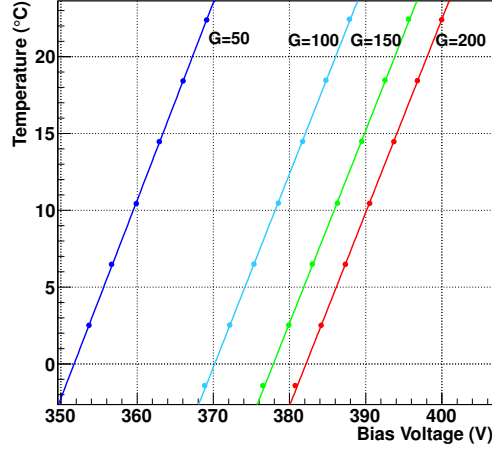


Figure 3.11: APD bias voltage corresponding to a fixed gain G_0 , as a function of the working temperature.

tions σ_{Q_n} due only to the intrinsic noise of the amplifier, I integrated the output signal out-of-time respect to the LED pulse, within the same gate.

Results are shown in Figure 3.12. The absolute value of the signal fluctuation σ_Q increases with the gain of the APD, as the measured output charge. The relative charge resolution σ_Q/Q instead decreases with the gain, reaching a minimum at $G \simeq 100$, and then gets slightly worse for larger bias voltages. This behavior is due to the amplifier noise, that contributes to the signal resolution with a constant term negligible at high APD gain. The degradation in the resolution for $G > 100$, known as “excess noise”, is instead related to inhomogeneities in the APD depletion region, where the charge multiplication process occurs.

From these measurements, we set the FT-Cal APD working point at the intrinsic gain of 150, to achieve the best resolution while keeping the dark current at a reasonable low level.

Excess Noise Factor F

APD signal statistical fluctuations arise from two different contributions. The first is related to the production of electron-hole pairs, so that when N_γ photons hit the photo-detector, the number of electron-hole pairs is distributed according to a Poisson distribution with mean N_e and standard deviation $\sigma_{N_e} = \sqrt{N_e}$. The second term, instead, originates from inhomogeneities in the depletion region that each electron-hole pair experiences independently during the avalanche process. This effect induces an effective fluctuation in the intrinsic gain G that corresponds to an additional term $\sigma_G \cdot \sqrt{N_e}$ in the signal resolution.

The “excess noise factor” F is thus introduced in the APD energy resolution parametrization to take this effect into account [77]:

$$\frac{\sigma_E}{E} = \frac{\sigma_Q}{Q} = \frac{1}{\sqrt{N_e}} \cdot \frac{\sqrt{G^2 + \sigma_G^2}}{G} \equiv \frac{\sqrt{F(G)}}{\sqrt{N_e}} \quad (3.10)$$

I measured the excess noise factor F for the APD already used to identify the working point of the FT-Cal photodetectors, as described in the previous section. For each value of the bias voltage, I measured the output charge Q and its fluctuation σ_Q , as well as the noise contribution due to the amplifier only σ_{Q_n} . Subtracting quadratically these two terms I obtained the *true* APD signal

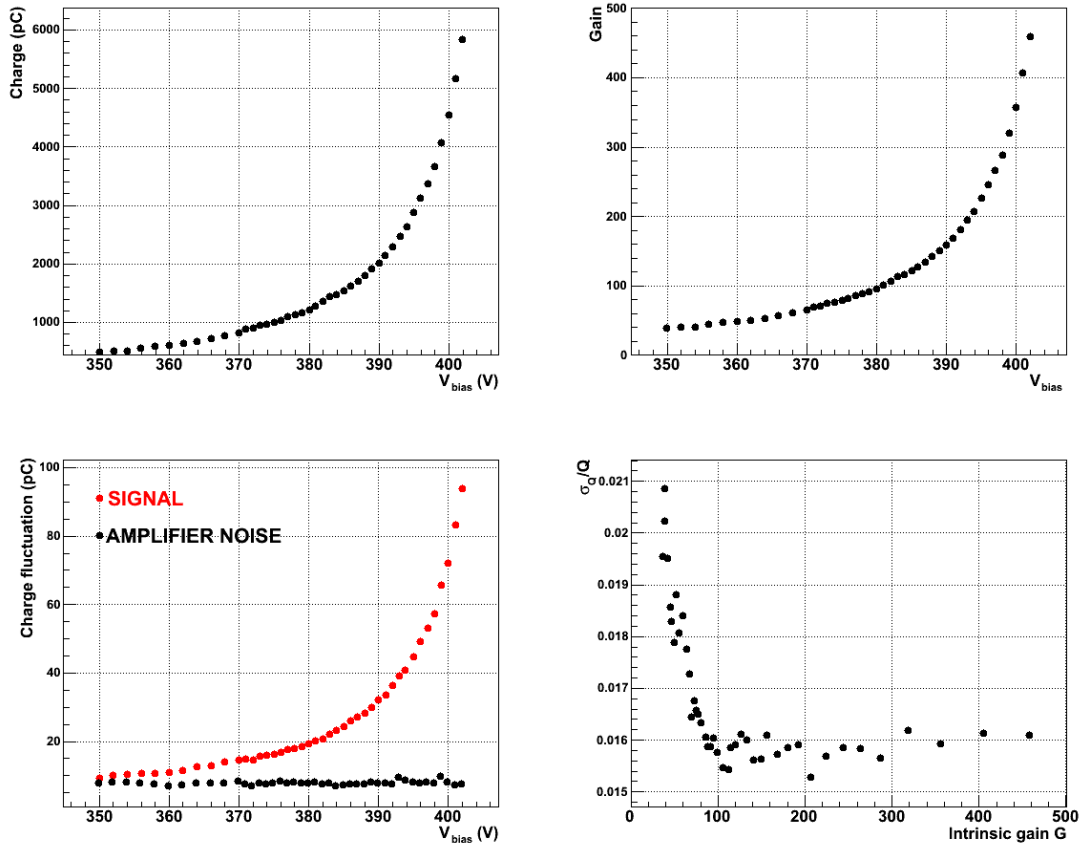


Figure 3.12: Results of the measurement to select the APD working point. Top left: measured signal charge as a function of the bias voltage V_b . Top right: APD intrinsic gain G . Bottom left: output signal fluctuations, in black the contribution of the preamplifier noise and in red the total fluctuation (APD + amplifier). Bottom right: output charge relative resolution as a function of the APD gain G .

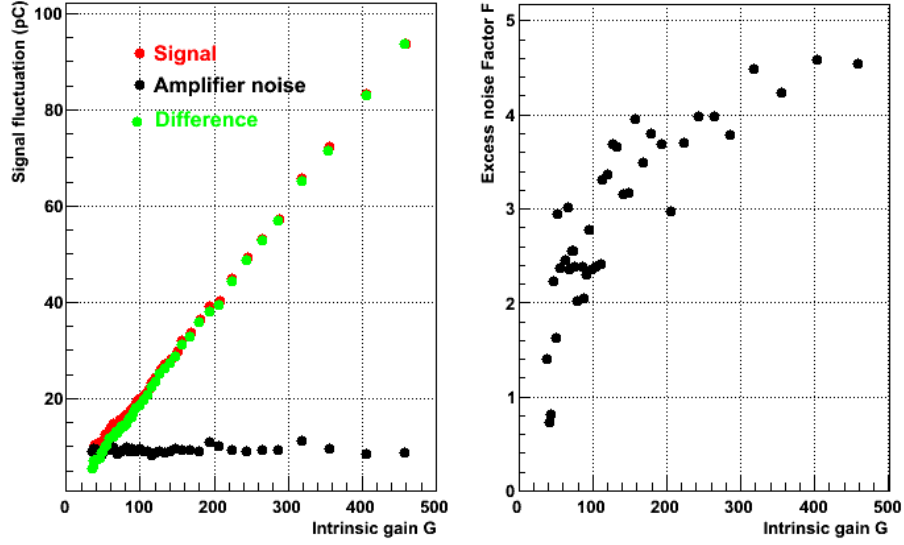


Figure 3.13: Left: measured charge fluctuations of signal and background, and their difference, as a function of the bias voltage. Right: the APD excess noise factor F as a function of the APD intrinsic gain G .

fluctuation:

$$\sigma_{Q_{APD}} = \sqrt{\sigma_Q^2 - \sigma_{Q_n}^2} \quad (3.11)$$

I estimated the number of primary electron-hole couples N_e from the measured charge Q_0 at the APD nominal working point, divided by the amplifier gain ($\simeq 1770$) and the nominal gain $G = 150$):

$$N_{phe} = \frac{Q_0}{q_e \cdot G_0 \cdot G_{ampl}} \simeq 45 \cdot 10^3 \quad (3.12)$$

Finally, I used Eq. 3.10 to evaluate F :

$$F = N_e \cdot \left(\left(\frac{\sigma_{Q_{APD}}}{Q} \right)^2 - (\delta_{LED})^2 \right) \quad (3.13)$$

In the formula above, δ_{LED} is the contribution to the resolution due to the LED pulser, arising from intrinsic fluctuations in the LED emission. I assumed this contribution to be $\simeq 1.0\%$.

Final results are reported in Figure 3.13. I obtained $F = 1.6$ for $G = 50$ and $F = 2.4$ for $G = 100$, in agreement with the measurement performed by PANDA collaboration for the same type of sensors [71].

3.2.4 Facility for APD Gain Measurement

In preparation of the full FT-Cal detector, I developed a facility to measure the APD intrinsic gain and dark current, as a function of bias voltage and operating temperature, in a semi-automatic way. This facility can characterize up to 24 devices together, in the bias voltage range (0 - 400) V and temperature range (-2° - $+25^\circ$). The measurement at each T takes approximately 4 hours,

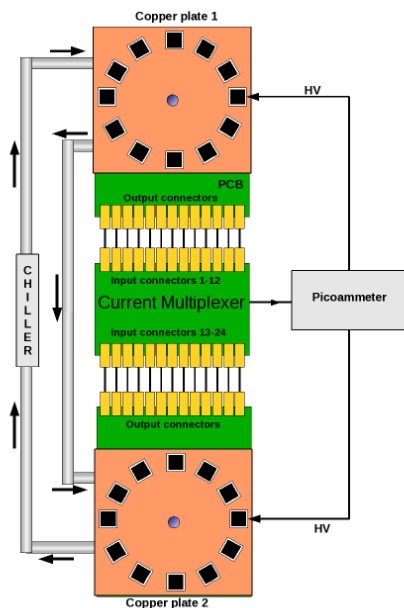


Figure 3.14: Simplified layout of the APD gain measurement facility.

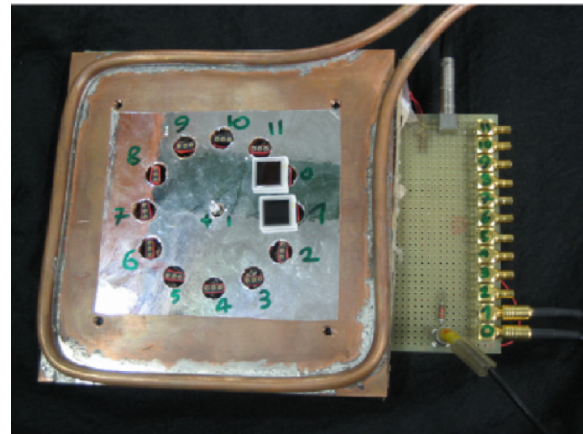


Figure 3.15: One of the metallic plates hosting APDs in the facility for APD gain measurement.

requiring one day to fully characterize sensors in the chosen temperature range. The full set of 380 FT-Cal APDs can be tested with this facility in approximately one month.

The gain of each APD is measured with the technique already described in previous section. The dark current and the photo-current are measured scanning the bias voltage range between 0 and 400 V, with programmable steps, and the gain is then calculated through Eq. 3.5. The stable light source for photo-current measurement is a blue LED of the same type mentioned before.

The general layout of the facility is shown in Figure 3.14. The 12+12 APDs under measurement are mounted on two drilled copper plates, both hosting a LED. Each APD is mounted in correspondence of a hole, and is connected to a PCB on the opposite side of the plate. The APDs are arranged circularly around the LED, that is also connected to the PCB (Figure 3.15). The PCB distributes the HV bias to each APD and feeds their currents to the input of a current multiplexer.

The current multiplexer is the “core” of the facility (see Figure 3.16), that employs a single picoammeter and a single HV source for all the APDs. During operation, the APD cathodes are all connected to the HV source through independent bias resistors, while the anodes are connected to the multiplexer inputs. The multiplexer single output is connected to the picoammeter. In this way, only one APD at a time is physically attached to the picoammeter, while the other 23 are coupled to ground.

I designed the current multiplexer using mechanical relays (type SPDT, “single pole, double throw”²). I chose to employ mechanical relays because the currents to be measured are of the order of 10-100 nA and other types of electronic switches, such as those based on transistors, would have introduced spurious currents of the same order of magnitude, leading to incorrect gain

²A SPDT relay is a 3-terminals device. One of them connects to either of two others, depending on the state of the magnetic coil.

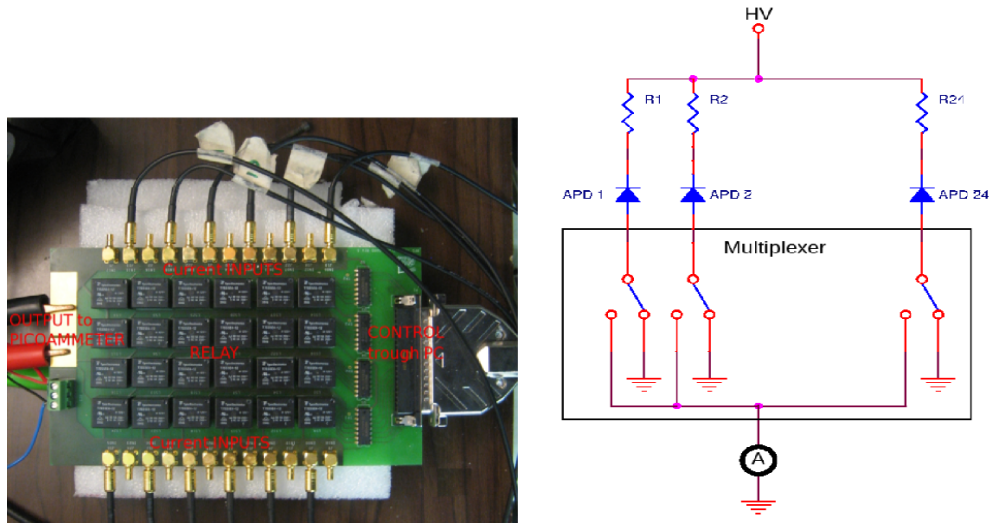


Figure 3.16: Left: picture of the current multiplexer of the facility for APD gain measurement. Right: simplified schematic of the gain measurement circuit (only three channels are reported). “HV” is the common high voltage source, “A” the picoammeter.

measurements.

The facility also includes a cooling system to keep APDs at a constant temperature. The coolant flows in a pipe welded on each of the two plates and connected to an external programmable chiller. The temperature is continuously monitored through 2 thermoresistors mounted on each plate. The chiller provides temperature feedback loop with 0.1° stability. Furthermore, during the operation, the copper assembly is inserted in a vacuum- and light-tight box flushed with nitrogen to prevent moisture formation.

The system, controlled through a Labview program running on a PC, works as follows. During the initial setup phase the user enters the values for the temperature scan and the number and IDs of the APDs to characterize. For each programmed temperature, APDs are individually enabled and their gain is measured. At the end of all measurements data is analyzed to obtain the intrinsic gain G of the APDs as a function of the bias voltage and temperature. Relevant parameters, such as the bias voltage corresponding to a gain of 150 at room temperature, the relative variation of the gain respect to the temperature and the bias voltage in the neighborhood of the nominal working point, and the k ratio, are then recorded in a file.

During the facility commissioning I investigated the relevance of possible systematic effects in the measurement, such as those due to long term fluctuations introduced by temperature drifts, residual moisture formation, variations in the LED emission. I repeatedly measured the gain of the same APD over a time period of 15 days, comparable with the overall time required to characterize all the sensors of the FT-Cal, calculating the bias voltage corresponding to its nominal gain at room temperature ($G = 150 @ T = +18^\circ\text{C}$). Results are reported in Figure 3.17. All the measurements show the working point within 0.1 V. This corresponds to a relative error on the measured gain lower than 1%, being $\frac{1}{G} \frac{\partial G}{\partial V} \simeq 6.1\%$ in the neighborhood of the working point. This value is sufficiently small respect to the accuracy that is needed in the FT-Cal application.

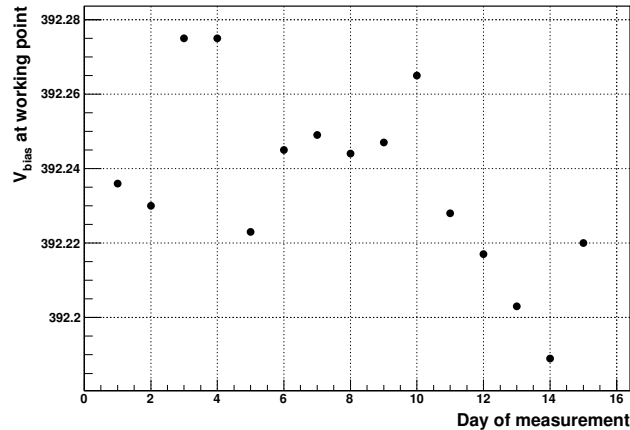


Figure 3.17: APD bias voltage corresponding to a gain $G=150$ at room temperature obtained in each of the 15 measurements performed to check system stability.

3.2.5 FT-CAL APDs characterization

At the moment of writing this document, all the 380 FT-Cal APDs (including spares) have been characterized employing the semi-automatic facility, and 96% of them were found to be within specifications. Only 18 showed an unexpected behavior at low temperature, and therefore need to be replaced.

Results are shown in Figure 3.18. The left panel reports the bias voltage required to operate photo-detectors at the nominal gain $G = 150$, for different operating temperatures. Photo-detectors are distributed in groups of tenths with similar characteristics, as requested during the purchase process. In the FT-Cal setup photo-detectors belonging to the same group will be supplied with the same bias voltage, thus reducing the number of required high-voltage channels. The APD grouping does not change with the operating temperature. The right panel, instead, shows the comparison between the *measured* bias voltage corresponding to APD gain $G = 150$ at 0°C , and the value obtained by *extrapolating* data measured at 20°C , using the above described procedure. The good agreement proves the reliability of the procedure, that can therefore be employed to calculate the APD gain at any (V, T) setting.

3.3 Amplifiers

The APDs output signal is too low to be directly acquired, and needs to be amplified by a suitable circuit, that must fulfill specific requirements dictated both by the physical application and by the overall setup of the FT-Cal, in particular the DAQ chain.

I developed this amplifier starting from the existing CLAS-IC [72] design, that was employed to read-out to a similar APD (Hamamatsu 8664-55, with active area $5 \times 5 \text{ mm}^2$). During the design, I collaborated with the “Servie d’Electronique Physique” (SEP) of the “Institut de Physique Nucleaire” (IPN) of Orsay. Here I present the scheme of the circuit, as well as the tests on few samples that I did to characterize it and verify it met the FT-Cal requirements. At the moment of the writing of this document, all the FT-Cal amplifiers have been produced and tested at IPN Orsay and delivered to Genova.

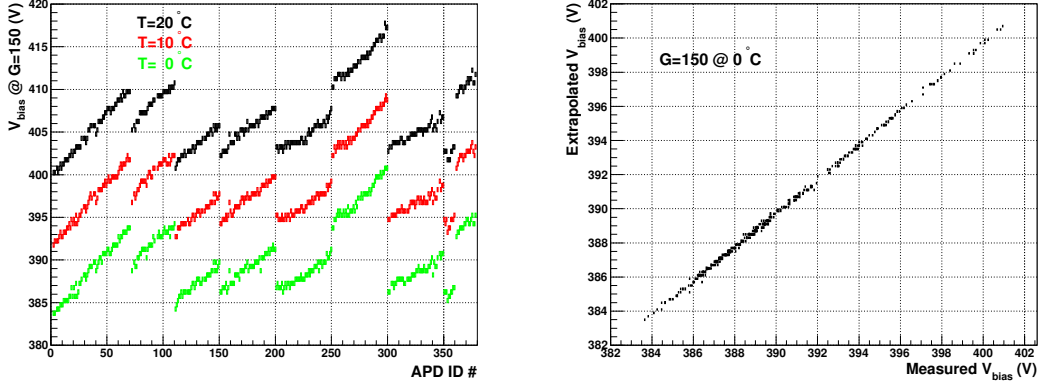


Figure 3.18: Left: Bias voltage corresponding to $G = 150$ for operating temperatures 20°C (black), 10°C (red), 0°C (green). Right: bias voltage for $G = 150$ at 0°C , measured (x axis) and extrapolated from 20°C (y axis).

3.3.1 Requirements

The main properties of the amplifier that were considered and tuned during the design phase were: the gain, the dynamic range, and the intrinsic noise, that were fixed according to the FT-Cal physical application. In particular, the dynamic range must be large enough to match with the deposited energy per channel, that, according to simulations, can spread from 10 MeV to 5 GeV. Thus a dynamic range of at least 500 is required.

The required gain can be estimated requiring that the output signal corresponding to the maximum energy deposited in each FT-channel (5 GeV) is matched to the maximum signal that the DAQ chain can acquire (4 V). Assuming a crystal light-yield at room temperature $LY \simeq 13$ phe/MeV, an APD quantum efficiency $\varepsilon \simeq 0.7$ and intrinsic gain $G \simeq 150$, and an output signal width $T \simeq 50$ ns, the output charge corresponding to 5 GeV deposited in the PbWO_4 crystals is roughly:

$$Q_{max} \simeq G_{ampli} \cdot 1.1 \text{ pC} \quad (3.14)$$

and this results in an output signal amplitude of:

$$A_{max} \simeq Q_{max} \frac{2R}{T} \quad , \quad (3.15)$$

where $R = 50 \Omega$ is the acquisition device input impedance. By imposing $A_{max} = 4 \text{ V}$ the required amplifier gain is $G_{ampli} \simeq 1800$.

The intrinsic noise of the amplifier must be small enough to detect the lowest energy deposited in each channel (10 MeV). This corresponds roughly to a RMS noise not larger than 5 mV.

Finally, the physical dimensions of the amplifier ($12 \times 60 \text{ mm}^2$) were imposed by the size of the PbWO_4 crystals and of the APD, and no modifications of the CLAS-IC design were required. Figure 3.19 shows the amplifier with its surface mounted components. The contacts on the rails ensure careful grounding when the amplifier is inserted in the FT-Cal copper structure.

3.3.2 Circuit design

The designed circuit is a 3-stages trans-impedance amplifier, which converts the APD current pulse to an output voltage, without performing any integration. The schematic is shown in Figure 3.19.

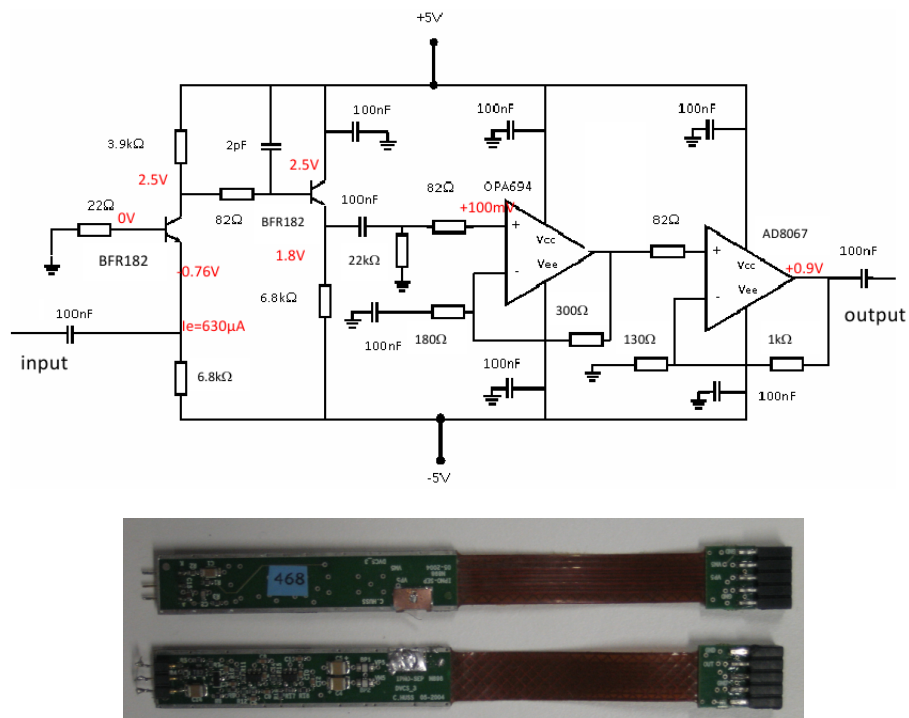


Figure 3.19: Top: schematic of the FT-Cal APD amplifier. DC characteristics are reported in red. The HV bias network is not shown. Bottom: Front and rear view of the FT-Cal APD amplifier.

The first stage is based on a BJT NPN transistor in common-base configuration, while the second and third are based on fast operational amplifiers in non-inverting configuration. The second transistor decouples the first stage from the second one, acting as a voltage follower. Both transistors (BFR182) have been chosen due to their low noise and high cut off-frequency, while the last operational amplifier is a rail-to-rail model (AD8067) used to have a maximum output signal of 5 V.

The amplifier also provides bias voltage to the APD, through a dedicated resistor network (not shown in Figure 3.19). The APD is coupled to the amplifier at the cathode through a 100 nF capacitor, while the anode is kept at ground.

The DC behavior of the first stage is calculated neglecting the small base current, therefore having equal collector and the emitter currents, $I_e = I_c$. Since the base is connected to ground, the emitter voltage V_e is equal to the transistor base-to-emitter voltage drop, $V_{be} = -0.76$ V. Thus $I_e = \frac{V_{EE}-V_c}{R_c} = 630$ μ A.

A current pulse at the input corresponds to a variation in the emitter current i_e and, since the collector current variation i_c is the same, the voltage signal at the collector is $v_c = i_e \cdot R_c$. The current-to-voltage gain of the first stage is therefore equal to the collector resistance, $G_1 = R_c = 3.9 \cdot$ V/mA. The voltage signal is then amplified by the second and the third stages, respectively with a gain $G_2 = 2.7$ and $G_3 = 8.7$.

The overall transimpedance gain of the amplifier, defined as the ratio between the output voltage pulse and the input current pulse, is $G = G_1 \cdot G_2 \cdot G_3 = 91 \cdot$ V/mA. The *charge-to-charge gain*³ depends on the input-impedance of the load the amplifier is connected to, according to the relation $G_c = \frac{G}{Z_{in}}$. For $Z_{in} = 50$ Ω the charge gain is $G_c \simeq 1800$.

The input impedance of the amplifier is related to the first transistor DC emitter current I_e , through the relation $Z_{in} = \frac{V_T}{I_e}$, where V_T is the thermal voltage (kT/e). For $T=300$ $^{\circ}$ K, $R_{in}=41$ Ω . The overall bandwidth is limited by the first stage collector resistance R_c (3.9 k Ω) and capacitance C_c (2 pF), resulting to a cut-off frequency $f_{cut} = \frac{1}{2\pi R_c C_c}$ of 20 MHz.

3.3.3 Performances

I measured both the charge-to-charge and charge-to-voltage gain of a FT-Cal amplifier prototype, injecting different input signals with known charges and measuring the amplitude and the area of the corresponding output pulses with a digital oscilloscope. The input signal rise time was 20 ns. Results are shown in Figure 3.20. The measured charge gain of 1679 is compatible with the one expected from the design and the offset is compatible with 0, proving the good linearity of the circuit.

I also measured the intrinsic noise of the amplifier, at different working temperatures, simulating the effect of the APD presence through a capacitor placed at the circuit input. I measured the RMS noise of the output signal from the amplifier, calculating the ENC (equivalent noise charge)⁴ using the following equation:

$$ENC = \frac{V_{RMS}}{G_v \cdot e} \quad , \quad (3.16)$$

³A transimpedance amplifier converts an input *current* to an output *voltage*, thus its intrinsic gain G is measured in V/mA. The *charge-to-charge gain* is defined as the ratio between the charge delivered by the output signal on a load Z and the charge corresponding to the input pulse, and its given by $G_c = G/Z$. Finally, the *charge-to-voltage gain* G_v is the ratio between the output signal amplitude and the input signal charge, and it is measured in V/pC. It depends also on the rise-time of the input signal.

⁴The “equivalent noise charge” of an amplifier is defined as the charge corresponding to an input signal that results in a output whose amplitude is equal to the RMS noise of the circuit. It is often expressed as an equivalent number of electrons.

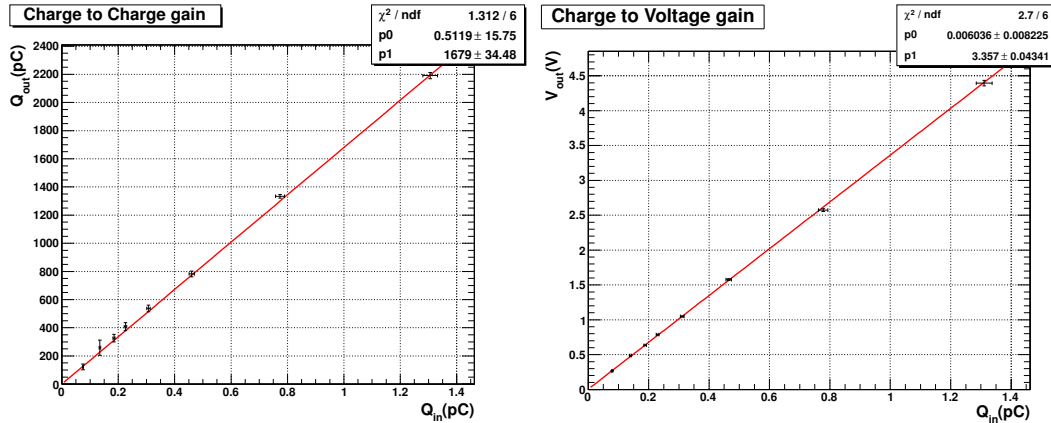


Figure 3.20: Measured charge-to-charge gain (left) and charge-to-voltage gain (right) of the prototype for the FT-Cal amplifier.

where V_{RMS} is the output signal fluctuation and G_v the amplifier charge-to-voltage gain. Results are reported in Figure 3.21 (left). Output noise increases with the input capacitance as expected, showing a saturation trend at high values, while the temperature dependence is weak. In particular, at $+20^\circ\text{C}$ the ENC for a detector capacitance of 280 pF the ENC is $(9000 \pm 100) e^-$ (RMS), roughly corresponding to a deposition of few MeV in the PbWO_4 crystals.

Finally, the amplifier power consumption is shown in Figure 3.21 (right), reporting the contributions for the $+5\text{ V}$ and -5 V supply lines and their sum. I performed this measurement injecting into the amplifier a signal roughly equivalent to 100 MeV deposited in the PbWO_4 crystal. At room temperature, the total power consumption is $\simeq 140\text{ mW}$, with equal contributions from the two supply lines. This value slightly decrease going at lower temperature, down to 135 mW at -20° . I did not observe any dependence of the power consumption on the input event rate, up to 500 kHz.

3.4 Readout electronics and raw data elaboration

After amplification, each FT-Cal channel signal is acquired and processed to extract the relevant physical quantities, i.e. the energy deposited in the crystal by the incident particles and the time of the corresponding hit. The CLAS12 DAQ system for fast detectors (time-of-flight counters and calorimeters) is entirely based on “Flash Digital to Analog Converters” (FADCs). These devices continuously digitize the amplitude of input signals and store the corresponding samples in their internal memory, leaving them available for readout when a trigger condition is satisfied. The main advantages of this solution, with respect to a “traditional” one based on QDCs (“charge to digital converter”), are the following:

- FADCs record the input signal as digital waveforms, therefore filter algorithms can be applied before proceeding further in the analysis to enhance the signal over noise ratio.
- The digitization is continuous and acquired samples are stored in a circular buffer inside the board. When a trigger is received, data are made available for readout while the acquisition process continues on another internal buffer. This reduces the overall dead time of the system.

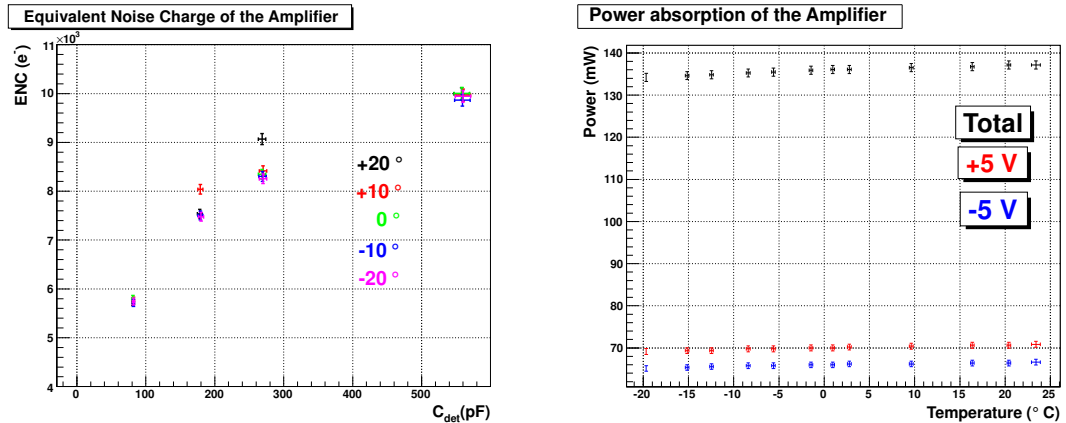


Figure 3.21: Left: FT-Cal amplifier ENC as a function of the input capacitance and operating temperature. Right: FT-Cal amplifier power absorption as a function of the operating temperature.

- FADCs are equipped with an on-board FPGA that elaborates digital waveforms to obtain *online* elaborated quantities, such as the signal charge and the corresponding hit time. This gives the opportunity to develop a “smart” trigger logic with sophisticated algorithms for events selection, and reduce the amount of data to be transferred to the storage disks.

Jefferson Lab developed a custom FADC board that will be employed by all the 12 GeV experiments: further details can be found in [78].

3.4.1 Signal integration

I developed the algorithm to perform digital waveforms integration, thus measuring the charge deposited in the corresponding FT-Cal channel. This algorithm was developed offline, working with acquired digital waveforms, and can be implemented in the JLab FADCs FPGA to run during data acquisition.

The algorithm works as follows (see also Figure 3.22). After finding the peak position and the corresponding amplitude, the samples belonging to a temporal window with fixed width, centered on the peak, are used to numerically integrate the waveshape using the trapezoidal rule. Then the pedestal is measured using the same integration window and technique applied to samples at the beginning of the acquisition window. These samples are also used to measure the RMS noise. Finally the charge of the signal is calculated subtracting the pedestal to the previously measured area. For a signal to be considered valid it is required that its amplitude is greater than three times the RMS noise, otherwise an error code is reported.

To see the effect on the charge resolution of the integration algorithm I implemented and tested different numerical methods, such as the Simpson’s rule or the discrete Gauss formula, running it on the same data set and looking for differences in the results. No appreciable variations were found. I also tuned the length of the integration window to maximize the charge resolution, obtaining the best results with a 160 ns window, beginning 40 ns before the peak pulse.

The algorithm has been successfully employed during all the tests of FT-Cal prototypes (see Sec. 3.6.1 and 3.6.2). The obtained data was also used to further optimize it [79], in particular employing an integration window with an event-by-event defined width.

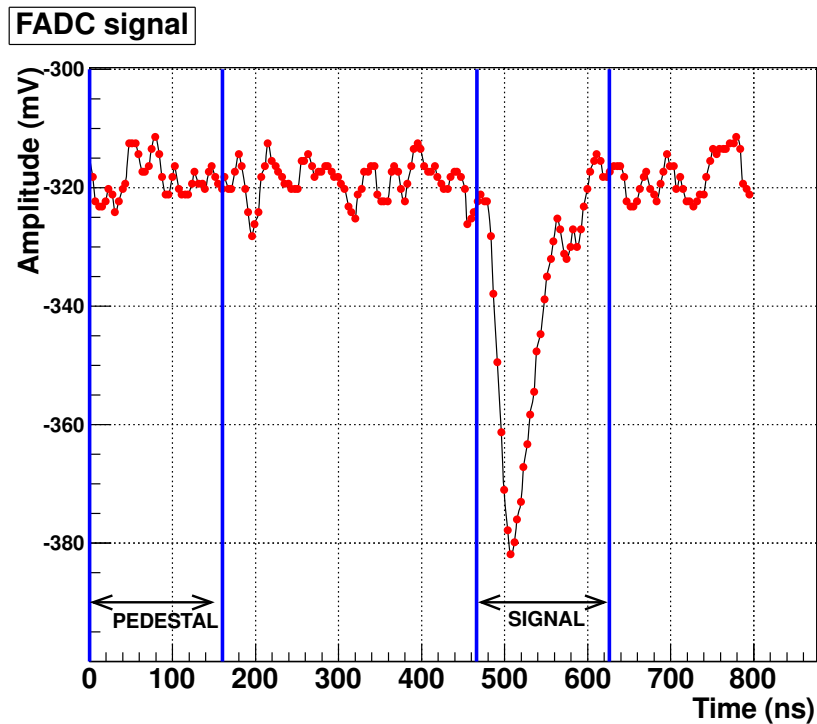


Figure 3.22: FADC acquired waveform for 100 MeV signal from PbWO_4 . Red dots are the FADC measured samples, while the black line connecting them has been added for clarity. This event has been measured with the 16-channel prototype of the FT-Cal during test at the “Beam Test Facility” of the INFN Frascati Laboratory, presented in Sec. 3.6.2. Acquisition boards were programmed with a 800 ns time window (200 samples @ 4 ns clock) and -320 mV DC offset, shifting the time scale to have the signal peak 500 ns after the beginning of the acquisition window. The two region between the blue lines, “pedestal” and “signal”, are used in the calculation of the signal charge, as explained in the text.

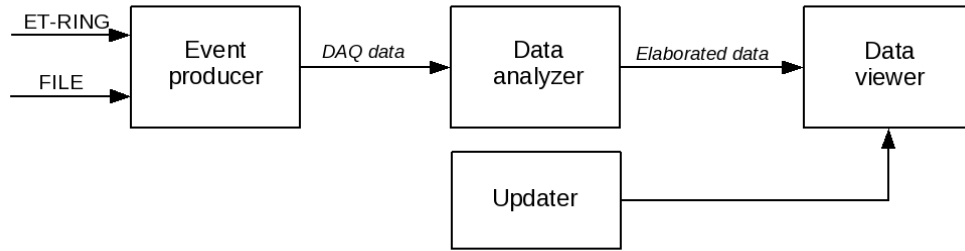


Figure 3.23: Simplified structure of the FT-Cal online monitoring system.

3.5 Online Monitoring System

During online operations, it is critical to have an immediate feedback of the detector response, to evaluate performances and to estimate data quality, without the necessity of running the full offline analysis chain.

To this end, I developed an online monitor software for the FT calorimeter. The physical quantities that need to be monitored spread from those specific to each channel, such as the waveforms acquired by the FADCs, the deposited energy, and the timing, to those more elaborated, like the total energy deposited in the detector by showering particles and the cluster distribution among the crystals. I specifically designed the program to fulfill these requirements, adapting it to the calorimeter 16-channels prototype. I matched all the involved algorithms to this specific detector, in particular to the format of the acquired raw data, but I structured the program so that only the specific algorithms implementation has to be changed to use it with the full FT-Cal, without modifying the general structure.

I wrote the online monitor software in C++ language, designing a modular program where each specific task is executed by a defined component. I realized a multi-thread program, assigning to each thread a specific operation. I took particular attention in thread synchronization, ensuring that no threads access to the same resource at the same time. For data visualization (histograms and graphs) and graphical interfaces I used ROOT [80] and GTK [81] libraries. I included in the program the possibility to run it offline on recorded data.

The structure of the program is shown in Figure 3.23. Each box represents a specific task executed by the program, while arrows are the connections in between them, for data and commands transferring. Depending on the way the program is employed, i.e. for online monitoring or to read a data file already written to the disk, data source is different. In particular, for the first case I used the “Event Transfer System (ET)” [82] that has been employed in the CLAS DAQ system and is foreseen also for CLAS12. The ET system provides a very fast and robust method of transferring events between different processes, in this case from the CLAS12 DAQ system to the monitoring program.

The main components of the system are the following:

- The “event producer” interfaces with the selected data source, the ET system or a data file, and acquires events from it. In the ET case, this operation is triggered by a programmable clock, while in the data file case it is up to the user to ask the visualization of new events, through a proper GUI. Raw data is then moved to the “data analyzer”, that converts them to an elaborated format containing the relevant quantities to monitor.
- The “data viewer” shows elaborated quantities to the user. It employs two sets of graphics,

“long-term” histograms populated with all the events coming from the event producer, and “short-term” plots, which show event-by-event data and are updated for each new event. In particular, long-term histograms show the energy deposited in each channel, the total energy in deposited in the calorimeter, the timing for each channel, and the occupancy. Short-term plots show the FADC waveforms and the energy center of gravity, one event at time.

- The “updater” ensures synchronization between different threads, and forces the update of the data-viewer graphycs, using the internal clock or by user request.

3.6 FT-Cal prototypes

The design of the full FT-Cal detector requires not only the detailed study of each single component, but also the realization of prototypes to test the whole assembly performances, and to validate the technical choices. To this end, two prototypes of the FT-Cal, with 9 and 16 channels respectively, have been assembled and tested with cosmic rays and electron beams. Prototypes were used to check the single crystal mechanical assembly, the thermal performances, the front-end and readout electronics, and the electrical connections. Response to cosmic rays was studied for both detectors, while the response to electromagnetic showers has been measured for the Proto-9 at JLab, using the electrons deviated by the Hall-B tagger system during a photon run (see Sec. 2.2), and for the Proto-16 at the LNF “Beam Test Facility”.

The main goals of these tests were: to measure the energy resolution of the calorimeter as a function of the operating temperature, to verify the linearity and stability of the system, to measure the electronic noise in realistic experimental conditions, and to validate MonteCarlo simulations.

3.6.1 FT Proto-9

The first prototype of the FT-Cal was made with 9 PbWO_4 crystals arranged in a 3x3 matrix, and surrounded by 7 stainless-steel “dummies” in a mechanical structure that simulates the real assembly. This configuration was chosen in anticipation of the later realization of a bigger prototype (see Sec. 3.6.2), with 16 crystals. Stainless steel was employed since its thermal properties are similar to PbWO_4 . Each crystal, wrapped in a VM2000 reflecting foil, was coupled to a Hamamatsu Large Area APD, whose output signal was read using a FT-Cal amplifier. The crystal assembly, shown in Figure 3.24, was hold by two PEEK supports, in the front and in the back, both glued to the the reflecting foil to form a whole rigid object with the crystal or the stainless-steel block.

The 9 crystals were inserted in a mechanical structure made by two copper plates, one on the top and one on the bottom of the crystals, and two copper grids that hold PEEK supports. Preamplifiers were connected to a PCB board to collect signals and provide low and high voltages. Proper amplifiers grounding was ensured trough copper rails.

The necessary cooling power to operate the prototype at constant temperature was provided by a liquid circulating in pipes soldered to the copper plates, and cooled by an external chiller. The rear copper grid thermally decouples the crystals from the preamplifiers, which are the main heat source in the prototype (approximately 150 mW/channel), and the whole assembly was surrounded by 5 cm thick insulating material.

With this configuration the prototype was operated in the temperature range between $-20\text{ }^\circ\text{C}$ and $+25\text{ }^\circ\text{C}$, with thermal stability of $0.1\text{ }^\circ\text{C}$: although not being foreseen in the final FT design, the prototype response was measured also at temperatures lower than $0\text{ }^\circ\text{C}$ for the sake of completeness. Temperature was monitored trough PT100 sensors located inside the insulation. During operations, the prototype was inserted into a black box flushed with nitrogen to prevent moisture formation, and to guarantee light tightness.

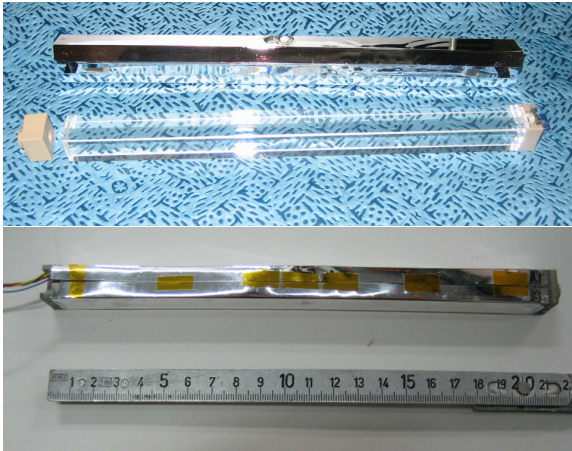


Figure 3.24: Top: a single FT Proto-9 crystal with its reflecting foil and the two PEEK support. Bottom: the full crystal assembly.

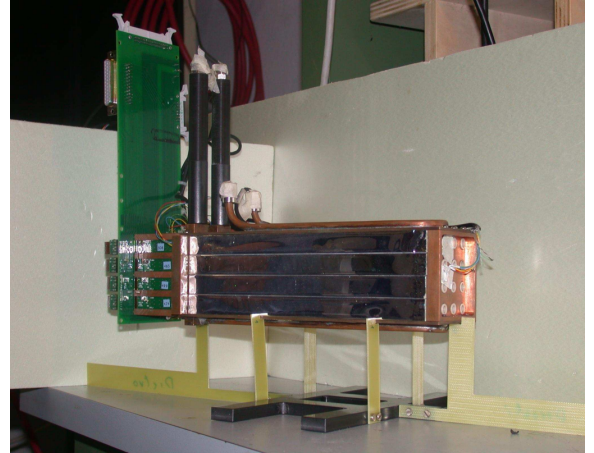


Figure 3.25: The 9-channels prototype of the FT-Cal assembled, before being inserted inside the black box.

The data acquisition system, based on the VME architecture, was similar to the one foreseen for the full FT-Cal integrated within CLAS12. It used commercial boards with similar characteristics of those that will be employed at JLab, and it was handled by the same DAQ program (“CODA”, Cebaf Online Data Acquisition [83]). The signal from each channel was splitted (50% - 50%) with a passive resistors network. One half of the signal was then sent to a 8-channel FADC (CAEN V1720), with 4 ns sampling period, 12 bits resolution and 2 V maximum input range, while the other was sent to a discriminator coupled to a multi-hit TDC (CAEN VX1290), with 25 ps intrinsic resolution.

Cosmic ray measurements

The FT Proto-9 response to cosmic muons was measured in Genova to obtain a first energy calibration point for each channel. The experimental setup is shown in Figure 3.26. The detector was inserted within three plastic scintillator bars vertically aligned and read on each side by a fast photomultiplier (Photronics XP2020 and Hamamatsu R2083). The 6-folds coincidence of the PMTs defined the trigger for data acquisition. Hit positions along the bars were reconstructed by the time hit difference between the two PMTs, thus allowing a precise geometrical reconstruction of the muon track. The time resolution of the over-constrained trigger system was estimated to be 75 ps.

Figure 3.27 shows the energy distribution of the cosmic muons detected in one of the Proto-9 crystals, at +19 °C. The red curve corresponds to the best-fit performed to extract the most probable value of the deposited energy. The fit was done with the convolution of a Landau and a Gaussian distribution, to include resolution effects.

The calibration constant used to convert the *charge* to the corresponding *energy* deposited in the crystal was derived comparing data to MC simulation, implemented in the GEMC program [84]. According to simulations, the most probable value of cosmic deposition is 16 MeV. These simulations contained a very detailed description of the prototype, including the signal elaboration chain (APDs and amplifiers), modeled according to the nominal parameters of each component [85]. Data collected with cosmic rays have been used to tune parameters and validate the re-

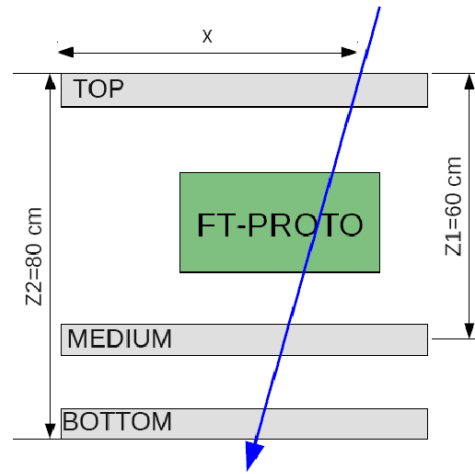
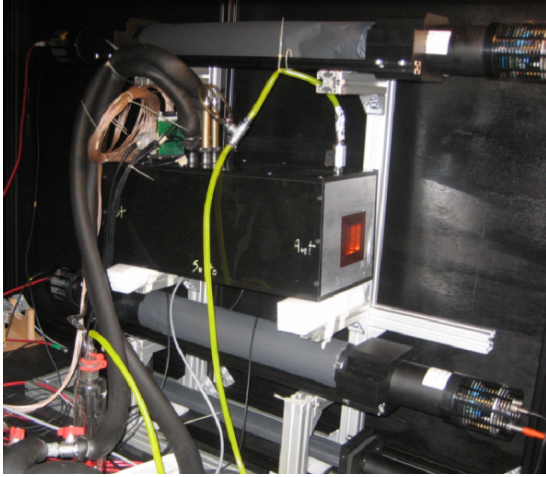


Figure 3.26: The experimental set-up used to measure the Proto-9 response to cosmic muons. The prototype is in the black box between the three plastic scintillator bars.

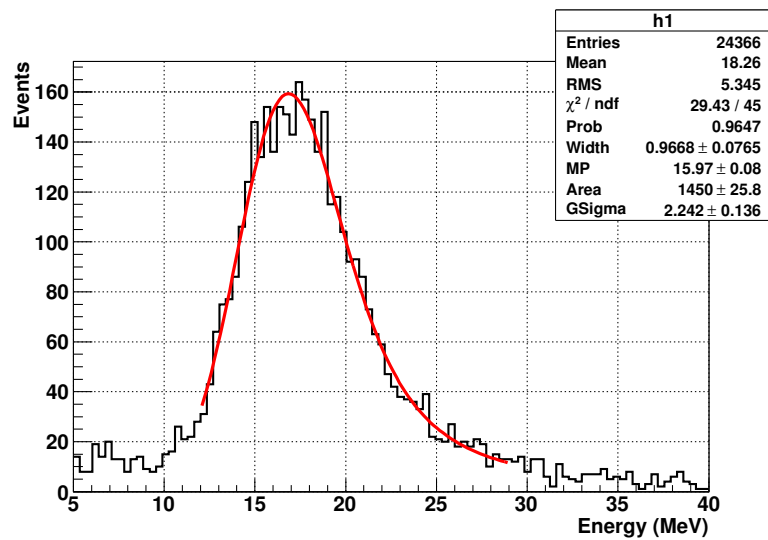


Figure 3.27: Cosmic-ray energy distribution measured by a single crystal of the Proto-9, at $+19^\circ\text{C}$.

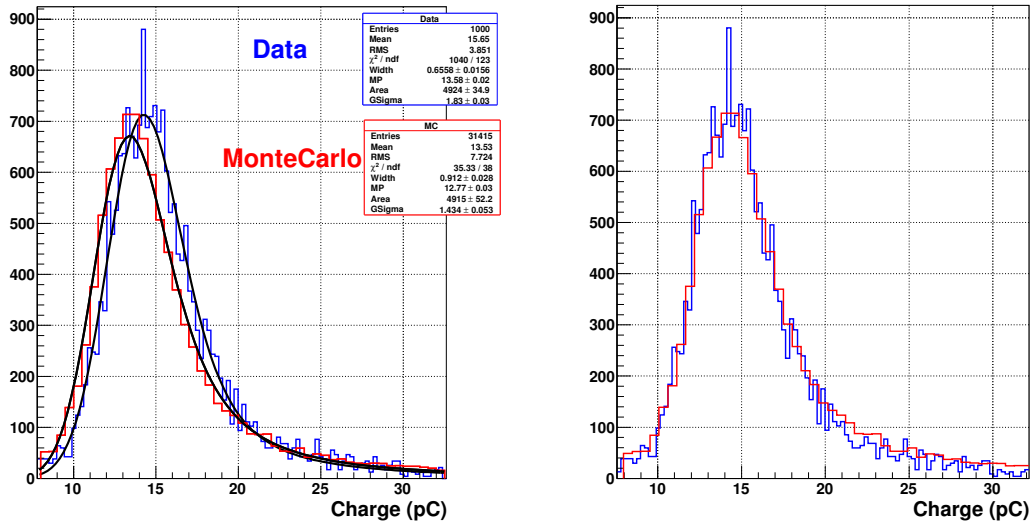


Figure 3.28: Left: Proto-9 comparison between data (blue histogram) and MonteCarlo (red histogram), for the *charge* deposited in a crystal by cosmic muons. The two fits with a Landau convoluted with a Gaussian, used to identify peak position, are superimposed. Right: the same comparison after applying the correction factor to the MonteCarlo distribution, as described in the text.

sults. Figure 3.28 shows this comparison for one of the Proto-9 crystals, in terms of the *charge* corresponding to the output signal. This variable has been chosen because it can be derived independently for data and for MonteCarlo, without any external input. The two spectra are quite similar, apart from an overall shift, that was corrected fitting them with a Landau convoluted with a Gaussian to identify precisely the two peak positions and to derive a multiplicative correction factor for MonteCarlo. Such a factor was found to be $(6.0 \pm 0.3) \%$.

During the cosmic ray tests the detector was operated at different temperatures, to see the light yield see variations for each crystal, and to compare them to the data obtained from the measurements performed with the single crystal setup. Results are shown in Figure 3.29, reporting the light-yield (in arbitrary units) as a function of the temperature for one of the crystals, as measured with different experimental conditions: single-crystal with PMT readout (red), single-crystal with APD readout (green), Proto-9 (black). APD results are consistent, showing an increase of a factor 2.7 in light yield between $+19^\circ$ and -25° , while the LY measured with the PMT at low temperature is slightly lower.

JLab Measurements

The Proto-9 response to electromagnetic showers was tested at Jefferson Laboratory, using electrons diffused by a Bremsstrahlung radiator placed along primary beam line during a photo-production experiment (see Sec. 2.2). The prototype was placed below the Hall-B tagger hodoscope, to detect electrons deflected by the Tagger magnet, after their interaction with the E^- and T^- Tagger scintillator counters, as shown in Figure 3.30. The detector was operated at $+19^\circ\text{C}$. During the measurement the prototype was hit by all the electrons whose trajectories, and thus momenta, were matched to the position of the detector. Coincidence with the Hall-B Tagger scintillation counters was thus required to select electrons with a well-defined energy.

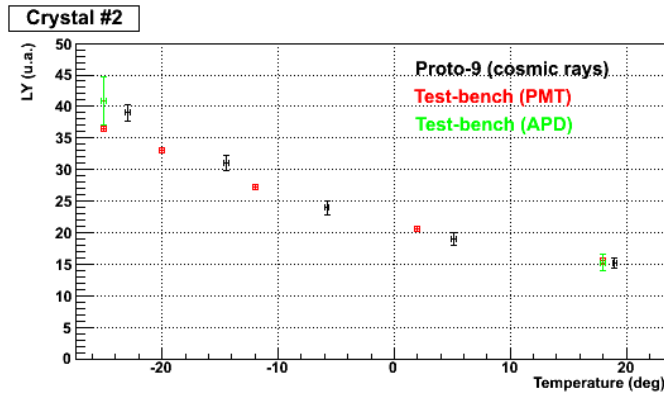


Figure 3.29: PbWO_4 light yield as a function of temperature measured with different experimental methods.

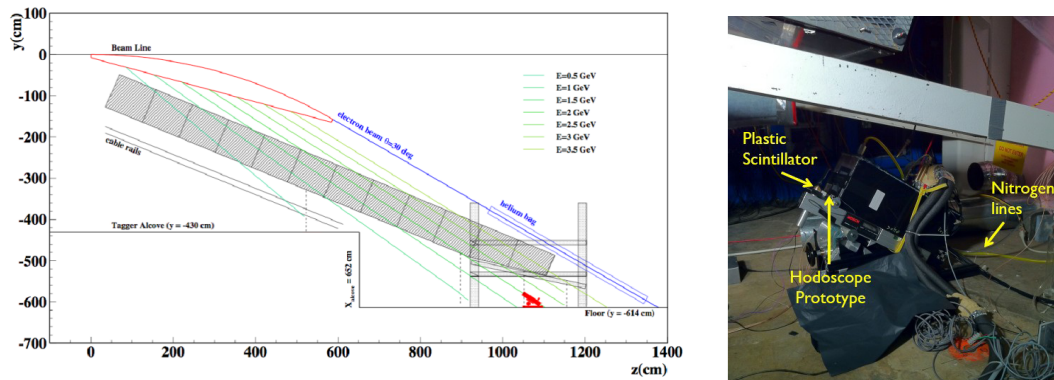


Figure 3.30: Left: scheme of the Proto-9 positioning under the Hall-B photon tagger at JLab. The prototype position is highlighted in red. Trajectories for electrons diffused by the Bremsstrahlung radiator and deflected by the Tagger magnet are shown, for different electron energies, and for a 2.282 GeV primary electron beam. Right: the experimental setup at JLab.

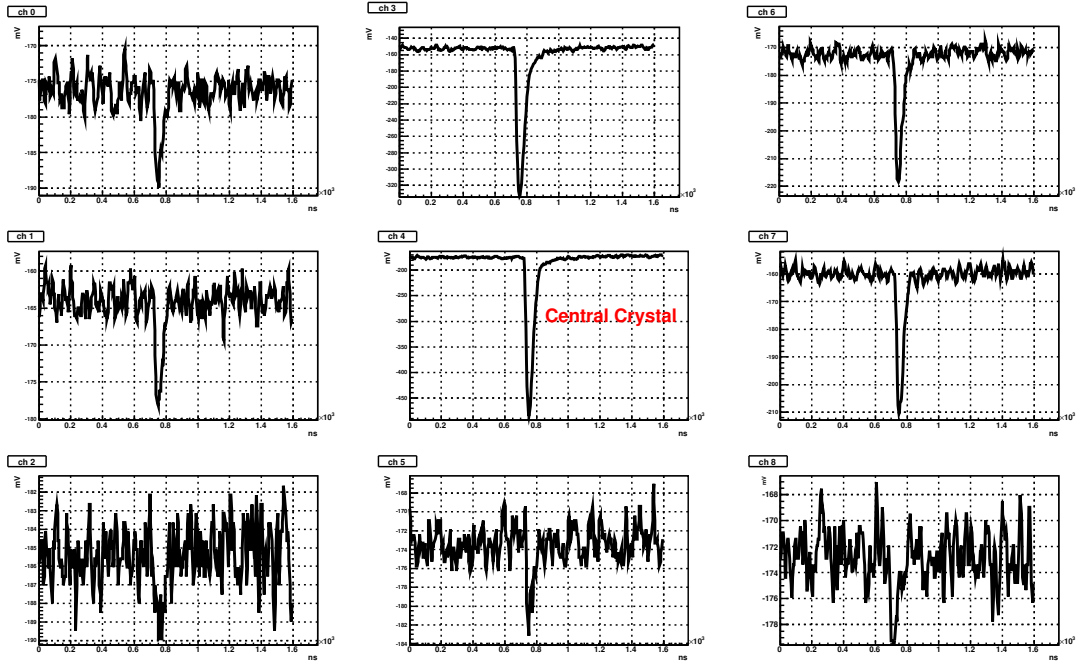


Figure 3.31: Signal induced by an electromagnetic shower in the crystals of the Proto-9.

The response to two different energies, 1.31 GeV and 1.92 GeV, was measured by changing the primary electron beam energy from 2.282 GeV to 3.356 GeV. The energy resolution was evaluated through detailed MonteCarlo simulations. The Tagger components (plastic scintillators), the air gap, and all other passive materials in front of the prototype were included to obtain a realistic estimate of the resolution, obtaining 2.2% and 1.8% respectively.

These tests also permitted to measure the performances of the amplifiers in a realistic experimental environment, with more potential noise sources than in the laboratory, where all the FT-Cal components were tested. Figure 3.31 shows the typical signal produced by a 1.31 GeV electron hitting the central crystal, as acquired with FADCs during the data-taking. The noise level, well visible in channel 8, is approximately 4 mV RMS. This value is compatible with what obtained from measurements performed in Genova (see sec. 3.3.3), thus showing the good performances of the detector electronics in a realistic experimental condition.

Before measuring the energy resolution, I equalized the peak positions to match the individual channel gains. First, data from cosmic ray measurements were used to obtain a first calibration constant for each channel. Then, events from the 1.31 GeV dataset having most of the energy released in one single crystal were selected, requiring an energy deposition in the crystal higher than 150 MeV, and the energy deposited in all the others lower than 250 MeV. In this way, a well defined peak in the energy distribution was identified for each channel. These peaks were aligned to the MonteCarlo pseudo-data, processed by the same algorithm, deriving a correction factor for the measured energy. I iterated this procedure until these correction factors were stable.

After equalization, I obtained the energy resolution of the prototype for 1.31 GeV incident electrons summing the 9 crystals contributions. I selected events with electrons hitting the central crystal, requiring to have more than 600 MeV released in it, and less than 500 MeV released in all the others. I obtained the energy resolution for 1.92 GeV incident electrons with the same

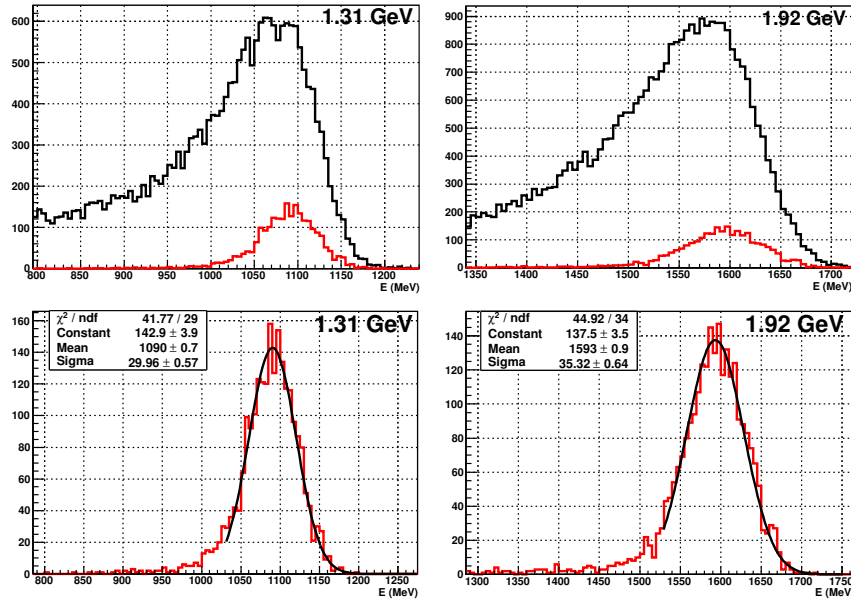


Figure 3.32: Top panels: energy deposition in the FT Proto-9 for 1.31 GeV (left) and 1.92 GeV (right) impinging electrons, with (red) and without (black) the cuts used to select hits in the center of the detector. Bottom panels: energy resolution obtained with the prototype.

procedure, increasing the threshold on the central crystal to 900 MeV.

Results are reported in Figure 3.32. Using the cuts described above, the left tail in the total energy distribution, corresponding to events with the electron impinging on one of the external crystals, is completely suppressed, as shown in the two top panels. It should be noted that, even for the selected events, the total energy released by the electromagnetic shower in the detector is lower than the electron energy, due to side leaks. The experimental energy resolution, normalized both to the measured energy and to the nominal, is reported in Tab. 3.1, together with values obtained from MonteCarlo simulations for comparison.

3.6.2 FT Proto-16

After the experience gained with the FT Proto-9, an improved version of the prototype, the FT Proto-16, was built assembling 16 PbWO_4 crystals in a 4x4 matrix. The mechanics of the Proto-16 was modified compared to the Proto-9, as shown in Figure 3.33. In particular, the single-crystal assembly was improved by using dedicated tools for the APD and the VM2000 foil gluing, and detailed quality assurance procedures were defined. The grounding of the FT-Cal amplifiers was improved by replacing the separated copper rails with horizontal plates with carved slots for their

Incident electron energy	$\frac{\sigma_E}{E_{meas}}$	$\frac{\sigma_E}{E_{nom}}$	$\frac{\sigma_E}{E_{nom}} MC$
1.31 GeV	$(2.75 \pm 0.05)\%$	$(2.29 \pm 0.04)\%$	2.2%
1.92 GeV	$(2.22 \pm 0.04)\%$	$(1.83 \pm 0.03)\%$	1.8%

Table 3.1: The measured energy resolution of the FT Proto-9, normalized both to the total energy deposited in the detector E_{meas} and to the nominal electron energy E_{nom} .

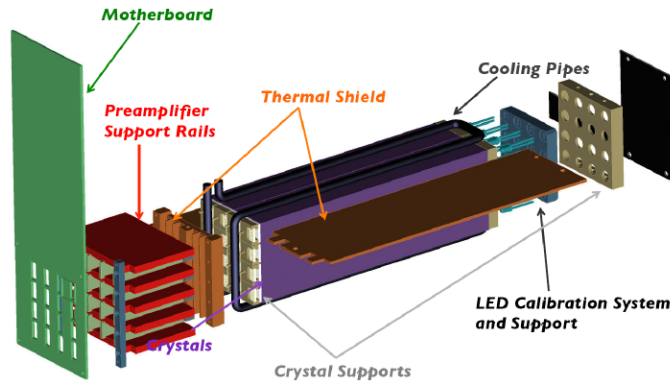


Figure 3.33: Exploded view of the Proto-16 assembly

insertion. The cooling system was simplified by soldering the cooling pipe to the thermal shield and to the back plate, which was shaped properly to host it. All these new features have been included in the final design of the FT-Cal that was presented at the end of the previous Chapter.

BTF Measurements

After a preliminary measurement with cosmic rays performed in Genova with the same setup employed for the FT Proto-9, the response of the prototype to electromagnetic showers was measured at the Beam Test Facility (BTF) [86, 87] of the INFN Frascati National Laboratory, part of the DAΦNE collider complex. Such a facility hosts an e^-/e^+ test beam, obtained by attenuating the primary Linac beam through a system of tunable targets, magnets and slits. Both the beam energy and intensity can be varied, from 25 to 500 MeV and from 1 to 10^5 particles per bunch. The possibility to lower the number of particles per bunch at the level of a few provides ideal conditions for detector testing, and gives the opportunity to study detector performances as a function of the number of electrons hitting the calorimeter, i.e. of the total deposited energy. Each bunch in the beam has an intrinsic width of 10 ns, and the repetition rate can be varied from 20 to 50 Hz, also depending on the other DAΦNE ongoing operations.

Figure 3.34 shows the BTF experimental hall after the installation of the prototype and associated equipment. The detector was placed on a movable table, that can be displaced in the x and y direction with 0.1 mm accuracy, z being the direction of the incident beam. This feature was exploited to move the calorimeter with respect to the beam, to center it on different crystals. A plastic scintillator slab, read at both ends by two fast PMTs (Hamamatsu R2083), was placed after the beam pipe exit window, in front of the calorimeter, to provide a fast coincidence signal and thus to determine precise event timing within the 10 ns time window of each bunch. The data acquisition system, the same employed for the Proto-9 expanded to accommodate all the detector channels, was triggered by the RF signal from DAΦNE.

Data from cosmic ray measurement was used to obtain a first calibration constant for each crystal, in a similar way as described for the Proto-9. The response of each crystal to the 500 MeV electron beam was then measured at the BTF. Different runs were taken, working at low particle multiplicity per bunch ($\overline{N}_e \simeq 1.5$), and centering the calorimeter to have the beam impinging on the center of a single crystal, by mean of the movable table. To isolate single-electron bunches events were selected requiring a total energy deposition lower than 600 MeV, and less than 200 MeV in the neighboring crystals. In this way, a well-defined peak in the energy distribution was isolated for each channel, and the corresponding calibration constant was fixed to have it at 330

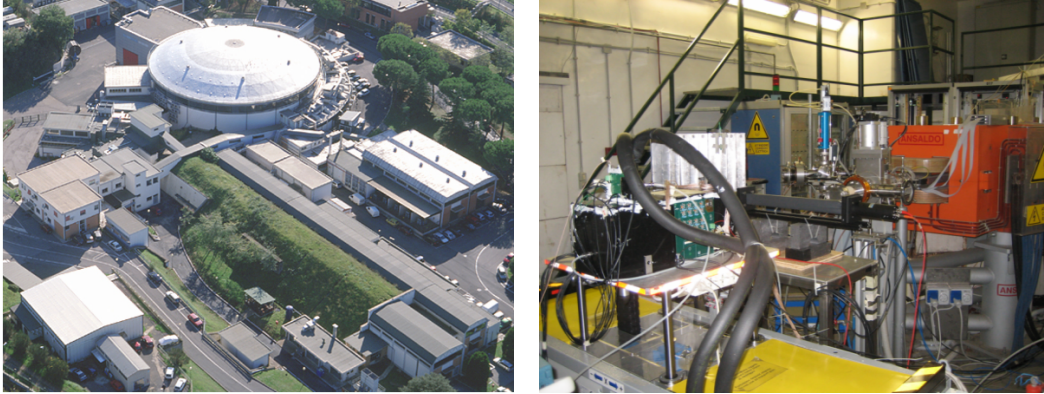


Figure 3.34: Left: aerial view of the Frascati DAΦNE accelerator complex, with the Linac, the storage ring, and the BTF highlighted. Right: experimental setup during the Proto-16 tests at the Frascati Beam Test Facility.

MeV, as indicated by MonteCarlo simulations. Finally, all the calibration constants were scaled by a common factor to have 440 MeV released in the whole calorimeter by a single electron hitting it the center.

After this procedure, the new calibration constants were found to be compatible with those obtained from the cosmic-rays measurement within 5 – 10%. This is an important result, that indicates that a preliminary calibration for the full FT-Cal can be performed without beam.

The position and width of the peaks in the total reconstructed energy distribution were found via Gaussian fits and analyzed to check system linearity and determine the experimental resolution. To this end, events were filtered introducing a threshold on the reconstructed energy of each channel equal to 5 MeV.

Measurements were repeated with different detector configurations, in particular changing the operating temperature, from +18 °C to 0 °C and -20 °C, the APD intrinsic gain, from 150 to 75, and the DAQ setup, removing the passive splitter and feeding output signals directly to the FADC boards. The aim of these tests was to determine the optimal setup of the detector in a real experimental environment, to finalize the design of the full FT-Cal. As for the FT Proto-9, the detector was operated also at -20° working point for the sake of completeness, although this working point is not foreseen in the FT-Cal design due to the limited advantages obtained, compared to the technical difficulties encountered in its implementation.

The best configuration was found to be $T = 0^\circ$, and APD intrinsic gain of 150, thus confirming what already known studying FT-Cal single components. No appreciable variations were found changing the DAQ chain. Results for the best configuration are reported in Figure 3.36. The response of the prototype in the whole energy range up to 4 GeV shows no deviations from linearity, and the resolution for energies greater than 2 GeV is comparable with MonteCarlo predictions. At lower energies there is a significant discrepancy between data and simulations, probably because of an underestimated constant contribution in the overall resolution. Full details and results of all the performed tests can be found in [68] and [79].

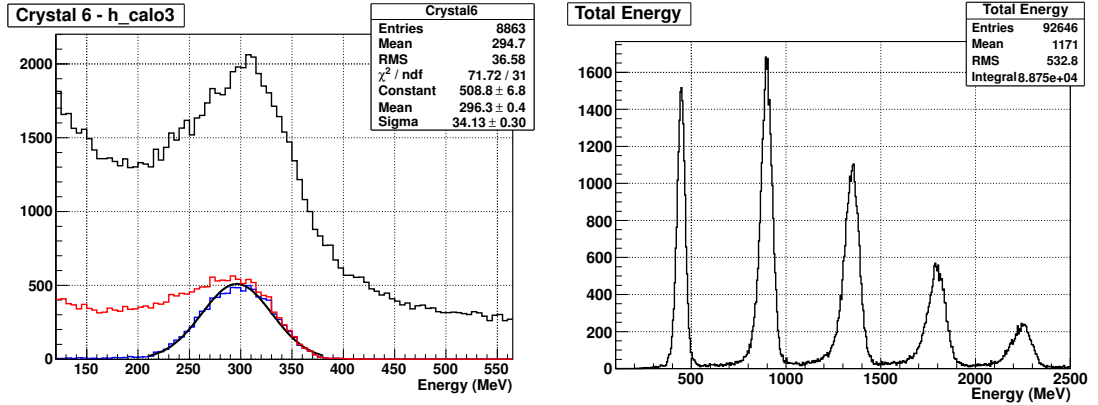


Figure 3.35: Left: energy deposition spectrum in a single crystal of the FT Proto-16. The black histogram includes all events, the red one includes only events with a single electron impinging on the calorimeter, and the blue one includes single-electron events with less than 200 MeV detected energy in the neighboring crystals. Right: the total energy detected by the Proto-16, after full calibration, for a mean electron multiplicity of the order of 1.5. Peaks corresponding to different bunch population are clearly separated.

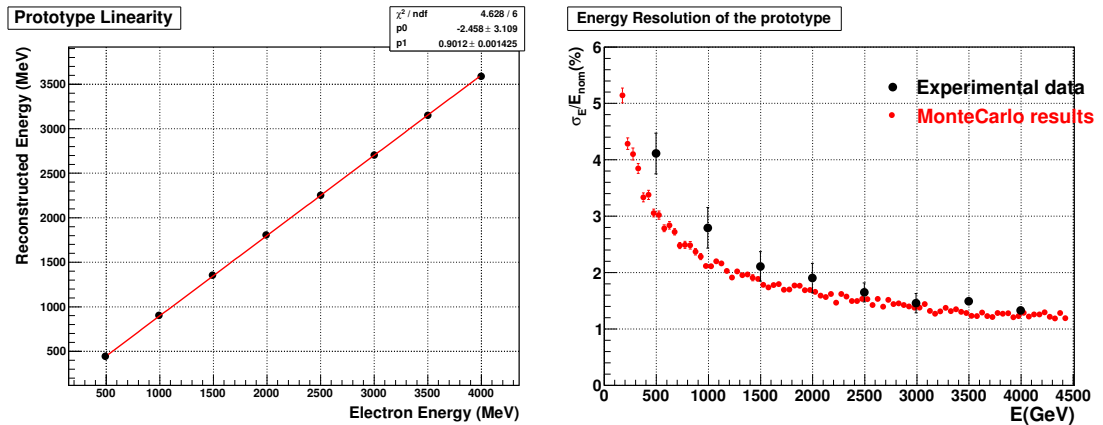


Figure 3.36: Left: FT Proto-16 reconstructed energy as a function of the incident electron energy. Right: FT Proto-16 experimental energy resolution (black points), compared with MonteCarlo results (black).

Chapter 4

The $\pi^0 \eta$ channel in the MesonEx experiment

I studied the reaction $\gamma^* + p \rightarrow p + \pi^0 + \eta$ in the framework of the MesonEx experiment. The $\pi^0 \eta$ final state is one of the “golden channels” that this experiment will measure, as part of a broader meson spectroscopy program. Therefore, a detailed preparatory study is required. First, the feasibility of the measurement within the foreseen experimental setup has to be evaluated, by estimating the acceptance and resolution. Second, given the experimental conditions, the capability to perform a full PWA has to be verified. This requires the development of all the necessary analysis tools and algorithms. Finally, the experiment sensitivity to a possible exotic state $J^{PC} = 1^{-+}$ has to be estimated, as a function of coupling and width.

I performed this study using a MonteCarlo simulation. I generated pseudo-data according to an amplitude derived within the Regge theory framework, in collaboration with V. Mathieu and A. Szczepaniak. The free parameters in the amplitude were tuned to fit $\gamma p \rightarrow p\pi^0\eta$ data collected at lower energy by the CLAS collaboration.

This preparatory work was not a pure “exercise” being an end in itself, but the tools, the algorithms, and the formalism that I derived actually constitute the basis for the analysis of the *real* experimental data. In fact, even if they were developed within a simulation, the generating amplitude is not just a model, but contains a detailed and rigorous description of the reaction. Consequently, the pseudo-data analysis faced most of the difficulties that would arise when treating the real experimental data, and the developed tools are matched to this realistic situation.

The description of the CLAS data analysis and the projection to CLAS12 is reported in the next two Chapters. Here, after an introduction to the $\pi^0 \eta$ channel phenomenology and a brief review of the existing experimental data, I discuss the reaction amplitude and the show the modifications needed to adapt it to the low Q^2 electron scattering were derived. Finally, I derive the formalism needed to perform the partial wave analysis of the $\pi^0 \eta$ channel.

4.1 Phenomenology of the $\pi^0\eta$ channel

Properties of the $\pi^0 \eta$ channel derive from the specific topology. In particular, the two mesons system has definite charge conjugation parity, and since both mesons do not carry spin, the total

angular momentum is equal to the relative orbital angular momentum of the two particles:

$$C = C_{\pi^0} \cdot C_{\eta} = +1 \quad (4.1)$$

$$J = L \quad (4.2)$$

$$P = P_{\pi^0} \cdot P_{\eta} \cdot (-1)^L = (-1)^L \quad (4.3)$$

Therefore, only the following $\mathbf{J}^{\mathbf{P}\mathbf{C}}$ quantum numbers are allowed for this final state:

$$0^{++}, 1^{-+}, 2^{++}, 3^{-+}, 4^{++}, \dots$$

Due to strong decays conservation laws, a resonance X^0 decaying to the $\pi^0 \eta$ final state would have the same quantum numbers. Recalling the discussion about *exotic quantum numbers* of Chapter 1, it follows that any state decaying with odd $\pi^0 \eta$ relative angular momentum, would have quantum numbers incompatible with a $q\bar{q}$ structure. Finally, the partial wave analysis formalism is simplified by having only two pseudo-scalar particles in the final state, and the associated discrete ambiguities can be dealt in a rigorous way [88].

For all these reasons, the $\pi^0 \eta$ system is an attracting candidate to measure when searching for *exotic mesons*, since it would provide an unambiguous signature for their presence in the hadronic spectrum.

In the past, this channel has been studied using different production mechanisms. The most employed has been the peripheral hadro-production, with a high energy pion beam impinging on a nucleon or nuclear target. It has also been studied via the annihilation of protons on anti-protons or anti-neutrons, or through the decay of heavy-quark mesons. Only recently this channel has been studied in a photoproduction experiment. It has to be noted, however, that the neutral $\pi^0 \eta$ channel has never been studied in a photo-production experiment related to meson spectroscopy. The only data available for the reaction $\gamma p \rightarrow p\pi^0\eta$ comes from the CB-ELSA experiment, that employed a Bremsstrahlung photon beam with energy between 0.9 and 3.0 GeV on a hydrogen target [89]. This experiment focused on the study of barionic resonances decaying to the $\Delta^+(1232) \eta$ state.

The first published analysis of the $\pi \eta$ channel comes from the NICE experiment, performed in 1981 in Protvino [90]. This experiment measured the charge-exchange reaction $\pi^- p \rightarrow \pi^0 \eta n$, with a 40 GeV/c pion beam impinging on a hydrogen target. Both the π^0 and the η were detected through their 2γ decay mode, while the neutron was identified through missing mass technique. The invariant $\pi \eta$ mass spectrum was dominated by the $a_2(1320)$ state. There was also a hint for the $a_0(980)$ state, but the authors did not exclude a leakage from the η' decay. For such a reason, they decided to concentrate only in the mass region above 1 GeV. The decay angular distributions were fitted with a combination of S, P, and D-waves, but no exotic 1^{-+} signal was found.

In 1988, the GAMS experiment at CERN SPS measured the same reaction, with a 100 GeV/c pion beam [91]. They performed a momentum analysis, obtaining the production amplitudes by solving the related system of algebraic equations. They claimed the observation of an exotic 1^{-+} state, by comparing the phase to the dominant $a_2(1320)$. Fitting the exotic wave with a Breit-Wigner distribution they obtained a mass and width of (1406 ± 20) MeV and (180 ± 20) MeV. However, in 1988 a critical review of the previous work highlighted some inconsistencies in the analysis, thus concluding that the 1^{-+} signal was only an artificial consequence of these inaccuracies [92].

In 1993, the VES collaboration studied the reaction $\pi^- N \rightarrow \pi^- \eta N$ with a 37 GeV/c pion beam impinging on a Beryllium target [29]. They performed an accurate partial wave analysis, parameterizing the reaction intensity with an S, a P, and a D-wave, and performing a maximum likelihood unbinned fit to the data to extract the production amplitudes. They found the $a_2(1320)$ in the D-wave to dominate the invariant mass spectrum. They also found some structures in the

Experiment	Reaction	Exotic signal	Notes	Ref.
NICE	$\pi^- p \rightarrow \pi^0 \eta n$	Not seen		[90]
GAMS	$\pi^- p \rightarrow \pi^0 \eta n$	$M = (1406 \pm 20)$ MeV $\Gamma = (180 \pm 20)$ MeV	New analysis discarded resonant interpretation	[91, 92]
VES	$\pi^- N \rightarrow \pi^- \eta N$	Found intensity in P-wave	No resonant interpretation	[29]
KEK	$\pi^- N \rightarrow \pi^- \eta N$	$M = (1323 \pm 4)$ MeV $\Gamma = (143 \pm 12)$ MeV	Possible leakage from D-wave	[93]
E852	$\pi^- p \rightarrow \eta \pi^- p$	$M = (1360 \pm 25)$ MeV $\Gamma = (385 \pm 40)$ MeV		[94]
E852	$\pi^- p \rightarrow \eta \pi^0 n$	Not seen		[95]
Crystal Barrel	$p\bar{p}$ annihilation	$M = (1360 \pm 25)$ MeV $\Gamma = (220 \pm 90)$ MeV		[96]
Crystal Barrel	$p\bar{n}$ annihilation	$M = (1400 \pm 20)$ MeV $\Gamma = (310 \pm 50)$ MeV		[97]
COMPASS	$\pi^- p \rightarrow \pi^- \eta p$	$M = (1556 \pm 25)$ MeV $\Gamma = (500 \pm 25)$ MeV		[98]
CLAS	$\gamma p \rightarrow \pi^- \eta \Delta^{++}$	Not seen		[99]

Table 4.1: Summary of the searches for exotic mesons in the $\pi\eta$ channel found in literature.

exotic P-wave, in the region near 1.4 GeV, without making any further conclusion about their origin and nature.

The same reaction was also studied by the KEK experiment, with a 6.3 GeV/c pion beam on a hydrogen target [93]. After an analysis similar to the VES experiment, they claimed an exotic signal in the P-wave, with mass and width respectively (1323 ± 4) MeV and (143 ± 12) MeV. However, the behavior of the $P - D$ phase difference, and the fact that resonance mass was close to the $a_2(1320)$, seemed to indicate a possible leakage from the dominant D-wave.

The E852 experiment studied the $\pi\eta$ final state in various charge modes, with different results. In 1997 they measured the reaction $\pi^- p \rightarrow \eta \pi^- p$, with a 18 GeV/c pion beam [94]. After performing a PWA which included S, P, and D-waves, they found a broad peak in the exotic 1^{-+} wave, with parameters $M = (1360 \pm 25)$ MeV and $\Gamma = (385 \pm 40)$ MeV. They also showed in detail the stability of the $P - D$ phase difference respect to possible systematic effects. In 2003 the E852 collaboration also reported results about the charge-exchange reaction $\pi^- p \rightarrow \eta \pi^0 n$ [95]. They confirmed structures in the exotic P wave, however their resonant interpretation was much more problematic, and no consistent set of P-wave Breit-Wigner parameters could describe the data. They also suggested that the $\pi\eta$ rescattering mechanism could explain the P wave behaviour.

Proton-antiproton and neutron-antiproton annihilation at rest have been exploited to study the $\pi\eta$ final state by the Crystal Barrel experiment [96, 97]. In both measurements, the Dalitz Plot analysis of the $\pi\pi\eta$ final state confirmed the requirement of introducing a $\pi\eta$ exotic P-wave to describe the data. The resonant behavior was seen via the interference with the dominant a_2 D-wave signal. The Breit-Wigner parameters obtained in $p\bar{p}$ measure were $M = (1360 \pm 25)$ MeV and $\Gamma = (220 \pm 90)$ MeV, while for the $n\bar{p}$ they found $M = (1400 \pm 20)$ and $\Gamma = (310 \pm 50)$.

The COMPASS experiment at CERN provided so far the most accurate dataset for the $\pi\eta$ final state, with more statistics than any other previous experiment. COMPASS measured the reaction $\pi^- p \rightarrow \pi^- \eta p$ with a 190 GeV/c pion beam, on a hydrogen target [98]. Exploiting the high accumulated statistics, they performed a full PWA analysis including contributions from S, P, D, and G-waves, finding a significant intensity in the exotic P-wave. Performing a mass-dependent fit of the production amplitudes with Breit-Wigner functions, they found a 1^{-+} state with mass

(1556 ± 25) MeV and a width (500 ± 25) MeV. A resonant interpretation of this state in the vein of previous analyses was possible, by including large background terms and by adding additional resonance terms into the D-wave.

Finally, the CLAS collaboration studied this state in a photoduction experiment, measuring the charge-exchange process $\gamma p \rightarrow \Delta^{++} \pi^- \eta$ with a Bremsstrahlung photon beam, with energy in the range between 4.5 GeV and 5.5 GeV, impinging on a hydrogen target [99]. The requirement to have a Δ^{++} in the final state was introduced to filter out possible background sources from other channels, in particular from barionic contributions, not negligible at these photon energies. The PWA clearly identified the $a_2(1320)$ D-wave signal, while no P-wave contribution was found. However, the analysis was limited by the available statistics: only 1200 events were accepted for the final PWA fits.

4.2 Production amplitudes in the Regge theory framework

A relativistic scattering process $a + b \rightarrow 1 + 2 + \dots + n$ of spinless particles is described by a complex amplitude A , function of the particles 4-momenta $P_a, P_b, P_1 \dots P_n$. The differential cross section $d\sigma$ is proportional to the modulus squared of the amplitude, through the kinematic phase space factor $d\Phi_n$, as $d\sigma = |A|^2 d\Phi_n$. When particles carry spin, there is a different amplitude A_i for each spin configuration i , and thus a corresponding cross-section $d\sigma_i$. If the initial state is unpolarized, and the spins of particles in the final state are not measured, the process cross-section is obtained by summing on the final state spins and averaging on the initial state.

For a two-body final state, only two independent variables are required to describe the reaction kinematic, as a consequence of energy and momentum conservation. Moreover, since the amplitude is invariant under Lorentz transformations, it is a function of Lorentz-invariant four-momenta combinations. Besides the particle masses, these are usually chosen as the Mandelstam variables s, t, u , defined as:

$$s = (P_a + P_b)^2 \quad (4.4)$$

$$t = (P_a - P_c)^2 \quad (4.5)$$

$$u = (P_a - P_d)^2 \quad , \quad (4.6)$$

where \sqrt{s} is the total energy in the center of mass frame, while t , the so-called ‘‘momentum transferred’’, and u , are related to the scattering angle in the CM frame θ_{CM} :

$$t = m_a^2 + m_c^2 - 2E_a^* E_c^* + 2P_a^* P_c^* \cos \theta_{CM} \quad (4.7)$$

$$u = m_a^2 + m_d^2 - 2E_a^* E_d^* - 2P_a^* P_d^* \cos \theta_{CM} \quad , \quad (4.8)$$

being E_X^* and P_X^* , respectively, the energy and the momentum of particle X in the CM frame. Since $s + t + u = m_a^2 + m_b^2 + m_c^2 + m_d^2$, only two of these variables are independent. The invariant amplitude can then be written as $A(s, t)$.

Important properties of the invariant amplitude A are derived from general principles of the scattering theory, such as causality and conservation of probability. Among these, crossing symmetry asserts that the scattering amplitude $A(s, t)$ for the reaction $a + b \rightarrow c + d$, where all particles are scalars, describes also the cross-channel processes, identifying $p_X^\mu = -p_{\bar{X}}^\mu$ for Mandelstam variables calculation:

$$a + \bar{c} \rightarrow \bar{b} + d \quad t\text{-channel process} \quad (4.9)$$

$$a + \bar{d} \rightarrow \bar{b} + c \quad u\text{-channel process} \quad (4.10)$$

In order to make the principle of crossing symmetry precise, it is necessary to consider $A(s, t)$ as a function of *complex* variables s and t . Physical processes are then described by this amplitude

when s and t take real values. This requires the study of the analytic properties of the amplitude $A(s, t)$, since the connection between different physical regions is made passing through non-physical territories of the $s - t$ plane.

When particles carry spin, crossing symmetry relates the helicity amplitudes in the t -channel to those in the s -channel. Relations are more complicated since the latter observable depends on the momentum direction and changes when moving from the t -channel to the s -channel. More precisely, the s -channel helicity amplitudes can be expressed in terms of t -channel helicity amplitudes as:

$$T_{\mu_3, \mu_4}^{\mu_1, \mu_2}(s, t) = \sum_{\lambda} d_{\lambda_1, \mu_1}^{s_1}(\chi_1) d_{\lambda_2, \mu_2}^{s_2}(\chi_2) d_{\lambda_3, \mu_3}^{s_3}(\chi_3) d_{\lambda_4, \mu_4}^{s_4}(\chi_4) T_{\lambda_3, \lambda_4}^{\lambda_1, \lambda_2}(s, t) \quad , \quad (4.11)$$

where μ are s -channel helicities and λ are t -channel helicities. Analytic expressions for the crossing angles χ can be found in [100].

In the following, I will focus on the case of scalar particles, deriving the properties of the production amplitudes within the Regge theory.

4.2.1 Two-body reactions

In its most general form, Regge theory is a very convenient framework to study the strong interaction of high-energy elementary particles, based on fundamental properties of the scattering theory, namely the analyticity of the scattering amplitude A and the crossing symmetry.

The basic idea behind the theory is the use of complex angular momentum, combined with relativistic scattering theory. Originally, T. Regge developed his work to study non-relativistic scattering on a Yukawa-like potential [101, 102]. The subsequent extension of the theory to the relativistic scattering of strong interacting particles was initially due to Blankenbecler and Goldberger [103], Chew and Frautschi [104, 105], and Gribov [106]. Very comprehensive and detailed reviews of the Regge theory and of the most important results have been written by Irving [107] and Eden [108].

For a two body scattering process $a + b \rightarrow c + d$, at high s and relatively low $|t|$, the scattering amplitude $A(s, t)$ is derived starting from the partial-wave expansion in the cross t -channel, corresponding to the reaction $a + \bar{c} \rightarrow \bar{b} + d$:

$$A(s, t) \propto \sum_{l=0}^{+\infty} (2l+1) f_l(t) P_l(\cos \theta_t) \quad , \quad (4.12)$$

where $t > 0$ is the energy squared in the center of mass frame, and $s < 0$ is related to the t -channel scattering angle θ_t . Crossing symmetry states that the *same* amplitude also describes the s -channel process under study, for which s and t have their conventional meaning and values. However, to move between the two kinematic regimes, passing through phase-space regions where s and t assume non-physical values, analytic continuation of the above expression is required.

Regge theory provides a practical way to perform such an analytic continuation. The idea is to “promote” the angular momentum l to a complex variable, and make an analytic extension $f_l(t) \rightarrow f(l, t)$. The amplitude $A(s, t)$ can then be written as a contour integral in the l -plane, making use of the Cauchy integral theorem: this is referred to as “Sommerfeld-Watson” transform. The result depends only on the location of the *poles* α_n of the analytic function $f(l, t)$ in the complex l -plane, as a function of t . In the limit $s \gg t$ the amplitude is:

$$A(s, t) \simeq \sum_n \frac{\beta_n(t) (-1)^{\alpha_n(t)}}{\sin(\pi \alpha_n(t))} \left(\frac{s}{s_0} \right)^{\alpha_n(t)} \quad (4.13)$$

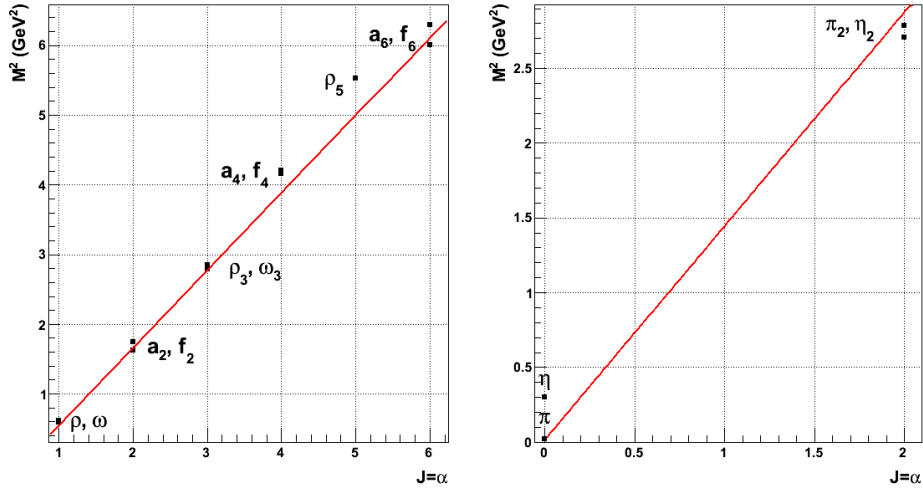


Figure 4.1: Chew-Frautschi diagrams for natural (left) and unnatural (right) mesons. The two trajectories are $\alpha_{\text{nat}} = 0.5 + 0.9 \cdot M^2$ and $\alpha_{\text{unnat}} = 0.7(M^2 - M_\pi^2)$. Data from [4].

Trajectory	Analytic form
N^*	$\alpha_{N^*}(t) = -0.37 + t \cdot 1.0 \text{ GeV}^{-2}$
Δ	$\alpha_\Delta(t) = 0.15 + t \cdot 0.9 \text{ GeV}^{-2}$
ρ, ω	$\alpha_\rho(t) \simeq \alpha_\omega(t) = 0.50 + t \cdot 0.9 \text{ GeV}^{-2}$
π, η	$\alpha_\pi(t) \simeq \alpha_\eta(t) = 0.7 \text{ GeV}^{-2} \cdot (t - m_\pi^2)$

Table 4.2: Analytic expression for Regge trajectories for known barion and meson resonances [108].

where $s_0 \simeq 1 \text{ GeV}$ is the hadron mass scale, and $\beta_n(t)$ is a “coupling factor”, related to the residual of n -th pole of $f(l, t)$. The complex functions $\alpha_n(t)$, that give the position of the n -th pole of $f(l, t)$ as a function of t in the complex l -plane, are the so-called “Regge-trajectories”.

The Regge amplitude in Eq. 4.13 provides the main features of the Regge theory. However, it is an approximation because it does not include relativistic effects¹. Also, unphysical poles of the Regge propagator $\sin^{-1}(\pi\alpha_n(t))$ for negative integer values of α needs to be canceled. To remove poles, it is conventional to invoke zeros in the residues $\beta_n(t) \propto \pi/\Gamma(\alpha_n)$. The relation $\Gamma(\alpha) \cdot \Gamma(1 - \alpha) \cdot \sin(\pi\alpha) = \pi$ can then be used to trade the $\sin^{-1}(\pi\alpha_n(t))$ term by $\Gamma(1 - \alpha_n)$ having only poles for positive spin, requiring couplings redefinition.

The physical interpretation of Regge poles and Regge trajectories follows from the fact that, for the t -channel process, a pole in the l -th wave should correspond to a physical resonance that decays to the $\bar{b} + d$ channel. Thus, when $\Re(\alpha_n(t)) = J$, the Regge pole $\alpha_n(t)$ corresponds to a resonance pole with mass m and spin J . The form of $\alpha_n(t)$ follows from the experimental evidence that known barionic and mesonic resonances show a linear relation between the spin and the mass squared, as shown in Figure 4.1. Remembering that in the cross t -channel t is the total energy squared, the following equation holds:

$$\alpha(t) \simeq \alpha_0 + t \cdot \alpha' \quad (4.14)$$

¹These require to separate even and odd partial waves in Eq. 4.12 before proceeding with the transformation.

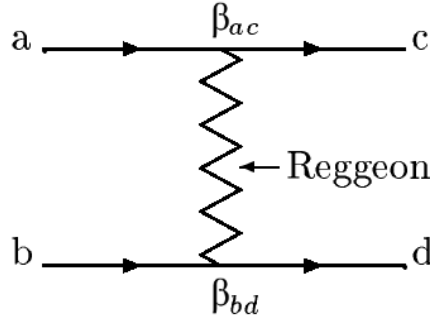


Figure 4.2: Regge description of the process $a + b \rightarrow c + d$, at high energy. Particles a and b interact through the exchange of one or more “Regge trajectories”, with “Regge couplings” $\beta_{a,c}^R(t)$ and $\beta_{b,d}^R(t)$.

Regge theory therefore connects the high-energy behavior of the scattering amplitude in the s -channel to resonance region in the t -channel.

The interaction between particles a and b is described through the exchange of one or more “Reggeons”, or “Regge trajectories”, as sketched in Figure 4.2. Trajectories have a defined relation between mass and intrinsic angular momentum, that is not restricted only to integer values. t -channel resonances lie on these trajectories, and correspond to integer spin values. The exchange of a “Regge trajectory” is then equivalent to the exchange of a whole family of particles, with different spins and same quantum numbers (charge, strangeness, C -parity, ...).

Moreover, if a Regge trajectory is allowed in two different reactions, there is a relation between contributions to the two amplitudes. This feature of the Regge theory is provided by factorization: the “coupling factor” $\beta_n(t)$ is written as the product of two “Regge couplings”, each specific to one of the two particle-particle-reggeon vertexes involved in the process:

$$\beta_n(t)_{a+b \rightarrow c+d} = \beta_{a,c}^R(t) \cdot \beta_{b,d}^R(t) \quad (4.15)$$

Considering only the leading Regge trajectory $\tilde{\alpha}$, i.e. the one with the largest real part, the scattering amplitude $A(s, t)$ is thus written as:

$$A(s, t) \propto \beta_{a,c}^R(t) \cdot \beta_{b,d}^R(t) \cdot s^{\tilde{\alpha}(t)} \quad (4.16)$$

The total cross-section for the process $a + b \rightarrow c + d$ is related to the imaginary part of the forward elastic amplitude via the optical theorem:

$$\sigma_{Tot}(a + b \rightarrow \text{anything}) \simeq \frac{1}{s} \Im(A_{el}(s, 0)) \quad (4.17)$$

Using Eq. 4.16 and taking only the leading Regge trajectory $\tilde{\alpha}$, the total cross section is then:

$$\sigma_{Tot}(a + b \rightarrow \text{anything}) \simeq \frac{1}{s} s^{\tilde{\alpha}_0} = s^{\tilde{\alpha}_0 - 1} \quad , \quad (4.18)$$

where $\tilde{\alpha}_0$ is the t -intercept of the (linear) leading Regge trajectory.

Experimentally, the hadronic total cross-sections increase at very high energy, with an approximate behavior $\sigma_{Tot} \simeq s^{0.081}$, corresponding to $\tilde{\alpha}_0 \simeq 1.081$ [109]. This Regge intercept is not compatible with any of the known mesonic or barionic trajectories (see Tab. 4.2): hence, the main process in high-energy scattering is not meson or baryon exchange in the t -channel, but the manifestation of something different. The corresponding Regge trajectory is referred to as

“Pomeranchuk” trajectory², α_P , and the corresponding exchanged Reggeon is called “Pomeron”. Since the Pomeron is exchanged in elastic processes, where the particle charges do not change, it must have vacuum quantum numbers, i.e. zero electric charge, strangeness, barionic number, positive C -parity, etc ...

4.2.2 Extension to multi-particles final states

Regge theory has been applied to reactions involving more than two particles in the final state by Kibble [110], Hong-Mo [111, 112], and Shimada [113]. In this multi-particle framework, the interaction between any pair of particles is parametrized using results obtained by applying Regge theory to $2 \rightarrow 2$ interactions, as outlined in the previous section.

The two body interaction is driven by the value of the invariant mass of the two interacting particles, \sqrt{s} . When the order of magnitude of this observable corresponds to the hadronic scale, i.e. $\sqrt{s} \simeq \text{GeV}$, the two particles interact by forming direct resonances, with defined spin and quantum numbers. Instead, for bigger s values, resonances are no longer produced in the direct channel, and the interaction proceeds through the exchange of Reggeons.

In the following I will focus on reactions involving three particles in the final state, $a+b \rightarrow 1+2+3$. The kinematics of these reaction is defined by five independent variables. A convenient choice makes use of the following five relativistic invariants:

$$\begin{aligned} s_{12} &= (P_1 + P_2)^2 & t_a &= (P_a - P_1)^2 \\ s_{23} &= (P_2 + P_3)^2 & t_b &= (P_b - P_3)^2 \\ s &= (P_a + P_b)^2 \end{aligned} \quad (4.19)$$

The physical meaning of these variables is the following: s is the conventional Mandelstam variable, corresponding to the total energy squared in the center of mass frame; s_{12} and s_{23} are, respectively, the invariant masses (squared) of the systems 1 – 2 and 2 – 3; t_a and t_b represent the momentum transferred squared between particles $a - 1$ and $b - 3$. The invariant mass s_{13} of the system 1 – 3 is related to the previous variables through the equation:

$$s = s_{12} + s_{23} + s_{13} - m_1^2 - m_2^2 - m_3^2 \quad (4.20)$$

This choice of variables is convenient because the physics of the reaction, and thus the form of the scattering amplitude, is directly related to the values of s , s_{12} , s_{23} , and s_{13} . At low energies, i.e. for \sqrt{s} smaller than few GeVs, the process is dominated by poles in the direct s -channel, which correspond to resonances, while at higher energy it is characterized by the cross-channel exchange of Regge trajectories. The interaction between particles i and j is governed by their invariant mass s_{ij} . At high s_{ij} a Reggeon exchange between them is expected, while for lower values ($s_{ij} \simeq \text{GeV}^2$) direct channel resonances are formed.

The high-energy behavior of the reaction $a + b \rightarrow 1 + 2 + 3$ is therefore characterized by two different dynamical processes: the exchange of a single Regge trajectory between one particle and a resonance formed by the other two, and a double Regge exchange. The relative strength of these mechanisms depends on the invariant masses of the final state particle pairs.

When s is large, it follows from Eq. 4.20 that at least one of the three invariant masses, say s_{ik} , has the same order of magnitude of s , resulting in a Regge exchange between particles i and k . If one of the other two invariant masses is small, of the order of few GeVs, the two corresponding particles form a direct-channel resonance, and the reaction thus corresponds to a quasi two-body process:

$$a + b \rightarrow i + (j, k) \quad (4.21)$$

²After Isaak Yakovlevich Pomeranchuk, the founder and first head of the theory division at ITEP, Moscow.

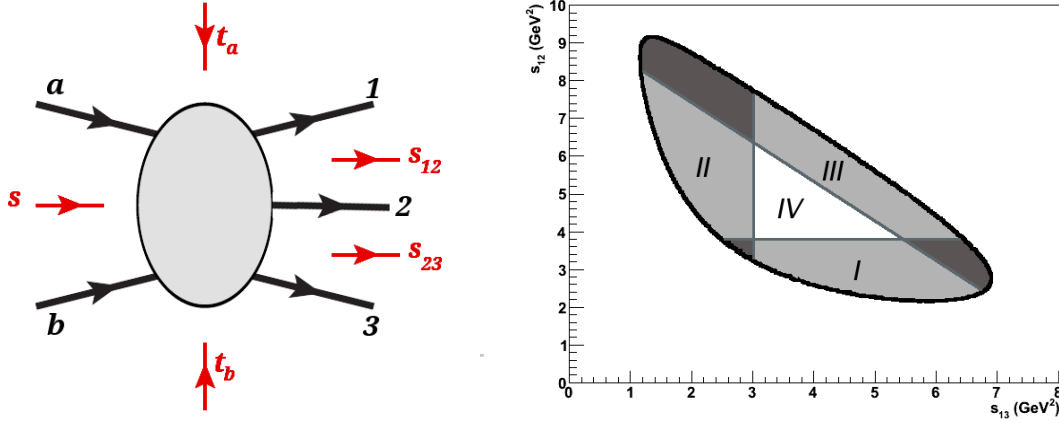


Figure 4.3: Left: sketch of the reaction $a + b \rightarrow 1 + 2 + 3$, with the kinematic variables highlighted. Left: Dalitz boundary for the reaction $\gamma + p \rightarrow p + \pi^0 + \eta$ as $s = 10 \text{ GeV}^2$, having $p \equiv 1$, $\eta \equiv 2$, $\pi^0 \equiv 3$. The boundaries corresponding to different kinematic regions are purely qualitative.

If *both* the other invariant masses s_{ij} and s_{jk} are small, the reaction dynamics is instead given by the coherent sum of the two amplitudes for the quasi two-body processes $a + b \rightarrow i + (j, k)$ and $a + b \rightarrow k + (i, j)$, that produces rescattering effects. However, for pure kinematic reasons, at high energy this case is not present.

Finally, if all the invariant masses are large, no direct channel resonances are formed, and two Reggeons are exchanged in between the three final state particles. This is referred to as “Double-Regge exchange”.

A convenient way to visualize this invariant-mass dependence of the reaction dynamics is through a Dalitz plot, as shown, for example, in Figure 4.3 for the process $\gamma + p \rightarrow p\pi^0\eta$ at $s = 10 \text{ GeV}^2$, having $p \equiv 1$, $\eta \equiv 2$, $\pi^0 \equiv 3$. The three shadowed regions I, II, and III correspond, respectively, to events with low s_{12} , low s_{13} , and low s_{23} . In these regions the reaction is expected to be dominated by the production of resonances, if any exist, i.e. by quasi two-body reactions, and the corresponding amplitude is thus derived from the $2 \rightarrow 2$ case, Eq. 4.13, completed with the description of the resonance decay. The three regions near the corners, instead, correspond to events with two low invariant masses, and rescattering effects in the final state are here expected.

Region IV finally corresponds to events with all invariant masses $s_{i,j}$ large. The reaction dynamics is dominated by the double Regge exchanges. Factorization suggests that the scattering amplitude in this kinematic region has the following form, for the specific case of final state particles ordered as in Figure 4.3 (left):

$$A(s, s_{1,2}, s_{1,3}, t_a, t_b) \simeq \sum_{R_i, R_j} \beta_{a,1}^{R_i}(t_a) \cdot \beta_{b,3}^{R_j}(t_b) \cdot \gamma_2^{R_i, R_j}(t_a, t_b) \cdot s_{12}^{\alpha_{R_i}(t_a)} \cdot s_{23}^{\alpha_{R_j}(t_b)}, \quad (4.22)$$

where R_i and R_j are the two exchanged Regge trajectories, that couples to particles a -1, and b -3 with couplings $\beta_{a,1}^{R_i}(t_a)$ and $\beta_{b,3}^{R_j}(t_b)$ respectively, while $\gamma_2^{R_i, R_j}(t_a, t_b)$ is the Reggeon-Reggeon-particle coupling, corresponding to the middle vertex of the diagram. Amplitudes for the different arrangements of particles 1, 2, and 3, are written in a similar way, but allowed Regge trajectories can be different. The full amplitude is the coherent sum of all these contributions.

4.3 Parametrization of the amplitude for the reaction

$$\gamma + p \rightarrow p + \pi^0 + \eta$$

The production amplitude for the reaction $\gamma + p \rightarrow p + \pi^0 + \eta$ that I developed consists of two contributions. The first describes the photo-production of a mesonic resonance X decaying to the $\pi^0 \eta$ final state, while the second corresponds to a non-resonant mechanism, given by double Regge exchange.

As discussed before, the dynamics of the $\pi^0 - \eta$ system is controlled by the two mesons invariant mass $M_{\pi^0 \eta}$, with direct resonances produced at low mass ($M_{\pi^0 \eta} \simeq \text{GeV}$), and reggeon exchange present only at higher mass. It is not correct to sum the two contributions in the whole invariant mass range, since this would correspond to a “double-counting”. The two mass regions are however related by duality arguments, in the form of “Finite Energy Sum Rules (FESR)” [114, 115]. In particular, the extrapolation of the double Regge contribution at low invariant mass should be, *on average*, equal to the resonant contribution there present.

In the context of the analysis of this reaction in the MesonEx framework, I mainly employed the amplitude to generate MonteCarlo events, that are then projected on the detector and reconstructed, to evaluate the experiment sensitivity to a possible exotic signal. The main amplitude requirement is thus to reproduce data in an effective way. Therefore, I included in the resonant contribution *only* the states that are significantly visible in the experimental data, and that are known to decay to the $\pi^0 \eta$ channel: the $a_0(980)$, the $a_2(1320)$, and the $a_2(1700)$. I also included a possible exotic state, the $\pi_1(1400)$, whose measure feasibility needs to be studied. The coupling was varied during the simulation to study the experiment sensitivity range. Finally, I decided to parametrize *also* the small residual, non-resonant background at low $M_{\pi^0 \eta}$ using a modified version of the double Regge amplitude, converging to the proper one at high invariant mass. This choice was motivated by the experimental evidence that the double Regge contribution effectively reproduces this background, as discussed in Chapter 5.

Given these assumptions, the total amplitude is the *incoherent* sum of the two contributions:

$$A_{\lambda h h'}(s, t, M_{\pi^0 \eta}, \Omega) = \sum_X A_{\lambda h h'}^X(s, t, M_{\pi^0 \eta}, \Omega) \oplus A_{\lambda h h'}^{DR}(s, t, M_{\pi^0 \eta}, \Omega) \quad , \quad (4.23)$$

where $\lambda = \pm 1$ is the photon helicity and $h(h') = \pm \frac{1}{2}$ is the target (recoil) nucleon helicity. The choice of an incoherent sum is motivated by the fact that, at high invariant mass, only double Regge contribution is expected, thus the first factor is negligible. At low invariant mass, instead, the above parametrization well reproduces the experimental data.

The kinematic variables used to describe the final state are the total momentum squared s , the exchanged momentum squared at the nucleon vertex $t = (p_{\text{target}} - p_{\text{recoil}})^2$, the invariant mass of the $\pi^0 - \eta$ system $M_{\pi^0 \eta}$, and the angle of the η in the meson rest frame Ω . All the expressions are explicitly derived in the Gottfried-Jackson reference frame³. This choice of kinematic variables, despite being not covariant, is convenient to describe resonances in the $\pi^0 \eta$ system, since they appear as structures in a defined invariant mass region, with specific $\pi^0 \eta$ angular distribution.

The differential cross-section is given by:

$$\frac{d\sigma}{dt dM_{\pi^0 \eta} d\Omega} = \frac{1}{4} \Phi \sum_{\lambda, h, h'} |A_{\lambda, h, h'}|^2 \quad , \quad (4.24)$$

where the factor 1/4 comes from averaging over the initial photon and target polarizations and the

³The Gottfried-Jackson reference frame is defined as the rest frame of the $\pi^0 \eta$ system, with the \hat{y} axis perpendicular to the production plane, and the \hat{z} axis oriented along the beam direction.

phase-space factor Φ is:

$$\Phi = \frac{2}{(2\pi)^4} \frac{1}{64F_I^2} \cdot q \quad , \quad (4.25)$$

where q is the center-of-mass momentum of the two mesons, and $F_I = P_{beam}^\mu P_\mu^{target}$ is the invariant flux factor.

4.3.1 Resonance production

This mechanism corresponds to the quasi-two body reaction:

$$\gamma + p \rightarrow p + X \rightarrow p + \pi^0 + \eta \quad , \quad (4.26)$$

and the corresponding amplitude is derived in the Regge framework of two-body scattering, completed with the description of the X propagation and decay. The full amplitude is:

$$A_{\lambda,h,h'}^X = \left[\sum_R \beta_{\gamma,X}^R \beta_{p,p}^R \frac{1}{2} (1 + \tau_R e^{-i\pi\alpha_R(t)}) \Gamma(j_0 - \alpha_R(t)) (\alpha' s)^{\alpha_R(t)} \right] \cdot g_{\pi^0\eta}^X BW(M_{\pi^0\eta}) \lambda^{(1-\delta_0^J)} Y^{J,\lambda}(\theta, \phi) \quad (4.27)$$

The first factor, inside squared parenthesis, contains the Regge description of the X resonance production on the proton, while the remaining terms parametrize, in an effective way, the propagation and subsequent decay.

The sum is extended only to the dominant Regge exchanges, i.e. those with the largest intercepts in the corresponding trajectory $\alpha_R(t)$, parametrized as:

$$\alpha_R(t) = \alpha_R^0 + \alpha' \cdot t \quad (4.28)$$

$\beta_{\gamma,X}^R$ and $\beta_{p,p}^R$ are, respectively, the photon-resonance-Reggeon coupling and the target-recoil-Reggeon coupling, depending explicitly on the photon helicity and on the spin configuration of the target and recoil proton. In particular, I assumed a spin-flip dominance mechanism, in analogy to the non-resonant contribution, where this is derived rigorously [116]. This, together with the application of the parity conservation to each Regge vertex (Eq. 4.48, 4.49), gives:

$$\begin{aligned} \beta_{\gamma,X}^R(\lambda) &= -\beta_{\gamma,X}^R(-\lambda) \\ \beta_{p,p}^R(h=+, h'=-) &= -\beta_{p,p}^R(h=-, h'=+) \\ \beta_{p,p}^R(h=h') &= 0 \end{aligned} \quad (4.29)$$

Finally, τ_R is the signature of the exchanged trajectory⁴, and j_0 the lowest spin of the physical particles belonging to it.

The resonance propagation and the subsequent decay are parametrized through a Breit-Wigner function, that effectively reproduces the mass distribution of the two mesons near the resonance mass, and a spherical harmonic function that accounts for the resonance spin J , related to the angular distribution of the two daughters. $g_{\pi^0\eta}^X$ is a properly dimensioned decay coupling factor, while the factor $\lambda^{(1-\delta_0^J)}$ guarantees parity invariance (see Eq. 4.44).

The Breit-Wigner expression I used is:

$$BW(M) = \frac{M_R \Gamma_0}{(M_R^2 - M^2) - i M_R \Gamma(M)} \quad , \quad (4.30)$$

⁴The signature τ of a particle with spin s and is defined as $\tau = (-1)^s$. For Regge trajectories, the signature coincide with that of the physical particles belonging to it.

Resonance	J^{PC}	Production			Propagation and decay		
		Reggeon	$\beta_{\gamma X}^R$	β_{pp}^R	M_R	Γ_0	$g_{\pi^0\eta}^X$
$a_0(980)$	0^{++}	ω	0.28	8.51	0.98 GeV	0.147 GeV	50 GeV $^{-1}$
		ρ	0.83	2.67			
$a_2(1320)$	2^{++}	ω	0.69	8.51	1.32 GeV	0.11 GeV	16 GeV $^{-1}$
		ρ	2.08	2.67			
$a_2(1700)$	2^{++}	ω	0.31	8.51	1.7 GeV	0.194 GeV	7.5 GeV $^{-1}$
		ρ	0.93	2.67			
$\pi_1(1400)$	1^{-+}	ω/ρ	Variable		1.35 GeV	0.33 GeV	1 GeV $^{-1}$

Table 4.3: Resonant contributions included in the amplitude for the reaction $\gamma + p \rightarrow p + \pi^0 + \eta$. Values in **bold** have been obtained from the analysis of CLAS data, as described in Chapter 5. Decay couplings g have been calculated from the experimental widths and branching ratios (see Appendix B).

with M_R and Γ_0 the nominal mass and width of the resonance, and q_0 the $\pi^0\eta$ center-of-mass momentum q evaluated at the resonance mass. $B'_L(q, q_0)$ are the so-called Blatt-Weisskopf barrier factors, tabulated in [117]. The mass-dependent width that appears in the denominator is:

$$\Gamma(M) = \Gamma_0 \frac{M_R}{M} \left(\frac{q}{q_0} \right)^{2L+1} (B'_L(q, q_0))^2. \quad (4.31)$$

The list of the resonances and of the corresponding Regge exchanges included in the amplitude is reported in Tab. 4.3. When possible, I exploited Regge factorization and thus used the couplings obtained from other reactions that involve common Regge exchanges and vertexes [118], while I used experimental data to fit the cross-section and obtain the missing couplings.

In particular, I derived the a_0 and a_2 couplings to the photon, $\beta_{\gamma a}^\rho$ and $\beta_{\gamma a}^\omega$. These are not independent, but are related, from isospin symmetry, by the relation:

$$\beta_{\gamma a}^\rho = 3\beta_{\gamma a}^\omega \quad (4.32)$$

I obtained the decay couplings g by comparing the Breit-Wigner expression with the experimental widths and branching ratios of the different resonances, as described in Appendix B.

Finally, I introduced a hypothetical 1^{-+} exotic state, the $\pi_1(1400)$, whose measurement sensitivity in MesonEx has to be evaluated. Mass and width were taken by PDG, from the average of the results reported by previous experiments. Since the branching fraction to the $\pi^0\eta$ is not known, I could not proceed as before to determine the decay coupling $g_{\pi_1^0\eta}^{\pi_1}$. Instead, I arbitrary set it to 1 GeV $^{-1}$, fixing the overall amplitude normalization through the Regge production coupling β . For each case I considered, I expressed the production coupling in terms of the relative π_1 total intensity with respect to the dominant a_2 signal.

4.3.2 Double Regge exchange

This mechanism corresponds to the non-resonant production of the $\pi^0\eta$ system on the proton, with two Reggeon exchanged between particles in the final state. Considering only the exchange of meson trajectories, there are two possible contributions to this amplitude, respectively for a “fast” η and for a “fast” π , as sketched in Figure 4.4.

The two amplitudes have a similar analytic structure, but the exchanged trajectories are different. For the amplitude A_t with a “fast” η , the possible exchanges at the top vertex are $x = \{\omega, \rho\}$ and

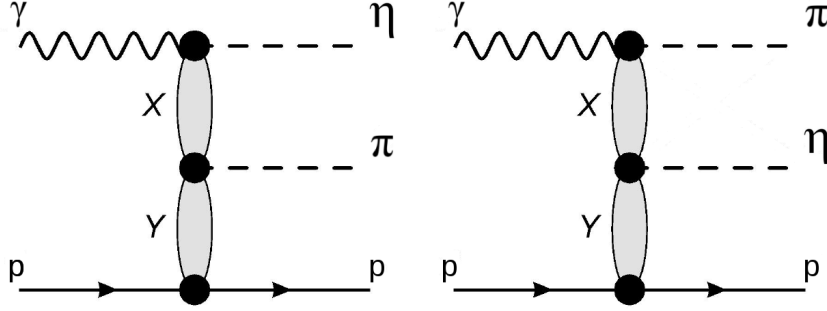


Figure 4.4: Double Regge exchange in the reaction $\gamma + p \rightarrow p + \pi^0 + \eta$. Left: amplitude A_t for a fast eta. Right: amplitude A_u for a fast pion.

correspondingly at the middle vertex there could be $y = \{\rho, \omega\}$. For the amplitude A_u with a “fast” π^0 , the possible exchanges at the top vertex are $x = \{\omega, \rho\}$, with $y = x$.

The amplitude A_t reads:

$$A_{\lambda,h,h'}^{DR-t} = \mathcal{K} \cos(\theta) e^{i\lambda\phi} \cdot \sum_{x,y} \beta_{\gamma\eta}^x \beta_{pp}^y \gamma_{\pi}^{xy} \cdot \frac{1}{\alpha_x - \alpha_y} \cdot [\xi_x \xi_{yx} (\alpha' s)^{\alpha_x - 1} (\alpha' s_2)^{\alpha_y - \alpha_x} \Gamma(1 - \alpha_x) - \xi_y \xi_{xy} (\alpha' s)^{\alpha_y - 1} (\alpha' s_1)^{\alpha_x - \alpha_y} \Gamma(1 - \alpha_y)] \quad (4.33)$$

where $s_1 = M_{\pi^0\eta}^2$, s_2 is the invariant mass squared of the $p - \pi$ system, and \mathcal{K} a proper kinematic factor [113].

The exchanged Reggeons x and y , corresponding to the trajectories α_x and α_y , couple to the external particles via the couplings $\beta_{\gamma\eta}^x$ and β_{pp}^y . These depend on the helicity configuration of the photon and on the spin state of the target and recoil proton, through Eq. 4.29. Finally, γ_{π}^{xy} is the Reggeon-reggeon-pion.

The signature factors are:

$$\xi_i = \frac{1}{2}(1 + \tau_i e^{-i\pi\alpha_i}) \quad ; \quad \xi_{ij} = \frac{1}{2}(1 + \tau_i \tau_j e^{-i\pi(\alpha_i - \alpha_j)}) \quad (4.34)$$

For $\alpha_x = \alpha_t$ the amplitude does not present an unphysical pole, since in that case the term inside squared parenthesis is zero for any x, y combination, being $\tau = -1$ for both the trajectories involved in the sum.

The amplitude A_u for a fast pion is simply obtained by making the substitutions $s_2 \rightarrow s_3$ and $t_a \rightarrow u$, with s_3 being the invariant mass of the $p - \eta$ system, and u the momentum transferred squared between the photon and the pion.

As before, due to Regge factorization, the β couplings can be obtained from other reactions involving same vertexes and trajectories. The procedure to calculate the reggeon-reggeon-particle coupling, detailed in [113], requires to compare this amplitude with the one for the two-body reaction obtained by removing the particle in the middle of the diagram, i.e. π for A_t and η for A_u . However, the $\pi - \omega - \rho$ coupling that appears in A_t is already known from [113], while I derived the $\eta - \omega - \omega$ and $\eta - \rho - \rho$ couplings from $SU(3)$ symmetry:

$$\gamma_{\omega\omega}^{\eta} = \gamma_{\rho\rho}^{\eta} = \frac{1}{2} \cos(\phi_{\eta}) \gamma_{\omega\rho}^{\pi} \quad , \quad (4.35)$$

Vertex	Exchanged trajectory		$\gamma_{\omega\rho}^\pi$	$\gamma_{\omega\omega}^\eta$	$\gamma_{\rho\rho}^\eta$
	ω	ρ			
pp	8.51	2.67	6.5	2.298	2.298
$\gamma\eta$	$0.378 \cdot e^{-2.0 \cdot t }$	$1.139 \cdot e^{-0.75 \cdot t }$			
$\gamma\pi$	0.763	0.148			

Table 4.4: Left: particle-particle-reggeon couplings for the double Regge exchange amplitude. t is the transferred momentum squared at the corresponding vertex. Right: particle-reggeon-reggeon couplings.

with $\phi_\eta \simeq 42^\circ$ the $\eta - \eta'$ mixing angle in the flavor basis.

The coupling values are reported in Tab. 4.4. It is worth to mention that there are no free parameters in this contribution to the full reaction amplitude.

4.4 Photo-production amplitudes in the low Q^2 framework

The two main “ingredients” needed to study the $\pi^0\eta$ channel in the MesonEx experiment are the properties of the quasi-real photon beam and the photo-production amplitude for the reaction $\gamma p \rightarrow p\pi^0\eta$, presented, respectively, in Sec. 1.6 and in Sec. 4.3. To proceed, is now time to couple them together.

I started from the amplitude expression for the full reaction that also involve an electron:

$$e(p) + p(k) \rightarrow e(p') + \pi^0(w_1) + \eta(w_2) + p(k') \quad , \quad (4.36)$$

where the four momenta of the particles are indicated in parenthesis. The leptonic vertex of the amplitude, in the one-photon-exchange approximation sketched in Figure 4.5, can be written using QED rules. The hadronic vertex is handled in an effective way introducing a hadronic current J_{hadr}^ν , that depends on the four momenta of the target, the recoil proton, and the mesons, as well as from their spins. Indicating with s (s') the spin of the beam (scattered electron) and with h (h') the spin of the target (recoil proton), the amplitude reads:

$$A = e^2 \bar{u}(p', s') \gamma^\mu u(p, s) \Delta_{\mu\nu} J^\nu(k, k', h, h', w_1, w_2) \quad , \quad (4.37)$$

where u and \bar{u} are the Dirac spinors associated to the initial and final state electron, and $\Delta_{\mu\nu}$ is the photon propagator, whose explicit form depends on the gauge fixing choice. However, since the electromagnetic current is conserved for both the electron and the proton vertexes, the gauge-dependent term in the photon propagator can be neglected:

$$A = \frac{i e^2}{Q^2} \bar{u}(p', s') \gamma^\mu u(p, s) g_{\mu\nu} J^\nu(k, k', h, h', w_1, w_2) \quad (4.38)$$

Eq. 4.38 is well known in the framework of electro-production experiments. To effectively use it, the explicit form of the hadronic current J^ν is required, and must be provided as an external input.

This expression has to be modified to also use real photo-production amplitudes. In this way, MesonEx can share amplitudes with other experiments performing meson spectroscopy with *real* photons, the same analysis tools can be used, and results can be directly compared. To do so, I re-wrote the reaction amplitude as the product of two factors. The first describes the emission of a quasi-real photon by the electron, and the second the subsequent interaction of the photon with the target. I did this exploiting the following completeness relation, that holds for virtual photon

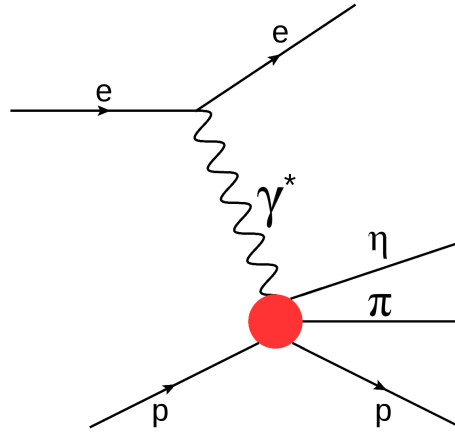


Figure 4.5: One-photon-exchange diagram for the reaction $e + p \rightarrow e + \pi^0 + \eta + p$. The red circle “hides” the strong interaction vertex, while γ^* is an internal photon line, also referred to as “virtual photon”.

polarization vectors⁵:

$$\sum_{\lambda=-1,1} \varepsilon_{\lambda}^{\mu} \varepsilon_{\lambda}^{\nu*} - \varepsilon_0^{\mu} \varepsilon_0^{\nu*} = -g^{\mu\nu} \quad (4.39)$$

where q is the four momentum of the quasi-real photon and λ the helicity. Combining Eq. 4.39 with Eq. 4.38, I finally derived the following reaction amplitude expression:

$$A = -i e^2 \sum_{\lambda=-1}^1 \left(\frac{1}{Q^2} \bar{u}(p', s') \gamma^{\mu} u(p, s) \varepsilon_{\mu}^*(q, \lambda) \right) \cdot (\varepsilon_{\nu}(q, \lambda) J^{\nu}) \equiv \sum_{\lambda} \mathcal{L}_{\lambda}^{s, s'} \cdot A_{photo} \quad (4.40)$$

The second factor in Eq. 4.40 is the Lorentz-invariant photo-production amplitude A_{photo} for the process $\gamma p \rightarrow p \pi^0 \eta$, that was presented in the previous section. It depends explicitly from the photon helicity λ , including the case $\lambda = 0$. However, it can be shown that longitudinal polarized photons do not contribute to the $\pi^0 \eta$ final state.

The first factor $\mathcal{L}_{\lambda}^{s, s'}$, instead, accounts for the quasi-real photon emission by the incident electron. Such a term is independent from the specific final state under study. It depends only from the scattered electron kinematics and helicity. Therefore I calculated it once, and then I included it in the amplitude calculation. The explicit $\mathcal{L}_{\lambda}^{s, s'}$ expression is reported in Appendix A.

4.5 Partial wave analysis formalism for $\gamma^* + p \rightarrow p + \pi^0 + \eta$

To derive the formalism needed in the partial wave analysis of the reaction $\gamma^* + p \rightarrow p + \pi^0 + \eta$, I started from the *real* photo-production case, and then I modified the results to account for the quasi-real nature of the photon beam, including a proper electron-scattering term. All the expressions are explicitly derived in the Gottfried-Jackson reference frame.

For the *real* photo-production process there are 8 independent amplitudes $A_{\lambda, h, h'}$, corresponding to the different helicity configurations of the photon (λ), target (h), and recoil nucleon (h'). Since

⁵In principle, the right side of Eq. 4.39 should contain other terms, proportional to the photon four momentum q^{μ} . However, since both the electron and proton vertexes in the OPE diagram conserve the electromagnetic current, these additional terms do not contribute to the reaction amplitude.

both π^0 and η are pseudo-scalar particles, these are decomposed in partial waves using spherical harmonic functions $Y_{J,M}(\theta, \phi)$ [119]:

$$A_{\lambda,h,h'}(s, t, M_{\pi^0\eta}, \Omega) = \sum_{J,M} V_{\lambda,h,h'}^{JM}(s, t, M_{\pi^0\eta}) Y_{J,M}(\Omega) \quad (4.41)$$

The complex production parameters V are extracted from the data, by performing a maximum likelihood fit with the intensity expression corresponding to the above amplitude. Invariance under parity can be used to reduce the number of independent amplitudes, and thus of parameters to be fitted to the data. I introduced the reflection operator in the \hat{y} direction Y :

$$Y = e^{i\pi J_y} P \quad (4.42)$$

The Y action on a single-particle helicity eigenstate, whose momentum \vec{k} lies in the xz plane, is:

$$Y|\vec{k}, \lambda \rangle = \eta(-1)^{s-\lambda} |\vec{k}, -\lambda \rangle, \quad (4.43)$$

where η is particle intrinsic parity ($P|\vec{0}, \lambda \rangle = \eta|\vec{0}, \lambda \rangle$), and s its spin. Parity invariance implies $A = Y^{-1}AY$, therefore:

$$\begin{aligned} A_{\lambda,h,h'}(\dots, \theta, \phi) &= \langle h', \dots, \theta, \phi | Y^{-1} A Y | h, \lambda \rangle = \\ &= \eta_\pi \eta_\eta \eta_p^2 \eta_\gamma (-1)^{s_p-h} (-1)^{s_p-h'} (-1)^{s_\gamma-\lambda} A_{-\lambda,-h,-h'}(\dots, \theta, -\phi) = \\ &= -(-1)^{h'-h} A_{-\lambda,-h,-h'}(\dots, \theta, -\phi), \end{aligned} \quad (4.44)$$

where \dots denote all scalars under Y , i.e. (s, t, M) . Meson momenta only do not lie in the xz plane, and thus are affected by the action of Y , $\phi \rightarrow -\phi$. Using Eq. 4.41 for the partial waves, I got:

$$\begin{aligned} V_{\lambda,h,h'}^{JM}(s, t, M_{\pi^0\eta}) &= \int d\Omega A_{\lambda,h,h'}(s, t, M_{\pi^0\eta}, \theta, \phi) Y_{J,M}^*(\Omega) = \\ &= -(-1)^{h'-h} \int d\Omega A_{-\lambda,-h,-h'}(s, t, M_{\pi^0\eta}, \theta, -\phi) Y_{J,M}^*(\Omega) = \\ &= -(-1)^{h'-h} \int d\Omega A_{-\lambda,-h,-h'}(s, t, M_{\pi^0\eta}, \theta, \phi) Y_{J,M}^*(\theta, -\phi) = \\ &= -(-1)^M (-1)^{h'-h} V_{-\lambda,-h,-h'}^{J-M}(s, t, M_{\pi^0\eta}), \end{aligned} \quad (4.45)$$

where I used $Y_{J,M}(\theta, -\phi) = (-1)^M Y_{J,-M}(\theta, \phi)$. Parity relations are thus summarized as follows, distinguishing between the spin-flip ($h \neq h'$) and the spin no-flip ($h = h'$) case:

$$V_{\lambda,h,h'}^{JM} = \begin{cases} (-1)^M \cdot V_{-\lambda,-h,-h'}^{J-M} & \text{spin-flip} \\ (-1)^{M-1} \cdot V_{-\lambda,-h,-h'}^{J-M} & \text{spin no-flip} \end{cases} \quad (4.46)$$

Furthermore, the two amplitudes corresponding to each proton spin configuration, i.e. $V_{\lambda,\pm,\pm}$ for the spin no-flip and $V_{\lambda,\pm,\mp}$ for the spin-flip, can be related by assuming a Regge pole model for the reaction $\gamma p \rightarrow p + (\pi^0 + \eta)$. The corresponding production amplitude has the form reported in Eq. 4.27,

$$A_{h,h'}^{\lambda,M} = \beta_{\lambda,M}^R \cdot \beta_{h,h'}^R \cdot f(s, \alpha_R(t)), \quad (4.47)$$

where β are the Regge coupling factors for each of the two vertexes and f it the Reggeized t -channel propagator.

Parity conservation applied separately at the two vertexes gives [107]:

$$\beta_{\lambda,M}^R = h_R \eta_\gamma \eta_{\pi^0\eta} (-1)^{s_\gamma - s_{\pi^0\eta} + \lambda - M} \beta_{-\lambda,-M}^R = -(-1)^M \beta_{-\lambda,-M}^R \quad (4.48)$$

$$\beta_{h,h'}^R = h_R (\eta_p)^2 (-1)^{s_p - s_p + h - h'} \beta_{-s,-s'}^R = (-1)^{h-h'} \beta_{-h,-h'}^R, \quad (4.49)$$

where I used $\eta_{\pi^0\eta} = (-1)^{s_{\pi^0\eta}}$ for the intrinsic parity and spin of the $\pi^0\eta$ system, and I assumed natural Regge exchange, i.e. $h_R = 1$.

These relations can be used to simplify the expression of the reaction intensity, used in the partial wave analysis, by eliminating terms with $M < 0$. In the following, I derive explicitly the intensity expression for the spin-flip case, considering only waves with $J \leq 2$, $|M| \leq 1$. The extension to higher partial waves, or to the spin no-flip case, proceeds in an similar way.

The intensity is obtained from the coherent sum of the different partial waves, summing incoherently on the photon helicity, and using Eq. 4.49 to simplify the sum on the two spin-flip configurations:

$$I(s, t, M_{\pi^0\eta}, \Omega) = \sum_{\lambda=\pm 1} \left| \sum_{J,M} V_\lambda^{JM}(s, t, M_{\pi^0\eta}) Y_{J,M}(\theta, \phi) \right|^2 \quad (4.50)$$

Parity relations (Eq. 4.46 and Eq. 4.49) can be used to eliminate terms with $M < 0$ and reduce the number of free parameters:

$$I = \sum_{\lambda=\pm 1} \left| V_\lambda^{0,0} Y_{0,0} + V_\lambda^{1,0} Y_{1,0} + V_\lambda^{1,1} Y_{1,1} + V_{-\lambda}^{1,1} Y_{1,-1} + V_\lambda^{2,0} Y_{2,0} + V_\lambda^{2,1} Y_{2,1} + V_{-\lambda}^{2,1} Y_{2,-1} \right|^2 \quad (4.51)$$

This expression, however, holds for the real photo-production reaction and has to be modified to adapt it to the *quasi-real* case. The virtual photon is no longer an external particle, and thus the sum over its polarization must be performed at the level of the amplitude, before taking its modulus squared. Also, the factor $\mathcal{L}_\lambda^{s,s'}$ that accounts for the quasi-real photon emission (Eq. 4.40) must be included in the amplitude. Finally, the incoherent sum over the beam and recoil electron helicities must be included.

$$\begin{aligned} I &= \sum_{s,s'} \left| \sum_{\lambda,J,M} \mathcal{L}_\lambda^{s,s'} V_\lambda^{JM} Y_{J,M} \right|^2 = \\ &= \sum_{s,s'} \left| \sum_{\lambda} \mathcal{L}_\lambda^{s,s'} (V_\lambda^{0,0} Y_{0,0} + V_\lambda^{1,0} Y_{1,0} + V_\lambda^{1,1} Y_{1,1} + V_{-\lambda}^{1,1} Y_{1,-1} + V_\lambda^{2,0} Y_{2,0} + V_\lambda^{2,1} Y_{2,1} + V_{-\lambda}^{2,1} Y_{2,-1}) \right|^2 = \\ &= \sum_{s,s'} \left| V^{0,0} Y_{0,0} (\mathcal{L}_+^{s,s'} - \mathcal{L}_-^{s,s'}) + V^{1,0} Y_{1,0} (\mathcal{L}_+^{s,s'} - \mathcal{L}_-^{s,s'}) + V^{2,0} Y_{2,0} (\mathcal{L}_+^{s,s'} - \mathcal{L}_-^{s,s'}) + \right. \\ &\quad \left. + V_+^{1,1} (Y^{1,1} \mathcal{L}_+^{s,s'} + Y^{1,-1} \mathcal{L}_-^{s,s'}) + V_-^{1,1} (Y^{1,1} \mathcal{L}_-^{s,s'} + Y^{1,-1} \mathcal{L}_+^{s,s'}) + \right. \\ &\quad \left. + V_+^{2,1} (Y^{2,1} \mathcal{L}_+^{s,s'} + Y^{2,-1} \mathcal{L}_-^{s,s'}) + V_-^{2,1} (Y^{2,1} \mathcal{L}_-^{s,s'} + Y^{2,-1} \mathcal{L}_+^{s,s'}) \right|^2, \quad (4.52) \end{aligned}$$

where the last equality is motivated from the parity relation $V_\lambda^{J,0} = -V_{-\lambda}^{J,0} \equiv V^{J,0}$, that holds in the spin-flip case.

This expression is finally fitted to experimental data, to extract the seven unknown complex production parameters V through a maximum likelihood unbinned fit, as explained in Sec. 1.5.1⁶. Fits are performed in independent bin of s , t , $M_{\pi^0\eta}$ to derive the dependence of the parameters on these kinematic variables.

⁶Actually, it is clear from Eq. 4.52 that the phase of the V coefficients can be determined apart from a global contribution Φ_0 , since the intensity is sensitive only to the relative phases difference.

Chapter 5

Analysis of the reaction $\gamma p \rightarrow p\pi^0\eta$ measured with CLAS

The study of the $\pi^0\eta$ channel in MesonEx requires pseudo-data to be generated, according to the amplitudes derived in the Regge framework, and described in the previous Chapter. However, to validate the amplitudes and tune free parameters, it is necessary to compare with *real* experimental data. This comparison ensures that the results are motivated not only from the theory, but also from the experimental point of view.

I analyzed the reaction $\gamma p \rightarrow p\pi^0\eta$ using the data measured with the CLAS detector during the g12 run period, when the HyCLAS experiment, specifically designed to study meson spectroscopy, took place. The experiment was performed using the Hall B Photon Tagger converting a 5.71 GeV electron beam from the CEBAF accelerator to a Bremsstrahlung photon beam impinging on a 40 cm liquid hydrogen target. The experiment collected 622 data taking runs, resulting in 25.8 billion events recorded. Different trigger configurations were employed, including two charged-particles events, or events with one charged-particle and two neutrals. A full description of the experimental conditions is reported in [120].

My goal was to obtain an estimate of the differential reaction cross-section, as a function of the $\pi^0\eta$ invariant mass, in different bins of the photon beam energy. This experimental observable can be directly compared with the theoretical prediction from the amplitudes, whose free parameters can be extracted by performing a fit to the data. Moreover, the analysis procedure employed to extract the signal can be exported from HyCLAS to MesonEx with minor modifications, since the kinematic regime and the detector design are similar in the two experiments. The analysis of the CLAS data thus provided a benchmark to test the event selection algorithm within a real experimental environment, including important systematic effects not present in the MonteCarlo simulation.

In this analysis, I used data that have already been reconstructed, or “cooked”, starting from the measured raw data, using the standard CLAS reconstruction framework. Details can be found in [121] and [99].

5.1 Events selection

The reaction I studied was:

$$\gamma + p \rightarrow p + \pi^0 + \eta \quad (5.1)$$

$$\pi^0 \rightarrow \gamma\gamma \quad (5.2)$$

$$\eta \rightarrow \gamma\gamma \quad (5.3)$$

where all the particles in the final state, the proton and the four photons, were measured. I made this choice because, from a preliminar analysis of events with only two photons measured, I realized that the resolution of the CLAS detector was not good enough to extract a clean signal, reconstructing one of the two mesons via the missing mass technique. The request to measure all the four photons reduces the background from other channels, and also permits to apply selection cuts on the data having the full reaction kinematic available.

After requiring one proton and four photons measured, and applying the standard CLAS fiducial cuts, 4.42M of the events were selected. These are the input for this analysis. I excluded runs with the ratio of the total number of $p\gamma\gamma\gamma\gamma$ events over the accumulated charge of the primary electron beam clearly different from the average.

I did not apply any selection on the trigger configuration during the event selection. However, I verified *a posteriori* that all the selected $p\pi^0\eta$ events were recorded by the same trigger, that required one charged particle and two neutrals.

5.1.1 Initial state photon selection

Information on the initial photon energy is provided by the CLAS Photon Tagger, described in Sec. 2.2. When the trigger condition is satisfied, all the hits measured in the detector within a $\simeq 100$ ns coincidence time window are recorded. Each hit corresponds to an electron belonging to one of the $\simeq 50$ bunches that passed trough the radiator during the coincidence time window¹, emitting a Bremsstrahlung photon. Depending on the primary electron beam intensity, and on the radiator tickness, the number of hits can vary from few to over a hundred.

To select the photon that actually triggered the hadronic event, it is necessary to match the time of the photon hit with the start time of the CLAS measured event. The CLAS start time is obtained from the time of the proton hit in the Start Counter, propagated back to the event vertex using the track information obtained by the Drift Chambers. The photon hit time is obtained from the Photon Tagger and is then propagated to the vertex location.

Photons produced by beam pulses other than the “true” one are rejected requiring a time coincidence between CLAS and the Photon Tagger in a 2.004 ns window. The coincidence window width is equal to the time distance between the beam bunches. However, if more than one photon is compatible with the CLAS start time within this coincidence window, it is not possible to identify which of them actually initiated the event. I decided to reject these “multiple-good-photons events”, introducing a proper correction factor to the overall normalization that accounts for their exclusion. The fraction of events having more than one photon in the “good” beam pulse is about 13%. I also excluded events that, despite triggering the CLAS detector, did not have any photon in the time coincidence window.

Finally, I imposed a constrain on the photon beam energy E_{beam} , keeping only events with $E_{beam} > 2.35$ GeV. This threshold is a trade-off between the high E_{beam} region, where the production of $\pi^0\eta$ resonances is favored, and the energy range covered by the CB-ELSA experiment

¹As previously described in Sec. 2.1.1, the electron beam is delivered to each experimental hall from the CEBAF accelerator with a 2.004 ns time period, independent from its intensity, therefore in a 100 ns time window 50 electron bunches are expected.

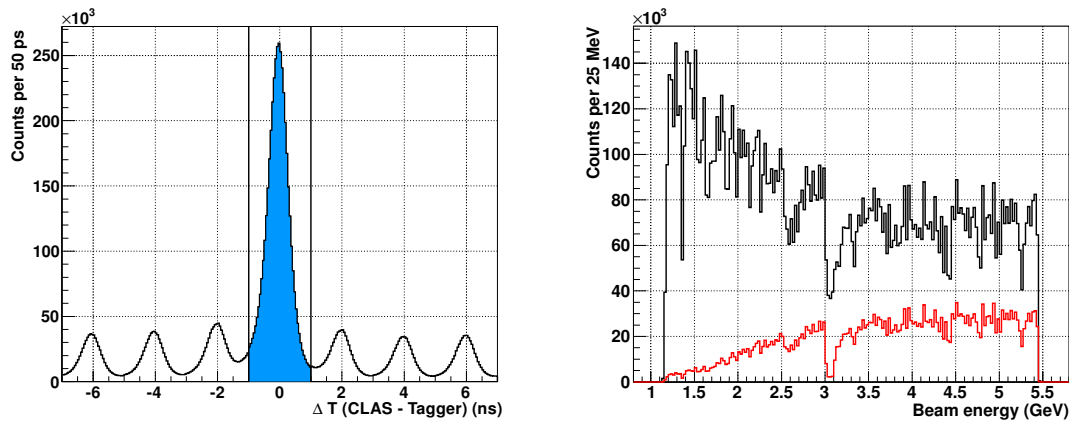


Figure 5.1: Left: time difference distribution between photon hits and CLAS start time. The 2.004 ns coincidence window is highlighted. Right: photon beam energy distribution. In black, all the photons measured by the Tagger. In red, “good” photons within the coincidence window, neglecting events with more than one hit. The “hole” at 3 GeV is due to a Photon Tagger T-counter with a malfunctioning phototube, that was not accounted for during reconstruction.

[89], between 0.9 and 3.0 GeV. This is the only reference found in literature where a measurement of this reaction is reported, and can be used to verify the consistency my results.

In summary, the fraction of events kept after the photon selection was 66.1%.

5.1.2 Vertex selection

The target used in the HyCLAS-g12 experiment was cylindrical in shape, 40 cm long and with 2 cm radius, centered 90 cm upstream from the CLAS center. For this analysis, involving only one charged particle, the event vertex is calculated from the distance of closes approach (DOCA) of its trajectory to the beam line. The vertex is then defined as the midpoint of the DOCA vector. I selected events with the z vertex position in the range (-110, -70) cm, while I did not put any requirement on the vertex radial distance r from the beam line². After this selection, 64.5% of the initial events survived.

5.1.3 Exclusive events selection of $\gamma p \rightarrow p \gamma \gamma \gamma \gamma$

The events used in this analysis require proton and four photons measured by CLAS. However, since the detector acceptance does not cover the whole 4π solid angle, in particular for neutrals, a consistent fraction of these events is expected to have particles not been measured by the detector. These events are a background source for the reaction under study and must be rejected.

The missing four-momentum in the reaction $\gamma p \rightarrow p \gamma_1 \gamma_2 \gamma_3 \gamma_4 X$, where X is the ensemble of the non-detected particles, is:

$$P_X = P_{beam} + P_{target} - P_p - P_{\gamma_1} - P_{\gamma_2} - P_{\gamma_3} - P_{\gamma_4} \quad (5.4)$$

²In the CLAS standard reference frame, the \hat{z} axis is parallel to the beam line, pointing toward the beam dump. The \hat{y} axis is vertical, and $\hat{x} = \hat{y} \times \hat{z}$.

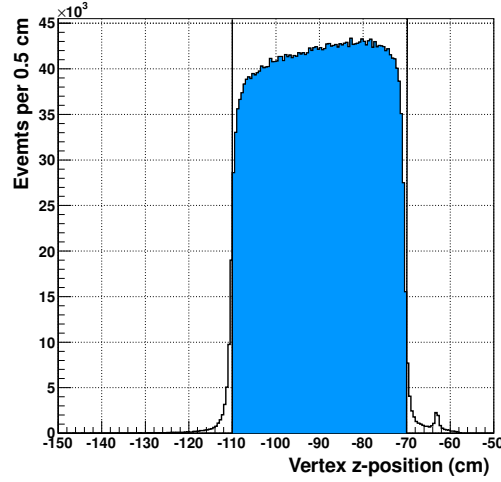


Figure 5.2: Event vertex z coordinate distribution. The target location matching cut is highlighted.

To select *exclusive* events, i.e. events with no missing particles, it is common to require that the total missing mass squared $m_X^2 \equiv P_X^\mu P_{\mu X}$ is compatible with zero. However, from a preliminary study, I concluded that cutting on the total missing mass squared does not help in background reduction, due to the poor resolution on the photon measurement. This is clearly seen in Figure 5.3 (left panel), where m_X^2 is plotted against the missing mass on the final state proton m_{ep} , defined as:

$$m_{ep}^2 = (P_{beam} + P_{target} - P_p)^2 \quad (5.5)$$

The missing mass for the *non-exclusive* events dominated by a single η or η' production on the proton is compatible with zero. The comparison of the missing mass distributions for all events, for exclusive η production, and for exclusive η' production, is shown in Figure 5.3 (right panel). This confirms that they all are compatible with zero, thus a cut on this variable would not reject them.

To select exclusive events, I therefore introduced a new variable K , defined as the difference between the missing mass squared on the proton, m_{ep}^2 , and the four photons invariant mass. This new variable is expected to be zero for exclusive events ($P_X = 0$), as follows from the four-momentum conservation equation:

$$P_p + P_{\gamma_1\gamma_2\gamma_3\gamma_4} + P_X = P_{beam} + P_{target} \quad (5.6)$$

$$P_{\gamma_1\gamma_2\gamma_3\gamma_4} + P_X = P_{beam} + P_{target} - P_p \quad (5.7)$$

$$2P_X P_{\gamma_1\gamma_2\gamma_3\gamma_4} + m_X^2 = (P_{beam} + P_{target} - P_p)^2 - P_{\gamma_1\gamma_2\gamma_3\gamma_4}^2 \equiv K \quad (5.8)$$

K is plotted against the missing mass on the final state proton in Figure 5.4. For events corresponding to the $p\eta$ or to the $p\eta'$ topology K is greater than zero, while exclusive events appear in the plot as a light vertical band centered at $K = 0$. I selected them keeping only events with K in the range $(-0.5, 0.052)$ GeV^2 . After this cut, only 5.0% of the initial events survived.

5.1.4 π^0 and η identification

Since the four photons from the π^0 and η decay are measured, I identify the two mesons from the invariant mass of the different photon pairs combinations. Having four photons, there are three

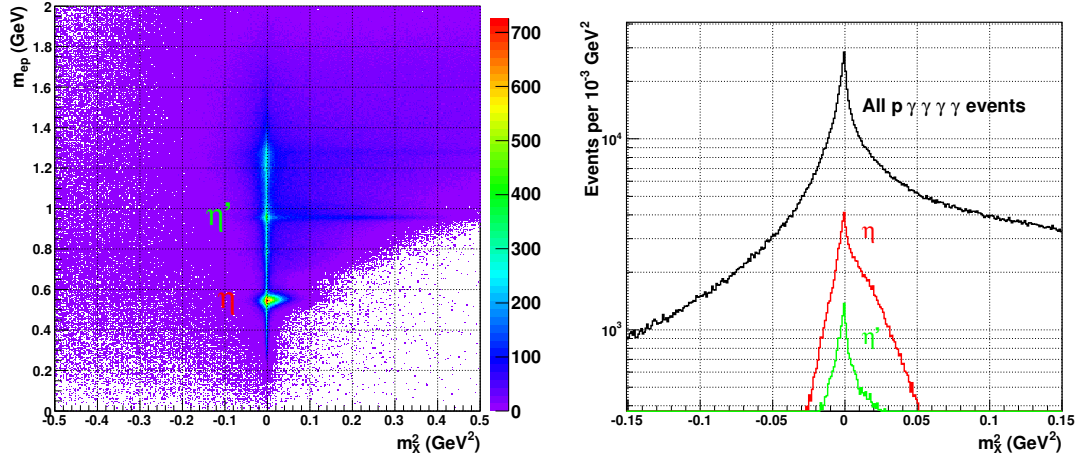


Figure 5.3: Left: missing mass on the proton m_{ep} against the total missing mass squared m_X^2 for $p\gamma\gamma\gamma$ events, with events corresponding to single η and η' production on the proton highlighted. Right: missing mass squared distribution for all $p\gamma\gamma\gamma$ events (black), for η events (red), and for η' events (green). The exclusivity cut is highlighted.

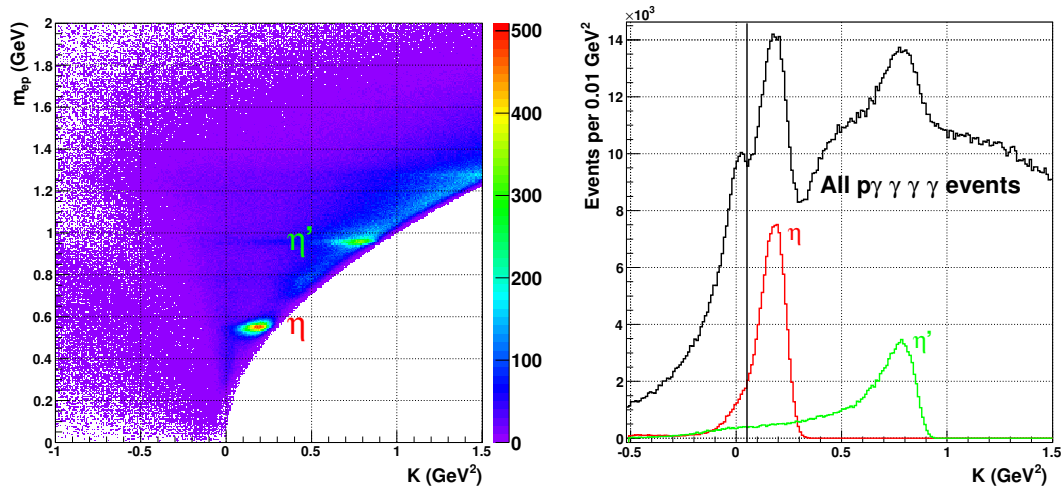


Figure 5.4: Left: missing mass on the proton m_{ep} against $K \equiv m_{ep}^2 - m_{\gamma\gamma\gamma\gamma}^2$ for $p\gamma\gamma\gamma$ events, with events corresponding to single η and η' production on the proton highlighted. Right: distribution of K for all $p\gamma\gamma\gamma$ events (black), for η events (red), and for η' events (green).

4 γ source	$\pi^0\eta$	$\pi^0\pi^0$
Identified as $\pi^0\eta$	82.0%	0.02 %
Identified as $\pi^0\pi^0$	1.4%	95.5%
Not identified	16.7%	4.4%

Table 5.1: Test of the mesons identification algorithm on MonteCarlo events. I generated a set of $\gamma p \rightarrow p\pi^0\eta$ (signal) and $\gamma p \rightarrow p\pi^0\pi^0$ (background) events, projected them on CLAS, and applied on both the particle identification algorithm.

different ways to sort them in pairs. To select the “best” photon combination compatible with the $\pi^0\eta$ topology, I exploited the kinematic properties of the mesons decay to two photons. For the process $\pi^0/\eta \rightarrow \gamma\gamma$ the *relative* angle in between the two photons in the laboratory frame can vary between θ_0 and π , with

$$\cos \theta_0 = \frac{E^2 - 2M^2}{E^2} = 1 - 2\frac{M^2}{E^2} \quad , \quad (5.9)$$

where E is the energy of the decaying particle and M its mass: the lower M , the smaller θ_0 . Also, since the decay is isotropic in the meson rest frame, at high enough energy ($E > 2M$) the photon relative angle distribution is strongly peaked at θ_0 , as a consequence of the Lorentz boost. Therefore, the photons emitted by the π^0 are expected, on average, to have a smaller relative angle than those emitted by the η .

I ordered the four photons calling γ_1, γ_2 the ones with the smallest relative angle and γ_3, γ_4 the other two. The by-dimesional distribution of $M_{\gamma_1\gamma_2}$ vs $M_{\gamma_3\gamma_4}$, reported in Figure 5.5, shows a strong enhancement of events belonging to the $\pi^0\pi^0$ topology, while $\pi^0\eta$ events appear as a less intense peak centered at $M_{\gamma_1\gamma_2} \simeq M_{\pi^0}$, $M_{\gamma_3\gamma_4} \simeq M_\eta$. Few signal events also appear in the opposite combination, corresponding to the two photons from the η having a smaller relative angle.

The selections that I used to identify $\pi^0\eta$ events are highlighted in the plot. They correspond to 3σ cuts around the π^0 and the η peaks. After their application, 37k events were kept, corresponding to the 0.78% of the initial $p\gamma\gamma\gamma$ samples.

I tested the efficiency and the rejection power of the identification algorithm on MonteCarlo pseudo-data. As possible contamination source, I only considered the $\gamma p \rightarrow p + \pi^0 + \pi^0$ channel, dominating the dataset. The results of this test are reported in Tab. 5.1. Even if the algorithm is not 100% efficient, i.e. a small fraction of “real” $\pi^0\eta$ events are not identified, the contamination introduced by the main background source is negligible³.

5.1.5 Further selections and signal events properties

The goal of this analysis is to measure the reaction cross section, differential in the $\pi^0\eta$ invariant mass, as a function of the photon beam energy. Therefore, after identifying a clean sample of exclusive $\gamma p \rightarrow p\pi^0\eta$ events, I performed a consistency check on the kinematic variables that are integrated over, since they can introduce systematic effects on the final result.

³ The photon pairs invariant mass resolution is a critical element for the identification algorithm. Before proceeding with the test on MonteCarlo events, I verified that the resolution in the simulation is matched to the corresponding experimental value. In particular, I measured the width of the π^0 and η peaks. The values I obtained are the following:

$$\begin{aligned} \sigma_{\pi^0}^{Data} = 16.4 \text{ MeV} &\iff \sigma_{\pi^0}^{MC} = 15.7 \text{ MeV} \\ \sigma_{\eta}^{Data} = 53.3 \text{ MeV} &\iff \sigma_{\eta}^{MC} = 47.0 \text{ MeV} \end{aligned}$$

A good agreement between data and MonteCarlo reconstructed events is seen.

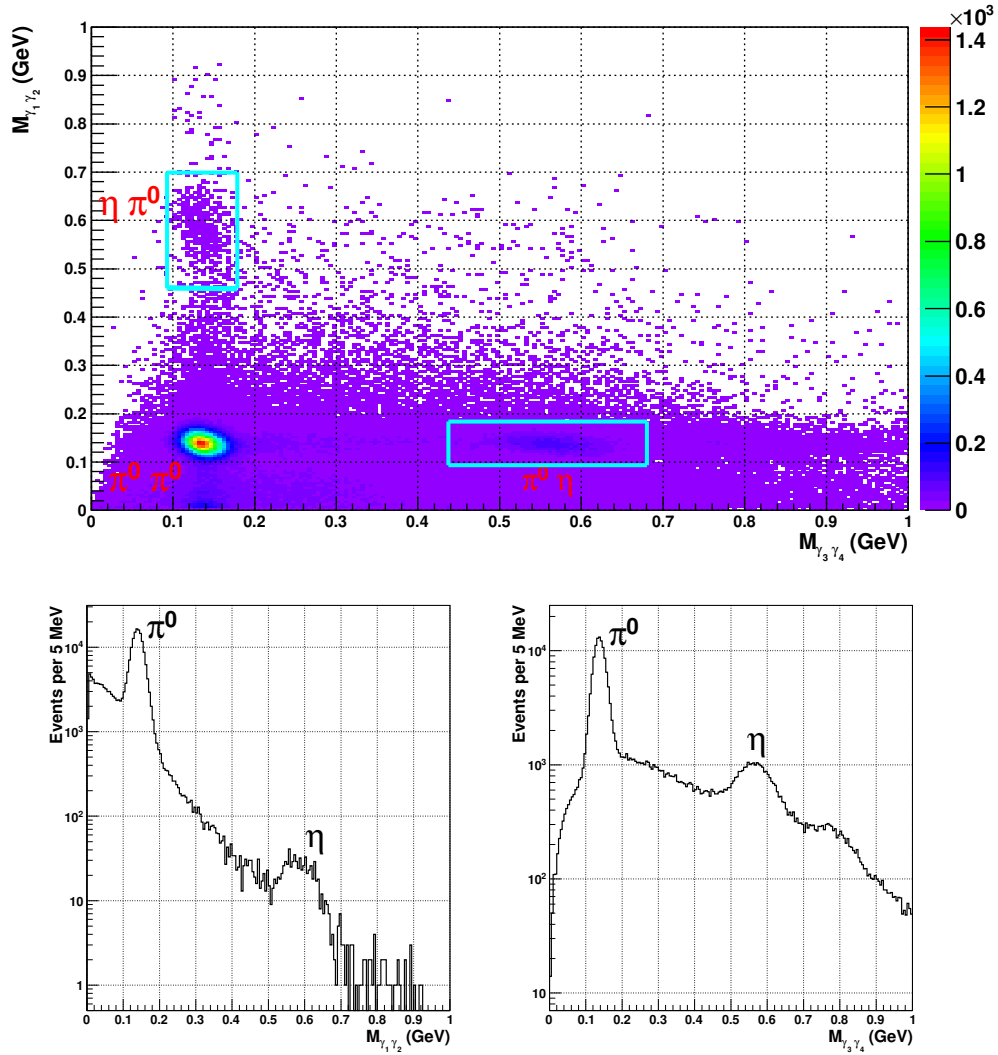


Figure 5.5: Top: by-dimensional distribution of $M_{\gamma_1\gamma_2}$ vs $M_{\gamma_3\gamma_4}$, where γ_1 and γ_2 are the two photons whose three-momenta form the smallest relative angle in the CLAS frame. Bottom: distribution of $M_{\gamma_1\gamma_2}$ (left) and $M_{\gamma_3\gamma_4}$ (right): in both cases, the second variable is integrated over the whole invariant mass range.

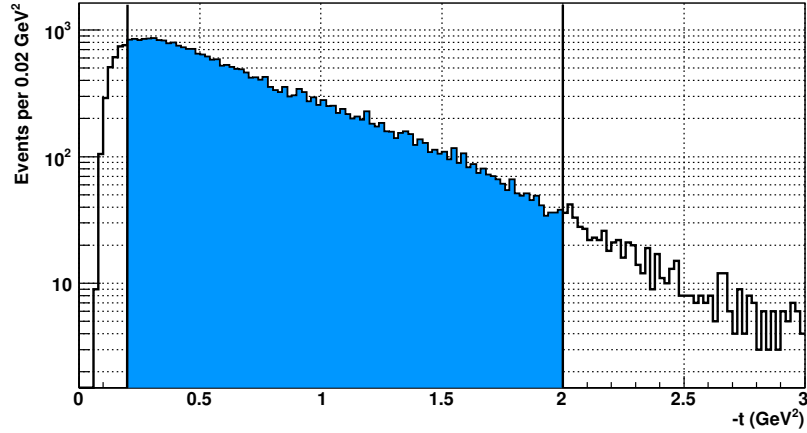


Figure 5.6: $-t$ distribution for exclusive $p\pi^0\eta$ events. The selection to exclude $-t$ values out of the CLAS acceptance is highlighted.

Cut used	Accepted events	Accepted events %
Photon beam selection	3.33M	75 %
Photon beam energy	2.92M	66 %
Vertex z -coordinate	2.85M	64 %
Exclusivity	221k	5 %
$\pi^0\eta$ topology	34.6k	0.78 %
t	30.3k	0.68 %

Table 5.2: Summary of data cuts used to select exclusive $\gamma p \rightarrow p\pi^0\eta$ events, from the initial sample of 4.42M $p\gamma\gamma\gamma$ events.

In particular, the distribution of the momentum transferred $-t$ from the photon beam to the $\pi^0\eta$ system, calculated as $-t = -(P_{target} - P_p)^2$, shows a rapidly falling exponential behaviour for $-t > 0.2 \text{ GeV}^2$. For smaller values, the distribution falls rapidly at zero. This effect is due to the limited CLAS acceptance for polar angles smaller than $\simeq 10^\circ$ (see Tab. 2.1): small $-t$ values correspond to events with particles emitted at very forward angles in the laboratory frame. To avoid a possible cross-section underestimation, that could result from the integration over the whole $-t$ range, I decided to keep only events in the $-t$ range between 0.2 and 2.0 GeV^2 , well inside the nominal CLAS acceptance region. I properly accounted for this $-t$ range limitation in the cross-section calculation, introducing a MonteCarlo-derived correction factor, as described in the following section.

After the application of all the cuts, summarized in Tab. 5.2, I ended up with 30.3k clean events for the exclusive $\gamma p \rightarrow p\pi^0\eta$ process, corresponding to the 0.7% of the initial $p\gamma\gamma\gamma$ sample. These events were used to calculate the reaction cross-section.

The invariant mass distribution $M_{\pi^0\eta}$ of the $\pi^0\eta$ system is shown in Figure 5.7. I derived $M_{\pi^0\eta}$ from the missing mass on the proton m_{ep} , rather than from the invariant mass of the four final state photons $M_{\gamma\gamma\gamma\gamma}$, since the CLAS experimental resolution is higher for charged particles. The most evident features of the distribution are the peak centered at $\simeq 1 \text{ GeV}/c^2$, that most likely corresponds to the known $a_0(980)$ resonance, and the pronounced shoulder at $\simeq 1.3 \text{ GeV}/c^2$, related to the $a_2(1320)$ state. At higher invariant mass the distribution is smoother and no sharp

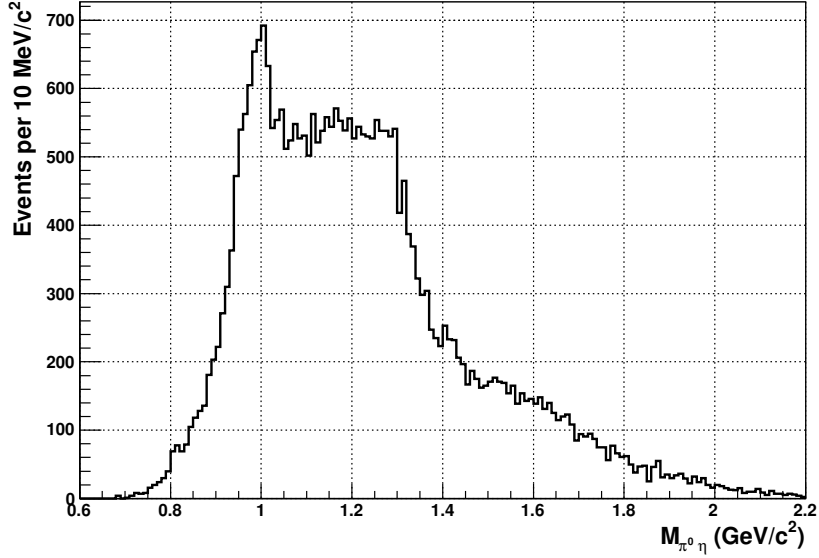


Figure 5.7: Invariant mass distribution of the $\pi^0\eta$ system for exclusive $\gamma p \rightarrow p\pi^0\eta$ events.

structures are seen.

5.2 Detector acceptance

To calculate the differential cross-section $d\sigma/dM_{\pi^0\eta}$, the knowledge of the CLAS acceptance $\varepsilon(E_{beam}, M_{\pi^0\eta})$, as a function of the photon beam energy and of the invariant mass of the $\pi^0\eta$ system, is required.

The procedure to calculate the experimental acceptance relies on a MonteCarlo simulation of the detector. First, a set of MonteCarlo events for the reaction $\gamma p \rightarrow p\pi^0\eta$ were generated according to a certain distribution which, as discussed later, should be as similar as possible to the real, acceptance-corrected, data. These pseudo-events are then projected on the CLAS detector using the `GSIM` program, based on the CERN `GEANT3` libraries. For each event, `GSIM` produces the same digitized response that CLAS would have reported if that event had been measured, by tracking particles through the detector components. To realistically model the detector response, and to account for its specific configuration during the `g12` run period, the `GSIM` output is then fed to the `GPP` program, that smears signals to match the actual experimental resolution, and removes hits from detectors channels that were broken or inactive during the run. The `GSIM` output, corresponding to CLAS raw output, is then reconstructed through the `a1c` program, as done for the real data. Finally, the reconstructed events are subject to the same analysis procedure used to select exclusive $\gamma p \rightarrow p\pi^0\eta$ signal events from experimental data.

The CLAS acceptance is defined as the ratio between the number of *reconstructed* and *generated* events. The acceptance dependence on the beam energy and on the $\pi^0\eta$ invariant mass is obtained binning the data with respect to these variables, and taking the ratio of reconstructed to generated events in each bin:

$$\varepsilon(E_{beam}^i, M_{\pi^0\eta}^j) = \frac{N_{acc}^{i,j}}{N_{gen}^{i,j}}, \quad (5.10)$$

where i and j label, respectively, the photon beam energy bin and the $\pi^0\eta$ invariant mass bin.

5.2.1 MonteCarlo events generation

The detector acceptance calculated using Eq. 5.10 strongly depends on the shape of the distribution used to generate the pseudo-data fed to the MonteCarlo simulation. This effect is in particular related to the kinematic variables from which the acceptance is not dependent explicitly, that are integrated over. A modification of the corresponding distribution shape would change the number of reconstructed events, while leaving unchanged the number of generated ones, and would therefore result in a *different* acceptance value for the *same* E_{beam} , $M_{\pi^0\eta}$ bin.

It is thus necessary to perform the acceptance calculation generating pseudo-data according to a kinematic distribution that is as similar as possible to the *real* one for the reaction under study. Since the latter has to be extracted from the experimental yield, properly corrected for the detector response, this results in an iterative process. First, the detector acceptance is calculated using zero-order pseudo-data, generated according to a “reasonable” kinematic distribution. The first-order acceptance is used to correct the experimental event yield, and to obtain an estimate of the reaction kinematics distribution. These are finally used to generate a new set of pseudo-data, that is fed again to the MonteCarlo procedure. The iterative procedure ends when MonteCarlo *reconstructed* events well reproduce the main features of the data or, in other words, when the acceptance calculated in the $(i + 1)$ -th iteration is not significantly different from the result obtained in the i -th iteration.

In this analysis, the kinematic variables from which the acceptance is not dependent explicitly are: the momentum transferred $-t$, and the polar and azimuthal angles θ_{GJ} , ϕ_{GJ} of one of the two mesons in the Gottfried-Jackson frame. I verified that MonteCarlo events generated with a flat distribution of the latter two variables well reproduce the main characteristics of the real data.

The t -distribution, instead, is more critical and has to be properly accounted for, applying the iterative procedure described above. I started the acceptance calculation generating zero-order MonteCarlo events with a t -distribution of the form $A \exp -B \cdot t$, with $B = -3$, as suggested from the experimental data. However, since the data t -slope reflects the dominant reaction mechanism, this can vary in different regions of the $\pi^0\eta$ spectrum, or for different beam energies. For this reason, after correcting the results with the first-order acceptance, I derived the t -slope for the reaction $\gamma p \rightarrow p\pi^0\eta$ in different bins of E_{beam} and $M_{\pi^0\eta}$, obtaining the following dependence:

$$t_{slope} = 2.23 + 0.28 \cdot E_{beam}(GeV) - 1.56 \cdot M_{\pi^0\eta}(GeV/c^2) \quad (5.11)$$

MonteCarlo *reconstructed* events obtained from the second iteration well reproduce the experimental data in all the bins E_{beam} , $M_{\pi^0\eta}$, confirming that the t -slope derived from Eq. 5.11 reproduces the behaviour of real data in a suitable way for acceptance calculation. Figure 5.8 shows the comparison between real events and MonteCarlo reconstructed data for a particular bin.

5.2.2 Results

To calculate the CLAS acceptance $\varepsilon(E_{beam}^i, M_{\pi^0\eta}^j)$, I generated 150M MonteCarlo events, that resulted in 400k total reconstructed events, approximately ten times more than the number of real experimental data. I divided them in 9 bins of E_{beam} between 2.35 GeV and 5.5 GeV, and in 50 bins of $M_{\pi^0\eta}$ between 0.6 GeV/c² and 2.5 GeV/c², for a total of 450 kinematic bins where I calculated the detector acceptance using Eq. 5.10.

The results of the acceptance calculation are reported in Figure 5.9. In all kinematic bins, the CLAS acceptance for the reaction $\gamma p \rightarrow p\pi^0\eta$ is always lower than 1%. Increasing the beam energy, the acceptance grows, reaching its maximum at higher $M_{\pi^0\eta}$ values.

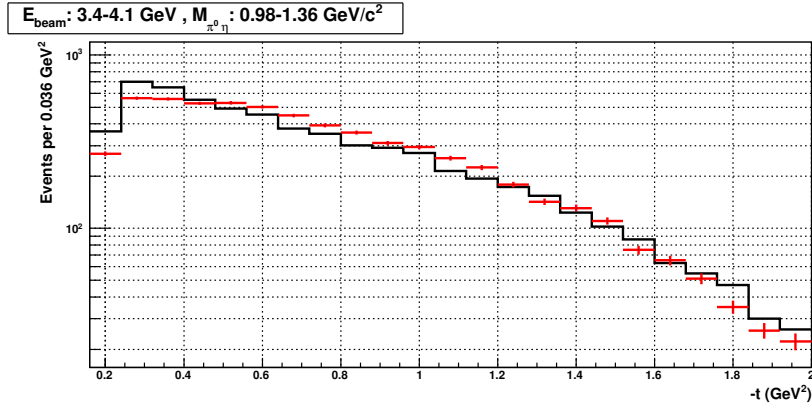


Figure 5.8: Comparison between t distribution of the experimental data (black) and of reconstructed MonteCarlo events (red) after the second iteration in the detector acceptance calculation, for a particular bin of E_{beam} and $M_{\pi^0\eta}$ as indicated in the histogram title. Both distributions are normalized to the same absolute number of events.

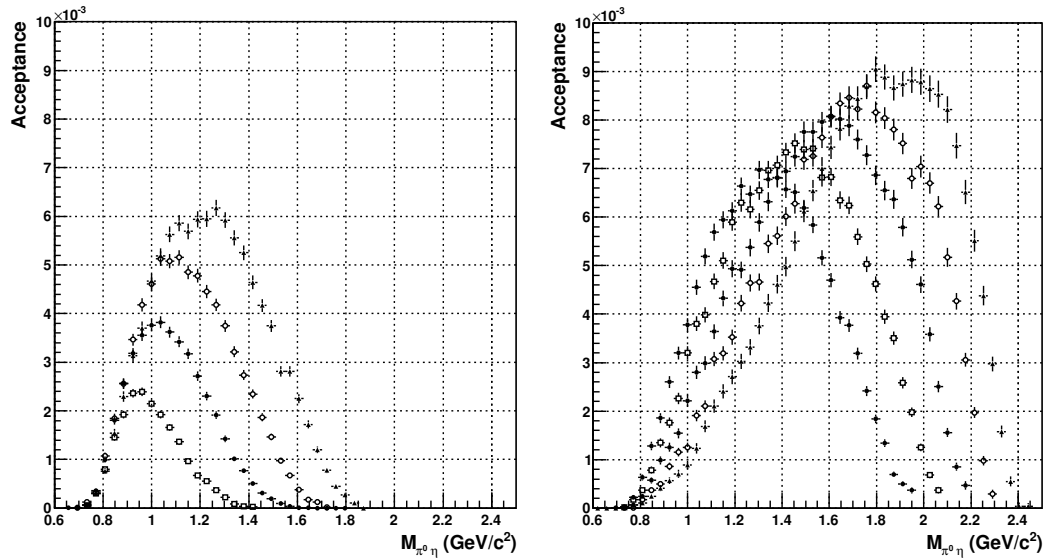


Figure 5.9: The CLAS detector acceptance for the reaction $\gamma p \rightarrow p\pi^0\eta$ as a function of the invariant mass of the $\pi^0\eta$ system, for different photon beam energies. Left panel: \square : 2.525 GeV, \bullet : 2.875 GeV, \circ : 3.225 GeV, \blacktriangle : 3.575 GeV. Right panel: \blacksquare : 3.925 GeV, \square : 4.275 GeV, \bullet : 4.625 GeV, \circ : 4.975 GeV, \blacktriangle : 5.325 GeV. All the photon energy bins have a 0.35 GeV width.

Kinematic variable	N_{bins}	Range (bin width)
E_{beam}	9	2.35 GeV - 5.5 GeV (0.35 GeV)
$M_{\pi^0\eta}$	50	0.6 GeV/c ² - 2.5 GeV/c ² (0.038 GeV/c ²)

Table 5.3: Kinematic bins used in the differential cross-section calculation.

I also used a MonteCarlo-based procedure to derive a correction factor that accounts for the momentum transferred cut, $0.2 < -t < 2.0$ GeV². In fact, to compute the reaction cross section, the experimental event yield must be extrapolated to the full t range. For each E_{beam} , $M_{\pi^0\eta}$ bin, the fraction α_t of MonteCarlo events *generated* in the accepted t -range respect to the total has been calculated. I assumed that data have the same fraction, since the MonteCarlo kinematic distribution was actually matched to *real* one. The number of measured events in each bin has then to be divided by this correction factor, other than by the detector acceptance, to obtain the proper event yield to be used in the cross-section calculation.

5.3 Reaction cross-section

The differential cross-section is calculated using the following equation:

$$\frac{d\sigma}{dM_{\pi^0\eta}^j} \Big|_{E_{beam}^i} = \frac{N_{evt}^{i,j}}{\varepsilon^{i,j} \cdot \alpha_t} \cdot \frac{1}{\Phi_\gamma^i} \cdot \frac{1}{\frac{N_{Av}}{A} Z \rho x} \cdot \frac{1}{\Delta M} \cdot \mathcal{C}_{tagger} , \quad (5.12)$$

where $N_{evt}^{i,j}$ is the number of measured events in the kinematic bin (E_{beam}^i , $M_{\pi^0\eta}^j$), $\varepsilon^{i,j}$ is the detector acceptance calculated for that bin and α_t the correction factor that accounts for the t -range cut in the analysis. Φ_γ^i is the integrated photon flux, for the specific beam energy bin. N_{Av} is the Avogadro number, and Z , A , ρ , x are, respectively, the target atomic number (2), atomic weight (2.02 g/mol), mass density (0.0707 g/cm³), and thickness (40 cm). ΔM is the width of the $\pi^0\eta$ invariant mass bins, 0.038 GeV/c². \mathcal{C}_{tagger} (1.15) accounts for excluded events having more than one “good” photon candidate hit in the Photon Tagger. The definition of the kinematic bins is reported in Tab. 5.3.

The integrated photon flux in the i -th beam energy bin corresponds to the number of photons N_γ^i that impinged on the target during the data taking. The photon flux, shown in Figure 5.10, was determined for g12 by means of sampling the “out-of-time” electron hits in the Photon Tagger, i.e. those hits measured in the tagger detector, but not matched in time to an hadronic event measured by CLAS [122].

Since final corrections to the absolute data normalization are still being discussed in the g12 run group, reported results are in arbitrary units. This does not preclude the extraction of the free parameters in the amplitude employed in the 12 GeV study of this reaction. In fact, what actually is needed in the MesonEx simulation is the *relative* weight of the different production amplitudes. The absolute normalization is fixed by the number of generated pseudo-events, that should resemble the expected statistics foreseen in the experiment⁴.

⁴To calculate the foreseen number of events in MesonEx, a reasonable estimate of the *total* reaction cross-section is required (see Sec. 6.2). I obtained this by integrating the differential cross-section, and applying a correction factor to the overall normalization. I estimated the correction factor by comparing the cross-section of well known-reaction that I obtained from the CLAS-g12 dataset to the corresponding results found in literature. The order of magnitude I got is:

$$\sigma(\gamma p \rightarrow p\pi^0\eta) \simeq 1 \mu\text{barn} \quad @ \quad s \simeq 5 \div 10 \text{ GeV}^2 \quad (5.13)$$

This is qualitatively in agreement with the result reported by the CB-ELSA experiment, extrapolated to the CLAS-g12 energy range[89].

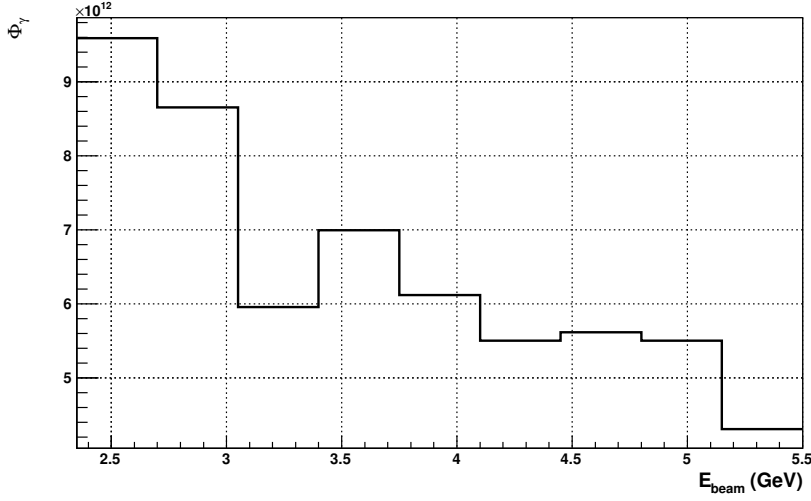


Figure 5.10: The integrated photon flux Φ_γ as a function of the beam energy E_{beam} for the **g12** data taking runs considered in this analysis. I used the **g12-gflux** program to calculate the flux in each bin.

Given this premise, the differential cross-section for the reaction $\gamma p \rightarrow p\pi^0\eta$, as a function of the the two mesons invariant mass, is reported in Figure 5.11. I calculated it trough Eq. 5.12, however, to avoid large statistical fluctuations, I excluded from the analysis those bins with less than 6 measured events. This resulted in a truncation of the differential cross-section at the $M_{\pi^0\eta}$ threshold and near its maximum value.

The behaviour of the differential cross-section strongly depends on the $M_{\pi^0\eta}$ value. From the threshold up to $\simeq 1.4 \text{ GeV}/c^2$ it is charaterized by two peaks, respectively near $1.0 \text{ GeV}/c^2$ and near $1.3 \text{ GeV}/c^2$, that are most likely related to production of the $a_0(980)$ and the $a_2(1320)$ resonances, both known to decay to the $\pi^0\eta$ final state.

The intensity and the relative weight of the two peaks depends on the beam energy. At low energy, $E_{beam} < 3 \text{ GeV}$, the $a_0(980)$ peak is well visible, and the $a_2(1320)$ signal appers only as a shoulder, while for higher energy the latter becomes more pronounced. Instead, at higher $M_{\pi^0\eta}$ values, the differential cross-section is smoother and exhibits a long tail, characterized by a shoulder at $\simeq 1.7 \text{ GeV}/c^2$, probably associated with the $a_2(1720)$ state, decreasing toward the $M_{\pi^0\eta}$ maximum.

5.4 Comparison with theoretical results

I compared the experimental cross-section for the reaction $\gamma p \rightarrow p\pi^0\eta$ measured with CLAS with the theoretical results predicted by Regge theory, presented in Chapter 4, to validate the corresponding production amplitude, and to tune free parameters before simulating the MesonEx experiment. These are the photon-resonance-Reggeon couplings $\beta_{\gamma,X}^R$ that appear in the resonant part of the amplitude, Eq. 4.27, for the $a_0(980)$, $a_2(1320)$, and $a_2(1700)$ states.

I first considered only the double Regge contribution, Eq. 4.33, that is expected to describe data at high $M_{\pi^0\eta}$, in the non-resonant region. The double Regge amplitude includes no free parameters, therefore the corresponding cross-section can be directly compared to the experimental data. The result is shown in Figure 5.12, with the red curve representing the double Regge cross-section,

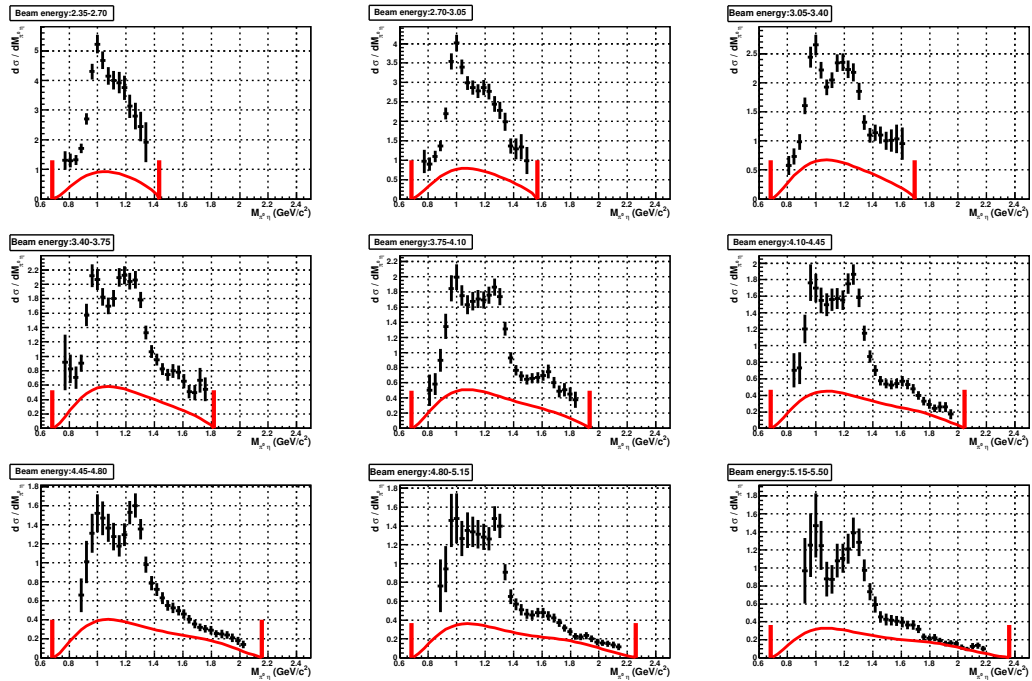


Figure 5.11: Differential cross-section for the reaction $\gamma p \rightarrow p\pi^0\eta$, as a function of the invariant mass of the $\pi^0\eta$ system. All the results are in arbitrary units, and the errors are only statistical. The photon energy bin limits, in GeV, is reported in the histogram titles. The vertical red lines show the allowed $M_{\pi^0\eta}$ kinematic range, calculated from the mean photon energy of each bin. The red curve is the theoretical prediction from the double Regge amplitude, scaled to the same cross-section units.

reported in the same arbitrary units through an overall scale factor. The agreement with the data is good for $M_{\pi^0\eta} \gtrsim 1.5$ GeV, and gets better increasing the photon beam energy. This proves that the double Regge amplitude well describes the high invariant mass data, in particular at high energy, and the corresponding parameters, obtained from other reactions by Regge factorization, are suitably tuned.

Also, the extrapolation of the double Regge cross-section to the low invariant mass region qualitatively confirms the duality argument. For $M_{\pi^0\eta} \simeq 1$ GeV, the reaction dynamics is characterized by the production of resonances, whose strength has, *on average*, the same order of magnitude of the extrapolated high-mass, non-resonant background.

To calculate the amplitude free parameters I proceeded as follows. First, I extracted from the data the total cross-sections for the three exclusive processes:

$$\begin{aligned}\gamma + p &\rightarrow p + a_0(980) \\ \gamma + p &\rightarrow p + a_2(1320) \\ \gamma + p &\rightarrow p + a_2(1700)\end{aligned}$$

Then I compared each result with the corresponding Regge theory prediction, Eq. 4.16, whose s -behaviour is only determined by the nature of the exchanged trajectories, and whose absolute value is directly proportional to the square of the Regge coupling to be determined.

I obtained the resonant cross-sections by performing a best-fit to the experimental data with a simplified version of the full reaction amplitude, adding the different resonances *incoherently*, and thus neglecting the possible interference between the two a_2 states, having the same J^{PC} quantum numbers. Then, I integrated each resonance contribution in the allowed mass range, to obtain the corresponding total cross-section, as a function of s .

To effectively parametrize the non-resonant background in the low-mass region, I tried different solutions, to see how sensitive the cross-sections extraction is to this variation, and to estimate the corresponding systematic effects on the extracted couplings. Each parametrization I tried followed these guidelines [123]:

1. It should converge to the double Regge expression at high invariant mass, where it is known and fixed.
2. It should have a smooth behaviour, without any sharp variations that would mimic a resonant contribution.
3. It should have an absolute strength lower than that of resonances, but with the same order of magnitude, as suggested from the duality arguments.

Among the different solutions, I obtained the best χ^2 by parametrizing the low-mass, non-resonant background intensity using the *same* double Regge expression that describes data at high invariant mass. I slightly modified it in the low-mass region, to better fulfil the last guideline, by scaling it through the following mass-dependent function:

$$f(M) = (1 + \alpha e^{-M/M_0}) \quad , \quad (5.14)$$

with α and M_0 free parameters to be extracted from the data. I also added a constant σ_0 smearing term to the fit, to account for the detector resolution. I fixed σ_0 to 20 MeV, as indicated from the MonteCarlo simulations. Finally, since the main goal of this comparison is to extract the Regge β couplings, and then to employ them in the MesonEx study of the $\pi^0\eta$ channel, at higher energy, I performed the fit considering only the 6 highest photon beam energy bins, where the resonant structures are more pronounced. I fit all bins simultaneously, leaving as free parameters the

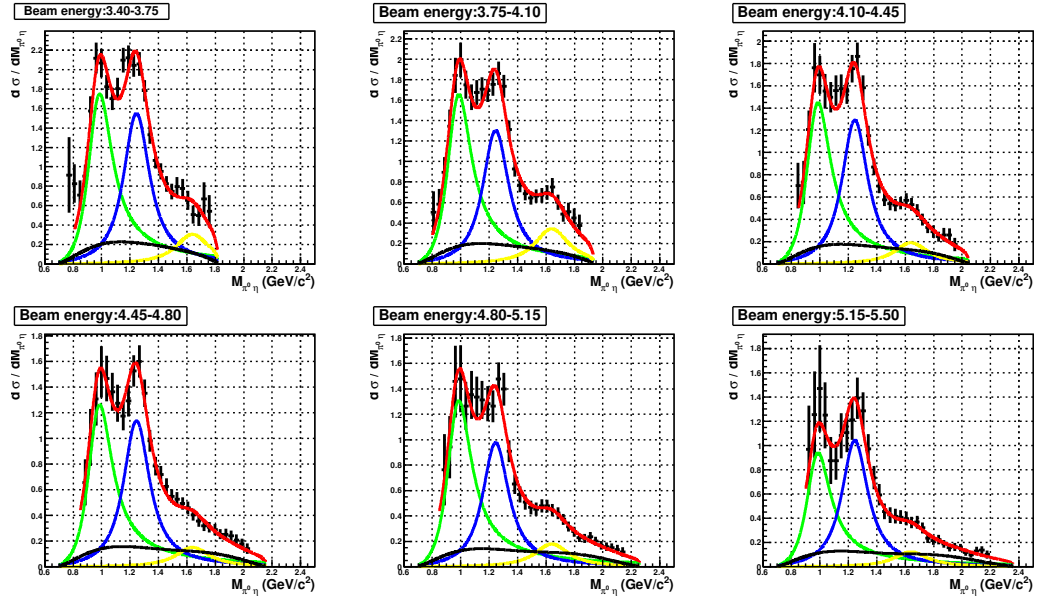


Figure 5.12: Comparison between experimental data and theoretical results. See text for the description of the different plotted curves.

resonance mass and widths, their intensity at each photon energy, and the background parameters α and M_0 , for a total of 27 free parameters.

The results are shown in Figure 5.12. The red line represents the fitted function, while the green, blue, and yellow curves are, respectively, the $a_0(980)$, $a_2(1320)$, and $a_2(1700)$ resonances alone. Finally, the black curve is the background contribution. The corresponding couplings that I obtained are reported in Tab. 5.4.

The fit consistency can be estimated, other than by looking at $\chi^2/NDF = 104.7/156$, by comparing the obtained resonance masses and widths to their “nominal” values, reported in the PDG. The three resonance masses are compatible with their nominal values within $\simeq 4\%$, while the widths are systematically larger, by a factor $\simeq 25\%$. This is, probably, due to a non-perfect cross-section parametrization, in particular in the incoherent states sum, or to residual background under the resonance peaks not properly parametrized. Finally, the systematic dependence of the couplings on the low-mass background parametrization, that I estimated varying its form, always following the three above guidelines, is $\simeq 15\%$.

Coupling	Value
$\beta_{\gamma a_0}^p$	(0.83 ± 0.03)
$\beta_{\gamma a_2}^p$	(2.08 ± 0.06)
$\beta_{\gamma a_2(1700)}^p$	(0.93 ± 0.03)

Table 5.4: Regge production couplings β , obtained from the fit of CLAS data. Errors are statistical only.

Chapter 6

Study of the reaction $\gamma^*p \rightarrow p\pi^0\eta$ in the MesonEx experiment

This Chapter presents the study of the reaction $\gamma^*p \rightarrow p\pi^0\eta$ performed in preparation for the MesonEx run. The goal was to obtain a preliminary estimate of the experimental sensitivity to a possible exotic state $J^{PC} = 1^{-+}$. This was evaluated by generating pseudo-data, projecting on the CLAS12 and Forward Tagger detector, and then performing a partial wave analysis of the reconstructed events, checking whether the reaction amplitude was correctly reconstructed. The procedure was then repeated by introducing different contributions in the generated pseudo-data, to check the sensitivity to the exotic wave.

The reaction amplitude constructed within the Regge theory framework, and the comparison to the experimental $\gamma p \rightarrow p\pi^0\eta$ data measured with the CLAS detector were presented in the two previous Chapters. Here, I present the MesonEx simulation results. First, I show the pseudo-events generation, the projection on the detector, and the acceptance calculation. Then, I discuss in detail the PWA results obtained from the different considered scenarios, differing by the exotic signal strength.

This work is intended to be the first step toward a systematic study of the above reaction in MesonEx, to be completed before the experimental run. Remaining issues are reported in the last section of this Chapter. It is worth mentioning that future work will clearly benefit from the use of the tools developed here.

6.1 AmpTools

I widely employed the AmpTools software both to generate pseudo-data according to the production amplitude, and to perform PWA fits to the reconstructed data. AmpTools, designed by H. Matevosyan, R. Mitchell, and M. Shepherd at Indiana University, is a collection of C++ libraries that are useful for performing unbinned maximum likelihood fits to data, using a set of interfering amplitudes [124]. It provides a set of routines that manage the technical aspects of performing fits to large sets of data, without imposing *any* constraints on the physics.

The AmpTools “core” is the `Amplitude` class. It contains the template of a physical amplitude involved in the process under study. On a general view, it is a mechanism to turn a set of four vectors describing an event into a complex number, representing the physics amplitude. The `Amplitude` class contains a pure-virtual method, `calcAmplitude(GDouble **pKin)`, that actually defines how the amplitude is calculated, given the particle four-vectors. The user has to write his

own amplitudes, overriding this method. The user also needs to specify how amplitudes have to be summed, i.e. coherently or not, and the free parameters to extract from the data.

The amplitudes describing the MesonEx low- Q^2 reactions are directly related to those of the corresponding photo-production processes, via the term $\mathcal{L}_{s,s'}^\lambda$ corresponding to the leptonic vertex (see also Section 4.4):

$$A = \sum_{\lambda} \mathcal{L}_{s,s'}^{\lambda} \cdot A_{photo}^{\lambda} \quad (6.1)$$

Since $\mathcal{L}_{s,s'}^\lambda$ does not depend on the specific reaction, I embedded it in the analysis framework. I introduced a new AmpTools class, the `Clas12PhotonsAmplitude`, that contains the $\mathcal{L}_{s,s'}^\lambda$ implementation, and overrides the `calcAmplitude` virtual method, as defined in the above equation. The user has to derive his amplitudes from this new class, providing the photo-production term A_{photo}^λ . This permits to use amplitudes specifically developed for photo-production reactions also in the MesonEx PWA framework, without any further modification.

6.2 Pseudo-events generation

The first step in the reaction study is the generation of pseudo-events, according to the reaction amplitude discussed in Chapter 4. This amplitude describes the full process $e^-p \rightarrow e^-p\pi^0\eta$, including the electron-scattering term $\mathcal{L}_{s,s'}^\lambda$ containing the quasi-real photon polarization information. It is therefore necessary to simulate the entire electro-production reaction, starting from a 11 GeV/c primary electron beam impinging on a hydrogen target, and generating genuine four-body final state events.

To have a realistic simulation, I estimated the expected number of events during the MesonEx run, proceeding as described in [125]. In the low Q^2 limit ($Q^2 \ll M_p^2$), the unpolarized differential reaction cross-section, with respect to the scattered electron angle Ω_e and energy E_e in the laboratory frame, is:

$$d\sigma(\Omega_e, E_e) = \sigma_\gamma(\nu) \cdot d\Gamma(\Omega_e, E_e) \quad , \quad (6.2)$$

with $\sigma_\gamma(\nu)$ the *total* cross section for the real photo-production reaction $\gamma p \rightarrow p\pi^0\eta$, being ν the virtual photon energy. The term $d\Gamma(\theta_e, E_e)$ is the equivalent flux of quasi-real photons, given by:

$$d\Gamma(\Omega_e, E_e) = \frac{\alpha}{4\pi^2} \frac{E_e}{E_0} \frac{\nu}{Q^2} \left[\frac{(2E_0 - \nu)^2}{\nu^2} + 1 \right] d\Omega_e dE_e \quad (6.3)$$

I calculated the *total* reaction cross-section by integrating numerically the photon flux in the kinematic range $2.5^\circ < \theta_e < 4.5^\circ$ and $0.5 \text{ GeV} < E_e < 4.5 \text{ GeV}$, corresponding to the Forward Tagger acceptance (see Tab. 2.3), and assuming $\sigma_\gamma(\nu) \simeq 1 \mu\text{barn}$, as estimated in the CLAS data analysis (see Sec. 5.3). The result is:

$$\Gamma \simeq 7 \cdot 10^{-4} \quad \rightarrow \quad \sigma_{tot} \simeq 7 \cdot 10^{-4} \mu\text{barn} \quad (6.4)$$

The corresponding event rate, at the CLAS12 nominal luminosity $10^{35} \text{ cm}^{-2} \text{ s}^{-1}$, is $R \simeq 70 \text{ events/s}$, resulting in $\simeq 500M$ produced events during the 80 day run of the MesonEx experiment¹.

¹ The equivalent real photon flux for a typical photo-production experiment (Bremmstrahlung beam on a $L_T = 40 \text{ cm}$ long liquid hydrogen target) that would give the same event rate is:

$$\Phi_\gamma = \frac{R}{L_T \cdot \rho_{LH_2} \cdot N_{Av} \cdot \sigma_\gamma(\nu \simeq 8 \text{ GeV})} = \frac{70 \text{ Hz}}{1.7 \cdot 10^{-6}} \simeq 4 \cdot 10^7 \gamma/\text{s} \quad (6.5)$$

This value is similar to what the GLUEX experiment is expecting to run with [38].

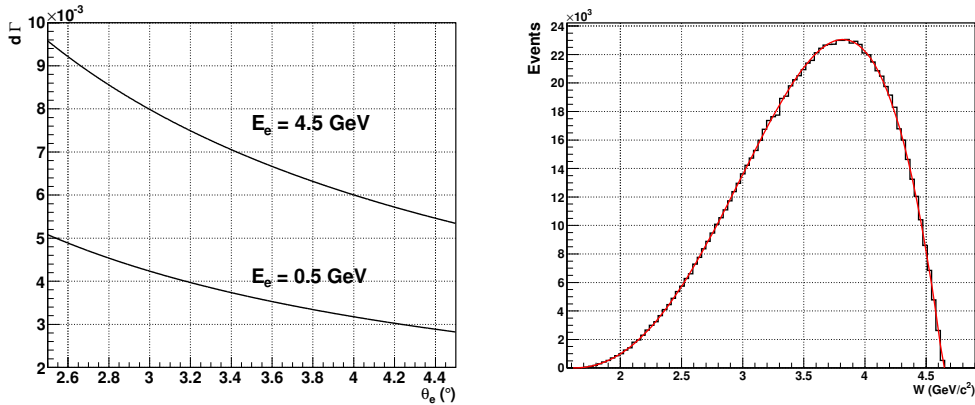


Figure 6.1: Left: Equivalent photon flux $d\Gamma$ as a function of the scattered electron angle, for two different energies. Right: the W distribution of phase-space inelastic events, obtained through GENBOD, with superimposed the fourth-order polynomial fit that I used to effectively parametrize it.

I employed the so-called “hit-or-miss” technique to generate these pseudo-data, according to the theoretical reaction intensity. First, a large set of events is generated according to a flat phase-space distribution. Then, the theoretical intensity I_i is calculated for each of them. Finally, if I_{max} is the maximum intensity for the generated events, each event is accepted with probability $P_I = I_i/I_{max}$. The resulting events are, by construction, distributed according to the theoretical intensity function I .

The main advantage of such a technique is that it is applicable independently on the analytical form of the corresponding amplitude, assuming it does not manifest any divergence in its domain. However, if the intensity has very strong variations over the phase-space, this method has a low computational efficiency.

6.2.1 Phase-space generator

Various algorithms exist to generate events for a $2 \rightarrow N$ reaction, according to a flat distribution, i.e. assuming a constant reaction amplitude over the whole final state phase-space. As an example, the ROOT framework [80] provides the class `TGenPhaseSpace`, based on the GENBOD algorithm [126], to generate N -body phase-space events, for N up to 18.

The use of these generators is very inconvenient for this specific analysis. In fact, the events of interest in MesonEx are those with the scattered electron within the geometrical acceptance of the Forward Tagger detector, $2.5^\circ < \theta_e < 4.5^\circ$ and $0.5 \text{ GeV} < E_e < 4.5 \text{ GeV}$, that represent only the $\simeq 1.3\%$ of the full available phase-space, for a primary 11 GeV/c electron beam impinging on a hydrogen target. `TGenPhaseSpace`, however, produces events over the whole phase-space, without the possibility to define a specific kinematic range. This would require to generate first a very large set of events, and then to keep only those of interest, resulting in a very low computational efficiency.

For this reason, I developed a specific phase-space event generator for the reaction $e^-p \rightarrow e^-p\pi^0\eta$, that employs the *inversion* algorithm to generate events with the scattered electron in the kinematic range of interest. I exploited the fact that the scattered electron angular distribution, in

	Custom	GENBOD	Performance ratio
Full phase space	53''	54''	$\simeq 1$
Limited phase space	54''	1260''	$\simeq 23$

Table 6.1: Performance comparison of the GENBOD and my custom phase-space generator, generating event over the full available phase-space (first line) and only in the kinematic range of interest (second line). Results refer to 1M events generated on a 2.4 GHz Intel processor machine.

the laboratory frame, *only* depends on the incident electron energy E_0 and on the target mass M :

$$\frac{dP}{d\Omega} = \frac{1}{4\pi} \frac{M(M + 2E_0)}{(M + E_0(1 - \cos\theta))^2} \quad (6.6)$$

This expression can be easily inverted to generate, event by event, the scattered electron only in the angular range of interest². Once the electron scattering angle is defined, its energy E_e is directly related to the $p\pi^0\eta$ system invariant mass W ,

$$W^2 = (M^2 + 2ME_0) - E_e(2M + 2E \cdot (1 - \cos\theta)) \quad (6.8)$$

$$(W_{min})^2 = (M^2 + 2ME_0) - E_e(2M + 2E_{max} \cdot (1 - \cos\theta)) \quad (6.9)$$

$$(W_{max})^2 = (M^2 + 2ME_0) - E_e(2M + 2E_{min} \cdot (1 - \cos\theta)) \quad (6.10)$$

The knowledge of the W distribution is therefore required to properly extract E_e . As explained in [127], this distribution depends only on E_0 and on the involved particles masses, and thus has to be calculated only once, before generating the events. However, its analytic expression involves an elliptic integral, that can not be written in a closed form. I therefore parametrized it in an effective way, through a simple fourth-order polynomial expression, that can be easily inverted and used to extract, event-by-event, W , and thus E_e .

Finally, once Ω_e , E_e , and W have been extracted, the four momenta of the final state hadrons are obtained from the “decay-like process” $W \rightarrow p + \pi^0 + \eta$, that I handled via the `TGenPhaseSpace` class. The performances obtained from this specific phase-space events generator, and those from GENBOD+rejection, are reported for comparison in Tab. 6.1.

6.2.2 Properties of generated events

The main features of the generated events for the reaction $\gamma^*p \rightarrow p + \pi^0 + \eta$ are here presented³. At this stage, the $J^{PC} = 1^{-+}$ exotic signal contribution is not included in the amplitude. The invariant mass of the $\pi^0\eta$ system is shown in Figure 6.2, left-panel, in the whole t -range. The two peaks corresponding to the $a_0(980)$ and to the $a_2(1320)$ states are clearly visible, as well as the pronounced $a_2(1720)$ shoulder. At high invariant mass, only a smooth background is present, related to the double Regge production mechanism. The extrapolation of the background to the lower invariant mass region has, *on average*, the same strength of the resonances contributions.

The left panel shows, instead, the t -distribution, for the whole invariant mass range, and for selected $M_{\pi^0\eta}$ values corresponding to the a_0 and a_2 peaks, and to the non-resonant background.

²This is performed by extracting a uniform random number u in the interval $[-1, 1]$, and then calculating $\cos\theta$ via:

$$\cos\theta = \frac{2u(E_0 + M) - M}{2uE_0 + M} \quad (6.7)$$

³All the results in this section refer to a reduced sample of data, corresponding to $\simeq 2.5\%$ of the total 500M statistics.

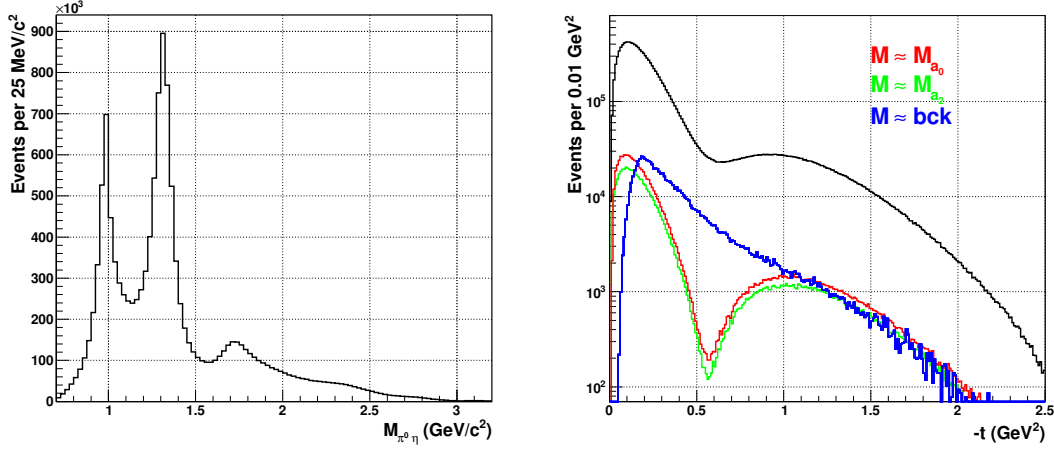


Figure 6.2: Left: invariant mass distribution of the $\pi^0\eta$ system for generated events. Right: generated events t -distribution, in the whole invariant mass range, and for selected $M_{\pi^0\eta}$ values. The background (blue) is evaluated at $M \simeq 2.0$ GeV/c^2 . The absolute normalization of the three colored histograms is arbitrary, to fit them in the same panel.

At low t -values, t -slope of resonances is more pronounced respect to the background, while for higher t they exhibit a similar trend. The dip near $t \simeq -0.6$ GeV^2 for resonant events is due to the Regge signature factor ξ in the production amplitude (see Eq. 4.27).

The angular distributions are reported in Figure 6.3. The left panel shows the correlation between the η polar angle, in Gottfried-Jackson frame, and $M_{\pi^0\eta}$. The characteristic resonances behavior are clearly seen, i.e. a flat band for the $a_0(980)$ and a fourth-order polynomial trend for the $a_2(1320)$ and $a_2(1700)$ states. The background, instead, exhibits a non-symmetric shape, peaked at forward angles. Finally, the right panel shows the correlation in between the η and the scattered electron azimuthal angles. The visible structures are related to the virtual photon polarization, whose polarization plane coincides, event by event, to the electron scattering one.

6.3 Detector simulation and acceptance evaluation

Pseudo-events were projected to the CLAS12+FT detectors, and then reconstructed. I considered, for both mesons, only the decay to two photons, as already done in the CLAS analysis (see Sec. 5.1).

Since the full CLAS12+FT simulation and reconstruction chain was not yet available, I used an “effective” MonteCarlo code to simulate the detector response. This accounts only for the detector geometrical acceptance and resolution, without including other effects, such as particles interaction with the detector materials, and the detection mechanisms. Each final state particle, i.e. the recoil proton, the scattered electron, and the four photons from π^0 and η decay, is projected individually on the detector. If it is within the nominal detector acceptance region, the four-momentum is smeared according to the expected resolution, otherwise it is discarded.

To reconstruct signal events, I employed the same algorithm developed for the CLAS analysis. I considered events with one proton, one electron, and four photons detected. Then, I applied the exclusivity cut on the K variable⁴. Finally, I selected events belonging to the $\pi^0\eta$ topology, by

⁴ K is defined as the difference between the proton missing mass squared and the four photons invariant mass

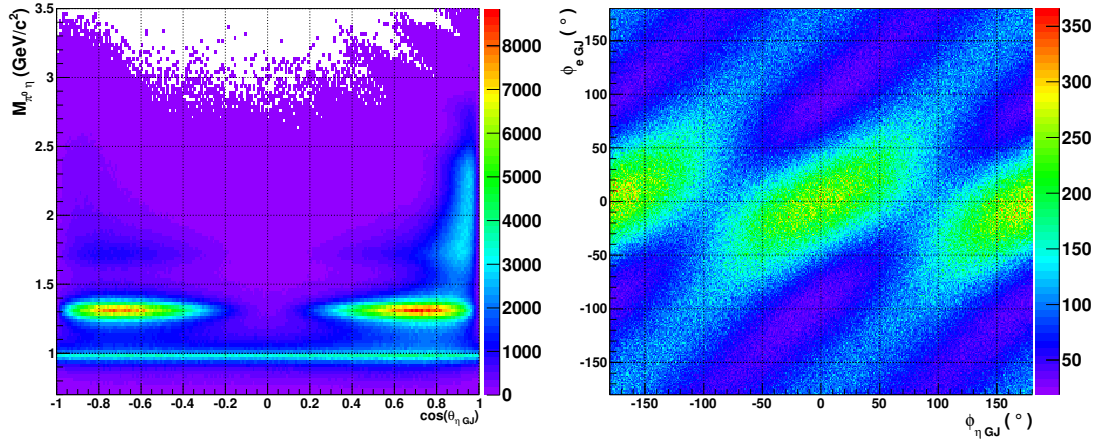


Figure 6.3: Left: η polar angle distribution in GJ frame, as a function of $M_{\pi^0\eta}$, for generated events. Right: correlation between η and e^- azimuthal angles, in GJ frame, for generated events.

looking at the invariant masses of photon pairs, properly ordered according to their relative angle in the laboratory frame.

In principle, since generated events do not contain the background contribution from other channels, all of them could be used, without necessity of any selection cut. However, the use of a realistic reconstruction algorithm, tested on real data, provides a more realistic analysis procedure that will be used in MesonEx.

Figure 6.4 shows the two mesons invariant mass spectrum for the reconstructed events. The resonances structures are still visible, while the high-mass non-resonant background is suppressed, for $M_{\pi^0\eta} > 2.5 \text{ GeV}/c^2$. The corresponding overall acceptance, from 0.7 to $3.0 \text{ GeV}/c^2$ of the $\pi^0\eta$ invariant mass, is $\simeq 3.0\%$, with a maximum of $\simeq 4.5\%$ at $1.2 \text{ GeV}/c^2$. This results in $\simeq 15M$ events expected during the 80 days of MesonEx run, from the $\simeq 500M$ produced.

The PWA procedure relies only on the angular distribution of the reconstructed events to extract the free parameters in the amplitude. It is therefore important to check that this is not too distorted by the detector acceptance. Qualitatively, this can be checked by looking at the reconstructed events and checking that the angular behaviour is still visible, as shown in Figure 6.5, left panel. The comparison with generated data (Figure 6.3) confirms that the main data features are preserved after the projection on the detector.

Another important test is to check if the asymmetries in the azimuthal angle, generated by the beam polarization, remains in despite the angular distribution distortion induced by the CLAS12 and FT acceptance and resolution. Figure 6.5, right panel, shows the correlation between ϕ_η and ϕ_{e^-} in GJ frame, that contains the information about polarization. The comparison shows that the structures in the azimuthal angle distribution, related to the beam polarization, are still present in the data after the projection on CLAS12+FT.

squared, see Eq. 5.6.

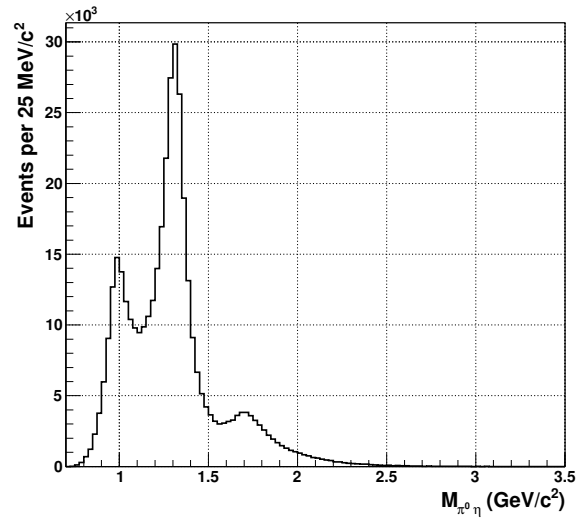


Figure 6.4: Reconstructed events invariant $\pi^0\eta$ mass spectrum.

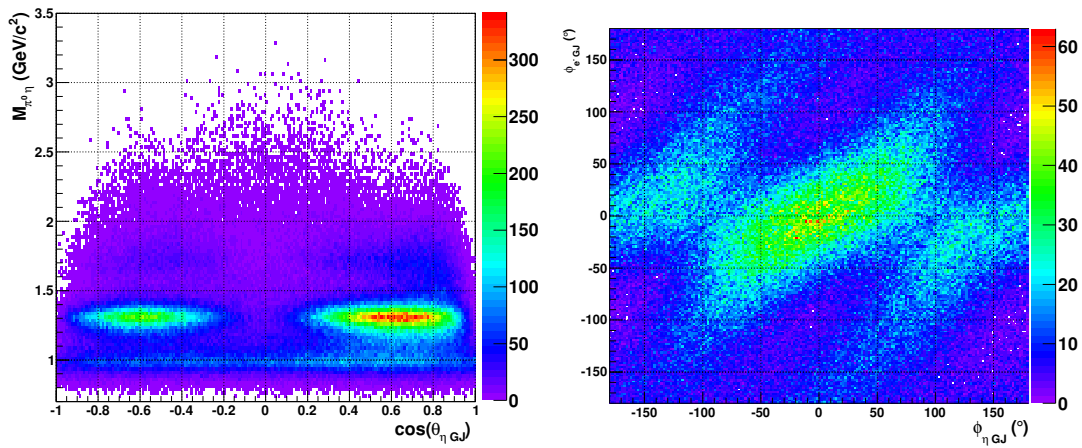


Figure 6.5: Reconstructed events angular distributions. Left: η polar angle distribution in GJ frame, as a function of $M_{\pi^0\eta}$. Right: correlation between η and e^- azimuthal angles, in GJ frame.

6.4 PWA procedure

I performed the PWA of pseudo-data using a procedure I derived from the analysis of CLAS data. I employed the high-invariant mass data to constrain the non-resonant background, and then I extrapolated the behavior to the low mass region.

To construct the intensity expression I made the following assumptions. First, I excluded contributions from states with $J \geq 3$, considering only the S , P , and D waves, as suggested by the previous analysis performed on this channel. Moreover, for each J , I only took the wave corresponding to the minimum spin-flip between the quasi-real photon and the $\pi^0\eta$ system. Finally, I parametrized the residual intensity via an incoherent background wave, having the same angular structure of the double-Regge contribution. The intensity expression is therefore:

$$I = |V^{0,0}Y_{0,0}(\mathcal{L}_+^{s,s'} - \mathcal{L}_-^{s,s'}) + V_+^{1,1}(Y^{1,1}\mathcal{L}_+^{s,s'} + Y^{1,-1}\mathcal{L}_-^{s,s'}) + V_+^{2,1}(Y^{2,1}\mathcal{L}_+^{s,s'} + Y^{2,-1}\mathcal{L}_-^{s,s'})|^2 + |V_{bck}A_{bck}|^2 \quad (6.11)$$

The intensity depends explicitly only on the angular variables of the two mesons system and of the scattered electron. The dependence on the other kinematic variables, in particular the $\pi^0\eta$ invariant mass, the momentum transferred t , and the photon-beam energy E_γ , are embedded in the production parameters V . Fits are thus performed in independent bin of E_γ , t , $M_{\pi^0\eta}$ to derive the dependence of the production parameters V on these kinematic variables.

One should note that, due to the explicit introduction of the background term A_{bck} , the intensity expression contains waves that are not orthogonal with each others. In particular, at low $M_{\pi^0\eta}$ values, the A_{bck} angular structure has a strong overlap with low partial waves. Increasing the two-mesons invariant mass, it instead exhibits a pronounced forward η peak, that suggests a projection over a larger set of angular momenta. In conclusion, a fit performed with the intensity expression in Eq. 6.11 over the whole invariant mass range would be ambiguous, preventing a proper estimate of the intensity leakage from one wave to another.

The procedure that I adopted to account for this problem is the following. I exploited the fact that, at high $M_{\pi^0\eta}$, the non-orthogonality is less pronounced, since only the background is present. Therefore, this region can be used to properly estimate the background contribution. Then, I extrapolated the results to the low $M_{\pi^0\eta}$ mass, fixing the background contribution, and not leaving the corresponding strength as a free parameter in the fit⁵. I verified the validity of this method performing a first, preliminary fit excluding the double-Regge background contribution, both in the generated pseudo-data and in the PWA intensity (see Sec. 6.5.1), comparing the results with those with the background included (see Sec. 6.5.3). The good agreement proofs that the PWA procedure works, and does not include significant systematic effects in the final results.

Events were divided in 72 $M_{\pi^0\eta}$ bins, from 0.7 to 2.5 GeV/ c^2 , each bin being 25 MeV/ c^2 width. Bins above 2.2 GeV/ c^2 were employed for the background estimation. The bin-width was a trade-off between the request to maintain large-enough statistics per bin, and the necessity to employ a fine-enough division to extract from the data the resonant properties, mostly related to this kinematic variable. Since resonances production is peaked at low t -values, I used a single t -bin, between -0.1 and -0.3 GeV/ c^2 . Finally, I considered together all the events in the whole E_γ range, between 6.5 GeV and 10.5 GeV.

In each bin, the PWA fit was independently performed, using random initial parameters. Also, I repeated the procedure many times (usually 3, and up to 6 for specific bins), taking as final result the solution with the highest likelihood.

A qualitative estimate of the fit goodness is given by the comparison of kinematic distributions from pseudo-data with those obtained by the PWA results. These are obtained by using the

⁵In practice, this required to fit the full intensity formula to the high-mass bins, calculate the mean value of the V_{bck} production factors, and use it as a fixed parameter in the low-mass fits. V_{bck} has no dependence from $M_{\pi^0\eta}$, since this is already embedded in the A_{bck} expression.

fitted production intensity to generate, in each bin, pseudo-events, through the same “hit-or-miss” technique already described before. The detector acceptance is explicitly taken into account, by working with a set of phase-space events already projected on the detector and reconstructed. The quality of the fit is then assessed by comparing the weighted and real data distributions. I went through this procedure at the end of each PWA fit, as quality check. An example is reported in Sec. 6.5.3.

6.5 PWA results

Here I report the results from the partial wave analysis of pseudo-data. To obtain a first estimate of the experiment sensitivity to a $J^{PC} = 1^{-+}$ exotic state, I repeated the procedure varying the production intensity of this state in the generated events.

6.5.1 Fit 0-a: no exotic contribution, no background

As explained above, the first test refers to a unphysical scenario without any background contribution included neither in the pseudo-data nor in the PWA intensity parametrization. This simplified case was used to verify that the overall fit procedure worked correctly. Also, I compared the results here obtained with those from the next case, where the background was properly included, both in the pseudo-data and in the PWA, to check that the procedure adopted to handle it was correct.

I performed the fit both on generated pseudo-events, not yet projected on the CLAS12+FT detector, and on reconstructed ones, to decouple effects in the PWA procedure from those induced by the detector acceptance and resolution. Results are reported in Figure 6.6, in terms of the event yield for each specific partial wave, and of their phase difference, as a function of $M_{\pi^0\eta}$. For direct comparison, I also show the results obtained by the analytic integration of the amplitude used to generate pseudo-events (see Eq.4.23 and 4.27).

The agreement of the PWA results with the theoretical expectation is good, both in terms of event yields and phase difference. No major distortions are induced by the detector, apart from the smearing of the resonance peaks due to the finite resolution, and a slightly different $S - D$ phase difference at very low $M_{\pi^0\eta}$ values. The deviation of data points from the predicted curve for $M_{\pi^0\eta} > 2 \text{ GeV}/c^2$ is irrelevant to the analysis, since the S and D waves intensity is negligible in this region.

Since no exotic $\pi_1(1400)$ contribution was introduced in the pseudo-data, the expected P wave event yield is zero. Non-zero results from the fit are due to the leakage from the dominant S and D waves. Leakage happens when the partial-wave basis is no longer orthogonal, typically due to the distortions induced by the non-uniform detector acceptance, or by the finite experimental resolution. When this occurs, events can have strong overlaps with more than one decay amplitude, and therefore produce intensity in a wave different from the right one.

Since the contribution of a possible 1^{-+} exotic signal is expected to be “small”, compared to those of the well-known resonance decaying to the $\pi^0\eta$ channel, i.e. the $a_0(980)$ and the $a_2(1320)$, it is crucial to estimate the leakage contribution from the non-exotic waves to the exotic one.

Generated events do not show leakage to the P - wave, being the results compatible with zero within the error in the whole invariant mass range. Some leakage to the P -wave is seen, instead, on the reconstructed event, at $M_{\pi^0\eta} \simeq 1 \text{ GeV}/c^2$. This contribution corresponds to $\simeq 0.1\%$ of the intensity of the $a_0(980)$ wave, dominating the intensity spectrum at $1.0 \text{ GeV}/c^2$. Finally, almost no leakage is seen in the mass region between 1.3 and $2.0 \text{ GeV}/c^2$, where the exotic contribution is expected.

In conclusion, the results obtained from this “simplified” case agrees with the theoretical prediction, thus confirming that the overall fit procedure works, and does not introduce any systematic

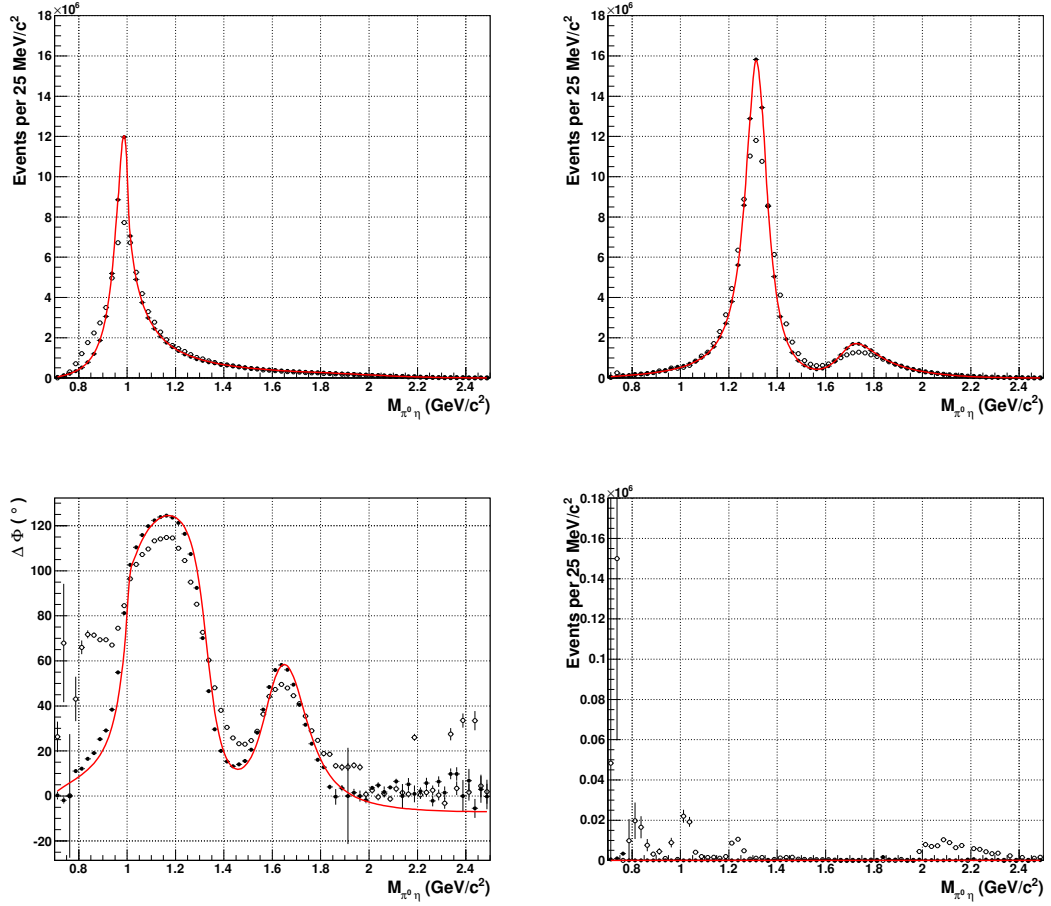


Figure 6.6: FIT 0-a, PWA results. Top: S -wave (left) and D -wave (right) event yield. Closed (open) circles refer to results obtained from generated (reconstructed) events, while the continuous red line is the analytical prediction from the amplitude, Eq. 4.23. Bottom left: phase difference between S and D wave. Bottom right: P -wave event yield. Note the difference in the y scale in between (S, D) and P waves results.

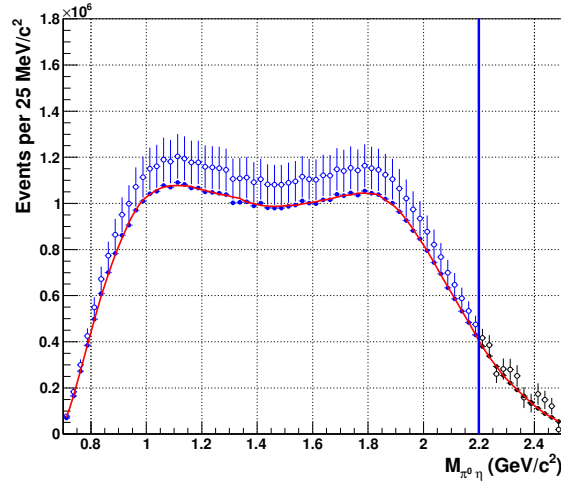


Figure 6.7: FIT 0-b, background estimate. Closed (open) circles refer to results obtained from generated (reconstructed) events, while the continuous red line is the analytical prediction from the amplitude, Eq. 4.23. Black points are those from the high-mass PWA fit, with free background strength, while blue ones are those in the low-mass region, with fixed background contribution.

effect in the amplitude reconstruction.

6.5.2 Fit 0-b: no exotic contribution

I performed a second fit on events generated including the double Regge background contribution. I evaluated the background contribution from the events in the invariant mass region above $2.2 \text{ GeV}/c^2$, performing the PWA fits where V_{bck} was a free parameter in the intensity formula. I used the average of the results to fix the background contribution in the lower invariant mass region. I repeated this procedure lowering the “mass-cut” down to $2.0 \text{ GeV}/c^2$, finding consistent $\overline{V_{bck}}$ values.

The results are shown in Figure 6.7, both for generated and for reconstructed events. Black points have been obtained from the high-mass PWA fits, where the background parameter is free, while blue ones are those from the low-mass PWA fits, with the background contribution fixed. The theoretical prediction from the amplitude is also reported for direct comparison. Not surprisingly, results from generated events agree with the theoretical curve, in the whole $M_{\pi^0\eta}$ range. Results from reconstructed events, instead, are compatible with the prediction within the errors, but show a systematic disagreement. In fact, the background wave event yield in the low mass bins is fixed, and proportional to $|\overline{V_{bck}}|^2$, evaluated from the high-mass data. Therefore, in each bin:

$$N_{bck} \propto |\overline{V_{bck}}|^2 \quad \rightarrow \quad \delta N_{bck} \propto 2 |\overline{V_{bck}}| \cdot |\delta \overline{V_{bck}}| \quad (6.12)$$

High mass results from reconstructed events (white points in Figure 6.7) are significantly higher than the theoretical prediction, and so their average, due to statistical effects in the PWA fits: this error translates to a *systematic* shift in the low-mass results.

After fixing the background contribution, I performed the PWA fits in the low invariant mass region. Results are reported in Figure 6.8, in terms of the event yield for each specific partial wave, and for the phase differences, as a function of $M_{\pi^0\eta}$. Again, for direct comparison, I also

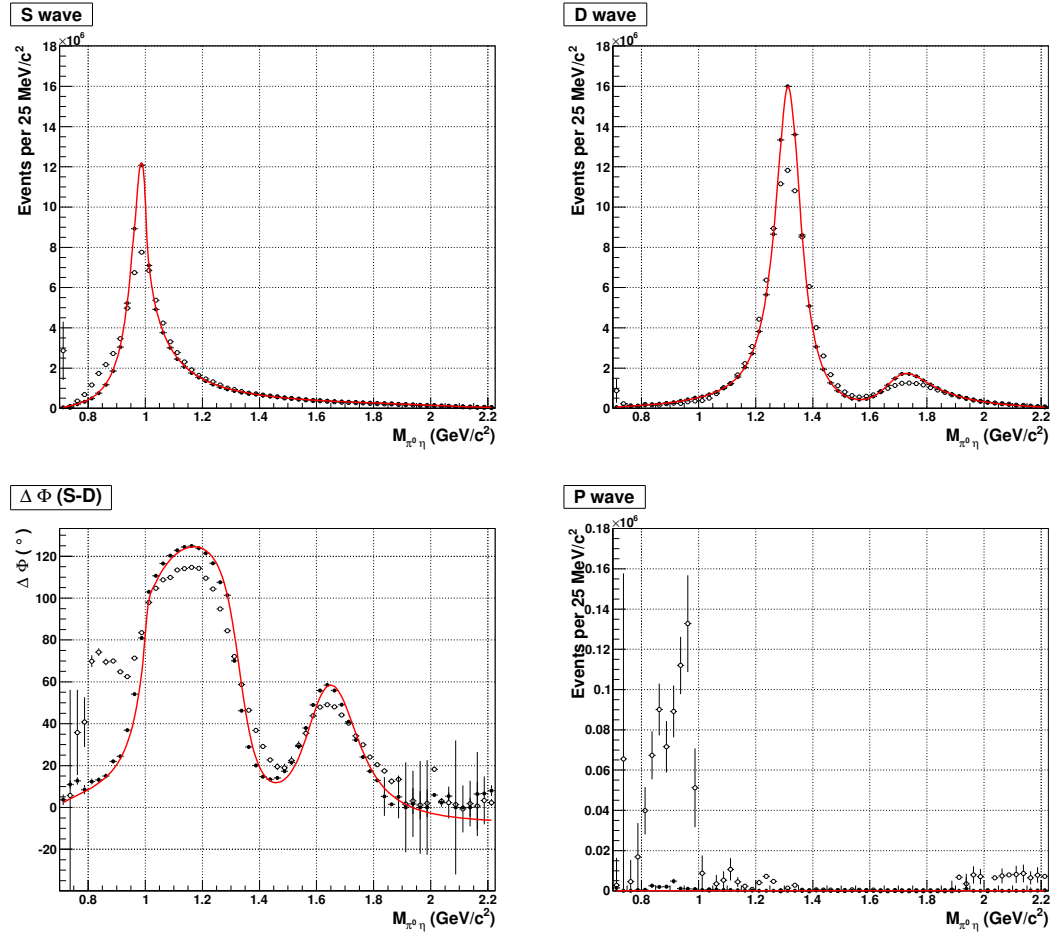


Figure 6.8: FIT 0-b, PWA results. Top: *S* wave (left) and *D* wave (right) event yield. Closed (open) circles refer to results obtained from generated (reconstructed) events, while the continuous red line is the analytical prediction from the amplitude, Eq. 4.23. Bottom left: phase difference between *S* and *P* wave. Bottom right: *P* wave event yield. Note the difference in the *y* scale in between (*S*, *D*) and *P* waves results. Results are shown in the “low-mass” region, below 2.2 GeV/c², where the background intensity is fixed.

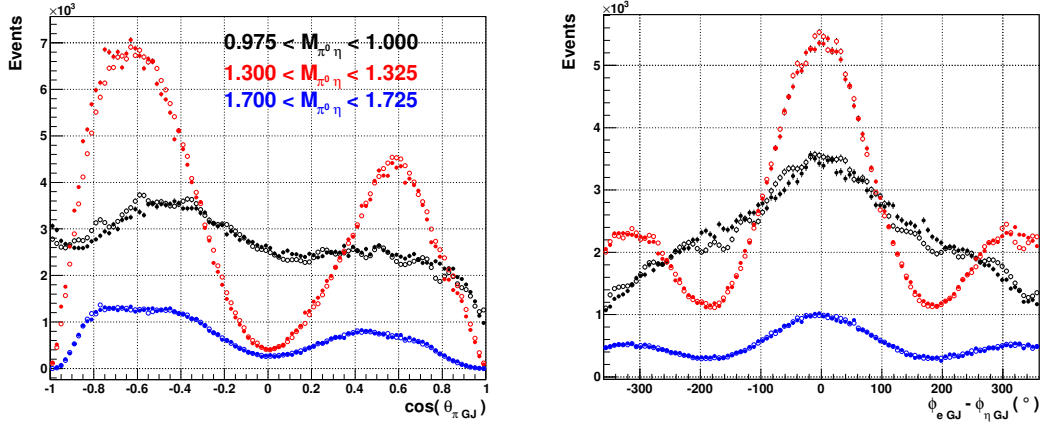


Figure 6.9: FIT 0-b, qualitative estimate of the fit goodness. Left: π angular distribution in GJ frame. Full circles: data (reconstructed events), open circles: fit prediction. The colors refer to different $M_{\pi^0\eta}$ intervals, as reported in the Figure. The red histogram normalization was scaled by a factor 2, to fit in the same panel. Right: $e^- - \eta$ azimuthal angles difference in GJ frame.

show the results obtained by the analytic integration of the Regge amplitude, used to generate pseudo-events. To evaluate the effect of the $\overline{V}_{bc\bar{k}}$ uncertainty on the S , P , D waves, I repeated the low-mass fits twice, fixing it at the nominal value, plus or minus the error. For S and D waves, this additional error was found to be negligible, with respect to the intrinsic statistical uncertainty of the production parameters obtained from the fit with the nominal $\overline{V}_{bc\bar{k}}$ value. For the P wave intensity, instead, it had the same order of magnitude of the statistical fluctuations.

Both the results obtained with generated and reconstructed events are compatible with the theoretical expectation, in terms of the event yields for different partial waves, and phase difference. In addition, they agree with those obtained from the previous scenario, where no background was included, confirming that the procedure I followed to deal with it is correct, and do not introduce any systematic effect in the final results.

The P -wave leakage seen at $M_{\pi^0\eta} \simeq 1$ GeV/ c^2 for reconstructed events is slightly larger than what was obtained from the previous case, while the two results agree in the invariant mass region above this value. The leakage is lower than 1% of the total S and D waves strength. This sets a limit to the experiment sensitivity for a possible low-mass exotic state with this mass and width.

Finally, I qualitatively verified the goodness of the fit by comparing significant pseudo-data kinematic distributions to the those obtained with the PWA, including the detector acceptance and finite resolution. Figure 6.9 shows the π angular distribution in the GJ frame, for three $M_{\pi^0\eta}$ values corresponding, respectively, to the $a_0(980)$, $a_2(1320)$, and $a_2(1700)$ peaks. In all cases, the agreement between the data and the fit prediction is good. The comparison for the azimuthal angles difference between the scattered electron and the η in the GJ frame is also shown.

6.5.3 Fit 1: 50% a_2 exotic contribution

In this case, I included in the generated pseudo-data an exotic $\pi_1(1400)$ contribution, with a total strength equal to the 50% of the $a_2(1320)$ cross-section. Clearly, this value corresponds to a very optimistic scenario, with the exotic signal produced with almost the same intensity as the “regular” resonances. However, it gives the possibility to verify the PWA procedure and to estimate

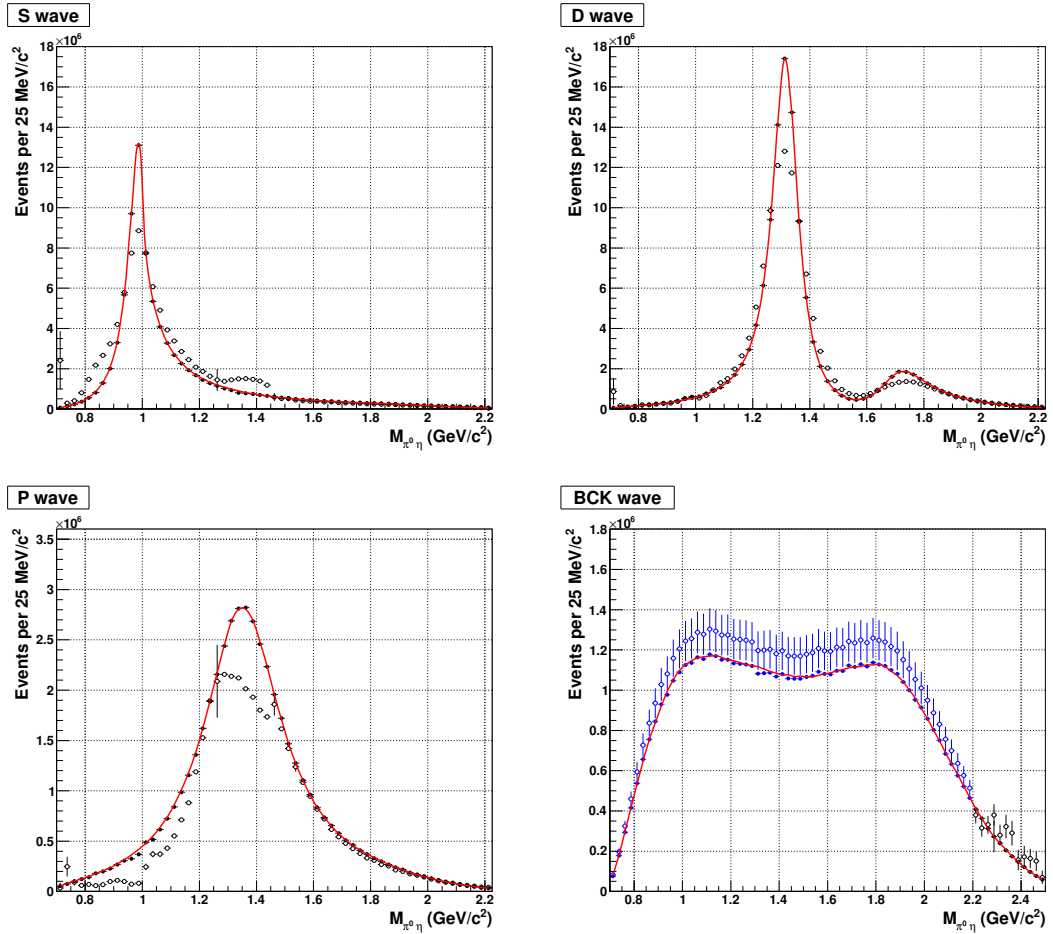


Figure 6.10: FIT 1, PWA results. Event yield for the different waves. Top: S wave (left) and D wave (right). Bottom: P wave (left) and background-wave (right). Closed (open) circles refer to results obtained from generated (reconstructed) events, while the continuous red line is the analytical prediction from the amplitude, Eq. 4.23. The color convention for the background wave is the same as in the previous case.

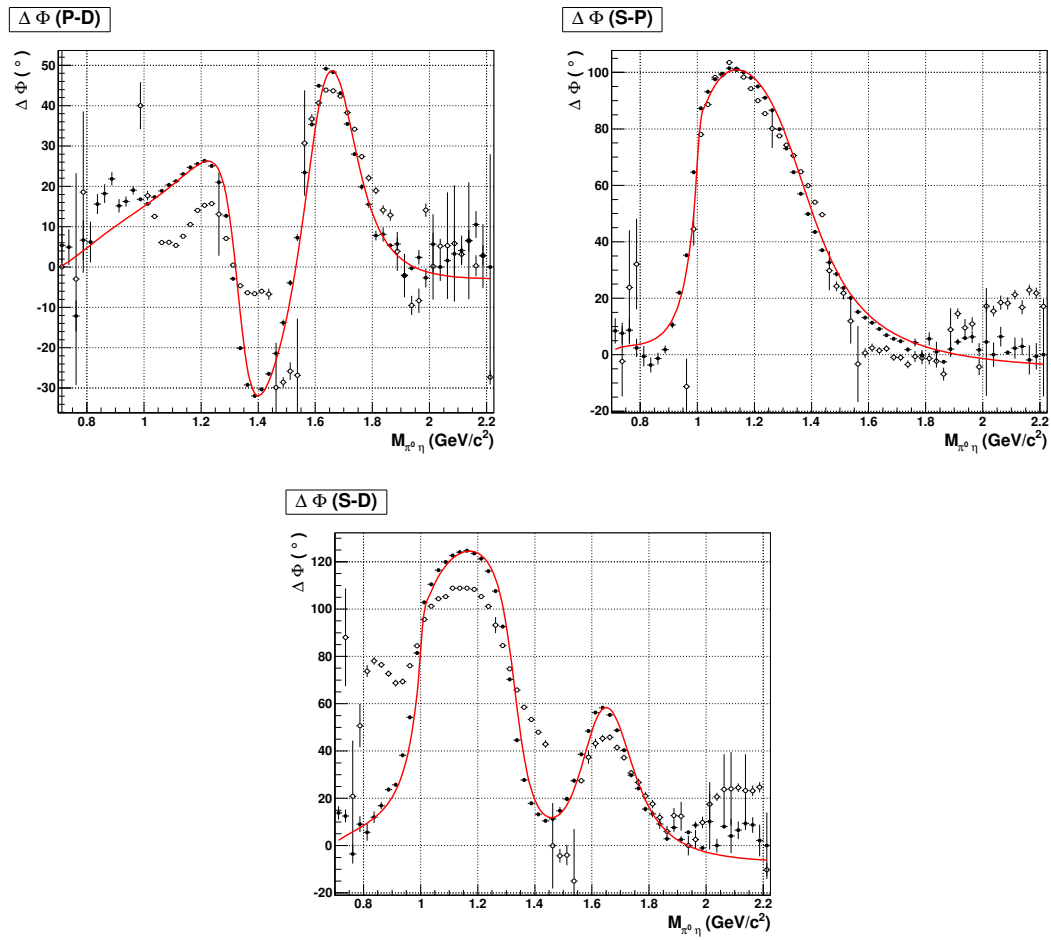


Figure 6.11: FIT 1, PWA results. S , P , and D waves relative phase differences.

the P -wave leakage to other waves. For the exotic mass and width, I used the values quoted in the PDG, obtained from the average of the results reported by past experiments: $M_{\pi_1} = 1.35 \text{ GeV}/c^2$ and $\Gamma_{\pi_1} = 0.33 \text{ GeV}/c^2$.

I treated the background below the resonances, in the low mass region, as in the previous case. I employed data in the high-mass region to constrain it, and then I extrapolated this result at the lower $M_{\pi^0\eta}$ values, employing the double Regge parametrization. I performed the PWA fits in the low mass region, to extract the S , P , and D waves intensities, and their phase differences.

Results, compared with the theoretical predictions, are shown in Figures 6.10 and 6.11. For the PWA fits performed on generated events, a very good overall agreement is seen, both for the non-exotic S and D waves and for the exotic P one. This confirms, once more, the reliability of the analysis procedure.

Results obtained from reconstructed events, which take into account detector effects, present instead more criticities, even if they are qualitatively in agreement with the amplitude predictions. In particular, the D wave intensity is reconstructed as the prediction from the amplitude, a part from the smearing introduced by the finite detector resolution.

The S and P wave results are, instead, more critical. Leakage from the P to the S wave is present at $M_{\pi^0\eta} \simeq 1.35 \text{ GeV}/c^2$, in correspondence of the $\pi_1(1400)$ mass and, less pronounced, at lower invariant mass too. This effect clearly manifest as a “shoulder” in the S wave intensity, and, correspondingly, as a distortion of the P wave peak, that reaches its maximum at a lower invariant mass, near $M_{\pi^0\eta} \simeq 1.3 \text{ GeV}/c^2$. Also the $P - D$ and $S - D$ phase differences are affected by the leakage and show, at these mass values, a discontinuity with respect to their neighborhoods. The $S - P$ phase difference, instead, is not altered by this effect, and well reproduces the theoretical curve. Finally, results above $M_{\pi^0\eta} \simeq 1.5 \text{ GeV}/c^2$ do not show any significant leakage effect.

In conclusion, if an exotic signal would be produced with 50% of the total $a_2(1320)$ cross-section, with this mass and width, the MesonEx experiment will be definitively capable to observe and identify it. However, leakage could introduce systematic effects in the extraction the exotic resonance properties.

6.5.4 Fit 2: 5% a_2 exotic contribution

The last case I considered foresaw an exotic signal contribution with a total strength in the $\pi^0\eta$ channel equal to the 5% of the $a_2(1320)$ cross-section. The mass and width values are those already employed in the previous case. This scenario corresponds to a very small $\pi_1(1400)$ exotic signal, that definitively is not visible as a structure in the two mesons invariant mass spectrum, and requires a full PWA to be extracted. I treated the non-resonant background as in the previous two cases, evaluating the contribution at high invariant mass, and then using the result to fix it in the lower mass region.

As expected, all the waves are correctly reconstructed from the generated data, i.e. when the detector acceptance and resolution effects are not included in the simulation.

When these are explicitly considered, instead, some problems arise, as already seen from the previous case. S and D waves intensities are correctly reproduced, a part from the resolution-induced smearing of the resonance peaks. The P to S leakage effect is not visible anymore, since the P wave intensity is much lower than the S one. Also, the $S - D$ phase difference is qualitatively in agreement with the prediction from the amplitude, and is similar to what obtained in the Fit-0b case (no exotic present in the data).

The reconstructed P wave is in general agreement with the theoretical curve, but presents more criticities. The intensity is significantly distorted by the the S wave leakage, since the strength of this effect has, almost, the same order of magnitude of the P wave intensity itself. Also, the $S - P$ and $P - D$ phase differences, despite showing a variation that reproduces the

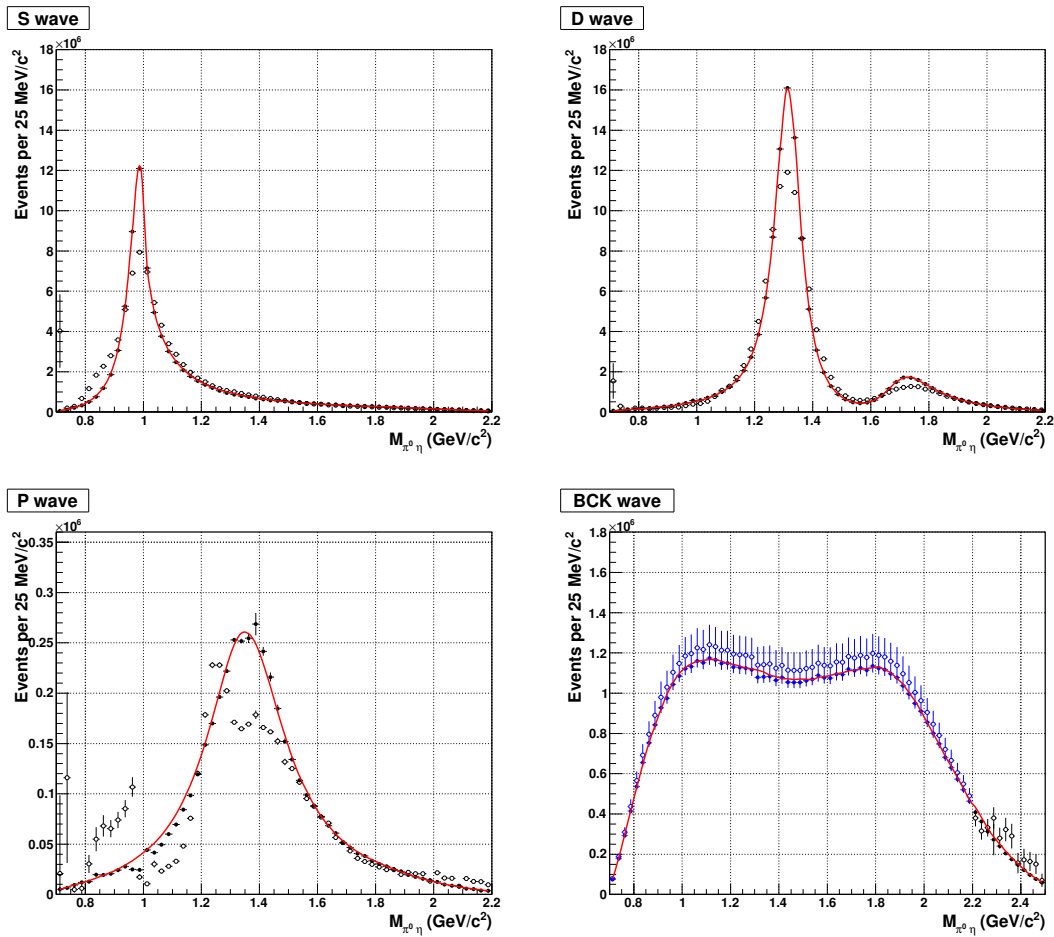


Figure 6.12: FIT 2, PWA results. Event yield for the different waves. Top: *S* wave (left) and *D* wave (right). Bottom: *P* wave (left) and background-wave (right). Closed (open) circles refer to results obtained from generated (reconstructed) events, while the continuous red line is the analytical prediction from the amplitude, Eq. 4.23. The color convention for the background wave is the same as in the previous case.

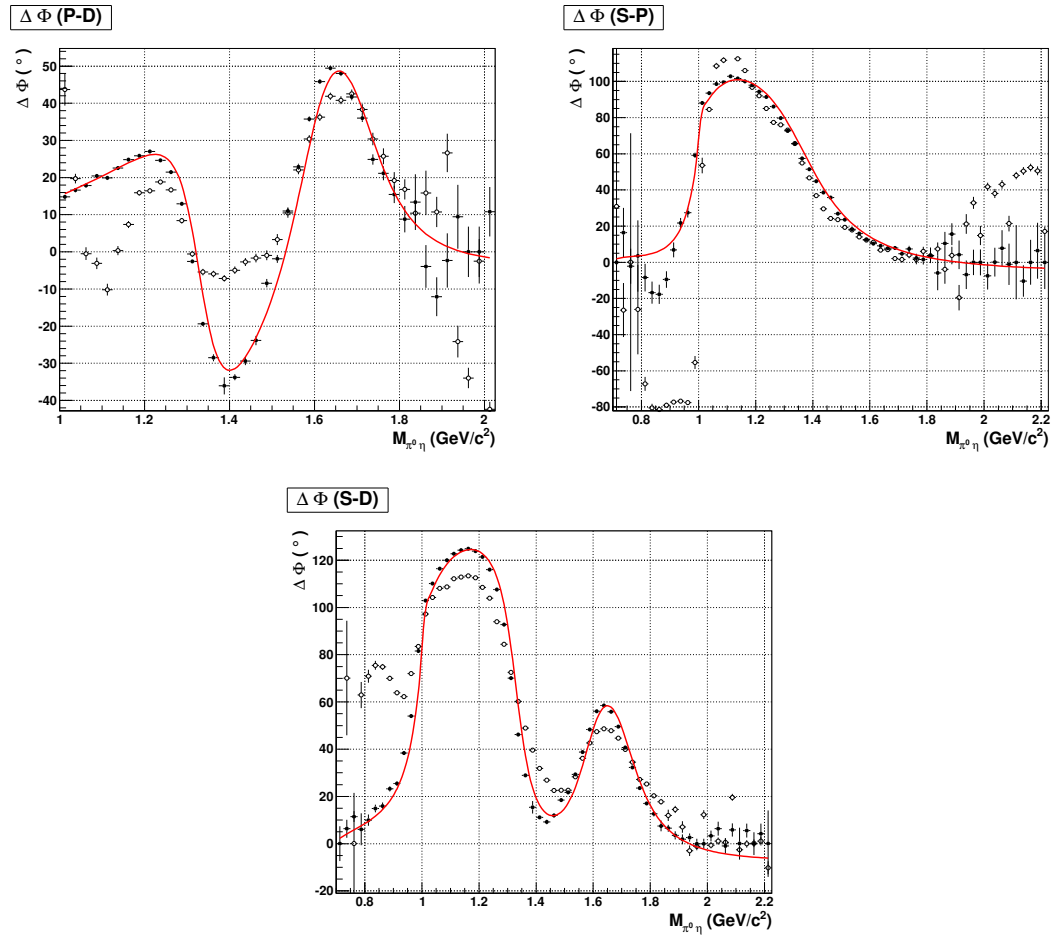


Figure 6.13: FIT 1, PWA results. S , P , and D waves relative phase differences.

theoretical one, manifest important distortions, respectively near 0.9 GeV/c² and 1.4 GeV/c², i.e. in correspondence of the $a_0(980)$ and $a_2(1320)$ nominal masses.

In conclusion, a $\pi_1(1400)$ produced with a cross section equal to the 5% of the $a_2(1320)$ strength, mass $M_{\pi_1} = 1.35$ GeV/c², and width $\Gamma_{\pi_1} = 0.33$ GeV/c², seems to be close to the sensitivity limit of the MesonEx experiment. Unambiguous indications of the exotic resonance are present in the data, but systematic effects would probably make difficult the correct determination of its properties, i.e. the mass, the width, and the strength, using a mass-dependent fit.

6.6 Summary and future perspectives

The obtained results show, at least qualitatively, that a full PWA of the reaction $\gamma^*p \rightarrow p + \pi^0 + \eta$ in the MesonEx experiment is feasible. The sensitivity to a possible exotic 1^{-+} $\pi_1(1400)$ meson was verified, for an overall production strength equal to 5% of the $a_2(1320)$ total cross-section. If the production strength is much lower than this value, systematic effects, such as waves leakage, would have a significant role in the waves reconstruction, and could prevent the clear identification of such a state.

Clearly, the study here presented is just exploratory. Other than giving a preliminary estimate of the experiment performances and capabilities, it served as the basis to develop all the tools and algorithms to perform the real data analysis.

Before the experimental run, a more detailed and systematic work on this channel has to be performed. In particular, the points that need to be addressed are the following:

- In this analysis, I treated the non-resonant background by employing the data in the high invariant mass region, and then extrapolating the obtained results in the low mass region, where it was fixed. I employed the same background parametrization in both regions, since this was the function used to produce the pseudo-data, in the whole kinematic range. This procedure was motivated by duality arguments, that connect the two invariant mass regions, and was already used, in a simplified way, for the CLAS data analysis.

However, in the real MesonEx data analysis, it would not be correct to use the double Regge formula *also* at low $M_{\pi^0\eta}$, where resonances lie, and to consider the low-mass background via a separate wave. The intensity should be parametrized only using spherical harmonics, adding to each of them a proper background contribution. Then, one should compare the two kinematic regimes, and use duality arguments, in the form of finite energy sum rules, and continuity in between the two regions, to check a-posteriori the results.

- The effect of the inclusion of more waves in the fit must be checked, taking care of the possible ambiguities, that could arise when the wave set grows. This extension is required because, even if no major resonances are expected, the background contribution on higher angular momenta could be not negligible.
- After the determination of the production parameters in independent $M_{\pi^0\eta}$ bins, the mass-dependent fit of the PWA results has to be performed, to verify also quantitatively that the masses and width of the simulated states can be retrieved.
- A complete systematic study of the experiment sensitivity to a 1^{-+} exotic state requires to vary also the resonance mass and width, other than its production strength. In fact, also these parameters are a priori unknown, and results reported by past experiments show a large range of possible variation.

- The CLAS12+FT detector introduces a distortion in the generated waves. Since the acceptance is not uniform in the t and E_γ kinematic variables, also different kinematic bins should be considered, and the corresponding detector-induced effects investigated, to see if this information can be useful in the analysis.
- The effect of the accumulated statistics must be investigated, to verify if it is the limiting factor to explore low coupling values, or, instead, other systematic effects, such leakage, are dominating.

Conclusions

This work was done as part of the MesonEx experiment, that will run in 2016 in Hall B of Jefferson Laboratory. The goal of the experiment is to perform a comprehensive study of the meson spectrum in the light quark sector, searching for rare and exotic states, with precise determination of masses and properties. Mesons are the simplest quark bound system and, therefore, the ideal benchmark to study the interaction between quarks, understand what the role of gluons is, and investigate the origin of color confinement. Meson spectroscopy is a unique tool to investigate how QCD partons manifest themselves under the strong interaction at the energy scale of the nucleon mass: a clear understanding of the non-perturbative regime is necessary, since in this condition we have the dominant manifestation of the strong force, binding quarks in hadrons constituting the bulk of the visible mass of the universe.

MesonEx will use low Q^2 electron scattering on a hydrogen target, providing an intense beam of high energy, linearly polarized, quasi-real photons. This technique has recently been suggested, by theoretical calculations, as an ideal probe for the production of unconventional meson states. The CLAS12 detector will be used to detect final state hadrons, while the electron scattered at low angle will be measured with a new, dedicated, facility: the Forward Tagger.

In preparation for the MesonEx experiment, a detailed study of the reactions that will be measured is required. The goal is to develop the necessary analysis tools, and then to verify that a Partial Wave Analysis is feasible, estimating the sensitivity to possible exotic states.

In this work, I investigated the reaction $\gamma^*p \rightarrow p + \pi^0 + \eta$. This is one of the experiment “golden-channels”, where a $\pi_1(1400)$ exotic state has been reported by past experiments, but is still missing a final confirmation. The study was performed by means of MonteCarlo simulations. The amplitude employed to generate pseudo-data was developed within the framework of Regge theory for high energy scattering. It was validated by comparing the predictions to the lower energy experimental data measured with the CLAS detector in the CLAS-g12 experiment.

The results confirmed that a full PWA of this reaction can be carried out within the MesonEx experimental framework. I obtained a preliminary estimate of the experiment sensitivity to a possible $\pi_1(1400)$ exotic state, that could be detected in MesonEx for a total production strength greater than 5% of the total $a_2(1320)$ cross-section.

In parallel to the analysis activity, I participated in the design of the Forward Tagger Calorimeter (FT-Cal), the “core” component of the Forward Tagger facility. It will detect electrons scattered in the angular range between 2.5° and 4.5° , and energy between 0.5 and 4.5 GeV, with an expected energy resolution of the order of 1%, and almost 100% efficiency. It will be installed in CLAS12 around the beam-line, in a region with a high magnetic field, reduced available space, and a high radiation field. To fulfill these constrains, and to meet the physics requirements, we designed a homogeneous calorimeter, made of 332 lead tungstate (PbWO_4) scintillating crystals, each coupled to an Avalanche PhotoDiode (APD), arranged symmetrically around the beamline.

As a first step, all the detector components needed to be characterized, to verify the compatibility with the requirements. This was performed through a series of dedicated measurements, in different

laboratories (Genova, CERN, Giessen University). At present, all the different components have been individually characterized, and are ready to be mounted in the FT-Cal.

Then, we built two prototypes, with 9 and 16 channels respectively, to validate the technical choices, and to demonstrate the detector capabilities. We measured the response to cosmic rays and to electromagnetic showers, at different facilities (Genova, JLab, BTF@LNF), finding consistent results with MonteCarlo simulation predictions.

As a result of this work, the Forward Tagger Calorimeter design has now been finalized, and the detector construction is in progress. The calorimeter is expected to be ready and operational in Spring 2014, when the first tests with cosmic rays are planned.

Appendix A

Leptonic vertex term in the low Q^2 reactions amplitudes

The amplitudes for the low Q^2 electron scattering reactions measured in MesonEx are written as the product of two factors. The first is related to the electron vertex of the OPE diagram, while the second describes the corresponding “quasi-real” photo-production process:

$$A = -i e^2 \sum_{\lambda=-1}^1 \left(\frac{1}{Q^2} \bar{u}(p', s') \gamma^\mu u(p, s) \varepsilon_\mu^*(q, \lambda) \right) \cdot (\varepsilon_\nu(q, \lambda) J^\nu) \equiv \mathcal{L}_\lambda^{s, s'} \cdot A_{photo}^\lambda \quad , \quad (\text{A.1})$$

where:

- p, p', q are the beam and the scattered electron momenta,
- s, s' are the beam and the scattered electron helicities,
- $q = p - p'$ is the virtual photon momentum,
- λ is the virtual photon helicity.

The explicit expression of the electron scattering term $\mathcal{L}_\lambda^{s, s'}$ term is here reported. I work in the Gottfried-Jackson reference frame, where:

$$\begin{aligned} q^\mu &= (E_\gamma; 0, 0, P_\gamma) & p^\mu &= (E; P \sin(\theta) \sin(\phi), P \sin(\theta) \cos(\phi), P \cos(\theta)) \\ Q^2 = -q^2 &= P_\gamma^2 - E_\gamma^2 & p^{\mu'} &= (E'; P' \sin(\theta') \sin(\phi'), P' \sin(\theta') \cos(\phi'), P' \cos(\theta')) \end{aligned} \quad (\text{A.2})$$

The three virtual-photon polarization vectors are [128, 129]:

$$\varepsilon^\mu(\lambda = \pm 1) = \frac{1}{\sqrt{2}}(0; \mp 1, -i, 0) \quad \varepsilon^\mu(\lambda = 0) = \frac{1}{\sqrt{Q^2}}(P_\gamma; 0, 0, E_\gamma) \quad (\text{A.3})$$

These are normalize to have:

$$q \cdot \varepsilon_\lambda = 0 \quad \text{and} \quad \varepsilon_\lambda \cdot \varepsilon_{\lambda'}^* = (-1)^\lambda \delta_{\lambda \lambda'} \quad (\text{A.4})$$

and satisfy the completeness relation:

$$\sum_{\lambda=-1,1} \varepsilon_\lambda^\mu \varepsilon_{\lambda'}^{\nu*} - \varepsilon_0^\mu \varepsilon_0^{\nu*} = -g^{\mu\nu} - \frac{q^\mu q^\nu}{Q^2} \quad (\text{A.5})$$

When this expression is contracted with a conserved current J^μ , like the electromagnetic current of the electron, the longitudinal term does not contribute since:

$$k_\mu J^\mu = 0 \quad (\text{A.6})$$

and in the calculation one can only use $-g_{\mu\nu}$.

The incident and scattered electron spinors are¹:

$$u(p^\mu, +) = \sqrt{E+m} \begin{pmatrix} \cos(\theta/2) \\ e^{i\phi} \sin(\theta/2) \\ \frac{p}{E+m} \begin{pmatrix} \cos(\theta/2) \\ e^{i\phi} \sin(\theta/2) \end{pmatrix} \end{pmatrix} \quad \bar{u}(p^\mu, -) = \sqrt{E+m} \begin{pmatrix} -e^{-i\phi} \sin(\theta/2) \\ \cos(\theta/2) \\ \frac{-p}{E+m} \begin{pmatrix} -e^{-i\phi} \sin(\theta/2) \\ \cos(\theta/2) \end{pmatrix} \end{pmatrix} \quad (\text{A.7})$$

Given these conventions, the explicit expression of the electron scattering term $\mathcal{L}_\lambda^{s,s'}$ is:

$$\begin{aligned} \mathcal{L}_\lambda^{s,s'} &= -ie^2/Q^2 \cdot \mathcal{F}_\lambda^{s,s'} \\ \mathcal{F}_{s=s'=+}^+ &= \sqrt{2EE'} e^{-i\phi'} \cos(\theta/2) \sin(\theta'/2) \\ \mathcal{F}_{s=s'=-}^+ &= \sqrt{2EE'} e^{-i\phi'} \sin(\theta/2) \cos(\theta'/2) \\ \mathcal{F}_{s \neq s'}^+ &= 0 \\ \mathcal{F}_{s=s'=+}^- &= -\sqrt{2EE'} e^{i\phi'} \sin(\theta/2) \cos(\theta'/2) \\ \mathcal{F}_{s=s'=-}^- &= -\sqrt{2EE'} e^{i\phi'} \cos(\theta/2) \sin(\theta'/2) \\ \mathcal{F}_{s \neq s'}^- &= 0 \\ \mathcal{F}_{s=s'=+}^0 &= -2 \frac{\sqrt{EE'}}{\sqrt{Q^2}} e^{-i\phi'} (e^{i\phi'} (E_\gamma - P_\gamma) \cos(\theta/2) \cos(\theta'/2) - e^{i\phi'} (E_\gamma + P_\gamma) \sin(\theta/2) \sin(\theta'/2)) \\ \mathcal{F}_{s=s'=-}^0 &= -2 \frac{\sqrt{EE'}}{\sqrt{Q^2}} e^{-i\phi'} (e^{i\phi'} (E_\gamma - P_\gamma) \cos(\theta/2) \cos(\theta'/2) - e^{i\phi'} (E_\gamma + P_\gamma) \sin(\theta/2) \sin(\theta'/2)) \\ \mathcal{F}_{s \neq s'}^0 &= 0 \end{aligned} \quad (\text{A.8})$$

¹ I work in the so-called ‘‘helicity’’ representation, where the explicit expression of Dirac matrices is:

$$\gamma^0 = \begin{pmatrix} I & 0 \\ 0 & -I \end{pmatrix} \quad \gamma^i = \begin{pmatrix} 0 & \sigma^i \\ -\sigma^i & 0 \end{pmatrix}$$

Appendix B

Resonances decay couplings

The amplitude describing the photo-production of a mesonic resonance X decaying to the $\pi^0 \eta$ final state has the form (Eq. 4.27):

$$A_{\lambda,h,h'}^X = (\beta \cdot A_{Regge}^{\lambda,h,h'}(s,t)) \cdot (g \cdot A_{Decay}(M_{\pi^0 \eta})) \cdot Y^{J,\lambda}(\theta, \phi) \quad , \quad (B.1)$$

where λ , h , and h' are, respectively, the photon, target, and recoil proton helicities. The main amplitude feature is the factorization between the *production* term and the *decay* term. The first, corresponding to A_{Regge} , was derived rigorously in the Regge framework of two-body scattering, for the process $\gamma + p \rightarrow p + X$. The second, instead, is motivated from a phenomenological description of the X resonance decay to the $\pi^0 \eta$ channel, that results in a Breit-Wigner form A_{decay} for the invariant mass dependence, and a proper spherical harmonics for the decay products angular distribution. In particular, the specific A_{decay} expression I used is normalized such that:

$$A_{decay} = \frac{M_X \Gamma_X}{(M_X^2 - M^2) - iM\Gamma(M)} \quad \rightarrow \quad A_{decay}(M = M_X) = i \quad (B.2)$$

As a result of this dual approach, the Regge coupling β involved in the production amplitude is unambiguously deduced from the theory, exploiting Regge factorization, while the decay coupling g depends on the particular A_{decay} functional form and normalization.

To derive g , I proceeded as follows. The ratio of the *total* cross-sections for the two reactions:

$$\mathcal{R}_2 : \quad \gamma + p \quad \rightarrow \quad p + X \quad (B.3)$$

$$\mathcal{R}_3 : \quad \gamma + p \quad \rightarrow \quad p + X \rightarrow p + \pi^0 + \eta \quad (B.4)$$

is given by the branching-ratio for the X resonance decay to the $\pi^0 \eta$ final state, i.e.:

$$\sigma_3 = \sigma_2 \cdot BR \quad (B.5)$$

Being $(\beta \cdot A_{Regge}(s,t))$ the two-body reaction amplitude, the two unpolarized differential cross-sections, already summed over the final state proton helicity, are:

$$d\sigma_2 = \frac{1}{64\pi F_I^2} |\beta \cdot A_{Regge}(s,t)|^2 dt \quad (B.6)$$

$$d\sigma_3 = \frac{2q}{64(2\pi)^4 F_I^2} |\beta \cdot A_{Regge}(s,t)|^2 \cdot |g \cdot A_{Decay}(M)|^2 dt dM \quad , \quad (B.7)$$

where q is the mesons break-up momentum in the X reference frame, and the decay-angle integration has already been carried out.

The total cross-sections are obtained by integrating the above expressions over the whole final state phase spaces. To perform the t -integral in the second expression, I made the following approximation. In principle, the kinematically allowed t -values depend on M , therefore the two integrations on t and M can not be factorized¹. However, since $|A_{Decay}|^2$ is strongly peaked at the resonance mass M_X , I assumed $t_{max,min}(M) = t_{max,min}(M_X)$. Therefore, making some simplifications, the g coupling is obtained:

$$\frac{1}{\pi}BR = \frac{2g^2}{(2\pi)^4} \int_{M_{min}}^{M_{max}} q |A_{Decay}(M)|^2 dM \quad \rightarrow \quad g = (2\pi)^{\frac{3}{2}} \sqrt{\frac{BR}{I}} \quad , \quad (\text{B.10})$$

with I the result of the M integral. The physical meaning of the above equation can be understood by approximating the Breit-Wigner expression $|A_{Decay}|^2$ with a Gaussian function, having the same FWHM Γ and the same height at the resonance mass, and then performing the integral analytically:

$$I \simeq \Gamma \cdot q^0 \quad \rightarrow \quad g \simeq (2\pi)^{\frac{3}{2}} \sqrt{\frac{BR}{\Gamma q_0}} \quad (\text{B.11})$$

As expected, the coupling g^2 is proportional to the inverse of the resonance width and to the branching ratio, so that the overall decay term reads:

$$|g \cdot A_{decay}|^2 \propto M_X^2 \Gamma_X BR \quad (\text{B.12})$$

Calculation results for the a_0 , a_2 , and $a_2(1700)$ states are reported in Tab. B.1, showing the comparison between the approximate analytical solution and the numerical I evaluation.

Resonance	Width Γ (GeV)	BR	$g_{analytical}$	$g_{numeric}$
$a_0(980)$	0.147 GeV	1	70.56 GeV ⁻¹	67.15 GeV ⁻¹
$a_2(1320)$	0.110 GeV	0.145	24.69 GeV ⁻¹	20.12 GeV ⁻¹
$a_2(1700)$	0.194 GeV	0.1	13.01 GeV ⁻¹	10.66 GeV ⁻¹

Table B.1: Decay couplings g .

¹ In the reaction $\gamma + p \rightarrow p + X(M)$, with M being the mass of the X system, the two kinematic limits on the momentum transferred t between the target and the recoil proton are:

$$|t|_{min} = (P_\gamma^{CM} - P_X^{CM})^2 - M^4/4s \quad (\text{B.8})$$

$$|t|_{max} = (P_\gamma^{CM} + P_X^{CM})^2 - M^4/4s \quad (\text{B.9})$$

Bibliography

- [1] M. Gell-Mann. “A schematic model of baryons and mesons”. In: *Physics Letters* 8.3 (1964), pp. 214–215.
- [2] G. Zweig. “An $SU(3)$ model for strong interaction symmetry and its breaking”. In: *CERN pre-print* (1964).
- [3] L. Burakovsky and L.P. Horwitz. “Mass spectrum of a meson nonet is linear”. In: *Foundations of Physics Letters* 9.6 (1996), pp. 561–574. URL: <http://dx.doi.org/10.1007/BF02190031>.
- [4] J. Beringer et al. In: *Phys. Rev. D* 86 (2012).
- [5] A. Chodos et al. “New extended model of hadrons”. In: *Phys. Rev. D* 9 (12 June 1974), pp. 3471–3495.
- [6] K. Johnson. “The M.I.T. Bag Model”. In: *Acta Phys. Polon.* B6 (1975), p. 865.
- [7] T. DeGrand et al. “Masses and other parameters of the light hadrons”. In: *Phys. Rev. D* 12 (7 Oct. 1975), pp. 2060–2076.
- [8] T. Barnes et al. “ $Q\bar{Q}G$ Hermaphrodite Mesons in the MIT Bag Model”. In: *Nucl.Phys.* B224 (1983), p. 241.
- [9] M. Chanowitz et al. “Hybrids: Mixed states of quarks and gluons”. In: *Nuclear Physics B* 222.2 (1983), pp. 211–244. ISSN: 0550-3213.
- [10] N. Isgur and J. Paton. “Flux-tube model for hadrons in QCD”. In: *Phys. Rev. D* 31 (11 June 1985), pp. 2910–2929.
- [11] F. E. Close and P. R. Page. “The production and decay of hybrid mesons by flux-tube breaking”. In: *Nuclear Physics B* 443.1-2 (1995), pp. 233–254.
- [12] R. P. Page, S. E. Swanson, and A. Szczepaniak. “Hybrid meson decay phenomenology”. In: *Phys.Rev.* D59 (1999), p. 034016. DOI: 10.1103/PhysRevD.59.034016. arXiv: [hep-ph/9808346](https://arxiv.org/abs/hep-ph/9808346) [hep-ph].
- [13] G.P. Lepage et al. “Constrained curve fitting”. In: *Nuclear Physics B - Proceedings Supplements* 106-107 (2002). LATTICE 2001 Proceedings of the XIXth International Symposium on Lattice Field Theory, pp. 12–20.
- [14] C. McNeile and C. Michael. “Mixing of scalar glueballs and flavor-singlet scalar mesons”. In: *Phys. Rev. D* 63 (11 May 2001), p. 114503.
- [15] C. McNeile. “Meson and Baryon Spectroscopy on a Lattice”. In: *Hadronic Physics from Lattice QCD*. Ed. by A. M. Green.
- [16] S. A. Gottlieb. “QCD spectrum - 1996”. In: *Nucl.Phys.Proc.Suppl.* 53 (1997), pp. 155–167. DOI: 10.1016/S0920-5632(96)00610-X. arXiv: [hep-lat/9608107](https://arxiv.org/abs/hep-lat/9608107) [hep-lat].

- [17] J. Dudek et al. “Toward the excited meson spectrum of dynamical QCD”. In: *Phys. Rev. D* 82 (3 Aug. 2010), p. 034508. DOI: 10.1103/PhysRevD.82.034508.
- [18] J. Dudek et al. “Isoscalar meson spectroscopy from lattice QCD”. In: *Phys. Rev. D* 83 (11 June 2011), p. 111502.
- [19] C. J. Morningstar et al. “The Glueball spectrum from an anisotropic lattice study”. In: *Phys.Rev. D* 60 (1999), p. 034509.
- [20] C. Bernard et al. “Exotic mesons in quenched lattice QCD”. In: *Phys. Rev. D* 56 (11 Dec. 1997), pp. 7039–7051.
- [21] P. Lacock and other. “Hybrid mesons from quenched QCD”. In: *Physics Letters B* 401.3-4 (1997), pp. 308–312. ISSN: 0370-2693. DOI: 10.1016/S0370-2693(97)00384-5.
- [22] C. Bernard et al. “Lattice calculation of 1^{-+} hybrid mesons with improved Kogut-Susskind fermions”. In: *Phys. Rev. D* 68 (7 Oct. 2003), p. 074505.
- [23] J.N. Hedditch et al. “ 1^{-+} exotic meson at light quark masses”. In: *Phys. Rev. D* 72 (11 Dec. 2005), p. 114507.
- [24] J. Kuti. “Exotica and the confining flux”. In: *Nuclear Physics B - Proceedings Supplements* 73.1-3 (1999), pp. 72–85. ISSN: 0920-5632.
- [25] C. McNeile and C. Michael. “Decay width of light quark hybrid meson from the lattice”. In: *Phys. Rev. D* 73 (7 Apr. 2006), p. 074506.
- [26] D. Aston et al. “The strange meson resonances observed in the reaction $K^{-}p \rightarrow \bar{K}^0 \pi^{+} \pi^{-}$ at 11 GeV/c”. In: *Nuclear Physics B* 292 (1987), pp. 693–713. ISSN: 0550-3213.
- [27] G. S. Adams et al. “Observation of a New $J^{PC} = 1^{-+}$ Exotic State in the Reaction $\pi^{P} \rightarrow \pi^{+} \pi^{-} \pi^{-} p$ at 18 GeV/c”. In: *Phys. Rev. Lett.* 81 (26 Dec. 1998), pp. 5760–5763.
- [28] S. U. Chung et al. “Exotic and $q\bar{q}$ resonances in the $\pi^{+} \pi^{-} \pi^{-}$ system produced in $\pi^{-} p$ collisions at 18 GeV/c”. In: *Phys. Rev. D* 65 (7 Mar. 2002), p. 072001.
- [29] G. M. Beladidze et al. “Study of $\pi^{-} N \rightarrow \eta \pi^{-} N$ and $\pi^{-} N \rightarrow \eta' \pi^{-} N$ reactions at 37 GeV/c”. In: *Physics Letters B* 313.1 2 (1993), pp. 276–282.
- [30] P. Abbon et al. “The COMPASS experiment at CERN”. In: *Nuclear Instruments and Methods in Physics Research Section A: Accelerators, Spectrometers, Detectors and Associated Equipment* 577.3 (2007), pp. 455–518. ISSN: 0168-9002.
- [31] T. H. Bauer et al. “The hadronic properties of the photon in high-energy interactions”. In: *Rev. Mod. Phys.* 50 (2 Apr. 1978), pp. 261–436.
- [32] A. Afanasev and P. R. Page. “Photoproduction and electroproduction of $J^{PC} = 1^{-+}$ exotics”. In: *Phys. Rev. D* 57 (11 June 1998), pp. 6771–6777.
- [33] A. P. Szczepaniak and M. Swat. “Role of photoproduction in exotic meson searches”. In: *Physics Letters B* 516.1-2 (2001), pp. 72–76.
- [34] G.R. Brookes et al. “A high resolution photon tagging system in the GeV region”. In: *Nuclear Instruments and Methods* 115.2 (1974), pp. 465–469. ISSN: 0029-554X. DOI: 10.1016/0029-554X(74)90248-1.
- [35] D.P. Barber et al. “A large aperture spectrometer for the study of multibody photoproduction in the incident energy range 1-5 GeV”. In: *Nuclear Instruments and Methods* 155.3 (1978), pp. 353–369.
- [36] C. W. Leemann, D. R. Douglas, and G. A. Krafft. “The Continuous Electron Beam Accelerator Facility: CEBAF at the Jefferson Laboratory”. In: *Ann.Rev.Nucl.Part.Sci.* 51 (2001), pp. 413–450. DOI: 10.1146/annurev.nucl.51.101701.132327.

- [37] D. I. Sober et al. “The Bremsstrahlung tagged photon beam in Hall B at JLab”. In: *Nucl.Instrum.Meth.* A440 (2000), pp. 263–284. DOI: [10.1016/S0168-9002\(99\)00784-6](https://doi.org/10.1016/S0168-9002(99)00784-6).
- [38] GlueX collaboration. *Mapping the Spectrum of Light Quark Mesons and Gluonic Excitations with Linearly Polarized Photons*. Proposal to Jefferson Laboratory PAC30. 2006.
- [39] CLAS collaboration. *Meson Spectroscopy with low Q^2 electron scattering in CLAS12*. Proposal to Jefferson Laboratory PAC37. 2011.
- [40] L. Bertolotto et al. “Results from $\bar{p}p \rightarrow \phi\phi$ at Jetset”. In: *Il Nuovo Cimento A Series 11* 107.11 (1994). URL: <http://dx.doi.org/10.1007/BF02733999>.
- [41] M. F. M. Lutz et al. “Physics Performance Report for PANDA: Strong Interaction Studies with Antiprotons”. In: (2009). arXiv: 0903.3905 [hep-ex].
- [42] E. Aker et al. “The Crystal Barrel spectrometer at LEAR”. In: *Nuclear Instruments and Methods in Physics Research Section A: Accelerators, Spectrometers, Detectors and Associated Equipment* 321.1-2 (1992), pp. 69–108. ISSN: 0168-9002.
- [43] C. Amsler et al. “High-statistics study of $f_0(1500)$ decay into $\pi^0 \pi^0$ ”. In: *Physics Letters B* 342.1-4 (1995), pp. 433–439. ISSN: 0370-2693.
- [44] F. E. Close and A. Kirk. “Implications of the glueball $q\bar{q}$ filter on the 1^{++} nonet”. In: *Z.Phys.* C76 (1997), pp. 469–474.
- [45] F. Close and A. Kirk. “A Glueball- $q\bar{q}$ filter in Central Hadron Production”. In: *Physics Letters B* 397.3-4 (1997), pp. 333–338. ISSN: 0370-2693.
- [46] T. A. Armstrong et al. “Observation of centrally produced $\vartheta/f_2(1720)$ in the reaction $p\bar{p} \rightarrow p_f(K\bar{K})p_s$ at 300 GeV/c”. In: *Phys. Lett. B* 227.CERN-EP-89-70 (May 1989), 186–190. 13 p.
- [47] S. Abatzis et al. “Observation of a narrow scalar meson at 1450 MeV in the reaction $p\bar{p} \rightarrow p_f(\pi^+\pi^-\pi^+\pi^-)p_s$ at 450 GeV/c using the CERN Omega spectrometer”. In: *Physics Letters B* 324.3-4 (1994), pp. 509–514. ISSN: 0370-2693. DOI: [http://dx.doi.org/10.1016/0370-2693\(94\)90231-3](http://dx.doi.org/10.1016/0370-2693(94)90231-3).
- [48] D. Barberis et al. “A kinematical selection of glueball candidates in central production”. In: *Physics Letters B* 397.3-4 (1997), pp. 339–344. ISSN: 0370-2693. DOI: [http://dx.doi.org/10.1016/S0370-2693\(97\)00223-2](http://dx.doi.org/10.1016/S0370-2693(97)00223-2).
- [49] D. Bisello et al. “The pion electromagnetic form factor in the time-like energy range $1.35 < \sqrt{s} < 2.4$ GeV”. In: *Physics Letters B* 220.1-2 (1989), pp. 321–327. ISSN: 0370-2693. DOI: [http://dx.doi.org/10.1016/0370-2693\(89\)90060-9](http://dx.doi.org/10.1016/0370-2693(89)90060-9). URL: <http://www.sciencedirect.com/science/article/pii/0370269389900609>.
- [50] M. R. Pennington D. Morgan and M. R. Whalley. “A compilation of data on two-photon reactions leading to hadron final states”. In: *Journal of Physics G Nuclear Physics* 20 (Aug. 1994), A1–A147.
- [51] A.D. Martin and T.D. Spearman. *Elementary Particle Theory*. North Holland Publishing Co., 1970.
- [52] M. Perl. *High Energy Hadron Physics*. John Wiley and Sons, 1975.
- [53] M. L. Goldberger and K. M. Watson. *Collision Theory*. John Wiley and Sons, 1965.
- [54] CLAS Collaboration. *CLAS12 Technical Design Report*. Tech. rep. Jefferson Laboratory, 2008.

- [55] D. Norman. “Scattering of Polarized Leptons at High Energy”. In: *Rev. Mod. Phys.* 41 (1 Jan. 1969), pp. 236–246. DOI: 10.1103/RevModPhys.41.236. URL: <http://link.aps.org/doi/10.1103/RevModPhys.41.236>.
- [56] K. Schilling and G. Wolf. “How to analyse vector-meson production in inelastic lepton scattering”. In: *Nuclear Physics B* 61 (1973), pp. 381–413. ISSN: 0550-3213. DOI: [http://dx.doi.org/10.1016/0550-3213\(73\)90371-4](http://dx.doi.org/10.1016/0550-3213(73)90371-4). URL: <http://www.sciencedirect.com/science/article/pii/0550321373903714>.
- [57] M. Atkinson et al. “A peak in the $\eta\omega$ mass spectrum from diffractive photoproduction”. In: *Z. Phys. C Particles and Fields* 34.3 (1987), pp. 303–306. ISSN: 0170-9739. DOI: 10.1007/BF01548811. URL: <http://dx.doi.org/10.1007/BF01548811>.
- [58] E. S. Ageev et al. “Gluon polarization in the nucleon from quasi-real photoproduction of high-p(T) hadron pairs”. In: *Phys.Lett.* B633 (2006), pp. 25–32. DOI: 10.1016/j.physletb.2005.11.049. arXiv: hep-ex/0511028 [hep-ex].
- [59] S. Chekanov et al. “Measurement of the photon proton total cross-section at a center-of-mass energy of 209-GeV at HERA”. In: *Nucl.Phys.* B627 (2002), pp. 3–28. DOI: 10.1016/S0550-3213(02)00068-8. arXiv: hep-ex/0202034 [hep-ex].
- [60] B. Andrieu et al. “Test beam results of the tungsten/quartz-fibre calorimeter for the luminosity measurement in H1”. In: (2000), pp. 121–130.
- [61] B. A. Mecking et al. “The CEBAF Large Acceptance Spectrometer (CLAS)”. In: *Nucl.Instrum.Meth.* A503 (2003), pp. 513–553. DOI: 10.1016/S0168-9002(03)01001-5.
- [62] Y. G. Sharabian et al. “A new highly segmented start counter for the CLAS detector”. In: *Nucl.Instrum.Meth.* A556 (2006), pp. 246–258.
- [63] M. D. Mestayer et al. “The CLAS drift chamber system”. In: *Nucl. Instrum. Methods Phys. Res.* A449.1-2 (2000), pp. 81–111.
- [64] E. S. Smith et al. “The time-of-flight system for CLAS”. In: *Nucl. Instrum. Methods Phys. Res.* A432 (1999), pp. 265–298.
- [65] M. Amarian et al. “The CLAS forward electromagnetic calorimeter”. In: *Nucl. Instrum. Methods Phys. Res.* A460 (2001), pp. 239–265. ISSN: 0168-9002.
- [66] Y. Giomataris et al. “MICROMEGAS: a high-granularity position-sensitive gaseous detector for high particle-flux environments”. In: *Nucl. Instrum. Methods Phys. Res.* A376.1 (1996), pp. 29–35. ISSN: 0168-9002. DOI: 10.1016/0168-9002(96)00175-1. URL: <http://www.sciencedirect.com/science/article/pii/0168900296001751>.
- [67] S. Aune et al. “Micromegas tracker project for CLAS12”. In: *Nucl. Instrum. Methods Phys. Res.* A604.1 (2009), pp. 53–55. ISSN: 0168-9002. DOI: 10.1016/j.nima.2009.01.047.
- [68] CLAS collaboration. *CLAS12 Forward Tagger (FT) technical design report*. Tech. rep. JLab, 2012.
- [69] CMS collaboration. *CMS Electromagnetic Calorimeter*. Tech. rep. Cern.
- [70] Zhou,D.C. and others (ALICE Collaboration). “PHOS, the ALICE-PHOton Spectrometer”. In: *J. Phys.* G34.8 (2007), S719.
- [71] PANDA Collaboration. *Technical Design Report for PANDA Electromagnetic Calorimeter (EMC)*. Tech. rep. 2008.
- [72] I. Bedlinskiy and others (CLAS Collaboration). *An Inner Calorimeter for CLAS/DVCS experiments*. Tech. rep.

- [73] I. Akushevich and others. “RADGEN 1.0. Monte Carlo Generator for Radiative Events in DIS on Polarized and Unpolarized Targets”. In: (1999). eprint: [hep-ph/9906408](http://arxiv.org/abs/hep-ph/9906408).
- [74] E. Auffray and others. “Performance of ACCOS, an automatic crystal quality control system for the PWO crystals of the CMS calorimeter”. In: *Nucl. Instrum. Methods Phys. Res., A* 456.3 (2001), pp. 325–41.
- [75] S. Agostinelli et al. “GEANT4—a simulation toolkit”. In: *Nuclear Instruments and Methods in Physics Research Section A: Accelerators, Spectrometers, Detectors and Associated Equipment* 506.3 (2003), pp. 250–303. ISSN: 0168-9002. DOI: [http://dx.doi.org/10.1016/S0168-9002\(03\)01368-8](http://dx.doi.org/10.1016/S0168-9002(03)01368-8). URL: <http://www.sciencedirect.com/science/article/pii/S0168900203013688>.
- [76] T. Ikagawa et al. “Study of large area Hamamatsu avalanche photodiode in a γ -ray scintillation detector”. In: *Nuclear Instruments and Methods in Physics Research Section A: Accelerators, Spectrometers, Detectors and Associated Equipment* 538 (2005), pp. 640–650.
- [77] F. Cavallari et al. “Progress on Avalanche Photodiodes as photon detectors for PbWO₄ crystals in the CMS experiment”. In: *Nuclear Physics B - Proceedings Supplements* 61.3 (1998), pp. 449–455. ISSN: 0920-5632. DOI: 10.1016/S0920-5632(97)00601-4. URL: <http://www.sciencedirect.com/science/article/pii/S0920563297006014>.
- [78] H. Dong et al. “Integrated tests of a high speed VXS switch card and 250 MSPS flash ADCs”. In: *Nuclear Science Symposium Conference Record, 2007. NSS '07. IEEE*. Vol. 1. 2007-Nov. 3, pp. 831–833.
- [79] F. Cipro. “Studio della risposta del prototipo di un calorimetro in PbWO₄ per CLAS12”. MA thesis. Università degli Studi di Genova, 2012.
- [80] R. Brun and F. Rademacher. “ROOT: An object oriented data analysis framework”. In: *Nucl. Instrum. Meth.* A389 (1997), pp. 81–86. DOI: 10.1016/S0168-9002(97)00048-X.
- [81] *GTK C libraries*. URL: <http://www.gtk.org/>.
- [82] C. Timmer. *ET system*. URL: [https://coda.jlab.org/wiki/index.php/ET_\(Event_Transfer\)_System](https://coda.jlab.org/wiki/index.php/ET_(Event_Transfer)_System).
- [83] *CODA*. URL: https://coda.jlab.org/wiki/index.php/Main_Page.
- [84] M. Ungaro. *GEMC*. URL: <https://gemc.jlab.org/gemc/Home.html>.
- [85] A. Casale. “Realizzazione e studio delle prestazioni del prototipo del Forward Tagger per il rivelatore CLAS12”. MA thesis. Università degli Studi di Genova, 2011.
- [86] G. Mazzitelli et al. “Commissioning of the DAΦNE beam test facility”. In: *Nuclear Instruments and Methods in Physics Research A* 515 (2003), pp. 524–542.
- [87] B. Buonomo et al. “Performance and upgrade of the DAΦNE beam test facility (BTF)”. In: *Nuclear Science Symposium Conference Record, 2004 IEEE*. Vol. 4. 2004, pp. 2240–2243.
- [88] S. U. Chung. “Techniques of amplitude analysis for two-pseudoscalar systems”. In: *Phys. Rev. D* 56 (11 Dec. 1997), pp. 7299–7316.
- [89] I. Horn et al. “Study of the reaction $\gamma p \rightarrow p\pi^0\eta$ ”. In: *The European Physical Journal A* 38.2 (2008), pp. 173–186. ISSN: 1434-6001. DOI: 10.1140/epja/i2008-10657-7.
- [90] W. D. Apel et al. “Analysis of the reaction $\pi^- p \rightarrow \pi^0\eta n$ at 40 GeV/c beam momentum”. In: *Nucl. Phys.* B193 (1981), pp. 269–286.
- [91] D. Alde et al. “Evidence for a 1^{-+} exotic meson”. In: *Physics Letters B* 205.2 3 (1988), pp. 397–400.

- [92] S. F. Tuan et al. “Comments on the evidence for a 1^{-+} exotic meson”. In: *Physics Letters B* 213.4 (1988), pp. 537–540.
- [93] H. Aoyagi et al. “Study of the $\eta\pi^{-}$ system in the $\pi^{-}p$ reaction at 6.3 GeV/c”. In: *Physics Letters B* 314.2 (1993), pp. 246–254.
- [94] S. U. Chung et al. “Evidence for exotic $J(PC) = 1^{-+}$ meson production in the reaction $\pi^{-}p \rightarrow \eta\pi^{-}p$ at 18 GeV/c”. In: *Phys.Rev.* D60 (1999), p. 092001. arXiv: [hep-ex/9902003](https://arxiv.org/abs/hep-ex/9902003) [[hep-ex](https://arxiv.org/abs/hep-ex)].
- [95] A. R. Dzierba et al. “A Study of the $\eta\pi^0$ spectrum and search for a $J^{PC} = 1^{-+}$ exotic meson”. In: *Phys. Rev.* D67 (2003), p. 094015. DOI: [10.1103/PhysRevD.67.094015](https://doi.org/10.1103/PhysRevD.67.094015). arXiv: [hep-ex/0304002](https://arxiv.org/abs/hep-ex/0304002) [[hep-ex](https://arxiv.org/abs/hep-ex)].
- [96] A. Abele et al. “Exotic $\eta\pi$ state in $\bar{p}d$ annihilation at rest into $\pi^{-}\pi^0\eta p_{spectator}$ ”. In: *Physics Letters B* 423.1-2 (1998), pp. 175–184. ISSN: 0370-2693.
- [97] A. Abele et al. “Evidence for a $\eta\pi$ -P-wave in $p\bar{p}$ -annihilations at rest into $\pi^0\pi^0\eta$ ”. In: *Physics Letters B* 446.3-4 (1999), pp. 349–355.
- [98] T. Schlüter. “The $\pi^{-}\eta$ and $\pi^{-}\eta'$ Systems in Exclusive 190 GeV $\pi^{-}p$ Reactions at COMPASS (CERN)”. PhD thesis. Ludwig-Maximilians-Universität München, June 2012.
- [99] D. Schott. “A search for an exotic meson in the $\gamma + P \rightarrow \Delta^{++} + \pi^{-} + \eta$ reaction”. PhD thesis. Florida International University, 2012.
- [100] A. D. Martin and T. D. Spearman. “Elementary Particle Theory”. In: Amsterdam: North-Holland Publishing Company, 1970. Chap. 7.2.3.
- [101] T. Regge. “Introduction to complex orbital momenta”. In: *Il Nuovo Cimento Series 10* 14.5 (1959), pp. 951–976. ISSN: 0029-6341.
- [102] T. Regge. “Bound states, shadow states and Mandelstam representation”. In: *Il Nuovo Cimento Series 10* 18.5 (1960), pp. 947–956. ISSN: 0029-6341.
- [103] R. Blankenbecler and M. L. Goldberger. “Behavior of scattering amplitudes at high energies, bound states, and resonances”. In: *Phys.Rev.* 126 (1962), pp. 766–786. DOI: [10.1103/PhysRev.126.766](https://doi.org/10.1103/PhysRev.126.766).
- [104] G. F. Chew and S. C. Frautschi. “Principle of Equivalence for all Strongly Interacting Particles within the S -Matrix Framework”. In: *Phys. Rev. Lett.* 7 (10 Nov. 1961), pp. 394–397. DOI: [10.1103/PhysRevLett.7.394](https://doi.org/10.1103/PhysRevLett.7.394). URL: <http://link.aps.org/doi/10.1103/PhysRevLett.7.394>.
- [105] G. F. Chew and S. C. Frautschi. “Regge Trajectories and the Principle of Maximum Strength for Strong Interactions”. In: *Phys. Rev. Lett.* 8 (1 Jan. 1962), pp. 41–44. DOI: [10.1103/PhysRevLett.8.41](https://doi.org/10.1103/PhysRevLett.8.41). URL: <http://link.aps.org/doi/10.1103/PhysRevLett.8.41>.
- [106] V. N. Gribov and I. Ya. Pomeranchuk. “Complex orbital momenta and the relation between the cross-sections of various processes at high-energies”. In: *Sov.Phys.JETP* 15 (1962), p. 788L. DOI: [10.1103/PhysRevLett.8.343](https://doi.org/10.1103/PhysRevLett.8.343).
- [107] A. C. Irving and R. P. Worden. “Regge phenomenology”. In: *Physics Reports* 34.3 (1977), pp. 117–231. ISSN: 0370-1573. DOI: [http://dx.doi.org/10.1016/0370-1573\(77\)90010-2](https://doi.org/10.1016/0370-1573(77)90010-2). URL: <http://www.sciencedirect.com/science/article/pii/0370157377900102>.
- [108] R. J. Eden. “Regge poles and elementary particles”. In: *Reports on Progress in Physics* 34.3 (1971), p. 995.
- [109] S. Donnachie et al. *Pomeron Physics and QCD*. Cambridge University Press, 2002.

- [110] T. W. B. Kibble. “Feynman Rules for Regge Particles”. In: *Phys. Rev.* 131 (5 Sept. 1963), pp. 2282–2291. DOI: 10.1103/PhysRev.131.2282. URL: <http://link.aps.org/doi/10.1103/PhysRev.131.2282>.
- [111] C. Hong-Mo et al. “A Regge model for high-energy collisions producing three final particles”. English. In: *Il Nuovo Cimento A Series 10* 49.1 (1967), pp. 157–182. ISSN: 0369-3546. DOI: 10.1007/BF02739081. URL: <http://dx.doi.org/10.1007/BF02739081>.
- [112] C. Hong-Mo et al. “Double Regge analysis of high-energy experiments producing three final particles”. English. In: *Il Nuovo Cimento A Series 10* 51.3 (1967), pp. 696–716. ISSN: 0369-3546. DOI: 10.1007/BF02721738. URL: <http://dx.doi.org/10.1007/BF02721738>.
- [113] T. Shimada, A. D. Martin, and A. C. Irving. “Double Regge Exchange Phenomenology”. In: *Nucl.Phys.* B142 (1978), p. 344. DOI: 10.1016/0550-3213(78)90209-2.
- [114] K. Igi. “ $\pi - N$ Scattering Length and Singularities in the Complex J Plane”. In: *Phys. Rev. Lett.* 9 (2 July 1962), pp. 76–79. DOI: 10.1103/PhysRevLett.9.76. URL: <http://link.aps.org/doi/10.1103/PhysRevLett.9.76>.
- [115] K. Igi. “Two Vacuum Poles and Pion-Nucleon Scattering”. In: *Phys. Rev.* 130 (2 Apr. 1963), pp. 820–827. DOI: 10.1103/PhysRev.130.820. URL: <http://link.aps.org/doi/10.1103/PhysRev.130.820>.
- [116] V. Mathieu. Private Communication.
- [117] S. U. Chung. “Formulas for Angular-Momentum Barrier Factors”. In: *BNL preprint* (2008). BNL-QGS-06-101.
- [118] V. Mathieu and A. P. Szczepaniak. Private Communication.
- [119] S. U. Chung. “Formulas for Partial-Wave Analysis (Version V)”. In: *BNL preprint* (2010). BNL-QGS-06-102.
- [120] *g12 run period web site*. URL: https://clasweb.jlab.org/rungroups/g12/wiki/index.php/Run_Parameters.
- [121] C. Bookwalter. “A search for exotic mesons in $\gamma p \rightarrow \pi^+ \pi^+ \pi^- n$ with CLAS at Jefferson Lab”. PhD thesis. Florida State University, College of Arts and Sciences, 2012.
- [122] J. Ball and E. Pasyuk. *Photon Flux Determination Trough Sampling of “out-of-time” hits with the Hall B Photon Tagger*. CLAS note. 2005.
- [123] A. P. Szczepaniak. Private Communication.
- [124] M. Shepherd H. Matevosyan R. Mitchell. *AmpTools*. 2011. URL: http://amptools.sourceforge.net/index.php/Main_Page.
- [125] V.M. Budnev et al. “The two-photon particle production mechanism. Physical problems. Applications. Equivalent photon approximation”. In: *Physics Reports* 15.4 (1975), pp. 181–282. ISSN: 0370-1573. DOI: [http://dx.doi.org/10.1016/0370-1573\(75\)90009-5](http://dx.doi.org/10.1016/0370-1573(75)90009-5). URL: <http://www.sciencedirect.com/science/article/pii/0370157375900095>.
- [126] F. James. *Monte Carlo Phase Space*. Tech. rep. CERN 68-15. CERN, 1968.
- [127] O. Skjeggstad. “Notes on Phase Space”. In: *3rd CERN School of Physics*. Vol. 2. 1964, pp. 1–73.
- [128] P. R. Auvil and J. J. Brehm. “Wave Functions for Particles of Higher Spin”. In: *Physical Review* 145 (May 1966), pp. 1152–1153. DOI: 10.1103/PhysRev.145.1152.
- [129] U. Jezuita-Dabrowska and M. Krawczyk. *Longitudinal virtual photons and the interference terms in ep collisions*. 2002. arXiv: [hep-ph/0211112](https://arxiv.org/abs/hep-ph/0211112) [hep-ph].

Ringraziamenti

Durante i tre anni di Dottorato ho avuto la possibilità ed il piacere di lavorare con moltissime persone, senza le quali non avrei potuto portare a termine questo lavoro. Grazie a tutti voi per tutto l'aiuto ed il supporto fornitomi, e scusate in anticipo se dimenticherò qualcuno in queste righe!

Marco, sicuramente sei la persona che maggiormente voglio ringraziare, per avermi seguito in questi tre anni, ed avermi dato la possibilità di lavorare con te in modo stimolante ed interessante. Da te ho imparato moltissimo, ed ogni giorno ho potuto capire qualcosa di nuovo, anche su concetti apparentemente "semplici", dei quali pensavo di aver colto tutti gli aspetti. Voglio soprattutto ringraziarti per avermi sempre coinvolto completamente in tutte le fasi di progettazione e realizzazione di MesonEx, ascoltando e discutendo assieme le mie idee, e per aver sempre valorizzato al massimo il mio lavoro. Grazie!

Voglio ringraziare il prof. Mauro Taiuti per le stimolanti discussioni avute insieme, in particolare per l'idea di includere in questo lavoro anche l'analisi dei dati sperimentali misurati da CLAS, senza limitarsi alla sola simulazione MonteCarlo. Anche se questo ha richiesto più lavoro (e fatica!), sono certo che il lavoro finale è così risultato molto più completo.

Adam, it was an unique opportunity to work with you during these three years. I can't count the number of things I learned discussing with you, and I really need to thank you for your patience in replying to all my questions during our weekly meetings, very precisely and concretely. You transmitted me the theoretical concepts and ideas in meson spectroscopy in fascinating way, giving me the possibility to deeply appreciate them.

Raffaella, voglio ringraziarti per avermi sempre seguito in questo lavoro come se fossi, a tutti gli effetti, la mia "terza" relatrice, lavorando insieme in modo affiatato. Lavorare con te e Marco è stato molto piacevole e stimolante, e spero di poter continuare a farlo anche nel prossimo futuro.

Vincent, grazie per l'aiuto che mi hai dato nella parte teorica di questo lavoro, e per aver risposto ad ogni mia richiesta sempre e subito!

Grazie a tutti i membri della sezione INFN di Genova con i quali ho lavorato. Grazie ai tecnici di Gruppo 3, Giacomo, Franco, Andrea, e Valerio, per tutto l'enorme supporto fornito, e per aver sempre accettato le richieste "per ieri" che vi abbiamo fatto! Grazie ai membri del servizio elettronica, Paolo, Fabio e Pino, per la possibilità che mi hanno dato di collaborare insieme a loro nei diversi progetti per MesonEx e per le discussioni che abbiamo avuto su tutte le schede che abbiamo realizzato e testato insieme. Infine, grazie ad Misha, Marco, Erica, Marco, Vladimir, Barbara, Andrea per il meraviglioso gruppo di lavoro nel quale ho potuto svolgere questa tesi.

L'ultimo ringraziamento, il più importante, è per la persona speciale ed unica che mi ha sostenuto, consolato e sopportato durante i tre anni di dottorato. Laura, ho raggiunto questo importante obiettivo solo perché tu eri al mio fianco, e senza di te non sarei mai giunto fino in fondo. Ti ringrazio per avermi sempre incoraggiato, per aver sopportato il fatto che lavorassi fino a tardi o durante i week-end, per aver pazientemente ascoltato le mie presentazioni e la conseguente mia arrabbiatura quando mi suggerivi dei cambiamenti, senza mai avermi fatto pesare questo in nessun modo. Spero,

ora, di poter “ricambiare” in qualche modo tutto quello che tu hai fatto per me. Ti devo davvero tanto, tantissimo.